SAIMM
JOURNAL OF THE SOUTHERN AFRICAN INSTITUTE OF MINING AND METALLURGY
FOUNDED 1894
VOLUME 116 NO. 6 JUNE 2016

UKWAZI
www.ukwazi.com

Independent mining advisers

	Commodity					Mining method			
Coal	Thermal Coal	Metallurgical Coal	Anthracite			Open pit	UG Coal	Strip mining	
Base metals	27 Co 58.9 Cobalt	28 Ni 58.6 Nickel	29 Cu 63.5 Copper	30 Zn 65.3 Zinc	82 Pb 207.2 Lead	Open pit	UG massive	UG narrow tabular	UG mechanised
Bulk minerals	13 Al 26.9 Aluminium	23 V 50.9 Vanadium	24 Cr 51.9 Chromium	25 Mn 54.9 Manganese	26 Fe 55.8 Iron	Open pit	UG massive	UG mechanised	Strip mining
Precious metals	45 Rh 102.9 Rhodium	46 Pd 106.4 Palladium	78 Pt 195.1 Platinum	79 Au 196.9 Gold	92 U 238 Uranium	Open pit	UG narrow tabular	UG massive	UG mechanised
Mineral sands & industrial minerals	$ZrSiO_4$ Zircon	$FeTiO_3$ Ilmenite	TiO_2 Rutile	Aggregates	Industrial minerals	Open pit	Wet mining	Dry mining	Strip mining
Diamonds & gemstones	Diamonds	Gemstones				Open pit	UG massive	Dry mining	

We are a group of 35 mining engineers, mine planners and project managers and take pride in our 12 year track record. Our in-house experience levels range from mine managers to mine planners. They all have practical mining experience to understand the real world constraints and opportunities that exist on mines. Our best-in-class, proven technical planning processes has withstood all external audits and reviews over the years. Our unique offering is that mining is our core business focus. We group our experts in teams based on their operational and expert technical experience on a commodity and mining method. We prepare and manage feasibility studies, our CP's and QP's compile compliant public technical reports, and we do on site mine planning and conduct on site mining production turnarounds.

Switch 5002283A

When moving tonnes of earth, we measure every detail, right down to the millimetre.

Tel: +27 11 606 0000
email: company.email@aelms.com
web: www.aelminingservices.com

inherently AECI

AEL Mining Services

OFFICE BEARERS AND COUNCIL FOR THE 2015/2016 SESSION

Honorary President
Mike Teke
President, Chamber of Mines of South Africa

Honorary Vice-Presidents
Mosebenzi Zwane
Minister of Mineral Resources, South Africa

Rob Davies
Minister of Trade and Industry, South Africa

Naledi Pandor
Minister of Science and Technology, South Africa

President
R.T. Jones

President Elect
C. Musingwini

Vice-Presidents
S. Ndlovu
A.S. Macfarlane

Immediate Past President
J.L. Porter

Honorary Treasurer
C. Musingwini

Ordinary Members on Council

Z. Botha
V.G. Duke
I.J. Geldenhuys
M.F. Handley
W.C. Joughin
M. Motuku
D.D. Munro
G. Njowa
A.G. Smith
M.H. Solomon
J.D. Steenkamp
M.R. Tlala
D. Tudor
D.J. van Niekerk

Past Presidents Serving on Council

N.A. Barcza
R.D. Beck
J.R. Dixon
M. Dworzanowski
F.M.G. Egerton
H.E. James
G.V.R. Landman
J.C. Ngoma
S.J. Ramokgopa
M.H. Rogers
G.L. Smith
W.H. van Niekerk

Branch Chairmen

Botswana	L.E. Dimbungu
DRC	S. Maleba
Johannesburg	I. Ashmole
Namibia	N.M. Namate
Northern Cape	C.A. van Wyk
Pretoria	P. Bredell
Western Cape	A. Mainza
Zambia	D. Muma
Zimbabwe	S. Ndiyamba
Zululand	C.W. Mienie

Corresponding Members of Council

Australia:	I.J. Corrans, R.J. Dippenaar, A. Croll, C. Workman-Davies
Austria:	H. Wagner
Botswana:	S.D. Williams
United Kingdom:	J.J.L. Cilliers, N.A. Barcza
USA:	J-M.M. Rendu, P.C. Pistorius

PAST PRESIDENTS

*Deceased

* W. Bettel (1894–1895)
* A.F. Crosse (1895–1896)
* W.R. Feldtmann (1896–1897)
* C. Butters (1897–1898)
* J. Loevy (1898–1899)
* J.R. Williams (1899–1903)
* S.H. Pearce (1903–1904)
* W.A. Caldecott (1904–1905)
* W. Cullen (1905–1906)
* E.H. Johnson (1906–1907)
* J. Yates (1907–1908)
* R.G. Bevington (1908–1909)
* A. McA. Johnston (1909–1910)
* J. Moir (1910–1911)
* C.B. Saner (1911–1912)
* W.R. Dowling (1912–1913)
* A. Richardson (1913–1914)
* G.H. Stanley (1914–1915)
* J.E. Thomas (1915–1916)
* J.A. Wilkinson (1916–1917)
* G. Hildick-Smith (1917–1918)
* H.S. Meyer (1918–1919)
* J. Gray (1919–1920)
* J. Chilton (1920–1921)
* F. Wartenweiler (1921–1922)
* G.A. Watermeyer (1922–1923)
* F.W. Watson (1923–1924)
* C.J. Gray (1924–1925)
* H.A. White (1925–1926)
* H.R. Adam (1926–1927)
* Sir Robert Kotze (1927–1928)
* J.A. Woodburn (1928–1929)
* H. Pirow (1929–1930)
* J. Henderson (1930–1931)
* A. King (1931–1932)
* V. Nimmo-Dewar (1932–1933)
* P.N. Lategan (1933–1934)
* E.C. Ranson (1934–1935)
* R.A. Flugge-De-Smidt (1935–1936)
* T.K. Prentice (1936–1937)
* R.S.G. Stokes (1937–1938)
* P.E. Hall (1938–1939)
* E.H.A. Joseph (1939–1940)
* J.H. Dobson (1940–1941)
* Theo Meyer (1941–1942)
* John V. Muller (1942–1943)
* C. Biccard Jeppe (1943–1944)
* P.J. Louis Bok (1944–1945)
* J.T. McIntyre (1945–1946)
* M. Falcon (1946–1947)
* A. Clemens (1947–1948)
* F.G. Hill (1948–1949)
* O.A.E. Jackson (1949–1950)
* W.E. Gooday (1950–1951)
* C.J. Irving (1951–1952)
* D.D. Stitt (1952–1953)
* M.C.G. Meyer (1953–1954)
* L.A. Bushell (1954–1955)
* H. Britten (1955–1956)
* Wm. Bleloch (1956–1957)
* H. Simon (1957–1958)
* M. Barcza (1958–1959)
* R.J. Adamson (1959–1960)
* W.S. Findlay (1960–1961)
  D.G. Maxwell (1961–1962)
* J. de V. Lambrechts (1962–1963)
* J.F. Reid (1963–1964)
* D.M. Jamieson (1964–1965)
* H.E. Cross (1965–1966)
* D. Gordon Jones (1966–1967)
* P. Lambooy (1967–1968)
* R.C.J. Goode (1968–1969)
* J.K.E. Douglas (1969–1970)
* V.C. Robinson (1970–1971)
* D.D. Howat (1971–1972)
  J.P. Hugo (1972–1973)
* P.W.J. van Rensburg (1973–1974)
* R.P. Plewman (1974–1975)
* R.E. Robinson (1975–1976)
* M.D.G. Salamon (1976–1977)
* P.A. Von Wielligh (1977–1978)
* M.G. Atmore (1978–1979)
* D.A. Viljoen (1979–1980)
* P.R. Jochens (1980–1981)
  G.Y. Nisbet (1981–1982)
  A.N. Brown (1982–1983)
* R.P. King (1983–1984)
  J.D. Austin (1984–1985)
  H.E. James (1985–1986)
  H. Wagner (1986–1987)
* B.C. Alberts (1987–1988)
  C.E. Fivaz (1988–1989)
  O.K.H. Steffen (1989–1990)
* H.G. Mosenthal (1990–1991)
  R.D. Beck (1991–1992)
  J.P. Hoffman (1992–1993)
* H. Scott-Russell (1993–1994)
  J.A. Cruise (1994–1995)
  D.A.J. Ross-Watt (1995–1996)
  N.A. Barcza (1996–1997)
* R.P. Mohring (1997–1998)
  J.R. Dixon (1998–1999)
  M.H. Rogers (1999–2000)
  L.A. Cramer (2000–2001)
* A.A.B. Douglas (2001–2002)
  S.J. Ramokgopa (2002-2003)
  T.R. Stacey (2003–2004)
  F.M.G. Egerton (2004–2005)
  W.H. van Niekerk (2005–2006)
  R.P.H. Willis (2006–2007)
  R.G.B. Pickering (2007–2008)
  A.M. Garbers-Craig (2008–2009)
  J.C. Ngoma (2009–2010)
  G.V.R. Landman (2010–2011)
  J.N. van der Merwe (2011–2012)
  G.L. Smith (2012–2013)
  M. Dworzanowski (2013–2014)
  J.L. Porter (2014–2015)

Honorary Legal Advisers
Van Hulsteyns Attorneys

Auditors
Messrs R.H. Kitching

Secretaries

The Southern African Institute of Mining and Metallurgy
Fifth Floor, Chamber of Mines Building
5 Hollard Street, Johannesburg 2001 • P.O. Box 61127, Marshalltown 2107
Telephone (011) 834-1273/7 • Fax (011) 838-5923 or (011) 833-8156
E-mail: journal@saimm.co.za

Typeset and Published by
The Southern African Institute of Mining and Metallurgy
P.O. Box 61127
Marshalltown 2107
Telephone (011) 834-1273/7
Fax (011) 838-5923
E-mail: journal@saimm.co.za

Printed by
Camera Press, Johannesburg

Advertising Representative
Barbara Spence
Avenue Advertising
Telephone (011) 463-7940
E-mail: barbara@avenue.co.za
The Secretariat
The Southern African Institute of Mining and Metallurgy

ISSN 2225-6253 (print)
ISSN 2411-9717 (online)

SAIMM
JOURNAL OF THE SOUTHERN AFRICAN INSTITUTE OF MINING AND METALLURGY
VOLUME 116 NO. 6 JUNE 2016

Contents

Journal Comment

Copper Cobalt Africa 6–8 July 2015

The African Copper Belt has experienced a huge resurgence of activity in the past decade following many years of political and economic instability. Today, an impressive proportion of capital spending, project development, operational expansions, and metal value production in the Southern African mining industry are occurring in this region. The geology and mineralogy of the ores differ significantly from those in other major copper-producing regions of the world, often having very high grades as well as the presence of cobalt. Both mining and metallurgy present some unique difficulties, not only in the technical arena, but also with respect to logistics and supply chain, human capital, community engagement, and legislative issues. With an increasingly mature industry developing in this region, the Metallurgy Technical Programme Committee took the decision to host the inaugural *Copper Cobalt Africa* conference, which also incorporated the *Eighth SAIMM Base Metals Conference*.

The conference was held in Livingstone, Zambia, a spectacular venue on the banks of the mighty Zambezi River and within walking distance of the world-famous Mosi-oa-Tunya (the *Smoke that Thunders* – better known as Victoria Falls). Despite an extremely difficult environment in the mining industry, interest in the conference was strong, consolidating the perception that this region is poised to become the leading global primary copper and cobalt producer in future years. The 54 papers presented represented authors from six continents and fifteen countries. The best of these are published for wider dissemination in this issue of the Journal.

The tone of the conference was set by the excellent keynote address of Jackson Sikamo, President of the Zambian Chamber of Mines, who provided an overview of the history of the Zambian mining industry (from private ownership, through nationalisation, and subsequent reprivatisation), and included views on challenges currently faced and suggestions as to how the industry can be nurtured to continue being a major driver for the Zambian economy and major player in the international copper mining business. Commissioning and ramp-up of the African Copper Belt's flagship operation, Tenke Fungurume Mining Company, was discussed by Scot Sandoval (Freeport McMoRan, USA), focussing particularly on electrowinning improvements that enabled current efficiency of 92% to be achieved at a current density of 400 A/m2, which is amongst one of the highest current densities employed for copper electrowinning worldwide. Other keynote presentations included contributions on recent developments at Glencore's Mopani operation by CEO Johan Jansen (Zambia), the successful commissioning and ramp-up of Tiger Resources' Kipoi heap leaching operation by Brendan Moseley (Democratic Republic of Congo), an overview of international best practice in Operations & Maintenance by Rebecca Siwale of FLSmidth (USA), and an engineering vendor's insights into project development on the Copper Belt over the last fifteen years by John Parker of Process Ideas (South Africa).

The papers presented in this issue reflect the quality and diversity of the conference proceedings, ranging from fundamental research studies, through modelling and flowsheet and project development, to plant and process optimisation. Courtney Young and Jesse Bowden of Montana Tech (USA) used electrochemical methods to further understanding of the mechanism of xanthate adsorption on chalcopyrite surfaces; Thandazile Moyo and Jochen Petersen of the University of Cape Town (South Africa) also used electroanalytical techniques to examine the leaching of chalcopyrite in ammonium solutions. Fadeela Salojee and Frank Crundwell (CM Solutions, South Africa) have derived an autoclave model combining mass,

Rodney Jones (President-Elect of SAIMM), Kathy Sole (Conference Chair) and Jackson Sikamo (President of the Zambian Chamber of Mines) at the opening of the conference. (Photograph courtesy of Barry Wills.)

Journal Comment *(continued)*

energy, and population balances for optimising the design of pressure leaching circuits for treating sulphide ores and concentrates. Peter Cole and colleagues (Cytec Industries) discussed the causes and mitigation of aqueous-in-organic entrainment in solvent extraction, a phenomenon that contributes to deteriorating electrolyte quality. A useful overview of the performance and behaviour of lead anodes for base-metals electrowinning, including practical information that is seldom reported, was given by Abbas Mirza and colleagues of RSR Technologies (USA).

New projects and flowsheet developments were also highlighted. Michael Valenta and Barbara Mulcahy (Metallicon Process Consulting, South Africa) described the development of a geometallurgical model for a copper concentrator in the Kalahari Copper Belt of Botswana, highlighting the synergies to project advancement when geology, mining, and metallurgy disciplines are all involved at early stages of the project. Vongani Nkuna and colleagues from Ivanhoe Mining Company discussed aspects of the metallurgical flowsheet proposed for the Giant Kamoa project in the Democratic Republic of Congo, which is ranked as the world's largest undeveloped high-grade copper deposit.

With respect to current operations, Kathy Sole (independent consultant, South Africa) and Owen Tinkler (Cytec Solvay, USA) reviewed the status of copper solvent extraction on the Copper Belt and its unique challenges compared with other global operations. Optimisation of plant operations was covered in a paper by Chanda Ngulube and colleagues from Kansanshi Mine (Zambia), which describes modelling and medication of the concentrator circuit to adapt to effectively treating increasingly complex mixed oxide–sulphide transitional ores. Justin Hagemann and Max Pelser provided a fascinating overview of Rustenburg Base Metal Refiners' response to debottlenecking with minimal capital expenditure while expanding production from 21 kt/a to 33 kt/a nickel, based on a fundamental and theoretical approach to the problem and that ultimately culminated in a successful commercially implemented solution.

The conference was attended by some 180 delegates from nineteen countries, comprising researchers and academics, mining services professionals, vendors and technology suppliers, operations personnel, and consultants. Tremendous support was also received from sponsors, with demand for sponsorship and exhibition opportunities outstripping availability. Following the success of this inaugural event, SAIMM has great pleasure in announcing that the *Second Copper Cobalt Africa Conference* will take place in July 2018.

The sun sets in Africa over the Zambezi River. (Photograph courtesy of Barry Wills.)

Delegates from the USA, Zambia, and DRC at the Welcome Event on the banks of the Zambezi River, including keynote speakers Rebecca Siwale (second from right) and Jackson Sikamo (right). (Photograph courtesy of Barry Wills.)

K.C. Sole
Chair of the Organising Committee

Perils of Conferencing

Many people who haven't travelled on business have the impression that it is a rather glamorous and pleasant task to attend a conference. And, of course, it can be wonderful to visit an interesting place for a few days, and come back refreshed with new ideas and perspectives, but this isn't the whole story. There is also the downside of cramped long-distance flights, disturbed sleeping patterns occasioned by differences in time zones, unfamiliar food, and lack of exercise. The American comedian Fred Allen (who incidentally was born in 1894, the same year that SAIMM was founded) said, rather cynically that 'A conference is a gathering of people who singly can do nothing, but together can decide that nothing can be done.' He also said 'I like long walks, especially when they are taken by people who annoy me.' However, all things considered, conferences still provide a great opportunity to exchange technical information, and to network with one's peers.

While it is true that all activities in life have some associated risk, attending or holding a conference is not usually ranked very highly among life's risky behaviours.

I have a friend, Mike, who travelled to Turkey in 2001 to attend Metal Bulletin's 12th International Iron Ore Symposium in Istanbul, along with about 250 delegates from 33 countries. The conference was to be held in the splendidly situated Swissotel overlooking the Bosphorus. On his way to the conference, Mike's luggage went missing, but he was hopeful that it would eventually find its way to the conference hotel. Not long after falling asleep on the night before the conference, he was woken by a phone call, around 1 am, from the hotel reception. The caller said he should come down to the lobby, as his life was in danger because the hotel had been stormed by Chechnyan gunmen. Mike initially thought that this must be some sort of practical joke. After looking out of his hotel window and seeing armoured vehicles in the street, he realized that this was no joke at all. He quickly dressed and went to the elevator which had a man with a shotgun inside. In the lobby, there was broken glass everywhere, and about 120 guests were held hostage and ordered to lie on the floor in case they were caught in any crossfire. One delegate from Iscor had a shotgun held to his head. The hotel was soon surrounded by hundreds of police, and a twelve-hour stand-off ensued. The 13 hostage-takers were supporters of independence for Chechnya, and were protesting at Russian attacks in Chechnya. The hostages were treated reasonably well, and after two or three hours were given water to drink and bread to eat. During the long wait, Chechnyan national music was played. After the Turkish interior minister held talks with the gunmen, they agreed to end the stand-off, shook hands with the military personnel, and surrendered to the police, feeling that they had made their point and gained the international publicity they wanted. All 120 guests that were held hostage were eventually freed unharmed, at least with no physical injuries. The conference was cancelled and delegates were provided with refunds.

So, what else could go wrong when holding a conference?

I once wanted to attend a conference on Pyrometallurgy that was to be held in Falmouth, England. Unfortunately, it was cancelled when the hotel burned down a few months before the event was to be held. (Perhaps someone didn't understand that it was supposed to be *pyrometallurgy*, not *pyromania*.) I have also attended a conference in Germany where an elderly delegate died of a heart attack. There was also a time when a few delegates suffered from food poisoning at a local conference. Earlier this year, at a conference in Seattle, the city experienced a power failure that shut down the conference for a few hours in the middle of the day. Without power, it can be difficult to obey the dictum that 'the show must go on', yet I have seen another Mike manage to continue with his talk at a Platinum conference despite the loss of power for projecting his slides; I vividly recall his hand gestures describing the graph that he had intended to project. Audiovisual problems are rather common at conferences, but the worst interruption I have seen was at a conference in Delhi when the presenting computer rebooted itself and was unavailable for about five or ten very long minutes, during which time the presenter had to stand waiting awkwardly in front of a very large audience. Two of SAIMM's own conferences have had to work around the complication of having a public holiday declared (for voting in an election) in the middle of the conference. Political disruptions can be even more serious than this, of course. A large international conference was granted to be held in Ukraine two years in advance of the event, but by the time the conference was held, war had broken out between Russian-backed forces and Ukrainian soldiers; quite a lot of soul-searching took place among the organizing body, but the conference eventually went ahead in the capital city very successfully despite the fighting that was taking place about a thousand kilometres away. Conferences held outside the organizer's own country can be especially challenging, and there have

Perils of Conferencing *(continued)*

been instances of audiovisual equipment and materials for exhibition booths being blocked or seriously delayed at country borders. It often happens that presenters don't arrive at a conference because they have been unable to secure the appropriate visas in time. These 'no-shows' can seriously disrupt the scheduling of conference sessions.

Despite all of this, conferences remain one of the pre-eminent ways for professionals to exchange technical information with colleagues working in related areas. This is well recognized by professional registration bodies, and Continuing Professional Development (CPD) is mandatory for continued registration, for example, as a Professional Engineer (PrEng) with the Engineering Council of South Africa (ECSA). In order to be recognized for CPD purposes, conferences have to be formally accredited. SAIMM has the role of providing accreditation, on behalf of ECSA, of content for all mining and metallurgy conferences. Reputable peer-reviewed events are hosted by a number of local and international professional associations, including other institutes within the Global Mineral Professionals Alliance (GMPA), such as AusIMM in Australia, or CIM in Canada, for example.

Unfortunately, there are also many low-quality events in existence, arranged by commercial conference organizers. There are some people who make a very good (if not entirely honest) living by arranging international conferences in exotic locations far off the beaten track. The warning signs are easy to spot: there is no backing of a professional institute (or at least someone with a well-established reputation in the field), no organizing committee, no peer review of papers or presentations, and topics that are unnecessarily wide, general, or unfocused. These organizers typically prey on early-career academics who are drawn in by the prospect of speaking at an international event at an interesting and attractive destination. I have heard of conferences where delegates have presented to very small audiences who have no overlapping interests. Of course, it would be rather embarrassing to blow the whistle after the event, as this would expose the delegate's lack of good judgement, and so these events continue to proliferate.

SAIMM has a particular style of conferencing. Delegates can be sure that the conference will be held at a high-quality and comfortable conference centre, with good audio-visual facilities, tasty catering, and many opportunities for networking. Where appropriate, peer-reviewed proceedings are produced and provided to delegates in electronic form, with an option to purchase a printed copy. Conferences are volunteer-driven, with the support of a small full-time conference organizing team. Oversight is provided by SAIMM's Mining and Metallurgy Technical Programme Committees (TPCs), who take responsibility for finances, marketing, and training. Conference topics are usually based on commodities (*e.g.*, platinum, base metals, diamonds, heavy minerals, sulphuric acid), disciplines (*e.g.*, pyrometallurgy, hydrometallurgy), or are problem-focused (*e.g.*, power crisis, mine safety, furnace tapping). Some of these conferences are once-off, but others are repeated on a regular cycle of one to five years. SAIMM also participates, from time to time, in hosting large international events (such as IMPC, Apcom, Infacon, and Molten Slags) that are held in a variety of countries around the world. It is interesting to note that other countries and regions do things differently, some of them holding one large event (such as the TMS, SME, and CIM MetSoc annual conferences) in a different city every year, and some (such as GDMB's European Metallurgical Conference) having a large event every second year.

Conferences provide a very important source of funding for technical societies, and are the means by which resources are generated to support other worthwhile initiatives.

I often wonder what the conferences of the future will look like. In the past decade, we have seen an increase in the use of electronic technologies. It has become quite routine to have website repositories of conference papers and proceedings. Audio and video recordings of presentations are becoming more familiar too. It is likely that streaming video will be one of the next developments, enabling people far away to observe talks while they are taking place. I also expect to see greater use of devices or applications that will allow the audience to interact with the speaker to a greater extent, perhaps posing questions, or providing answers to snap surveys. I hope you will tell us what you would like to see in the future.

R.T. Jones
President, SAIMM

ProProcess

Innovate Design Fabricate

ProProcess *- Engineered with passion, executed in excellence*

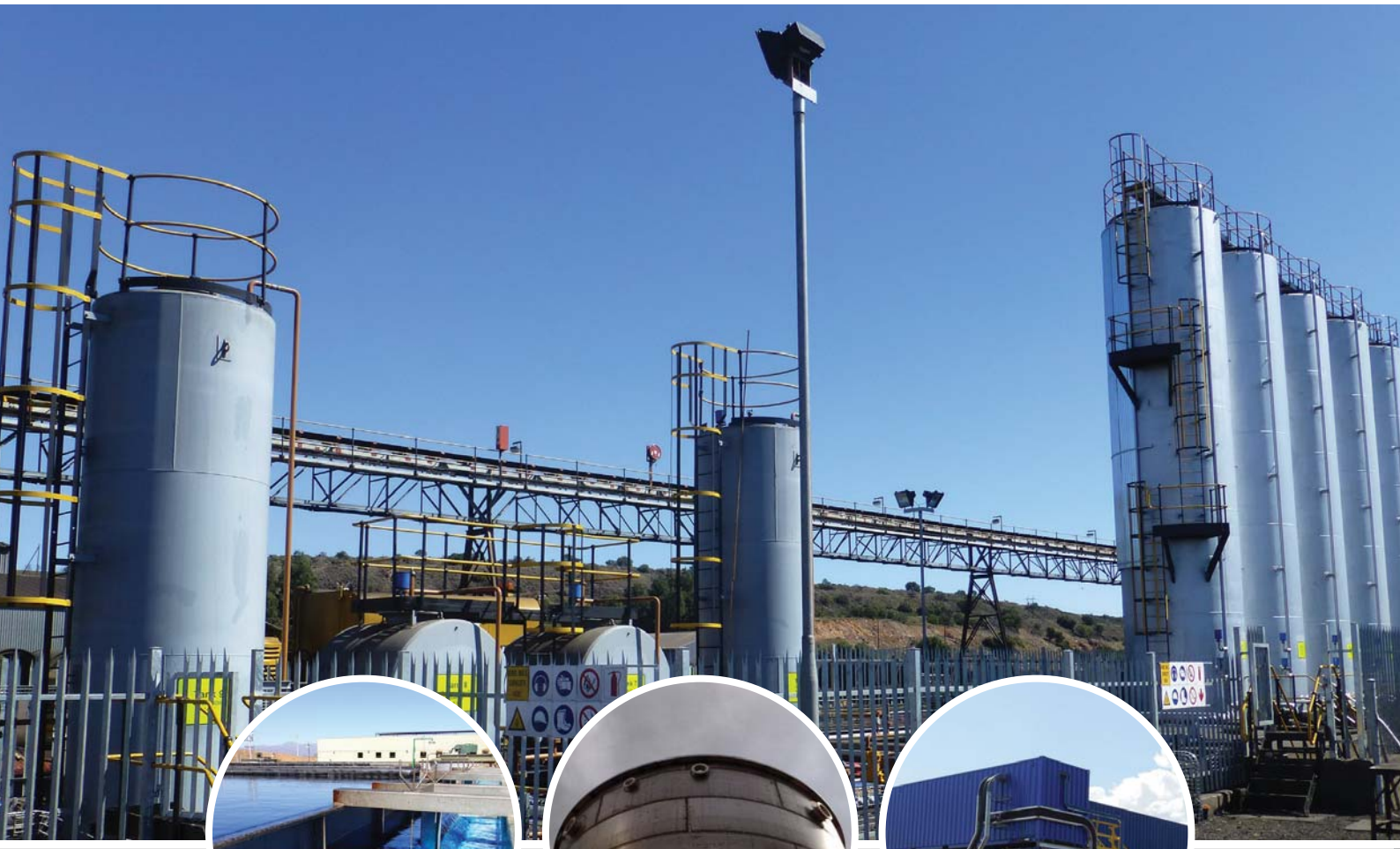

ProProcess provides engineering solutions to the chemical, metallurgical & petroleum industries. A professional approach focused on cost effective process engineering ensures that maximum benefit is derived from our client's assets.

We offer the following services:

- Project Management
- Detailed Engineering & Design
- Specialised Solutions
- Plant Construction & Equipment Supply
- Modular Process Plant Construction & Equipment Supply

8 Viscount Road, Bedfordview,
2008, JHB, South Africa
www.proprocess.co.za

PAPERS IN THIS EDITION

These papers have been refereed and edited according to internationally accepted standards and are accredited for rating purposes by the South African Department of Higher Education and Training

Papers – Copper Cobalt Africa Conference

These papers will be available on the SAIMM website
http://www.saimm.co.za

Papers of General Interest

THE POWER OF **PROFESSIONAL THINKING**

HOW A PHYSIO IS HELPING TO STRENGTHEN THE BACKBONE OF A CONTINENT.

2005: A physiotherapist notices that disadvantaged young South Africans are developing scoliosis: a condition exacerbated by carrying heavy school backpacks over long distances.

They face expensive fusion surgery. An unnecessary burden, according to LouAnn Rivett. She develops an exercise programme designed to straighten and permanently strengthen young spines. Her methods are successful. Today, with assistance and funding, she also treats young people from Zimbabwe, Nigeria, Congo, Ethiopia and Mozambique.

LouAnn is just one of the PPS members who uses the power of professional thinking to bring about positive change. Her story highlights just how unique a breed of graduate professionals are.

Through deep understanding of the world, needs and wants of graduate professionals like LouAnn, we've been the proud providers of bespoke financial services for 75 years.

pps

FOR PROFESSIONALS

SINCE 1941

For more inspirational stories like this, visit pps.co.za

Celebrating the power of professional thinking for 75 years

75 YEARS

Life Insurance | Investments | Financial Planning | Short-Term Insurance | Medical Aid

PPS offers unique financial solutions to select graduate professionals with a 4-year degree. PPS is an authorised Financial Services Provider

http://dx.doi.org/10.17159/2411-9717/2016/v116n6a1

Copper mining in Zambia - history and future

by J. Sikamo*†, A. Mwanza†, and C. Mweemba†

Synopsis

The Zambian copper mining industry as we know it today had its genesis in the 1920s. Consistent private sector-driven investment in the industry over a period of over 50 years in exploration, mine development and operation, development of minerals processing facilities, building of infrastructure for pyrometallurgical and hydrometallurgical processing, with attendant support facilities, including building of whole new towns, resulted in copper production rising to a peak of 769 000 t in 1969, providingover 62 000 direct jobs. The industry was nationalized in 1973 and remained in government hands for just over 24 years. During this period, the industry experienced a serious decline in production levels, reaching the lowest level in the year 2000 when production was 250 000 t. An average of just under 2000 jobs were lost every year in the 24-year period, reaching just over 22 000 direct jobs in 2000.

Following the return of Zambian politics to pluralism and liberalized economic policies, the government decided to privatize the mining industry. The process started in 1996 and by the year 2000 all the mining assets had been privatized. The new investors embarked on serious investment to upgrade the assets and to develop greenfield mining projects. Fourteen years later and after more than US$12 billion investment, production levels increased year-on-year to a peak of 763 000 t in 2013 with direct jobs reaching 90 000.

This paper discusses the impact of the mining industry in Zambia on the economy in areas such as employment, support for other industries, direct contribution to the national gross domestic product (GDP), foreign exchange earnings, and social amenities. The paper also focuses on the performance of the mines during these periods *vis-à-vis* mineral availability, mineral grades and complexity, new technologies, and human capital. This is looked at particularly in the light of current challenges the industry is facing. Suggestions are proposed on how the industry can be nurtured to continue being a major driver for the Zambian economy and a major player in the international copper mining business.

Keywords
copper mining, Zambia, history, nationalization, privatization, production, national economy.

Introduction

Mining had been going on in the region known today as Zambia long before the white settlers came on the scene. The mining was of a traditional and subsistence nature and confined to surface outcrop deposits. The natives of Zambia would melt and mould the copper into ingots used as a medium of exchange and other metal products, such as hand tools and weapons.

Although on a small scale, the mining activities by the natives were wide spread across the Copperbelt region and other places. In fact, most of the deposits discovered by the settlers were found with the assistance of local scouts, who had knowledge of the whereabouts of the copper minerals. The Chibuluma mine deposits are the only ones in Zambia known to have been discovered without information passed on from the local people.

It was the presence of copper in Zambia which led to the region being put under British indirect rule in 1889 (About.com, 2015) after the partition of Africa. The years following 1889 saw extensive exploration activities in the region by western companies and individuals. Exploration activities led to the first commercial copper being produced at Kansanshi, Solwezi, in 1908 (Roan Consolidated Copper Mines, 1978). Later, prospectors obtained concessions from the British South African Company (BSA) which had obtained mining rights in the area from King Lewanika of the Lozi in 1900 (About.com, 2015). As more copper deposits were found, Zambia was put under direct British rule as a protectorate under the Colonial Office in 1924.

Post-1924 saw the beginning of massive investments in mine developments, led mainly by American and South African companies. As a result, there was an influx of white settlers into the area as well as natives who migrated from their villages to provide labour on the mines. Table I shows the increase in the white population during this period.

* *Zambia Chamber of Mines.*
† *Chibuluma Mines Plc, Zambia*

 This paper was first presented at the, Copper Cobalt Africa Conference, *6–8 July 2015, Avani Victoria Falls Hotel, Victoria Falls, Livingstone, Zambia.*

Table I

White population in Northern Rhodesia – 1923 to 1929 (SARPN, 2015)

Year	1923	1924	1925	1926	1927	1928	1929
White population	260	438	474	756	1038	1066	1861

Table II

Mines established in Northern Rhodesia and their processing infrastructures (Roan Consolidated Copper Mines, 1978)

Owner	Mine	Year started	Infrastructure					
Rhodesia Selection Trust (RST)	Luanshya Mufulira Chibuluma Chambishi Kalengwa	1928 1933 1955 1965 1969	Underground Underground Underground Underground Open pit	Concentrator Concentrator Concentrator Open pit Concentrator	Smelter Smelter Leach plant Concentrator	Refining Leach plant	Refining	
Anglo American Corporation (AAC)	Nchanga Rhokana Bancroft	1937 1931 1957	Underground Underground Underground	Open pit Open pit Concentrator	Concentrator Concentrator	Roaster leach Roaster leach	Leach plant Smelter	Refining Refining

Population increase lead to the establishment of settlements which rapidly grew into new towns. Support industries emerged and infrastructure such as hospitals, schools, roads, markets, and recreational facilities were built. Thus, by 1964, when Zambia was born, it had a strong economy driven by the mining sector.

From the beginning to nationalization (1928–1973)

Although copper had been produced at Kansanshi and Bwana Mkubwa in 1908 and 1911, respectively, the first commercial mine in Zambia was established in Luanshya in 1928 (Roan Consolidated Copper Mines, 1978). Opening of other mines followed, as shown in Table II.

The owners of these mines were driven by the high demand and favourable prices of copper and the need to maximize their profits. Flotation technology for separating copper sulphide minerals from ores had been commercialized and this advance enabled large quantities of copper to be produced. The mine owners therefore invested in concentrators, smelters, and other metal extraction facilities, a situation which continued until 1969.

By 1964, Zambia was a major player in the world copper industry, contributing over 12% of global output (Sikamo, 2015). The economy grew to an extent where, in 1969, the nation was classified a middle-income country (Sardanis, 2014a) and had one of the highest gross domestic products (GDPs) in Africa, higher than Ghana, Kenya (see Figure 1), and South Korea, whose per capita income in 1965 was US$106 compared with Zambia's US$294 (SARPN, 2015). The mining sector continued providing direct and indirect employment, such that, by 1972, 62 000 people were directly employed by the mines (Sikamo, 2015). Growth in the economy also led other sectors of the economy to grow, such as transport, construction, manufacturing, and trading. The national GDP growth was above 5% between 1964 and 1970 (Figure 2).

However, the period 1964 to 1969 saw reduced investments in the mining industry, due to the issue of royalties between the government and the mine owners. Mineral royalties in Zambia were held by the BSA Company from inception to 1964, when the country achieved independence (Roan Consolidated Copper Mines, 1978). After 1964, the mineral rights went to the government without changing the taxation structure. However, the cost became real for the owners since they were shareholders of BSA Company and never used to view the royalties paid to BSA as a real cost. As such, their arguments to have the mineral royalty tax reduced were denied by the Zambian government.

During this period (1964–1969), the government was not happy with the level of participation of the indigenous population in the national economy in general and the mining sector in particular. A number of reforms were embarked upon. The Mulungushi reforms in 1968 gave 51% ownership in major industries to the Zambian government, managed under the parastatal Industrial Development Corporation (INDECO). In 1969, the Matero reforms were announced, which gave the government 51% ownership of the mines, managed under Mining Development Corporation (MINDECO). Thus began the era of mining nationalization, which was completely effected by 1973 (Sardanis, 2014b; SARPN, 2015).

Nationalization of the mines (1973–1996/2000)

Nationalization of the Zambian mines began with the Matero declaration of 1969, when the government obtained a 51% shareholding in the then two existing mining companies. These were Roan Selection Trust and Anglo American Corporation, which owned all the operating mines in the country between them. Prior to the Matero declarations, the government had issued the Mulungushi declarations, under which 51% of the shares in all the major industries (except mines) were put in state hands. This led to the formation of INDECO as the holding company for these shares. The Matero

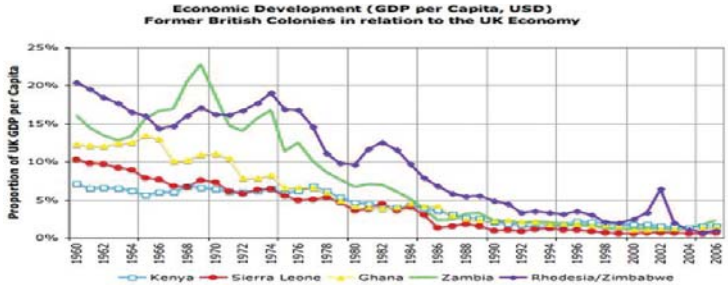

Figure 1—GDP of some British former colonies as a fraction of the GDP of the United Kingdom. (Source: http://www.bing.com/images/GDP per capital for UK colonies)

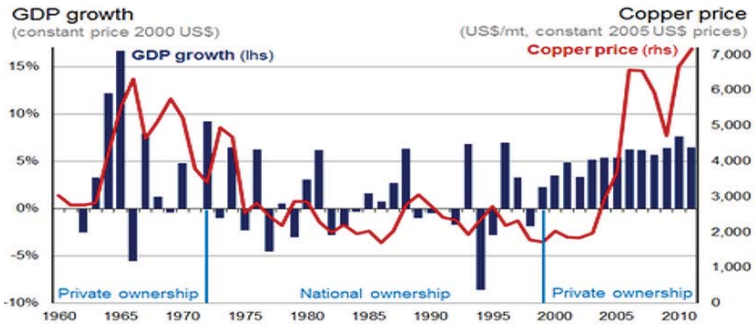

Figure 2—Zambia's GDP growth and copper prices between 1960 and 2010. (Source: Roe *et al.*, 2014)

reforms resulted in the formation of a holding company for the mines' shares to be called MINDECO. An umbrella company for MINDECO and INDECO was formed and was called Zambia Industrial and Mining Corporation (ZIMCO). Roan Selection Trust became Roan Consolidated Copper Mines (RCM), comprising Mufurila, Luanshya, Chibuluma, Chambishi, Kalengwa, and Ndola Copper Refinery. The Zambian arm of Anglo American Corporation became Nchanga Consolidated Copper Mines (NCCM) and was in charge of Rhokana, Nchanga, and Konkola mines.

The Matero reforms were implemented in January 1970 and the government was to pay for those shares over a period of roughly 10 years (SARPN, 2015). However, in 1973, the government decided to redeem all the outstanding bonds and made the following changes in the management structure. MINDECO was no longer in charge of RCM and NCCM, but other small mines in the country. INDECO, MINDECO, RCM, and NCCM all fell under the management of an overarching parastatal Zambia Industrial and Mining Corporation (ZIMCO). All the managing directors of RCM and NCCM as well as the chairman of ZIMCO were political appointees. The Minister of Mines was the chairman of RCM, NCCM, and ZIMCO. In the same year, the country changed its constitution and became a one-party state.

The government started using the revenues from the mining sector to advance the national developmental agenda. Massive projects were embarked upon, such as the Kafue and Itezhi Tezhi hydropower stations, the TAZARA rail line, housing projects, schools, hospitals, and road infrastructure.

The education sector is one area that received massive investments from the mines during this period. Both the mines and the country benefited both in the short and long term. Prior to nationalization, private owners did very little to advance the knowledge base of the indigenous population—all measures were meant to benefit the settlers and their children. However, after nationalization, there was a deliberate policy by government through the mines to educate the children of Zambians. High-standard schools were built where excelling children of miners and sometimes non-miners were enrolled. These students were later sent to top universities all around the world to train, mainly in mining disciplines. Artisan training colleges were also set up for miners and school leavers who were to be employed by the mines. Gradually, the gap left by the white settlers in areas of skilled manpower was greatly reduced. The mining skill level of Zambia improved so much that later, when the mines were re-privatized, the new owners did not need to employ many expatriates. In some cases, Zambian mining professionals were appointed as chief executive officers (CEOs) of foreign mining companies after re-privatization.

Meanwhile, there was no letting up on the government's stranglehold on the mines. In 1982, the government merged RCM and NCCM into one entity called Zambia Consolidated Copper Mines (ZCCM), which continued financing national programmes at the expense of its own operations. This financial burden on ZCCM took its toll. The mines suffered undercapitalization and could not replace worn and obsolete machinery. There was little investment in technological upgrades, despite the increasing difficulties in mining and processing as mining proceeded deeper and the mineral grades leaner and more complex. Inevitably, production output declined while production costs were soaring. Employment levels reduced as the mines downsized their labour forces. The price of copper remained low while that of

oil was skyrocketing. The business prospects of the mines were bleak, and so were those for the national economy, which was heavily reliant on mining.

Shortage of consumer commodities in shops became the order of the day and political agitation for the end of one-party rule started. In 1990, the country reverted to multi-party politics and a new government, which promised to privatize the mines, was voted into office in 1991.

Re-privatization

Although the new government, which had promised privatization of the mines, was in place by 1991, the privatization exercise started only in 1996 and was not completed until 2000. Critics had mixed views on the pace of the re-privatization process, but, with hindsight, one cannot help but think that it should have been faster. This is because the decline in copper production continued in this period, exacerbated by job uncertainties, as mines continued the exercise of labour reduction. The national economy was not doing any better, although the effects were being mitigated by donor financing in a spirit of goodwill to the new government.

When re-privatization started, the government decided to unbundle ZCCM into smaller units. Smaller mines were the first to be put into private hands. However, privatization can be said to have happened only when the two big units, Konkola Copper Mines (KCM), which comprised Nchanga, Konkola, Nampundwe and part of Nkana assets, and Mopani Copper Mines, which comprised assets at Nkana and Mufulira, were privatized in 2000. Mopani Copper Mines was sold to Glencore as the major shareholder, while KCM was offered to Anglo American Corporation (AAC). In 2002, AAC returned the mines to the government, which offered them to Vedanta of India in 2004.

The new mine owners invested massively in the mines and there was a sudden economic upturn, not only on the Copperbelt but in the country as a whole, with the mining industry as a pivotal contributor. Investments went into new machinery, new mining methods, and new mineral processing and metal extraction technologies. There were also massive greenfield projects at Kansanshi and Lumwana, both in the North West Province of Zambia, which brought newer technologies into the industry. These mines were able to process large quantities of low-grade copper ores at very low cost.

Copper production reached a peak of 720 000 t in 1969, the same year that the nationalization discussions picked up speed. By the time nationalization was being completed in 1973, production had dropped slightly to 700 000 t. This resulted from the fact that immediately the nationalization discussions started, investment in the mining industry started falling. After nationalization, production continued to drop and, in the subsequent 24 years of nationalization, production dropped to 250 000 t by the year 2000. Following the massive investment of the new mine owners in refurbishing the mines, which had not been seeing any investment, and investment in greenfield projects (see Table III), production levels began to increase. By 2013, production had reached 763 000 t (see Figure 3) and the industry had over 90 000 direct employees from the low of 22 000 at the time that privatization was completed. It is worth noting that the amount of copper produced per person in 2013 is lower than in 1972 due to the fact that, before re-privatization, mines were jointly owned and overhead services were shared. Furthermore, the copper grades were higher, which increased unit labour productivity.

Contribution of the mining industry to the Zambian economy

Although it is the desire of the Zambian government to diversify the economy, the Zambian copper mining industry will remain the engine that will drive this diversification for a long time to come. In the work done by International Council on Metals and Mining (ICMM), verified data from 2012 statistics shows that, in that year, 86% of the foreign direct investment that came into Zambia was due to the mining industry, 80% of the country's export earnings came from the mining industry, as well as over 25% of all revenues collected by government. The mining industry contributed more than

Table III

Mines investments since re-privatization, US$ billion (Roe *et al.*, 2014; Sikamo, 2015)

Mopani	KCM	Lubambe	FQM	Lumwana	Kansanshi
2.24	2.9	0.49	2.23	2.0	2.54

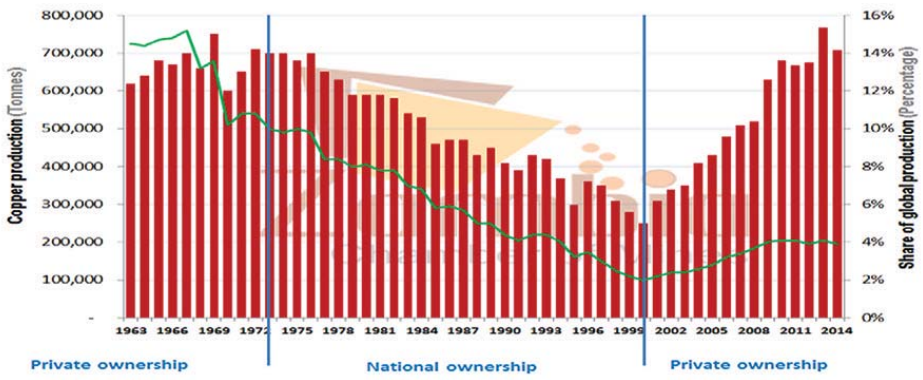

Figure 3—Zambia's copper production and its share in global production (Sikamo, 2014)

10% to the GDP, and more than 1.7% of all formal employment in the country (see Figure 4). These parameters show that Zambia's reliance on the mining industry is way above that of other countries that are similar to Zambia in terms of their dependence on the extractive industries.

The same ICMM study looked in more detail at the contribution to government revenue in terms of all taxes paid, as shown in Figure 5. It is clear that, during the period 1995 to 2000, taxes paid by the mines constituted around 1% to 2% of all taxes. As investments began to mature and improvements put in place began to bear fruit, all the taxes paid began to show an upward trend—to the extent that, by 2011, taxes collected from the mines averaged 35% of the total taxes. This trend shows that increasing revenues to government can be guaranteed by increasing production and a favourable price. This is clearly seen in Figure 6, by the doubling of revenue collection between 2010 and 2011 without a change in tax regime.

In terms of revenue collection, Zambia joined the Extractive Industries Transparency Initiative (EITI) as a candidate in May 2009 and was fully compliant in September 2012 (Moore Stephens, 2013, 2014). EITI is an international organization that promotes transparency in the declaration of earnings and revenues arising from the extractive industries. In Zambia, the local organization is called Zambia Extractive Industries Transparency Initiative (ZEITI) and it monitors what the mining companies say they have paid into government and government agencies and what government acknowledges as having received. The overall objectives of the reconciliation exercise are to assist the government of Zambia in identifying the positive contribution that mineral resources are making to the economic and social development of the country, and to realize their potential through improved resource governance that encompasses and fully implements the principles and criteria of the EITI. ZEITI has so far released six reports for 2008 to 2013. These reports show remarkable agreement between what government acknowledges as having received and what the mining companies say they have paid. From the reports, and as summarized in Figure 6, it is clear that the mining industry has been contributing revenues to the treasury on an increasing basis in line with increasing production and copper price fluctuations (Moore Stephens, 2013, 2014). For comparison with international currencies, refer to Figure 7, which shows the Zambian kwacha (ZWK) exchange rate against the US dollar in the period 2008–2013, which averages between ZWK 4 and ZWK 5 to US$1.

Conclusion – the future of mining in Zambia

The geology of Zambia shows great potential for further investment in mining. The past few years have seen significant instability in the fiscal regime and this has undermined new investment into the sector. The challenges of the 2013 to 2014 fiscal regime resulted in copper production dropping from 763 000 t in 2013 to 708 000 t in 2014. The first half of 2015 saw a further decline in production, particularly following the uncertainty brought about by the Mineral Royalty Taxation regime of 2015. It is gratifying to see that the government has shown serious desire to engage in dialogue to arrive at optimum levels of taxation which will ensure that government continues to receive taxes from the mines, and also that the mines continue to thrive and invest, on a sustainable basis. Clearly

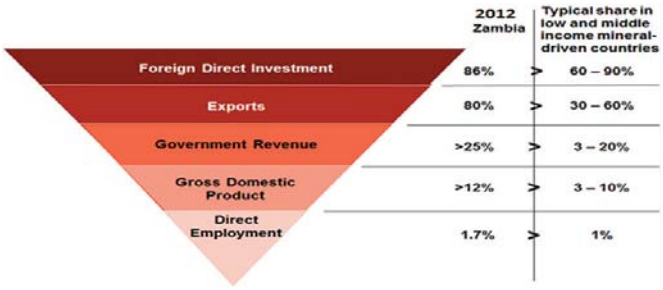

Figure 4—Mining's contribution to Zambia's economic pillars (Roe *et al.*, 2014)

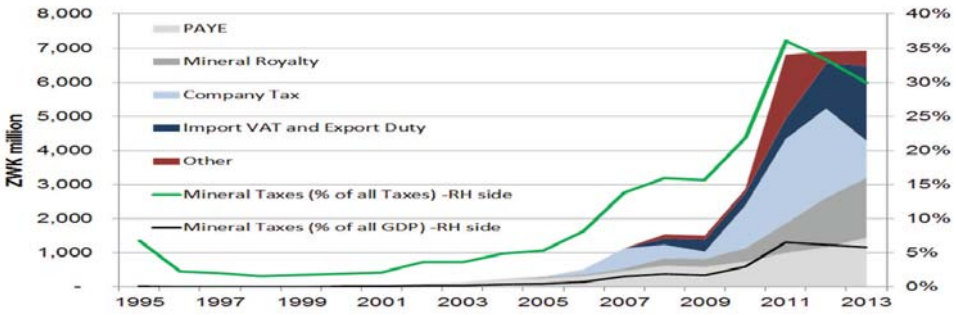

Figure 5—Mining's contribution to Zambia's revenue in taxes. (Moore Stephens, 2013, 2014; Sikamo, 2015)

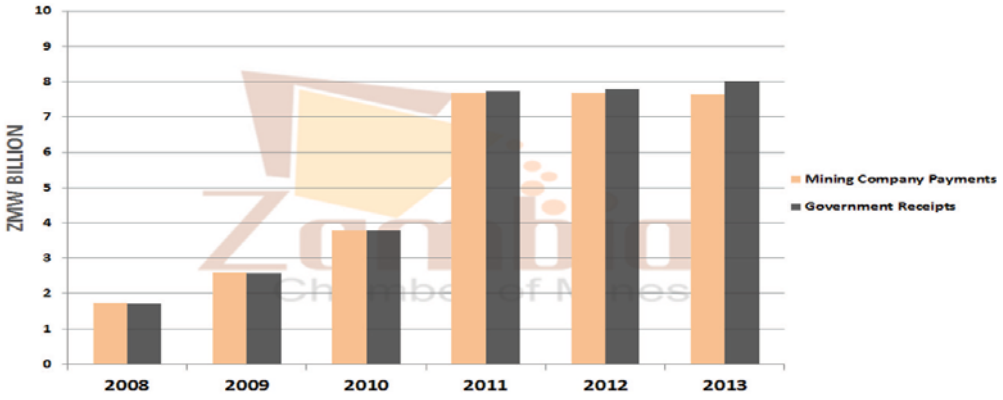

Figure 6—Mining's contribution to Zambia's revenue (Sikamo, 2014)

Figure 7—Zambian kwacha (ZWK) exchange rate against the US dollar between 2008 and 2014 (Source: www.tradingeconomic.com)

this is the way to go. This state of affairs has been confirmed by government, which has said that it is committed to putting in place a taxation regime that is stable, predictable, consistent, and transparent. Investors have welcomed this and obviously this should translate into a very bright future for the Zambian mining industry.

The mines performed badly during the period of nationalization, since they lost focus from their core business. Continuous re-investment in machinery and new technology is very important for increasing productivity. Investing in human capital is another area that is very important and new mine owners will do well not to neglect this aspect. It is gratifying to see that the mining companies operating in Zambia are taking all these important aspects of mine development into consideration, and the results are visible.

For its part, government should continue providing policies that will attract capital into the mining industry. These policies should be dynamic in nature so that the country remains competitive with other major players on the global market. The key here is continuous engagement with stake holders so that the government is abreast of the changing challenges and other requirements in the industry. To counter the legacy of prolonged undercapitalization of the old mines, particularly regarding modern machinery and technology, government should encourage greenfield projects that are able to build low-cost mining operations that can withstand the constant shock of copper price fluctuations.

References

About.com. 2015. African history. http://www.africanhistory.about.com/od/zambia/ l/Bl-Zambia-Timeline.htm

Moore Stephens. 2013. Zambia Extractive Industries Transparency Initiative. Fifth reconciliation report based on the financial year 2012.

Moore Stephens. 2014. Zambia Extractive Industries Transparency Initiative. Sixth reconciliation report based on the financial year 2013. https://eiti.org/files/zeiti_2013_ reconciliation_ final_ report_18_12_14%20%281%29%20%282%29.pdf

Roan Consolidated Copper Mines. 1978. Zambia's Mining Industry: the First 50 Years. (Privately published).

Roe, A., Dodd, S., Ostensson, O., Henstridge, M., Jakobsen, M., Haglund, D., Dietsche, E., and Slaven, C. 2014. Mining in Zambia–ICMM Mining Partnerships for Development. Toolkit Implementation. International Council on Mining and Metals. http://www.icmm.com/ document/7066

Southern African Regional Poverty Network (SARPN). 2015. www.sarpn.org/documents/ d0002403/3-Zambia_copper-mines_Lungu.

Sikamo, J. 2015. Presentation on the state of the Zambian Mining Industry. Zambia Chamber of Mines, Lusaka.

Sardanis, A. 2014a. Zambia: the First 50 Years. I.B. Tauris.

Sardanis, A. 2014b. Africa: Another Side of the Coin. Northern Rhodesia's Final Years and Zambia's Nationhood. I.B. Tauris. ◆

http://dx.doi.org/10.17159/2411-9717/2016/v116n6a2

Improvements in copper electrowinning at Tenke Fungurume Mining Company

by S. Sandoval*, N. Goel*, A. Luzanga*, and O. Tshifungat*

Synopsis

Tenke Fungurume Mining Company (TFM), located in Katanga Province, Democratic Republic of Congo (DRC), began production of copper cathode and cobalt hydroxide in March 2009. Copper production capacity was 115 000 t/a utilizing a semi-autogenous grinding, agitated leach, counter-current decantation process followed by solvent extraction and electrowinning (SX-EW). Cobalt production capacity (as cobalt hydroxide) was 8000 t/a utilizing a three-stage purification/precipitation process treating raffinate from the copper SX-EW process. Recently a phase II expansion was completed, in which copper electrowinning capacity was doubled and four stages were added to the SX plant. Corresponding enhancements were made to mining, milling, and processing to bring production to 195 kt/a copper and 15 kt/a cobalt. An additional sulphuric acid plant is currently being constructed, adding 1400 t/d sulphuric acid to bring total acid production to 2250 t/d for use in leaching at TFM.

Initial copper electrowinning results were satisfactory, but cathode quality and current efficiency decreased as copper production increased. The Freeport-McMoRan (FCX) Technology Centre and TFM personnel began operation of two bench-scale copper electrowinning cells in the tankhouse to diagnose chemistry effects on the cathode and anode. The results indicated an excellent electrolyte chemistry, producing finely crystalline copper at 430 A/m^2 current density with 98% current efficiency. Attention next turned to the physical factors of the electrowinning cells, including electrode insulator geometry and performance. A demonstration cell was selected in the tankhouse and was operated with varying cathode and anode insulator geometries. Operation of the demonstration cell with a three-side cathode edge strip, A-style anode insulators, and an improved cell furniture design increased current efficiency from 77% to 89% at 400 A/m^2 current density. Cathode quality improved correspondingly. TFM is now operating at 92% current efficiency.

Keywords

copper, cobalt, electrowinning, cathode quality.

Introduction

Tenke Fungurume Mining Company (TFM), an affiliate of Freeport-McMoRan Inc., has invested over US$3 billion in its copper and cobalt operations in Katanga Province, Democratic Republic of Congo (DRC) since 2006 when construction began. The concession lies 110 miles northwest of Lubumbashi, Katanga Province, in the southeast of the DRC. Ownership is by a consortium consisting of Freeport-McMoRan Inc. (56%), Lundin Mining Corp. (24%), and Las Généralé des Carrières et des Mines (Gécamines, 20%). The mine produces copper as electrowon cathode and cobalt as cobalt hydroxide.

Production began in March of 2009. A process flow diagram is shown in Figure 1. Surface-mined ore reported to a single-stage semi-autogenous grinding (SAG) mill at a rate of 8000 t/day. The thickened pulp was then subjected to an agitated sulphuric acid leach at atmospheric pressure. Sulphur dioxide gas was introduced in the agitated leach to reduce Co^{3+} to Co^{2+} in the leach liquor. The leach discharge thickener overflow produced high-grade pregnant leach solution (HG PLS) containing about 13 g/L copper. The HG PLS was sent to solvent extraction–electrowinning (SX-EW) for recovery of the copper at a rate of 115 000 t copper per year. The HG raffinate from SX, containing about 20 g/L sulphuric acid, was returned to leaching for utilization of the acid.

The leach discharge thickener underflow was processed by countercurrent decantation (CCD) to produce a low-grade pregnant leach solution (LG PLS) that contained about 6 g/L copper. Copper was recovered from the LG PLS by SX-EW and the raffinate, which contained about 2 g/L cobalt, was sent to the cobalt recovery circuit. This circuit first oxidized Fe^{2+} to Fe^{3+} and Mn^{2+} to Mn^{4+} using a mixture of sulphur dioxide and air, then the iron, manganese, and aluminium were precipitated by limestone addition. In a second precipitation stage, residual copper was precipitated using lime addition. This led to the third stage of the cobalt recovery circuit where cobalt hydroxide was precipitated using magnesium oxide. The resultant cobalt hydroxide cake could then be bagged either moist or dry for shipment at a rate of 8000 t cobalt per year.

* *Tenke Fungurume Mining Company (an Affiliate of Freeport-McMoRan Inc)., Democratic Republic of Congo.*

Improvements in copper electrowinning at Tenke Fungurume Mining Company

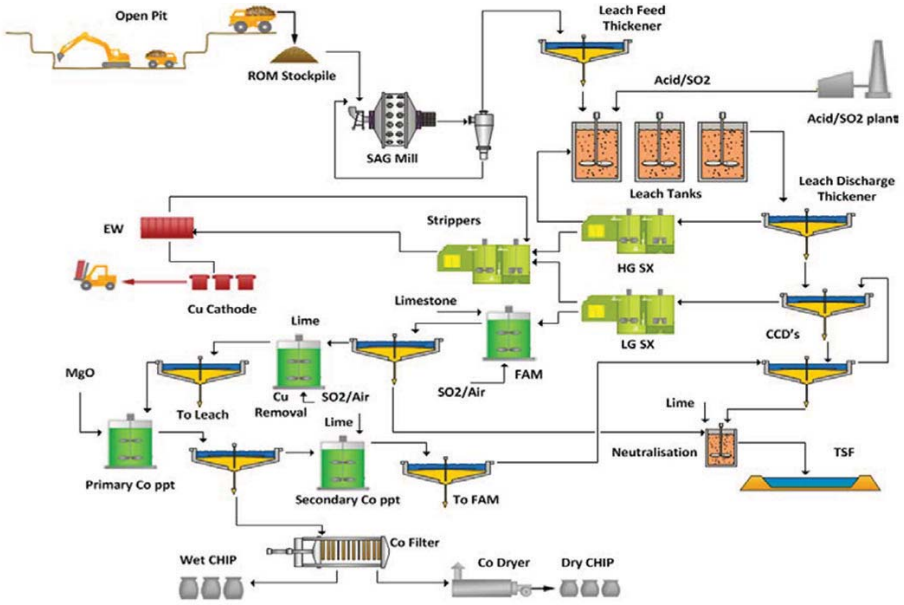

Figure 1—TFM process flow diagram

This paper summarizes the history of TFM developments and also presents the improvements that have been implemented in the production process since start-up. Steps to improve copper cathode quality are also described.

History

Exploration of the TFM deposits began as early as 1917 and continued intermittently through 1970. The first drilling was conducted in 1918 by Union Minière de Haut Katanga, but no mining ensued at that time. In 1970, the Societé Minière de Tenke Fungurume and Gécamines were awarded the concessions and began to study the feasibility of constructing a mine. Some infrastructure, including access roads, was constructed. This work was abandoned in 1976 because of the falling copper price, a delay in the construction of a power line, and a deteriorating political and social situation in DRC.

In 1996, TFM was established and the concessions transferred from Gécamines. In 1998, TFM and Lundin Holdings began a feasibility study, but the work was abandoned in 1998 due to the outbreak of a civil war in DRC and the study was left unfinished. In 1998, TFM concluded an option agreement with BHP Billiton that would allow BHP to acquire a controlling interest in TFM. This option was transferred to Phelps Dodge in 2002. In 2003, Phelps Dodge commissioned a study for processing the Kwatebala orebody to produce 30 000 t/a copper and 1800 t/a cobalt. Studies continued to progress until in 2006 the plant capacity was set at 8000 td of ore throughput to produce 115 000 t/a copper and 8000 t/a cobalt. The initial mine life expectancy was 20 years. Construction of the project began in 2006 and first copper and cobalt were produced in 2009. In 2007 Freeport-McMoRan Inc. acquired Phelps Dodge.

TFM developments

Phase I

Analysis of TFM ore showed that the major copper oxide mineral was malachite. The major cobalt oxide mineral was heterogenite. The gangue matrix consisted of quartz, muscovite (mica), chlorite, tourmaline, and dolomite, with minor concentrations of iron oxides/hydroxides, clays, and feldspars. Metallurgical development of the extraction process began with batch and semi-continuous test work conducted at Freeport-McMoRan's Technology Centre in Safford, AZ and at Hazen Research Centre in Denver, CO. In 2006, three integrated pilot plant campaigns were completed at Hazen, as shown in Figure 2.

Results from the metallurgical testing were used as a basis for inputs to the process design criteria and to the mass and energy balances. A detailed plant model was developed using METSIM.

Construction of the plant required a little over two years and the first copper and cobalt were produced in March 2009.

Copper quality

The Phase I tankhouse contained four banks of 70 cells each for a total of 280 cells. Each cell contained 66 cathodes with approximately 2.4 m^2 of plating surface per cathode. Two rectifiers per tankhouse side provided a maximum amperage of 66 kA per cell, or a maximum current density of 420 A/m^2. The tankhouse utilized three Metso cathode stripping machines at a six-day harvest cycle. The TFM tankhouse is displayed in Figure 3.

Also displayed in Figure 3 are two bench-scale copper electrowinning cells operated in the tankhouse. As tankhouse amperage increased, current efficiency decreased and cathode quality also suffered. The FCX Technology Centre and TFM personnel began operation of two bench-scale copper electrowinning cells to demonstrate the current efficiency and copper quality achievable using TFM electrolyte. The bench-cells by design provide a perfect electrowinning environment. Key parameters included excellent current distribution, electrode contact system, electrode straightness and alignment, and electrolyte distribution. Perfect conditions are

Figure 2—Pilot plant campaigns at Hazen Research Centre

Figure 3—TFM copper electrowinning tankhouse, and two bench-cells operated in the tankhouse

not obtained in commercial cells because of scale-up imperfections. However, the bench-cells provide a useful benchmark.

The bench-cells utilized stainless steel cathodes and standard lead anodes. Operating current density was 430 A/m^2. Four bench-cell tests were completed to evaluate cathode deposits with 1, 2, 3, and 4 days of plating time. Current efficiency results are shown in Table I. Typical cathodes harvested from the bench-cells are shown in Figure 4.

The TFM electrolyte was unique in that in contained 43 g/L Cu, 1 g/L Co, and 1 g/L Fe. The cathodes exhibited excellent apparent deposit morphology and current efficiency was 98%. The deposits were smooth and finely crystalline. The bench-cell testing demonstrated excellent current efficiency, excellent cathode quality, and good lead anode performance. Attention next turned to the physical factors of the TFM electrowinning cells, including electrode insulator geometry and performance. A demonstration cell was selected in the tankhouse and was operated with varying cathode and anode insulator geometries. Three demonstration tests were performed as shown in Table II.

Included in the demonstration cell testing was an improved cell furniture design, as shown in Figure 5. Contact clearance was an issue in the old furniture, creating electrode no-contacts because the hanger bar touched the cap block and not the copper conductor bar. This affected current distribution within the cell and contributed to short-circuits.

Experience at the El Abra tankhouse (FMI's El Abra Operations, Calama, Chile) showed that the A-style bottom corner anode insulators provided strong alignment of anodes and cathodes, which would be a significant benefit because TFM cathodes utilized a 1.2-m long cathode plating area. It became of interest to test the A-style anode insulator using

Table I

Current efficiency of bench-cell tests using TFM electrolyte

Days of plating	Current efficiency (%)
1	98
2	98
3	97
4	98

Figure 4—Bench-cell cathodes produced using TFM electrolyte at 430 A/m^2

Table II

Tankhouse demonstration cell tests

Demonstration test	Cathode insulator	Anode insulator
1	Single-side edge strip	Blue star
2	3-side edge strip	Blue star and hairpin
3	3-side edge strip	A-style bottom corners and blue star

Figure 5—Old cell furniture (right), showing poor clearance between cap block and contact. On left is new cell furniture with robust contact clearance

Figure 6—A-style bottom corner and blue star insulators on anodes, three-side edge strip on cathodes

TFM anodes in demonstration test 3. The single-side edge strips in use on TFM cathodes were also causing difficulty in the tankhouse because the bottom corners would separate from the stainless steel blanks, exposing the cathodes to nodulation during plating, a significant problem for LME visual grading of cathode and for formation of short-circuits. It became of interest to evaluate the Morenci (FMI's Morenci Operations, Morenci, Arizona) three-side cathode edge strip for TFM cathodes because this would correct the nodulation problem and would also cover the cathode bottom V-groove, which tended to cut off anode insulators during the harvest cycle. Figure 6 displays the A-style anode insulator and the three-side cathode edge strip on TFM electrodes. Typical electrolyte conditions during the tankhouse demonstration cell testing were 57°C electrolyte temperature, 0.12 $m^3/h/m^2$ electrolyte flow rate, and 400 to 410 A/m^2 current density. Commercial electrolyte measured 43 g/L copper. Results of the demonstration cell testing are displayed in Table III.

Demonstration test 3 was superior in both current efficiency and visual quality of product, increasing current efficiency from 77% to 89%. The A-style anode insulators and three-side cathode edge strips provided strong alignment of anodes and cathodes, a significant benefit at current density over 400 A/m^2.

The insulator geometry of demonstration test 3 was installed in the TFM tankhouse along with the new furniture design. Tankhouse results are displayed in Figures 7 and 8. Current efficiency was increased by 12% and cathode quality was reversed, decreasing off-grade copper to below 5%. Copper production increased from 7.2 to 8.9 t per cell over days. To help sustain the improved performance, single carts (Figure 9) were implemented in the tankhouse for short-circuit correction. Up to four single carts per tankhouse side were operated daily. At present the TFM tankhouse is operating at 92% current efficiency.

Table III

Summary of TFM tankhouse demonstration cell results

Demonstration test	Average current density (A/m^2)	Current efficiency (%)	Grade of copper produced
1	410	75	High grade
2	410	77	High grade
3	400	89	High grade

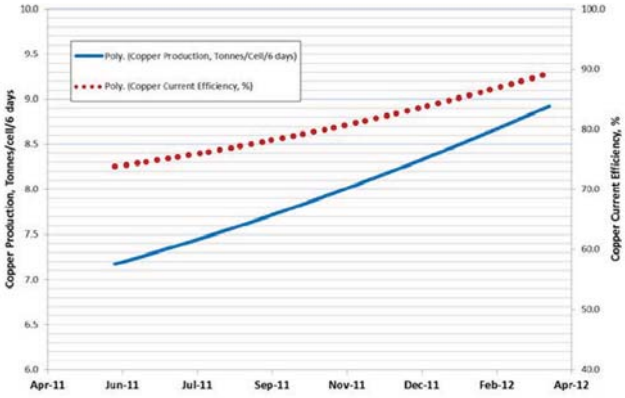

Figure 7—Increase in current efficiency and production with transition of tankhouse

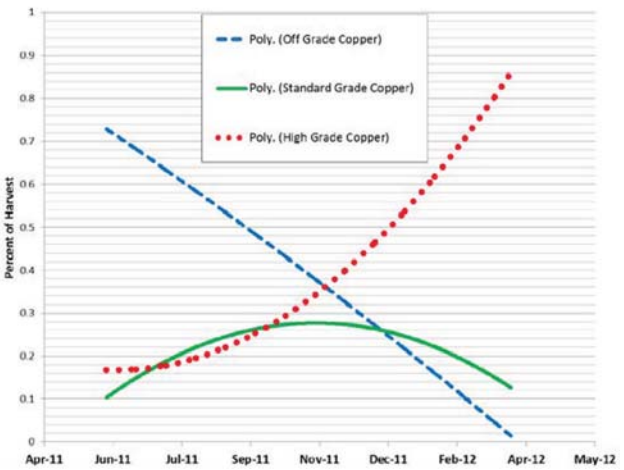

Figure 8—Reversal of cathode quality with transition of tankhouse

Phase II

Analysis of the Phase I production plant identified limiting process steps or bottlenecks in the circuit. The bottlenecks resided primarily in the milling, SX-EW, and cobalt hydroxide handling portions of the plant. In addition, electrolyte temperature was deemed too high at 57°C. A cooling tower was needed to eliminate overheating of the tankhouse. In 2011, Freeport-McMoRan commissioned a Phase II feasibility study to increase plant capacity to 14 000 t ore per day for production of 195 kt copper and 15 000 kt cobalt per annum,

Figure 9—Single-pull cart used to correct short-circuits in tankhouse

Figure 10—Phase II copper production

representing a 70% increase in copper production and an 87% increase in cobalt production from the original capacities. In that same year, the Phase II expansion began and was completed in 2012. The major addition was a second electrowinning tankhouse with 280 new cells that doubled copper electrowinning capacity to a total of 560 cells. Four SX mixer–settlers were added to the high-grade circuit along with four garnet/anthracite-rich electrolyte filters, increasing the total number of filters to eight.

On the front end of the plant a pebble crusher and a jaw crusher were added to the SAG mill circuit. In the cobalt process, the cobalt hydroxide handling system was expanded. Two additional sulphur dioxide burners were added for increased sulphur dioxide addition to the agitated leach. Figures 10 and 11 show the increase in copper and cobalt production achieved in Phase II. Table IV displays TFM copper and cobalt production in 2013 and 2014.

Table IV

TFM production

Year	Copper (t)	Cobalt (t)
2013	205 933	11 340
2014	192 779	13 608

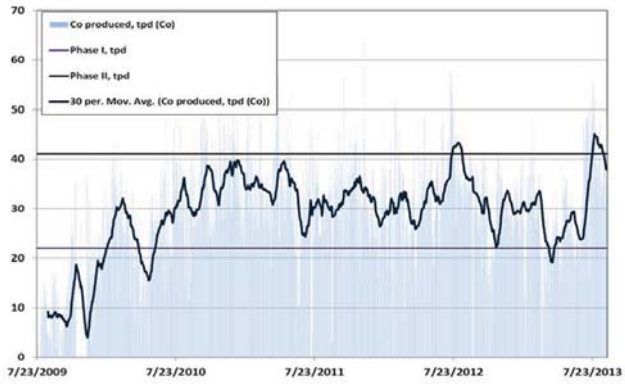

Figure 11—Phase II cobalt production

Present

To become less dependent on third-party sulphuric acid for leaching, TFM is now constructing a new 1400 t/d sulphuric acid plant to bring total site acid production to 2250 t/d. The new plant is targeted to begin operation in 2015. Currently, TFM is producing 850 t/d sulphuric acid for leaching. In addition, the site operates a total of five separate sulphur burners to produce sulphur dioxide, two at 60 t/d sulphur dioxide and three at 50 t/d, for use as reagent in the agitated leach.

By the 2018 to 2020 time frame, production from leaching of oxides is expected to begin to decline. Planning is now underway for the processing and treatment of mixed sulphide ores at TFM.

Summary

Tenke Fungurume Mining Company, in the Katanga Province of DRC, has developed through two phases into a major copper and cobalt producer with a nameplate capacity of 195 kt/a copper and 15 000 kt/a cobalt. Electrowinning current efficiency and copper quality increased dramatically with optimization of the cathode and anode insulator geometry and improvements in the electrowinning cell furniture. Currently the plant is operating at 92% current efficiency and greater than 95% high-grade copper

Phases I and II progressed from integrated pilot-plant campaigns to plant construction beginning in 2006. Debottlenecking of the Phase I installation led to a doubling of electrowinning capacity in Phase II with a total of 560 electrowinning cells.

Currently a new sulphuric acid plant is being constructed on site that will increase sulphuric acid production from 850 to 2250 t/d. Looking to the future, attention is now turning to plans to process mixed sulphides beginning in the 2020 time frame. Expectation of mine life now exceeds 40 years. ◆

http://dx.doi.org/10.17159/2411-9717/2016/v116n6a3

Xanthate chemisorption at copper and chalcopyrite surfaces

by J.L. Bowden* and C.A. Young*

Synopsis

Cyclic voltammetry experiments were conducted on copper and chalcopyrite ($CuFeS_2$) in the absence and presence of ethyl xanthate, and compared to mass-balanced E_H–pH diagrams. The results for copper duplicate those found in the literature and confirm xanthate chemisorption. However, the, results indicate that chalcopyrite oxidizes to chalcocite (Cu_2S) and only afterwards is chemisorption observed due to small currents appearing with xanthate. This phenomenon suggests that the mineral's hydrophobicity is induced by more than dixanthogen and copper xanthate. Hydrophobicity was found to be pH-dependent over a range of alkaline conditions (pH 7–11) at narrow potentials (0 to –200 mV). An E_H–pH diagram for chalcopyrite with xanthate is presented to illustrate the conditions under which chalcopyrite would be hydrophobic and thereby more thoroughly explain the results in the literature.

Keywords
copper, chalcopyrite, xanthate, chemisorption, isotherms, voltammetry.

Introduction

Sulphide minerals are generally concentrated from ores by froth flotation, a physiochemical process that induces separation based on differences in hydrophobicity. In this process, a gas is bubbled into a slurry and the minerals that are hydrophobic (water-repelling) adhere to the bubbles and float to the surface while the hydrophilic (water-loving) minerals remain in the slurry. With sulphide minerals, the hydrophobicity is generally established in two ways. The first is by the addition of a collector, which is a heteropolar molecule with a reactive inorganic head group and an inert organic tail. Typically, the head group bonds with the sulphide mineral surface by adsorbtion either chemically (chemisorption) or physically (physisorption) or by complexing with atoms that solubilize somewhat at the surface (surface precipitation). These interactions leave the organic tail protruding from the mineral surface, thereby inducing hydrophobicity. The second method is by oxidation of the mineral surface to form a layer that is metal-deficient/sulphide-rich or comprised of elemental sulphur. Because the layer mimics naturally hydrophobic sulphur, this enables 'collectorless' flotation. Furthermore, this oxidation phenomenon adds an electrochemical dimension to the understanding of sulphide mineral flotation.

In this regard, the literature on sulphide mineral flotation abounds with studies conducted in the absence and presence of collector, typically involving electrochemical experiments such as cyclic voltammetry, galvanostatic polarization, and impedance measurements coupled with thermodynamic speciation calculations typically plotted as E_H–pH/Pourbaix diagrams. Most studies involve xanthate as collector but have included, for example, mercaptans, mercaptobenzothiazoles, and dithiophosphates. Many were also accompanied by analytical measurements involving various spectroscopic tools, including (but not limited to) Fourier transform infrared spectroscopy (FTIR), Raman spectroscopy, X-ray photoelectron spectroscopy/electron spectroscopy for chemical analysis (XPS/ESCA), atomic force microscopy (AFM), mineral liberation analysis/quantitative scanning electron microscopy (MLA/QEM-SEM), and time-of-flight secondary-ion mass spectrometry (ToF-SIMS) (Smart *et al.*, 2014). Although these studies have allowed the conditions under which sulphide minerals float to become better understood, there still remains uncertainty as to how the collectors interact with the mineral surfaces. 'Surface electrochemistry' knowledge allows flotation separations of sulphide minerals to be made more efficiently and with improved selectivity.

* *Metallurgical and Materials Engineering, Montana Tech, Butte MT, USA.*

 This paper was first presented at the, This paper was first presented at the, Copper Cobalt Africa Conference, *6–8 July 2015, Avani Victoria Falls Hotel, Victoria Falls, Livingstone, Zambia.*

Xanthate chemisorption at copper and chalcopyrite surfaces

Typical copper sulphide minerals include covellite (CuS), chalcocite (Cu_2S), chalcopyrite ($CuFeS_2$), bornite (Cu_5FeS_4), enargite (Cu_3AsS_4), tennantite ($Cu_{12}AsS_{13}$), and tetrahedrite ($Cu_{12}SbS_{13}$). Of these, chalcopyrite is the most common. Most studies involving chalcopyrite flotation were conducted with and without xanthate. Results show distinctions between a chemisorbed layer and a secondary co-adsorbed layer of xanthate components corresponding to surface-precipitated copper xanthate and physisorbed dixanthogen (Fuerstenau, 2007). These species are respectively illustrated by the following reactions:

$$Cu^+ + X^- \leftrightarrow CuX \quad [1]$$

$$2X^- \leftrightarrow X_2 + 2e^- \quad [2]$$

where X represents the xanthate molecule. However, it has been debated whether there exists a region of chemisorbed xanthate (Suoninen and Laajalehto, 1993):

$$X^- \leftrightarrow X_{ads} + e^- \quad [3]$$

and whether the region results in an increased flotation recovery of chalcopyrite (Suoninen and Laajalehto, 1993). It is important to point out that the oxidation reactions leading to dixanthogen (Equation [2]) and chemisorbed xanthate (Equation [3]) only increase the complexity of the surface electrochemistry involved.

The purpose of this investigation was to study the surface electrochemistry of chalcopyrite with xanthate at various E_H potentials and pH values in the hope of observing xanthate chemisorption. To do this effectively, it was felt that experiments with a known system should also be conducted and, in regard, copper was first investigated.

Experimental

Cyclic voltammetry

Cyclic voltammetry (CV) experiments were conducted with an EG&G Princeton Applied Research 263A potentiostat/galvanostat. A standard three-electrode system was employed with the reference electrode being Ag/AgCl and the counter-electrode being graphite. Working electrodes were made from either electrical grade copper wire obtained from VWR Scientific or natural chalcopyrite from Butte, MT, provided by the mineral museum at Montana Tech. MLA/SEM revealed that the copper wire was pure and the chalcopyrite contained minor amounts of quartz inclusions but not more than 5%. All potentials are reported as SHE/E_H potentials. Typical scans in the absence of xanthate were initiated at 0 mV and scanned negatively to a lower potential of –1000 mV and then reversed positively to +1000 mV for as many as six cycles. Copper voltammograms in both the absence and presence of xanthate were initiated between –240 and –440 mV in increments of 25 mV, scanned negatively to a lower potential of –600 mV, and then positively to the final potential of –240 mV. Chalcopyrite voltammograms in the absence and presence of xanthate were restricted to –50 mV as the initial and upper potentials and –600 mV as the lower potential. For all experiments, the initial potential was held constant for approximately 5 minutes and scan rates of 15 mV/s were used. In addition, 1 L electrochemical cells were used with 500 mL solutions and 5-minute nitrogen purges. Solutions were buffered at pH values between 7 and 12.

Materials

Working electrodes were mounted in polyvinylchloride (PVC) tubing using epoxy and polished between CV scans using 400- grit paper. To fit in the tubing, the copper wire was wound into a cylindrical shape and chalcopyrite was cut into approximate dimensions of 3×3×8 mm with the 3×3-mm face being the electrode surface. Electrodag was used to connect the chalcopyrite to the wiring needed to bridge the circuit to the potentiostat. The pH buffers were made up from reagent-grade chemicals of potassium and sodium phosphate as well as sodium carbonate and bicarbonate, all from Fischer Scientific. Potassium ethyl xanthate (KEX) was formulated using potassium hydroxide, ethanol, and carbon disulphide obtained from VWR Scientific following the procedure of Nedjar *et al.* (2009).

E_H–pH diagrams

E_H–pH diagrams were generated with StabCal (Gow *et al.*, 2015; Huang, 2015) using thermodynamic data from Forssberg *et al.* (1988) for the copper/xanthate/water and chalcopyrite/xanthate/water systems.

Results and discussion

Copper

Cyclic voltammetry

A typical CV scan for copper is shown in Figure 1. In this example, results were obtained at pH 9 and illustrate that copper oxidizes at approximately 0.0 V and again at 0.2 V, as indicated by the increase in anodic current as the scan progresses from negative to positive voltage. When these values are plotted on the E_H–pH diagram of the copper/water system in Figure 2, it is clear that 0 V corresponds to Cu oxidation to CuOH (equivalent to Cu_2O) and that 0.2 V correlates with CuOH oxidation to $Cu(OH)_2$ (equivalent to CuO). The dashed lines in the diagram illustrate the conditions where water is stable. When this is repeated for the CVs determined at the other pH values, the results also compare quite well with the stability lines between the species on the E_H–pH diagram. Because of the good correlation between the thermodynamically predicted and experimentally obtained results, it is concluded that the wire is an effective copper electrode.

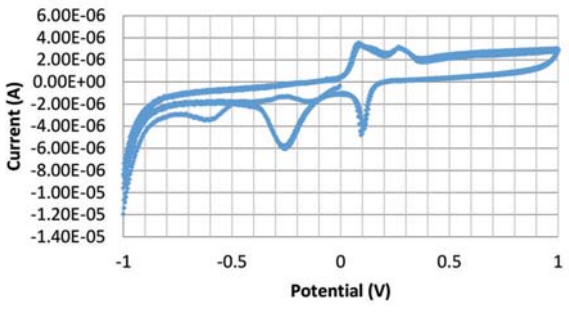

Figure 1—Cyclic voltammograms of copper at pH 9 without xanthate

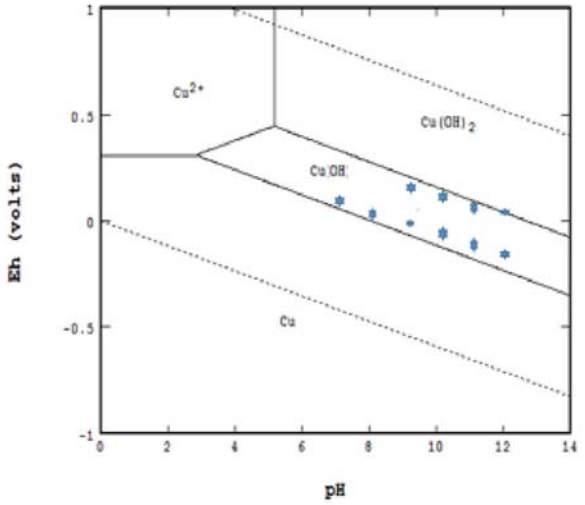

Figure 2—E_H–pH diagram of copper/water system with data points determined from cyclic voltammetry

Chemisorption

Woods *et al.* (1990) developed a technique to calculate adsorption isotherms for chemisorbed xanthate on copper and chalcocite (Cu_2S). With this technique, they obtained CVs in the absence and presence of xanthate by holding the initial potential constant for 5 minutes and then collecting the CV. Afterwards, the initial potential was incrementally changed until the complete range at which chemisorption occurred was covered and no change was observed between the tests performed with and without xanthate. By integrating the area covered by each CV and dividing by the scan rate, the charge passed for each CV was calculated. Subtracting the charge without xanthate from the charge with xanthate at each potential yielded the charge caused solely by xanthate chemisorption. When all charges were divided by the maximum charge obtained, chemisorption isotherms resulted with fractional surface coverage, θ, plotted as a function of potential.

To validate the work of Woods *et al.* (1990) and simultaneously establish a procedure for testing on chalcopyrite, we repeated their technique for copper. Voltammograms are presented in Figure 3a without xanthate and Figure 3b with xanthate. In Figure 3, the voltammograms determined with an initial potential near –0.5 V are the same, thereby explaining why no xanthate chemisorption was calculated at this potential (see Figure 4). Likewise, the voltammogram determined with an initial potential of –0.24 V in Figure 3b shows a second cathodic peak appearing near –0.60 V, which is caused by the surface precipitation of copper xanthate (see Equation [1]). In this regard, it is concluded that xanthate chemisorption is at a maximum at –0.265 V and therefore yields complete monolayer coverage (*i.e.*, $\theta = 1$) at this potential. Likewise, the other voltammograms in Figure 3 yielded fractional coverages between these values (*i.e.*, $0 < \theta < 1$).

As with Woods *et al.* (1990), it is assumed the resulting chemisorption isotherm follows the Frumkin equation in the form adopted by Schultze (1980):

$$\left[\frac{\theta}{1-\theta}\right] e^{g\theta} = K a_A e^{\gamma FE/RT} \quad [4]$$

where θ is the fractional surface coverage, a_A is the activity of the adsorbate, g and K are constants, and γ is the electrosorption valency. Assuming the activity is equal to the xanthate concentration, $[X^-]$, the following equation is determined:

$$\left[\frac{\theta}{1-\theta}\right] = 6.68 \times 10^{11}[X^-]e^{E/0.0257} \quad [5]$$

which agrees well with the chemisorption isotherm determined by Woods *et al.* (1990):

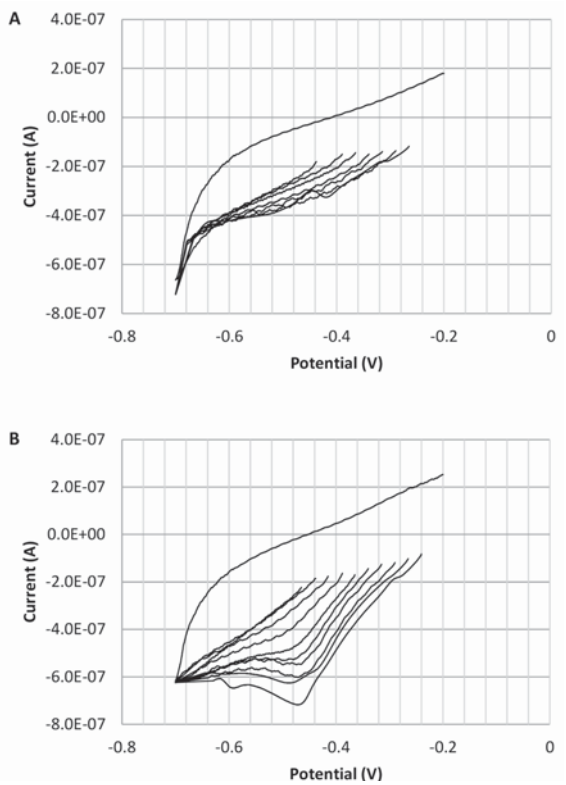

Figure 3—Voltammograms of copper at pH 9 (a) without and (b) with 1E-4 M xanthate

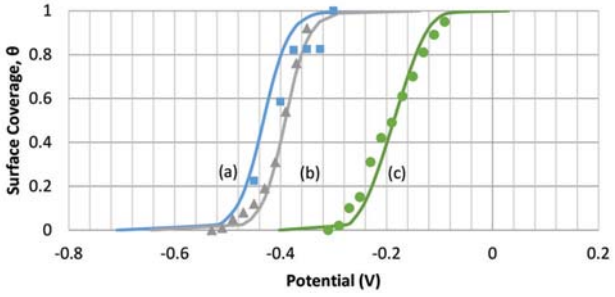

Figure 4—Chemisorption isotherms determined for copper at pH 9 with 1E-4 M xanthate (a) in this investigation, compared to those similarly determined by Woods, Young, and Yoon (1990) on (b) copper and (c) chalcocite

$$\left[\frac{\theta}{1-\theta}\right] = 5.3 \times 10^{11}[X^-]e^{E/0.022} \quad [6]$$

Chalcopyrite

Cyclic voltammetry

An example CV for chalcopyrite in the absence of xanthate is shown in Figure 5. In this case, results were obtained at pH 8 and the anodic portions show that chalcopyrite oxidizes at approximately –0.75 V, –0.05 V, and 0.35 V. When these values are plotted on the E_H–pH diagram of the chalcocite/water system in Figure 6, it is clear that the potentials correspond to oxidation of Cu to $CuFeS_2$ to Cu_2S to CuOH to $Cu(OH)_2$, respectively. Oxidation is also observed at 0.8 V but was not plotted because this correlated with oxygen evolution and therefore is not relevant. Although there is more overall scatter in this data, it does match reasonably well with the thermodynamic calculations. Of course, it is understood that chalcopyrite is a semiconductor (unlike copper being a pure conductor) and electrochemical reactions are partially irreversible as a result.

Because chalcocite is a product of chalcopyrite oxidation, it is reasonable to expect that xanthate chemisorption on chalcopyrite would occur in regions similar to copper and chalcocite (see Figure 4). Furthermore, because chalcopyrite/xanthate flotation is predominantly accomplished near pH 9, initial testing was done at pH 9 such that the starting potential was changed from 0 to –0.3 V in increments of 0.05 V until the reaction was no longer seen. Xanthate chemisorption was no longer observed at potentials below –0.25 V, the same potential shown in Figure 4 and observed by Young *et al.* (1991) for chalcocite (Cu_2S) in a separate study. However, an isotherm could not be ascertained because the results appeared to depend on the prior amount of chalcocite that formed. Similar tests were repeated at pH 7 and 11 but in these cases no chemisorption was observed.

Rather than incrementally change the initial potential, tests were repeated at a single initial potential of –0.05 V. A lower potential of –600 mV was used to ensure the charge due to xanthate chemisorption could be determined. Results in the absence and presence of xanthate for the three pH values of 7, 9, and 11 are shown in Figure 7a-c, respectively. Results for pH 7 and 11 clearly show that the CVs with and without xanthate are the same, illustrating that xanthate chemisorption is indeed absent. However, at pH 9, there appears to be significant current flow in both the absence and presence of xanthate. According to the E_H–pH diagram in Figure 8, at –0.05 V, $CuFeS_2$ is stable at pH 7 (no current was observed), Cu_2S is stable at pH 9 (current was observed), and CuOH is stable at pH 11 (no current was observed). Clearly, xanthate chemisorption does not occur on $CuFeS_2$ and CuOH but does occur on Cu_2S, even if it is an oxidation product of chalcopyrite. This suggests that chalcopyrite flotation can be attributed to dixanthogen and copper xanthate surface precipitate as well as chemisorbed xanthate. Unfortunately, these thermodynamic calculations do not show dixanthogen being co-stable with chalcopyrite. In fact, dixanthogen predominates only at potentials more oxidizing than the stability region of CuX.

Chemisorption

The collectorless flotation of chalcopyrite can be attributed to elemental sulphur formation and is depicted by the following reaction, which also yields chalcocite:

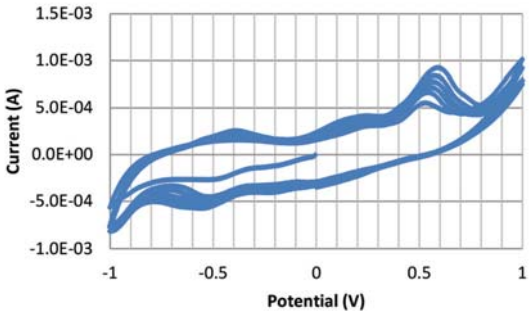

Figure 5—Cyclic voltammograms of chalcopyrite at pH 8 in the absence of xanthate

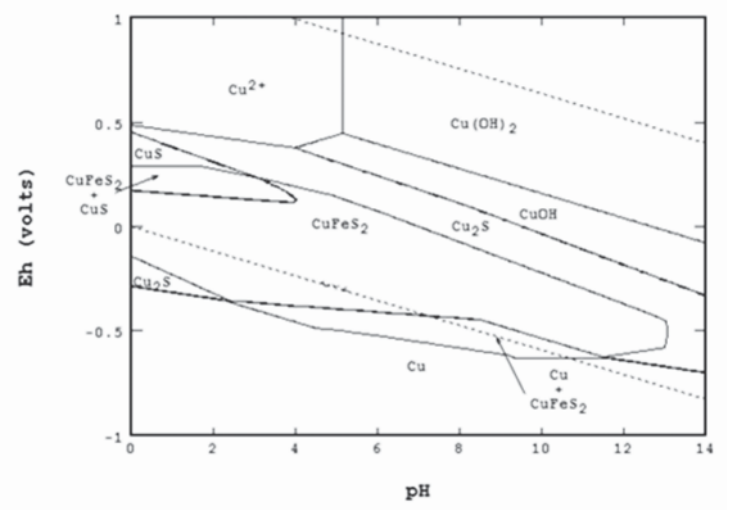

Figure 6—E_H–pH diagram of chalcopyrite/water system with data points determined from cyclic voltammetry. Sulphide oxidation to elemental sulphur only (*i.e.*, sulphoxy species are not considered)

Xanthate chemisorption at copper and chalcopyrite surfaces

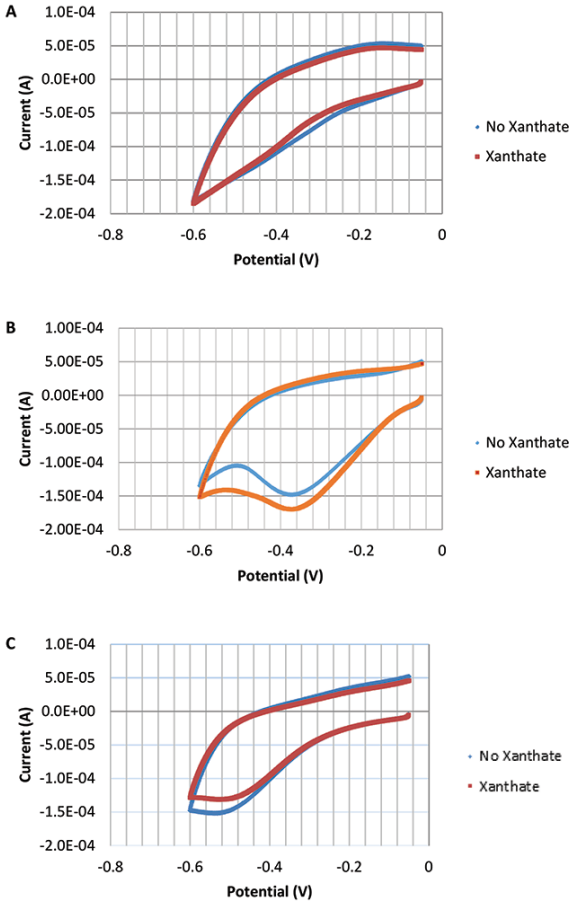

Figure 7—Voltammograms of chalcopyrite at (a) pH 7, (b) pH 9, and (c) pH 11 with and without 1E-4 M xanthate

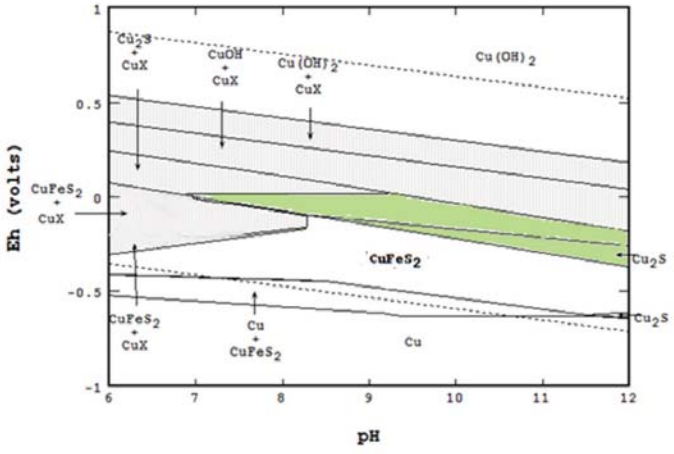

Figure 8—E_H-pH diagram of chalcopyrite/xanthate/water system as concluded from this investigation. Grey indicates regions of CuX formation and green indicates regions of chemisorbed xanthate

$$2CuFeS_2 + 6H_2O \leftrightarrow Cu_2S + 3S^{\circ} + 2Fe(OH)_3 + 6H^+ + 6e^- \quad [7]$$

In order to estimate the charge passed by this reaction, the CVs without xanthate in Figures 7a and 7b were integrated and divided by the scan rate. Because the charge passed in Figure 7a did not change with xanthate, it is assumed that it emanates from IR drop and is the same as that passed in Figure 7b without xanthate. The difference between the two therefore yields the charge passed due solely to chalcocite formation. Based on the molar charge of electrons being 9.65×10^4 coulombs and the reaction producing six moles of electrons, an estimated 1.95×10^{-9} moles of chalcocite form. Likewise, the difference in charges determined for the two CVs in Figure 7b yields the charge

passed due solely to xanthate chemisorption on the resulting chalcocite. In this regard, an estimated 7.98×10^{-10} moles of chemisorbed xanthate formed. According to Liu (2014), the area of surface that is accessible for intermolecular contact in the S–S atoms of a xanthate molecule is 19.2 Å^2. In a Cu_2S lattice, there is approximately one Cu atom per 9 Å^2 according to the studies by Evans (1979). From this data, the surface area of the Cu_2S available for adsorption was found to be 2.11×10^{-4} m^2 and the surface area of xanthate formed was found to be 9.23×10^{-5} m^2. By dividing the amount of chemisorbed xanthate by the amount of Cu_2S formed, a surface coverage of over 40% is calculated. Since Woods *et al.* (1990) noted that 20% coverages yielded 50% chalcocite recoveries and 50% coverages yielded 90% chalcocite recoveries, a 40% coverage would be adequate to yield a high flotation recovery.

Luttrell and Yoon (1984) showed that chalcopyrite will start to float (defined as 10% recovery) at pH 10 near –100 mV *vs* SHE in the absence of collector. Woods (1996) obtained similar results near 0 mV *vs* SHE at pH 11. By comparison, when Roos *et al.* (1990) added 1.5×10^{-4} M KEX, they found that the onset of chalcopyrite flotation occurred near –150 mV *vs* SHE at pH 9.2. Similarly, Chander (2003) floated chalcopyrite ore with various collectors and found flotation did not occur until potentials exceeded 0 mV *vs* SHE at pH 10.5–11. These E_H-pH data points plot near the shaded region in Figure 8, with two points close to the border at low potentials, commonly referred to as the lower flotation edge. However, it is strongly suggested that Equation [7] indicates elemental sulphur will likely be present as well, making it difficult to differentiate between collectorless flotation and xanthate flotation caused by chemisorption on chalcocite (see Equation [3]). Furthermore, even though Equation [3] is pH-independent, xanthate cannot chemisorb unless the surface it forms at is present. Hence, the pH-dependency is due directly to chalcocite being produced as a result of Equation [7]. This would help explain why the data from these studies is scattered (Luttrell and Yoon, 1984; Woods, 1996; Roos *et al.*, 1990; Chander, 2003).

In an attempt to more definitively prove that a layer of chemisorbed xanthate was forming on the surface of the chalcopyrite, *in situ* and *ex situ* test work with Raman spectroscopy was performed. Spectra were generated for mineral samples at pH 9 and 0 V *vs* SHE both with and without xanthate in solution. The results did not definitively show the chemisorbed xanthate species. Work in the Metallurgical and Materials Engineering Department at Montana Tech is continuing along these lines.

Conclusions

Although it is known that xanthate can be used to increase the flotation recovery of chalcopyrite there is still uncertainty as regards the exact nature of the surface chemistry and all the areas that xanthate might be interacting with the chalcopyrite surface. This research shows evidence that the chemisorption of xanthate onto a chalcopyrite surface will occur in regions where Cu_2S formed upon oxidation of the chalcopyrite surface. At pH 9 it was shown that this reaction occurs between –0.05 and –0.25 V *versus* SHE, similar to what Woods *et al.* (1990) observed on chalcocite. To help validate the study, previous experiments of Woods *et al.* (1990) on copper were also validated. The results are corroborated by flotation results noted in the literature.

Acknowledgements

The authors thank Newmont Metallurgical Services and Newmont Mining Corporation for their generous support for this research. Newmont's goal of advancing mineral processing and extractive metallurgical knowledge by investing in graduate research at Montana Tech is greatly appreciated.

References

Chander, S. 2003. A brief review of pulp potentials in sulfide flotation. *International Journal of Mineral Processing*, vol. 72, no. 2. pp. 141–150.

Evans, H.T. 1979. The crystal structures of low chalcocite and djurleite. *Zeitschrift fur Kristallographie*, vol. 150. pp. 299–320.

Forssberg, K.S.E., Antti, B-M., and Palsson, B.I. 1984. Computer-assisted calculations of thermodynamic equilibria in the chalcopyrite-ethyl xanthate system. *Reagents in the Minerals Industry*. Jones, M.J. and Oblatt, R. (eds). Institute of Mining and Metallurgy, London, UK. pp. 251–264.

Gow, R., Huang, H., and Young, C. 2015. Utility of mass balanced E_H-pH diagrams II: stoichiometry of the Cu-As-S-H2O system. *Mineral and Metallurgical Processing Journal* [in press].

Huang, H.H. 2015. STABCAL, Version 9.1., Montana Tech, Butte, MT, USA.

Fuerstenau, M.C., Chander, S., and Woods, R. 2007. Sulfide mineral flotation. *Froth Flotation: A Century of Innovation*. Fuerstenau, M.C., Jameson, G., and Yoon, R.H. (eds.). Society for Mining, Metallurgy and Exploration, Littleton, CO, USA. pp. 425–465.

Liu, J. Wen, S, Deng, J., Chen, X., and Feng, Q. 2014. DFT study of ethyl xanthate interaction with sphalerite (1 1 0) surface in the absence and presence of copper. *Applied Surface Science*, vol. 311. pp. 258–263.

Luttrell, G.H. and Yoon, R.H. 1984. Surface studies of the collectorless flotation of chalcopyrite. *Colloids and Surfaces*, vol. 12. pp. 239–254.

Nedjar, Z., Bouhenguel, M., and Djebaili, A.E. 2009. Synthesis and structural characterization of xanthate (KEX) in sight of their utilization in the processes of sulfides flotation. *Journal of Minerals and Materials Characterization and Engineering*, vol. 9. pp. 469–477.

Roos, J.R., Celis, J.P., and Sudarsono, A.S. 1990. Electrochemical control of metallic copper and chalcopyrite-xanthate flotation. *International Journal of Mineral Processing*, vol. 28. pp. 231–245.

Schultze, J.W. 1980. The role of elementary steps in the kinetics of adsorption processes. *Proceedings of the Third Symposium on Electrode Processes*. Bruckenstein, S., McIntyre, J.D.E., Miller, B., and Yeager, E. (eds.). The Electrochemical Society, Princeton, NJ, USA. pp. 167–189.

Smart, R.S.C., Gerson, A.R., Hart, B.R., Beattie, D.A., and Young, C.A. 2014. Innovation in measurement of mineral structure and surface chemistry in flotation: past, present, and future. *Mineral Processing and Extractive Metallurgy: 100 Years of Innovation*, Anderson, C.G., Dunne, R.C., and Uhrie, J.L. (eds). Society for Mining, Metallurgy and Exploration, Littleton, CO, USA. pp. 577–602.

Suoninen, E. and Laajalehto, K. 1993. Structure of thiol collector layers on sulphide surfaces; *XVIII International Mineral Processing Congress*. Australasian Institute of Mining and Metallurgy, Carlton, Victoria, Australia. pp. 625–629.

Woods, R. 1996. Chemisorption of thiols on metal and metal sulphides. *International Journal of Mineral Processing*, vol. 29. pp. 401–453.

Woods, R., Young, C.A., and Yoon, R.H. 1990. Ethyl xanthate chemisorption isotherms and E_H-pH diagrams for the copper/water/xanthate and chalcocite/water/xanthate systems. *International Journal of Mineral Processing*, vol. 30. pp. 17–-3.

Young, C.A., Basilio, C.I., and Yoon, R.H. 1991. Thermodynamics of chalcocite-xanthate interactions. *International Journal of Mineral Processing*, vol. 31. pp. 265–279. ◆

http://dx.doi.org/10.17159/2411-9717/2016/v116n6a4

Study of the dissolution of chalcopyrite in solutions of different ammonium salts

by T. Moyo* and J. Petersen*

Synopsis

The oxidative leaching of chalcopyrite in ammoniacal solutions has been evaluated using electro-analytical techniques and controlled bulk leaching studies. The anodic dissolution process has been established to be a seven-electron transfer process under nitrogen in ammonia–ammonium sulphate solutions and ammonia–ammonium carbonate solutions, which suggests that the sulphur is oxidized to thiosulphate and the copper and iron released as Cu^{+} and Fe^{2+} in these systems. The deportment of Fe^{2+} and $S_2O_3^{2-}$ is affected by choice of the ammonium salt used in the leaching process. In the perchlorate salt, only five electrons are transferred, supporting formation of different sulphur species as proposed for the sulphate and carbonate salts. Scanning electron microscopy and energy-dispersive spectroscopic analysis of the mineral surface after leaching indicate presence of an iron–sulphur surface layer completely free of copper in the sulphate system, an iron-rich surface layer in the perchlorate solutions, and absence of surface layer build-up in carbonate solutions. XRD analysis of a bulk leach residue from leaching in ammonia-ammonium sulphate solutions showed the surface layer to be mostly amorphous (90%). The crystalline content (10%) is composed of 95% polymorphs of anhydrous iron oxide hydroxide FeO(OH). Choice of ammonium salt and the hydrodynamic environment of leaching have been shown to influence the presence or absence of the surface product, as well as its nature.

Keywords
chalcopyrite, ammonia, surface deposits, coulometry, iron oxy-hydroxide.

Introduction

Hydrometallurgical processes for copper extraction provide a viable route to recover the metal from mixed and low-grade ores, as well as overcome the environmental challenges faced by the traditional pyrometallurgical processes. Chalcopyrite is not only the most abundant of the copper sulphides, but also the most stable, making it recalcitrant to hydrometallurgical processes. Hence, hydrometallurgical processing of chalcopyrite continues to be an attractive area of research due to the vaguely understood surface chemistry of the mineral in different aqueous media. Different routes for hydrometallurgical treatment of chalcopyrite can be followed. These include thermal treatment prior to leaching, direct leaching and direct electrochemical leaching (Venkatachalam, 1991). Direct leaching of chalcopyrite can be carried out in various solution systems, as reviewed by Roman and Benner (1973) and Venkatachalam (1991). Ammoniacal solutions are attractive and effective lixiviants that form stable amine complexes with some base metal cations while rejecting iron. Leaching of chalcopyrite in ammoniacal solutions in the presence of an oxidant is possible due to the stabilization of copper (I) and copper(II) by ammonia at elevated pH levels. In oxygenated ammonia solutions, it has been suggested that chalcopyrite dissolves according to Equation [1] (Beckstead and Miller., 1977a):

$$CuFeS_2 + 4NH_3 + 17/4O_2 + 2OH^- \rightarrow Cu(NH_3)_4^{2+} + \tfrac{1}{2}Fe_2O_3 + 2\,SO_4^{2-} + H_2O \quad [1]$$

Chalcopyrite is characterized by very slow leaching kinetics and this has been strongly linked to the formation of a passive film on its surface. Researchers have not reached a consensus on the actual composition or degree of stability of this passive surface film. Fe_2O_3 or its hydrated form $Fe_2O_3.xH_2O$ (Beckstead and Miller, 1977b; Yin *et al.*, 1995; Forward and Mackiw, 1955; Feng and Van Deventer, 2002) and $Fe(OH)_3$ (Yin *et al.*, 1995; Warren and Wadsworth, 1984) have been reported to be the surface products of chalcopyrite oxidation. Warren and Wadsworth (1984) studied the electrochemical oxidation of chalcopyrite in ammonia–ammonium sulphate solutions and reported significant amounts of ferrous iron (3–20%) in the product film. The authors postulated that a ferrous iron intermediate was formed, which can be readily oxidized to ferric, and the oxidation can be achieved even if only traces of dissolved oxygen are present. If ferrous iron is formed from chalcopyrite dissolution, it is expected that its further reactions would be affected by the solution conditions, hence the different surface effects as observed under the

* *Mineral to Metal Research Initiative, University of Cape Town, Cape Town, South Africa.*

 This paper was first presented at the, Copper Cobalt Africa Conference, *6–8 July 2015, Avani Victoria Falls Hotel, Victoria Falls, Livingstone, Zambia.*

carbonate and sulphate ammonium salts. Asselin (2011) reported that Fe(II) ammines are thermodynamically stable only under reducing conditions and concluded that they were unlikely to be formed if oxygen is present. He presented quasi-equilibrium Pourbaix diagrams for the Fe–NH_3–H_2O system. According to the diagram, $Fe(OH)_3$ is the species present at noble potentials across all pH ranges, while $Fe(OH)_2$ is present only above pH 11.

Forward and Mackiw (1955) suggested that sulphide minerals, chalcopyrite in this case, react with oxygen, water, and ammonia to produce soluble salts in such a way that the iron present in each mineral particle is converted to hydrated iron oxide *in situ*, with the result that the particles, when leaching is complete, consist of hydrated iron oxide pseudomorphic with the original mineral. Beckstead and Miller (1977b) discuss the nucleation and growth of the haematite passivating layer (in ammonia–ammonium sulphate solutions), stating that this occurred on the anodic sites, thus limiting the overall reaction by limiting the anodic reaction. Agitation at speeds up to 3000 r/min increased the rate of reaction, possibly by abrading the haematite layer and exposing more of the anodic sites. The contradiction between these two studies stems from the fact that Beckstead and Miller looked at the nucleation and growth of the Fe product and identified it as haematite, while Forward and Mackiw looked at 'an ion substitution mechanism, resulting in a Fe product atypical of chalcopyrite'. In a study on the surface oxidation of chalcopyrite in alkaline solutions, Yin *et al.* (2000) reported that the iron in the top layer of chalcopyrite oxidized, forming a monolayer of $Fe(OH)_3$ and Fe_2O_3, while the copper and sulphur remained unoxidized in the original chalcopyrite crystal structure, forming a phase they designated as CuS_2*, which together with the $Fe(OH)_3$ and Fe_2O_3 retarded the oxidation of the mineral. The abrasion of the passivating layer, although not widely researched in ammoniacal media, has been demonstrated to have potential to increase copper recoveries and a process, the FLSmidth® Rapid Oxidative Leach (ROL), has been patented (Eyzaguirre *et al.*, 2015). This process uses very low-energy interstage attrition to enhance dissolution of copper-bearing minerals, primarily chalcopyrite, through a mechano-chemical process that is based on the removal of the passivating product layers. The application of such a process agrees well with results from Beckstead and Miller's (1977b), in which the chalcopyrite surface was observed to be free of surface deposit at high agitation speeds, possibly due to increased abrasion.

Literature on iron chemistry in ammonia–ammonium carbonate solutions is limited for the chalcopyrite leaching process, thus reference will be made to the Caron process. Studies have been carried out on the leaching of nickel from pre-reduced laterite ores (nickel and iron are present as reduced metallic grains and metal alloys) (Das and Anand, 1995; Jandová and Pedlík, 1994, Kim *et al.*, 1991; Lee, Osseo-Asare, and Pickering, 1985; Nikoloski, 2002; Nicol, Nikoloski, and Fittock, 2004). At a pH of about 9.8 in ammoniacal solutions, the dominant dissolved iron species is the ferrous tetra-ammine ion and the dissolution reaction has been postulated to occur according to Equation [2] (Nikoloski, 2002; D'Aloya and Nikoloski, 2012; Subrata, 2010; Nikoloski and Nicol, 2006; Osseo-Assare and Asihene, 1979):

$$Fe + 4\ NH_3 \rightarrow Fe(NH_3)_2^{2+} + 2e \quad [2]$$

$$FeNi + 8NH_3 \rightarrow Fe(NH_3)_2^{2+} + Ni(NH_3)_6^{2+} \quad [3]$$

The ferrous ammine is oxidized in aerated solutions to form ferric, which does not form ammines and is thus precipitated as $Fe(OH)_3$ releasing the ammonia:

$$Fe(NH_3)_2^{2+} + 0.25\ O_2 + 2OH^- + 0.5\ H_2O \rightarrow Fe(OH)_3 + 2NH_3 \quad [4]$$

Nikoloski (2002) showed that iron is prone to passivation in solutions typical of those used in practice, and confirmed its occurrence in leaching reactors of a commercial scale in the Caron process. Passivation was shown to occur due to the formation of an oxide layer at the potentials that can be attained in the presence of high concentrations of dissolved oxygen.

An earlier study by the authors (Moyo *et al.*, 2015) investigated chalcopyrite dissolution in ammonia–ammonium sulphate solutions. Coulometric measurements on a chalcopyrite electrode resulted in postulating a seven-electron transfer mechanism, with the potential formation of thiosulphate as the product of sulphur oxidation. Copper(II), rather than oxygen, was found to be the primary oxidant on the mineral surface. Rapid formation of an iron oxide layer on the electrode surface was observed, which did not inhibit, but slowed down, the rate of anodic dissolution over time. No iron was found in solution, whereas no copper was found in the surface layer.

The present study aims to elucidate the nature of the surface deposits and to what extent anions in the ammoniacal solution might have an effect on their formation. Tests were done in ammonium sulphate, carbonate, and perchlorate solutions. Coulometric tests were done in each case to ascertain if the dissolution mechanism remained the same in the different solutions before investigating the surface layers formed on the chalcopyrite electrode.

Experimental

Chalcopyrite electrodes

Samples of natural chalcopyrite from Durango, Mexico (supplied by Wards Natural Science) were mounted on brass stubs with conductive silver epoxy and the assembly then imbedded in non-conductive epoxy resin. X-ray diffraction (XRD) analysis of the mineral sample indicated it to be 100% chalcopyrite, while quantitative electron microscopy (QEMSCAN™) indicated it to be 95% chalcopyrite, with 3% sphalerite and 1% calcite. The electrode surface was polished on 1200-grit SiC abrasive paper, then on 1 μm, 0.3 μm, and 0.05 μm aluminium oxide prior to each experiment, except where stated. Only one electrode was used for the purposes of this study and the exposed surface area of the electrode was measured to be 0.36 cm^2 using imagej™ for image analysis. The surface area was measured intermittently during the course of the study and was found not to change significantly.

Electrochemical measurements

A standard three-electrode cell with a chalcopyrite rotating-disk working electrode was used for all electrochemical

measurements. A saturated calomel reference electrode and platinum wire auxiliary electrode were used. A freshly polished chalcopyrite electrode was placed into an electrolyte of desired composition and rotated at 1600 r/min. Rest potentials were measured for 30 minutes. A Gamry Series G 300/750 potentiostat was used. Coulometric experiments were carried out by fixing the potential at a value measured during the rest potential measurements described above (after 30 minutes) in a solution of similar composition but in the *absence* of copper(II) ions. Total charge was obtained by integration of the current–time curves. The current response of the electrode was then measured for 2 hours. Additional coulometric experiments were carried out for 5 hours or 22 hours at the rest potential or the vicinity of the rest potential in a minimum volume of solution. At the end of the experiment, the solutions were analysed for copper using inductively coupled plasma optical emission spectroscopy (ICP-OES). All potentials are reported against the standard hydrogen electrode (SHE) unless stated otherwise. Experiments were conducted at 25°C in a thermostatted cell containing 30 mL solution. The total Cu concentration in solution at the end of the coulometric experiments was established by ICP-OES.

Controlled leaching experiments

Three tests were carried out, two in which blocks of chalcopyrite 5 mm × 5 mm × 5 mm were leached (reactors A and B) and a third one in which micronized chalcopyrite (81% passing -75 μm) was leached in 3 M total ammonia–ammonium sulphate solutions at 1% solids (reactor C). Reactor A had glass beads added, which allowed for the abrasion of the surface product from the chalcopyrite blocks, while reactor B had no beads in it. The leaching experiments went on for a period of 5 days, allowing for significant amounts of surface product to be generated. Magnetic stirrers were used; this was adequate to keep the sample in swirling motion but could not suspend the sample in solution for reactors A and B, while the micronized sample in reactor C was effectively suspended. The lixiviant was first placed in the reactors and brought to the desired reaction temperature, 25°C. The temperature was controlled by a thermostatted water bath circulating water around the jacketed reactors. Oxygen was bubbled into the solution for 10 minutes prior to the experiment, allowing the solution to be saturated with dissolved oxygen, and a blanket of oxygen gas was maintained over the solution through the entire experiment. Solution pH was 9.6±0.15 from the buffer of the ammonia-ammonium sulphate. The mineral sample was then placed into the reactor, marking the onset of the reaction. Solution samples were taken intermittently and analysed for copper using atomic absorption spectrophotometry (AAS).

Solution preparation

Deionized water and reagent-grade $CuSO_4.5H_2O$, NH_4OH, $(NH_4)_2SO_4$, $(NH_4)_2CO_3$, NH_4ClO_4, H_2SO_4, and NaOH were used. All solutions were prepared by mixing 1:1 molar ratio ammonium hydroxide to ammonium salt based on the ammonium ion, *i.e.*, a 1 M (NH_3+NH_4^+) solution was made by mixing 1 M NH_4OH with 0.5 M $(NH_4)_2SO_4$. Rest potentials that were later used for the coulometric experiments, were measured in the presence of 5 g/L initial copper(II). Either oxygen (99.99%) or nitrogen was bubbled into the electrolyte for 10 minutes prior to starting the experiment, and bubbling was continued throughout the experiment, taking care to ensure that gas bubbles did not accumulate on the chalcopyrite electrode surface (in electrochemical experiments). This was established to be sufficient time to either saturate the solution with dissolved oxygen or remove it from solution.

Surface measurements

The surface of the chalcopyrite was examined by scanning electron microscopy (SEM) and QEMSCAN. An elemental analysis was done on the surface using energy-dispersive X-ray spectroscopy (EDS) in an attempt to characterize the surface effects and products under the conditions of this study. The leach residue was further analysed using X-ray diffraction (XRD), Brunauer-Emmett-Teller (BET) surface analysis, as well as digested and subjected to chemical analysis using atomic absorption spectroscopy.

Results and discussion

Coulometry

Coulometry studies were done in the different salt media, as described in the methodology. The stoichiometry of the anodic dissolution reaction was determined by this method. The coulometric results shown in Table I include data from our previous study (Moyo *et al.*, 2015) on the sulphate system. Table I shows the number of electrons transferred per molecule of chalcopyrite (measured as copper released into solution) at potentials corresponding to rest potentials measured in 1 M (NH_3+NH_4^+) with 5 g/L Cu(II) at 25°C, but here in the *absence* of initial Cu in solution. All measurements were repeated at least three times and the calculated number of electrons transferred was found not to vary by more than 5%.

Table I

Determination of number of electrons transferred per mole of copper at rest potential

Ammonium salt	E_0 (V *vs* SHE)	Total Cu from ICP (mol/L)	Total charge *Q* (C)	*n*(e)=*Q*/F	No of electrons/mole Cu
Carbonate N_2	0.231	9.47E-07	0.635	6.58E-06	7
Sulphate* N_2	0.26	3.96E-07	0.261	2.71E-06	6.8
Perchlorate N_2	0.013	1.01E-06	0.473	4.90E-06	4.8

*Data from Moyo *et al.* (2015)

In the carbonate system, as previously found for the sulphate system, approximately seven electrons are transferred per mole of copper. This suggests the formation of a thiosulphate intermediate and that the copper and iron are in the cuprous and ferrous states. The cuprous and ferrous ions would then be subsequently oxidized in solution, in non-faradaic reactions, to the cupric and ferric state. The stoichiometry of the reaction would be approximated by Equation [5]. In perchlorate solution, on the other hand, approximately five electrons are transferred, suggesting the potential formation of elemental sulphur and the formation of cupric and ferric (Equation [6]), *i.e.*, the oxidation of the iron and the copper take place as faradaic reactions:

$$CuFeS_2 + 4\ NH_3 + 6\ OH^- \rightarrow Cu(NH_3)_2^{+} + Fe(NH_3)_2^{2+} + S_2O_3^{2-} + 3\ H_2O + 7e^- \quad [5]$$

$$CuFeS_2 + 4\ NH_3 + 3\ OH^- \rightarrow Cu(NH_3)_2^{2+} + Fe(OH)_3 + 2\ S + 5e^- \quad [6]$$

Topological effects

The visual differences between the chalcopyrite surfaces after polarization were apparent even to the naked eye, with those treated in the sulphate and perchlorate solutions having lost their lustre and exhibiting a reddish-brown colouration, while that treated in the carbonate solution had lost its lustre but did not exhibit any colour changes. Figure 1A shows optical microscope images of a freshly polished chalcopyrite surface and 1B shows chalcopyrite after oxidation in ammonia–ammonium sulphate solutions – the difference is quite clear. Freshly polished chalcopyrite prior to leaching was analysed using SEM (image not shown). Atomic percentages, 24.62% Cu, 25.67% Fe and 49.71% S, measured by bulk EDS, are consistent with those of pure chalcopyrite. This provides a basis of comparison for the samples analysed post-leaching. Figure 2 shows a SEM image of a chalcopyrite surface after 22 hours of oxidation in ammonia–ammonium sulphate solutions under nitrogen. It is copper-free and has significant amounts of sulphur and iron. EDS shows the surface composition to be 22.85 at.% Fe, 12.18 at.% S, 2.48 at.% Si, and 62.49 at.% O. The Fe:S ratio is 1.9:1, which represents a significant shift from the 1:2 ratio of pure chalcopyrite. The presence of sulphur on the surface was previously reported by Warren and Wadsworth (1984), who upon scraping off and dissolving the surface film from their experiments identified some orthorhombic sulphur, confirming that elemental sulphur was present in both the surface film and leachate. The researchers attributed this to the disproportionation of some of the intermediate sulphur species expected to be found in the leachate. Kuhn, Arbiter, and Kling (1974) presented the possibility of the recrystallization of sulphur from the sulphide to form rhombic or monoclinic sulphur, which would be expected to be found in localized sites within the mineral, while cations diffuse out of the mineral. Therefore, the presence of sulphur on the mineral surface, as observed in this study, is possible although not widely reported.

The morphology of the surface layer suggests that it may have been formed by precipitation, which is in contradiction to the ion-substitution mechanism proposed by Forward and Mackiw (1955). This is more apparent when looking at residue on the surface of a chalcopyrite block leached for 5 days in the absence of glass beads (reactor B) (Figure 5), which shows what appears to be an agglomerate of small particles. This surface product readily dissolved upon short contact with concentrated sulphuric acid solutions, leaving behind an etched but pure chalcopyrite surface. The acid solution used to wash off the surface layer was analysed using ICP and found to contain 16.05 mg/L iron but only 0.095 mg/L copper, confirming the SEM results which indicated it to be an iron-rich surface layer.

As stated in the introduction, the presence of a relatively small amount of sulphur in the surface deposit prompted the investigation of chalcopyrite dissolution in non-sulphate media. Figure 3 shows the mineral surface after 22 hours of oxidation in ammonia–ammonium carbonate solution. All other solution conditions were maintained the same. The bulk EDS results indicates 23.78% Fe, 44.12% S, 20.82% Cu, and 11.28% O. Copper accounts for 20.82% of the surface. Assuming that this comes from the chalcopyrite then, in terms of atomic ratios, this agrees well with the amount of sulphur present, leaving a small proportion of excess iron, *i.e.*, 2.96 percentage points more iron than copper. The ratio of Fe:S is 1:1.85, fairly close to that of pure chalcopyrite. This suggests that only a very thin film of an iron-rich phase

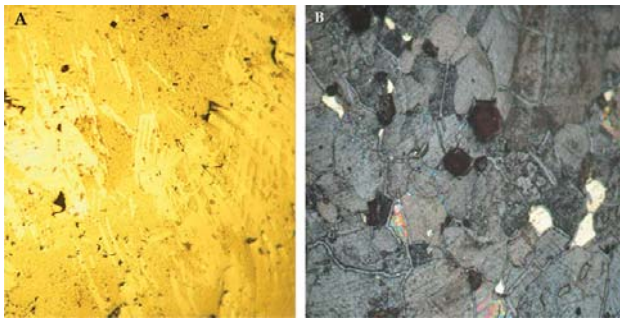

Figure 1—Optical microscope images of chalcopyrite electrode (A) freshly polished and (B) 22 hours' oxidation at 0.255 V (SHE) in 1 M [1 M ammonium hydroxide + 0.5 M ammonium sulphate] at 25°C under nitrogen

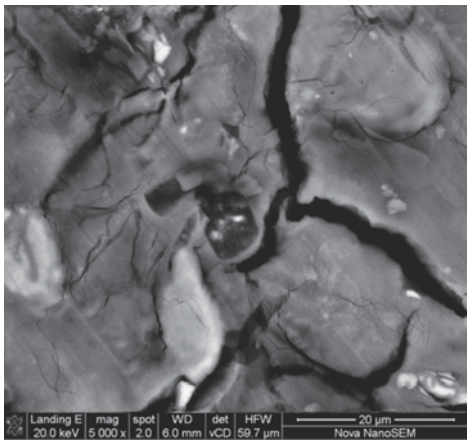

Figure 2—SEM image of chalcopyrite immediately after oxidation for 22 hours at 0.255 V (SHE) in 1 M [1 M ammonium hydroxide + 0.5 M ammonium sulphate] at 25°C under nitrogen. The sample was washed in distilled water and dried under vacuum. Bulk EDS (in atomic per cent) 22.85% Fe, 12.18% S, 2.48% Si, 62.49% O

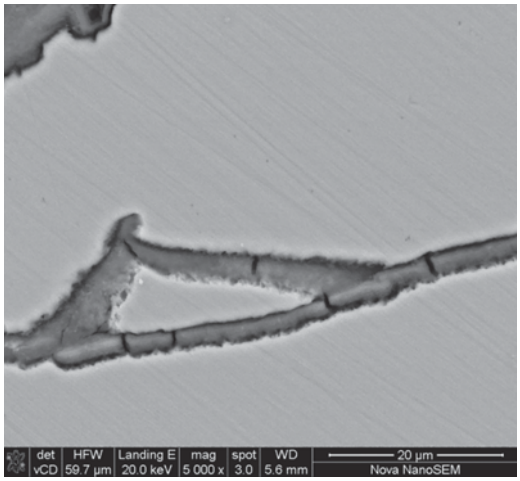

Figure 3—SEM image of chalcopyrite immediately after leaching in ammonia–ammonium carbonate solution. Bulk EDS (in atomic per cent) 23.78% Fe, 44.12% S, 20.82% Cu, 11.28% O, and a spot EDS within the grain boundary 26.19% Fe, 10.51% S, 3.87% Cu, 58.67% O, 0.8% Si

would be present. The visible cracks were observed to be more copper-depleted. EDS analysis of the crack areas showed only 4–6% to be copper, suggesting these to be areas of preferential chalcopyrite dissolution in the carbonate medium. This is further supported by the visibility of polishing marks on the unleached areas in Figure 3. The differences in surface effects between the sulphate and carbonate solutions suggest that the surface reaction mechanism varies, although the same number of electrons is transferred. Iron carbonate complexes potentially form in this system, and tend to stay in solution, whereas the formation of a surface precipitate in the sulphate system is more likely to be linked to the formation of iron sulphate complexes that precipitate.

The behaviour of iron in ammonium carbonate solutions has been explored by some researchers, with the focus on improving the leaching kinetics in the Caron process. Kim *et al.* (1991) studied the active–passive behaviour of sintered iron in ammoniacal ammonium carbonate solutions at pH 9.7 and reported that surface films were formed on the bulk iron during exposure to air or immersion in ammoniacal solutions. The authors characterized the surface films using X-ray photoelectron spectroscopy (XPS) and generated cathodic reactivation transients; they reported that in the presence of air Fe_3O_4 was formed. Caldeira, Ciminelli, and Osseo-Asare (2008) investigated the effect of carbonate on pyrite oxidation in alkane solutions and identified (using diffuse reflectance infrared spectroscopy) iron carbonate compounds as one of the products of pyrite oxidation. The authors explain that the increased oxidation rate typically observed on pyrite in carbonate solutions is possibly due to the formation of Fe(II)–CO_3 complexes, the buffering effect of the carbonate and the fact that complexation with bicarbonate/carbonate provides a stronger Fe(III)/Fe(II) redox couple, increasing the Fe(III) solubility. This could be an explanation for the apparent lack of significant surface layer formation on chalcopyrite in the carbonate system, through the possible formation of soluble Fe(II)–CO_3 complexes which are then transported away from the vicinity of the mineral surface. It should be noted that, although other studies of the carbonate system reported the presence of an oxide layer, the obvious lack of any significant layer in this study could also be attributed to the hydrodynamics around the electrode area. Rotating at 1600 r/min may be sufficient to allow the transport of the metastable iron carbonates away from the mineral surface before they have a chance to nucleate and precipitate. The effect of electrode rotation speed on the extent of surface layer build-up and its morphology in the sulphate system have been reported by Beckstead and Miller (1977b), who found that chalcopyrite surfaces were much cleaner and relatively free of surface product at agitation speeds higher than 1100 r/min. They postulated that increased agitation speeds improved leaching by increasing turbulence, which in turn allowed for the abrasion of the surface product, thereby exposing a fresh mineral surface for leaching.

To provide further assessment, especially with regard to the sulphur deportment, tests were done in ammonia–ammonium perchlorate solutions, as the perchlorate ions are not expected to complex with the oxidation products of chalcopyrite.

Figure 4 shows an SEM image of a chalcopyrite sample after 22 hours of leaching in ammonia– ammonium perchlorate solutions. Visually, the surface appears not dissimilar to that observed in the sulphate system. However, the bulk surface EDS gave an Fe:S atomic ratio of 1:1.1 and copper is present at a S:Cu of 1:0.38. Analysis of isolated flaky areas on the sample showed these areas to be more iron-rich: Fe:S is 2:1 whereas the S:Cu remains at 1:0.38. The results suggest the presence of an iron-rich surface together with a sulphur species. The atomic ratios of the sulphur and iron are not consistent with the stoichiometric ratios suggested by coulometry (Equation [6]), which would require all sulphur to accumulate on the surface as elemental sulphur and hence there should be twice as much sulphur as iron. However, tests done so far cannot be used to make any conclusive deductions as to whether the sulphur observed to be present on the mineral surface is elemental sulphur or some form of Fe–S complex. Furthermore, the fact that copper

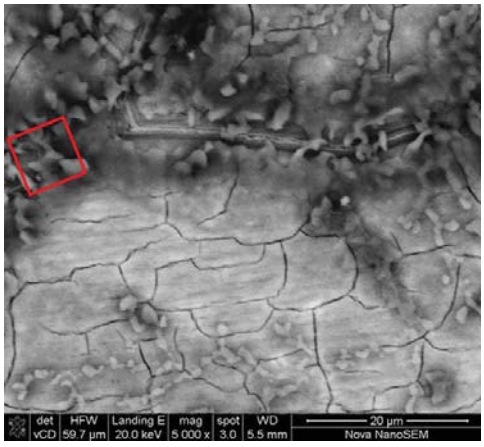

Figure 4—SEM image of chalcopyrite immediately after leaching in ammonia–ammonium perchlorate solution. Bulk EDS (in atomic per cent) 16.25% Fe, 17.33%S, 6.77% Cu, 53.92%O, 4.03%Si. Analysis of the highlighted area 25.56 Fe, 13.08%S, 5.11% Cu, and 56.24% O

was retained on the surface could have affected the copper balance during the coulometric study of the perchlorate system, thus leading to an under-estimate of electrons transferred.

Experiments were done in which 5 mm blocks of the same sample of chalcopyrite were leached in ammonium sulphate, as described in the methodology. In both instances, the remaining pieces of the blocks, as well as any residue that accumulated in the reactor at the end of the experiment, were washed in distilled water, dried, and analysed under the microscope and by QEMSCAN. Figure 5 shows a SEM image of the residue collected from the reactor that contained the beads. Neither sulphur nor copper were found on the residue, and EDS of the residue gave a ratio of O:Fe 1.1:1, fairly close to the 1.5:1 ratio typical of haematite, although this is unlikely to form under the present experimental conditions.

XRD analysis of the residue indicated it to be 90% amorphous, and of the 10% crystalline content 95% comprised polymorphs of anhydrous iron oxide hydroxide FeO(OH) as shown in Table II. ICP and LECO analysis indicated the residue to contain 44% iron and less than 1% of both copper and sulphur.

It should be noted that the leach reaction proceeded much faster in the reactor containing glass beads, with copper recoveries at the end of the 5-day leaching period at 54.9%, whereas in the reactor without glass beads merely 14.7% was leached. It is apparent that the continuous removal of the surface deposits in the reactor with beads had a positive impact on the recoveries. This is in agreement with Beckstead and Miller (1977b), who reported that at low stirring speeds the rate of the reaction was significantly reduced: they related this to the growth and nucleation of a haematite phase. They also reported on the possible impact of stirring speed on the morphology of the haematite phase they observed. In the development of the Sherritt–Gordon process, critical agitation speeds were reported (Forward and Mackiw, 1955) and these are said to have allowed for the abrading of the 'haematite' layer, thus improving leaching rates. Also, in the Arbiter process (Kuhn *et al.*, 1974), intense mixing is used to abrade the haematite phase from the Cu–Fe–S phase, thus exposing a fresh surface for reaction, as well as achieving good oxygen transfer rates.

Figure 6 shows QEMSCAN and SEM images of one of the sample blocks placed in the reactor without beads. An iron-rich surface deposit is visible at the edge on the mineral, and the morphology of this surface layer can be seen on the BSE image to be similar to that of the debris in Figure 5. The bulk phase, orange in colour, has been identified as chalcopyrite, while the yellow is an iron-rich phase containing small percentages of sulphur and the black phase is an iron- and oxygen-rich phase without any sulphur. An EDS analysis of the surface layer showed it to be 57.7% Fe, 32.12% O, 1.45% S, and the rest reported to be silica and calcium.

Leach residue from reactor C (finely ground material) was washed, dried, and analysed. Figure 7 shows a QEMSCAN and SEM image of part of the debris. It is apparent that an iron-sulphur-based layer formed around a chalcopyrite core. The layer also contained iron which is not associated with

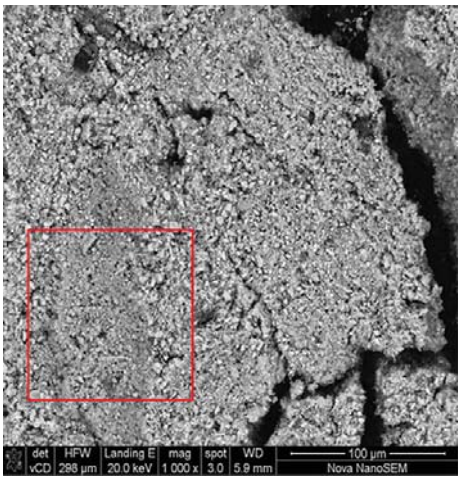

Figure 5—SEM image of chalcopyrite leach residue abraded off the mineral surface by glass beads in a 3 M equimolar ammonia–ammonium sulphate solutions at 25°C under oxygen. Sample taken after 5 days of leaching. EDS of the marked area (in atomic per cent) 45.41% Fe, 51.53% O, 3.06% Si

Table II

XRD results of the crystalline phases found in the chalcopyrite debris recovered from reactor B

XRD results of the crystalline component of the leach residue	
Phase	**Composition (%)**
Chalcopyrite ($CuFeS_2$)	4.89
Quartz (SiO_2)	0.48
Geothite (α-FeO(OH))	5.8
Lepidocrite (γ-FeO(OH))	51.5
Akaganeite (β-FeO(OH))	37.4

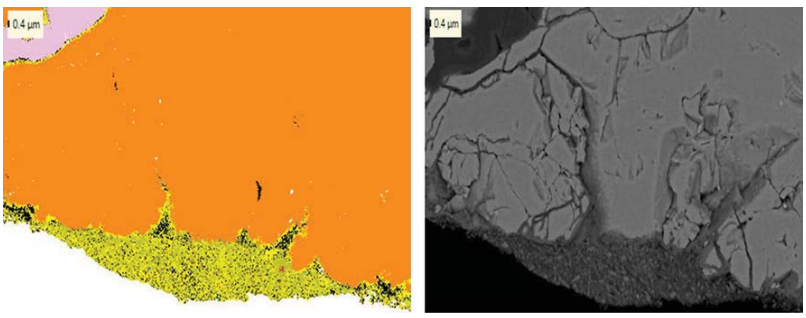

Figure 6—QEMSCAN and BSE images of a section of the chalcopyrite blocks after leaching in 3 M (NH_3+NH_4^+) at 25°C under oxygen

sulphur, which was identified as an iron oxy-hydroxide species. It is worth mentioning that all species that contained iron and sulphur in Fe:S ratios higher than 0.5 reported to pyrite and pyrrhotite, but this classification does not in any way mean this phase is in actual fact pyrite or pyrrhotite.

From Figures 5 to 7, the morphology of the surface product appears to be significantly different from that of the initial sample. The layer appears to be composed of an agglomeration of smaller particles as to it be relatively porous compared to chalcopyrite. Surface area and porosity were measured using the Brunauer-Emmett-Teller (BET) method on the micronized sample prior to and after leaching (Table III). It is apparent that the surface area and surface pore volume of leached particles increased significantly relative to that of the non-leached chalcopyrite. It is also notable that the percentage of particles less than 25 μm (diameter) increased significantly in the leach residue samples, from 67% in an unleached sample to about 90% in leached samples. This suggests that although oxidation of chalcopyrite may occur *in situ* as suggested by Forward and Mackiw (1955), this surface layer is in fact quite friable and would be easily abraded, hence the formation of smaller sized particles, also confirmed by the increased surface area per gram of the samples. These observations are consistent with findings by Guan and Han (1997), who identified a friable and porous surface product while oxidizing chalcopyrite in ammonia-ammonium iodide solutions. The readily soluble nature of the surface layer observed when washing the electrode layer in acid solutions indicates that this surface layer is not stable.

Conclusions

1. The number of electrons (seven) transferred per mole copper during anodic oxidation is similar for the ammonia–ammonium sulphate and ammonia–ammonium carbonate solutions
2. Ammonia–ammonium perchlorate solutions promote a five-electron transfer/copper reaction, possibly forming elemental sulphur on the mineral surface
3. Ammonium sulphate leaching results in the formation of a Fe-oxyhydroxide layer with low sulphur on the mineral surface
4. Ammonia–ammonium carbonate solutions resulted in marginal accumulation of iron on the mineral surface, but no formation of a layer was observed
5. Ammonium perchlorate leaching results in the formation of a Fe-oxyhydroxide layer with moderate sulphur on the mineral surface
6. The surface product was largely amorphous (90%) and significantly more porous (9-12 times) than unleached chalcopyrite. The observed morphology of the surface product suggests that it is formed through secondary precipitation rather than as part of the chalcopyrite dissolution mechanism
7. Surface abrasion allows for the removal of the surface product, leading to improved leaching recoveries
8. The abraded surface product from the small particles leaching experiment contained no sulphur, while surface products found on the stationary block of mineral contained small quantities of sulphur.

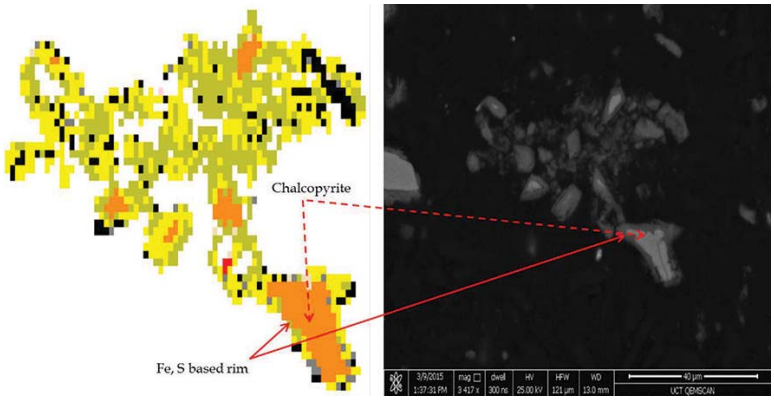

Figure 7—QEMSCAN and SEM images of chalcopyrite leach residue after 15 days of leaching in ammonia-ammonium sulphate solutions 3 M (NH_3+NH_4^+), 25°C, pH 9.6±0.15 under oxygen

Table III

Surface analysis results of chalcopyrite prior to and post leaching at 1% solids, pH 9.6±0.15, 25°C in the presence of oxygen in solutions of different total ammonia concentration

	Surface area and porosity		
Sample	**Surface area (m^2/g)**	**Pore volume (m^3/g)**	**% passing 25 μm**
chalcopyrite	1.275	0.0055	66.61
1M leached surface	57.346	0.0642	94.07
3M leached surface	57.734	0.0503	89.89
6M leached surface	59.526	0.0577	89.52

It has thus been shown that a relatively unstable iron product forms on the surface of chalcopyrite through secondary reactions to the faradaic oxidation reaction. This product may contain small percentages of sulphur but, regardless of system, the majority of leached sulphur reports to the solution. Choice of ammonium salt and the hydrodynamic environment of leaching influence the presence or absence, as well as the nature, of the surface product. It appears that the formation of surface products in turn influences the reaction mechanism of chalcopyrite dissolution, and the two aspects need to be studied in conjunction.

Acknowledgements

The authors would like to acknowledge the Centre for Bioprocess Engineering Research, the Centre for Imaging and Analysis at the University of Cape Town, and Professor M.J. Nicol for their contribution to this work.

This project has been funded through the Minerals to Metals Research Initiative, which is supported by the South African Research Chairs Initiative of the Department of Science and Technology and National Research Foundation (NRF) of South Africa. Any opinion, finding, and conclusion or recommendation expressed in this material is that of the authors and the NRF does not accept any liability in this regard.

References

Asselin, E. 2011. Thermochemistry of the Fe, Ni and Co-NH_3-H_2O system as they relate to the Caron process: a review. *Minerals and Metallurgical Processing*, vol. 28, no. 4. pp. 169–175.

Beckstead, L. and Miller, J. 1977a. Ammonia, oxidation leaching of chalcopyrite—reaction kinetics. *Metallurgical and Materials Transactions B*, vol. 8, no. 1. pp. 19–29.

Beckstead, L. and Miller, J. 1977b. Ammonia, oxidation leaching of chalcopyrite—surface deposit effects. *Metallurgical and Materials Transactions B*, vol. 8, no. 1. pp. 31–38.

Caldeira, C.L., Ciminelli, V.S.T., and Osseo-Asare, K. 2008. Pyrite oxidation in alkaline solutions: the carbonate effect. *Hydrometallurgy 2008: Proceedings of the Sixth International Symposium*. Young, C.A., Taylor, P.R., Anderson, C.G., and Choi, Y. (eds.). Society for Mining, Metallurgy and Exploration, Littleton, CO, USA. pp. 990–999.

D'Aloya, A. and Nikoloski, A.N. 2012. The passivation of iron in ammoniacal solutions containing copper (II) ions. *Hydrometallurgy*, vol. 111–112. pp. 58–64.

Das, R.P. and Anand, S. 1995. Precipitation of iron oxides from ammonia-ammonium sulphate solutions. *Hydrometallurgy*, vol. 38, no. 2. pp. 161–173.

Eyzaguirre, C., Rocks, S., Klepper, R., Baczek, F., and Chaico, D. 2015. The FLSmidth® Rapid Oxidative Leach (ROL) Process: A mechano-chemical approach for rapid metal sulphide dissolution. Graber, T., Taboada, M.E., and Valenzuela, F. (eds). *Proceedings of the 7th International Seminar on Process Hydrometallurgy, Hydroprocess 2015*, 22–24 July 2015. Gecamin, Santiago, Chile.

Feng, D. and Van Deventer, J.S.J. 2002. Leaching behaviour of sulphides in ammoniacal thiosulphate systems. *Hydrometallurgy*, vol. 63, no. 2. pp. 189–200.

Forward, F.A. and Mackiw, V.N. 1955. Chemistry of ammonia pressure process for leaching Ni, Cu, and Co from Sherritt Gordon sulphide concentrates. *Transactions AIME, Journal of Metals*. pp. 457–463.

Guan, Y. and Han, K. 1997. The leaching kinetics of chalcopyrite ($CuFeS_2$) in ammonium iodide solutions with iodine. *Metallurgical and Materials Transactions B*, vol. 28, no. 6. pp. 979-985.

Jandová, J. and Pedlík, M. 1994. Leaching behaviour of iron-nickel alloys in ammoniacal solution. *Hydrometallurgy*, vol. 35, no. 1. pp. 123–128.

Kim, H.S., Kho, Y.T., Osseo-Asare, K., and Pickering, H.W. 1991. Active and passive behaviour of sintered iron in ammoniacal ammonium carbonate solution. *Metallurgical Transactions B*, vol. 22, no. 3. pp. 323–332.

Kuhn, M.C., Arbiter, N., and Kling, H. 1974. Anaconda's Arbiter process for copper. *CIM Bulletin*. pp. 6762–6773.

Lee, J.W., Osseo-Asare, K., and Pickering, H.W. 1985. Anodic dissolution of iron in ammoniacal ammonium carbonate solution. *Journal of the Electrochemical Society*, vol. 132, no. 3. pp. 550–555.

Moyo, T., Petersen, J., Franzidis, J.-P., and Nicol, M.J. 2015. An electrochemical study of the dissolution of chalcopyrite in ammonia-ammonium sulphate solutions. *Canadian Metallurgical Quarterly*, vol. 3. pp. 368–27.

Nicol, M.J., Nikoloski, A.N., and Fittock, J.E. 2004. A fundamental study of the leaching reactions involved in the Caron process. *Proceedings of the International Laterite Symposium*. Imrie, W.P. and Lane, D.M. (eds.). The Minerals, Metals and Materials Society, Warrendale, PA. pp. 369–384.

Nikoloski, A.N. 2002. The electrochemistry of the leaching of pre-reduced nickel laterites in ammonia-ammonium carbonate solution. PhD thesis, Murdoch University, Perth, Australia.

Nikoloski, A.N. and Nicol, M.J. 2006. The electrochemistry of the leaching reactions in the Caron process 1. Anodic processes. *Electrochemical Society Transactions*, vol. 2, no. 3. pp. 197–207.

Osseo-Asare, K. and Asihene, S.W. 1979. Heterogeneous equilibria in ammonia/laterite leaching systems. *Proceedings of the International Laterite Symposium*. Evans, D.J.I., Shoemaker, R.S., and Vetman, H. (eds.). Society of Mining Engineers of the American Institute of Mining, Metallurgical, and Petroleum Engineers, New York. pp. 585–609.

Subrata, R. 2010. Electrochemical dissolution and passivation behaviour of iron in ammoniacal Caron leaching solution. MSc thesis, University of British Columbia, Canada.

Warren, G. and Wadsworth, M. 1984. The electrochemical oxidation of chalcopyrite in ammoniacal solutions. *Metallurgical and Materials Transactions B*, vol. 15, no. 2. pp. 289–297.

Yin, Q., Kelsall, G.H., Vaughan, D.J., and England, K.E.R. 1995. Atmospheric and electrochemical oxidation of the surface of chalcopyrite ($CuFeS_2$). *Geochimica et Cosmochimica Acta*, vol. 59, no. 6. pp. 1091–1100.

Yin, Q., Vaughan, D.J., England, K.E.R., Kelsall, G.H., and Brandon, N.P. 2000. Surface oxidation of chalcopyrite ($CuFeS_2$) in alkaline solutions. *Journal of the Electrochemical Society*, vol. 147, no. 8. pp. 2945–2951. ◆

INNOVATIVE TECHNOLOGIES TO IMPROVE PROCESS EFFICIENCY AND METAL RECOVERY

At Kemira, we understand the industry challenges of declining ore quality, water scarcity and more stringent environmental regulations. We offer a full portfolio of technologies designed to improve process yield and efficiency, while minimizing water and energy consumption.

From Superfloc®, the name trusted by generations of miners for its high-quality flocculants and coagulants, to KemGuard® scale and deposit control products; our extensive portfolio includes rheology modifiers, dispersants, coagulants, biocides, defoamers and organic binders. Let our team of experts help improve your process efficiency and keep your operation profitable.

Reliable chemistries for your mining operations

- Superfloc® flocculants and coagulants
- Superfloc® RH rheology modifiers
- KemPel™ iron ore organic binders
- KemEcal™ dispersants
- KemGuard® scale and deposit control
- KemFoamX™ antifoamers and defoamers
- Kemira aluminum-based and iron-based inorganic coagulants
- Kemira AMA® biocides

kemira
Where water meets chemistry™

oil&mining@kemira.com
www.kemira.com

CM solutions

metallurgical consultancy & laboratories

maximizing metallurgy

Our four-in-one solution.
We do your test work,
interpret it,
model it
and integrate the results
in metallurgical designs.

Our laboratory areas of expertise

- Mineral processing
- Hydrometallurgy
- Chemical analysis
- Process development
- Solid liquid separation
- Pyrometallurgy

CM SOLUTIONS IS AN
ISO 9001:2008
ACCREDITED COMPANY
Certificate 91215729,
audited by DEKRA GmbH, Stuttgart

T 011 608 0019
F 011 608 4067
C 082 441 2788
E consultants@cm-solutions.co.za

Pinelands Office Park
Unit T5, 1 Ardeer Road
Modderfontein, 1609
South Africa

Find us on www.cm-solutions.co.za




conductivity leaching test rig calcining wet chemistry sulfides shaking agitation electrowinning filtration furnace ion exchange open tanks roasting solvent extraction batch tests milling DMS pressure oxidation TCLP cyclone Isotherms PSD pilot plant cathode kinetics cell design flocculant screening flotation crushing ICP-OES crushing pyrometallurgy cyanidation attritioning water analysis thickening pressure oxidation heap pH control solid liquid separation

http://dx.doi.org/10.17159/2411-9717/2016/v116n6a5

Optimization of circuits for pressure leaching of sulphide ores and concentrates

by F. Saloojee* and F.K. Crundwell*

Synopsis

Pressure leaching is an option for copper recovery from chalcopyrite. Leaching takes place at high temperatures and pressures in the presence of an oxidizing agent. This work shows how the performance of pressure leaching circuits may be improved by optimizing the configuration of autoclaves and the heat removal method. The objective was achieved by creating an autoclave model that combines mass balances, energy balances, and population balances. A base case circuit consisting of a single autoclave was chosen, and this base case was compared with options for increasing capacity by adding more autoclaves to the circuit. These capacity increase options include circuits in which the additional autoclave is added in parallel, in series, and in series with thickening between the two autoclaves. The copper extraction, productivity, and cooling requirements for these options are compared. The series circuit with interstage thickening has the highest extraction and productivity; however, the cooling duty in the first autoclave is high. In addition to comparing circuit options, three options for heat removal were investigated: cooling coils, quench water, and flash recycling. The flash recycle option results in the highest copper extraction, and the quench water option the lowest copper extraction.

Keywords
pressure leaching, autoclave, flash recycling, heat removal.

Introduction

Background

Copper sulphide ores and concentrates containing chalcopyrite are typically hard to leach under atmospheric conditions. Smelting of these ores may also be a challenge, due to the inability of smelting processes to handle low-grade ores, as well as impurities such as arsenic and antimony. Alternative hydrometallurgical routes to treating chalcopyrite are therefore required. One option is pressure leaching, which is the focus of this work.

In the pressure leaching process, sulphide ores and concentrates are leached in autoclaves at temperatures of 200 to 220°C and a pressure of about 3000 kPa (Schlesinger *et al.*, 2011). An oxidizing agent, usually oxygen, is required to oxidize sulphide ions to sulphate ions. The oxidation of sulphur to sulphate is exothermic; consequently, a method of heat removal is necessary in order to maintain the temperature in the autoclave.

The dissolution of chalcopyrite is given by Equation [1]. Chalcopyrite in flotation concentrates is frequently accompanied by pyrite. Pyrite dissolution is given by Equation [2] (McDonald and Muir, 2007).

$$4CuFeS_2 + 17O_2 + 2H_2SO_4 \rightarrow 4CuSO_4 + 2Fe_2(SO_4)_3 + 2H_2O \quad [1]$$

$$4FeS_2 + 15O_2 + 2H_2O \rightarrow 2Fe_2(SO_4)_3 + 2H_2SO_4 \quad [2]$$

At temperatures above 200°C, the ferric sulphate reacts to form haematite, as shown in Equation [3]:

$$Fe_2(SO_4)_3 + 3H_2O \rightarrow Fe_2O_3 + 3H_2SO_4 \quad [3]$$

The kinetics of the leaching reactions can be described by the shrinking particle model. The reaction kinetics can be incorporated into a mathematical model of a continuous reactor, as described by Crundwell (1995). This approach is useful in the design of autoclave circuits, and has been used to design a copper leach autoclave at a base metals refinery (Crundwell, 2005), to predict the performance of a zinc pressure leaching operation (Crundwell and Bryson, 1992), and to model and optimize bacterial leaching reactors (Crundwell, 2000).

Aims and objectives

The aim of this work is to demonstrate two ways of optimizing a pressure leaching circuit, namely:

- Optimizing the configuration of autoclaves
- Optimizing the heat removal method.

* *CM Solutions, Johannesburg, South Africa.*
 ISSN 2225-6253. This paper was first presented at the, Copper Cobalt Africa Conference, *6–8 July 2015, Avani Victoria Falls Hotel, Victoria Falls, Livingstone, Zambia.*

Optimization of circuits for pressure leaching of sulphide ores and concentrates

These optimization studies were conducted by building a detailed model of the pressure leaching autoclave, including the reaction kinetics and heat removal methods. This model was then extended to simulate different configurations for autoclave circuits. The different configurations and options were compared in terms of copper extraction, productivity, and energy balance.

Problem statement

A hypothetical pressure leach plant has a single autoclave of volume *V*. Consider this as the base case circuit, shown in Figure 1. The temperature of the autoclave is maintained by running cooling water through coils in the vessel. The residence time in the autoclave is approximately one hour.

The plant is required to double its capacity. To maintain the residence time of the leach, an additional autoclave must be added to make up a total volume of 2*V*. The autoclaves can be configured in one of the following ways:

- Two autoclaves, each with volume V, in parallel, as shown in Figure 2
- Two autoclaves, each with volume V, in series, as shown in Figure 3
- Two autoclaves, each with volume V, in series with a thickener between the two, as shown in Figure 4. The product from the first autoclave is thickened to 45% solids. The thickener underflow is then repulped with fresh lixiviant to make up a slurry with 30% solids.

The options for heat removal from the autoclaves are:

- Cooling coils, as used in the base case circuit
- Quench cooling, shown in Figure 5, where cold water is added directly to the autoclave compartment
- Flash recycling, shown in Figure 6. A portion of the slurry is removed from the first compartment of the autoclave and recycled to the feed tank. As the pressurized slurry enters the feed tank, water evaporates and the slurry temperature is reduced to the boiling point temperature. The proportion of recycled material is controlled to maintain the autoclave temperature.

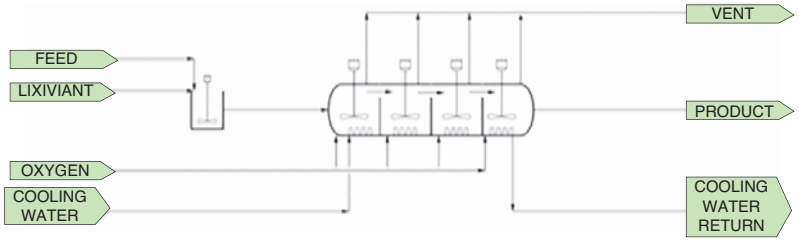

Figure 1—Base case circuit for pressure leaching

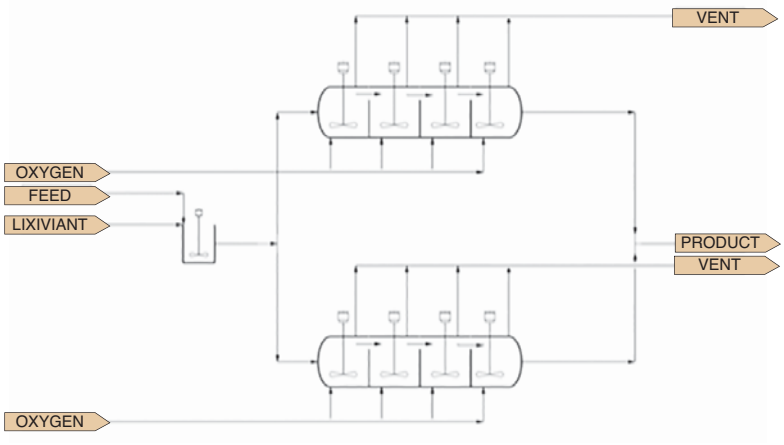

Figure 2—Parallel circuit for pressure leaching

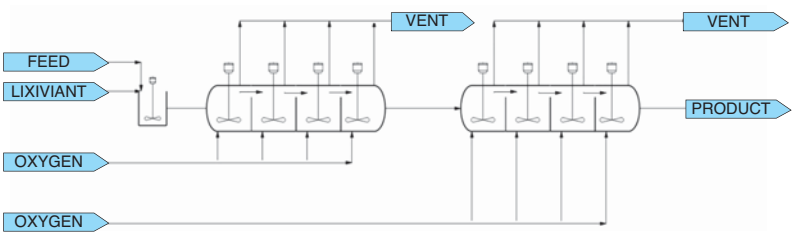

Figure 3—Series circuit for pressure leaching

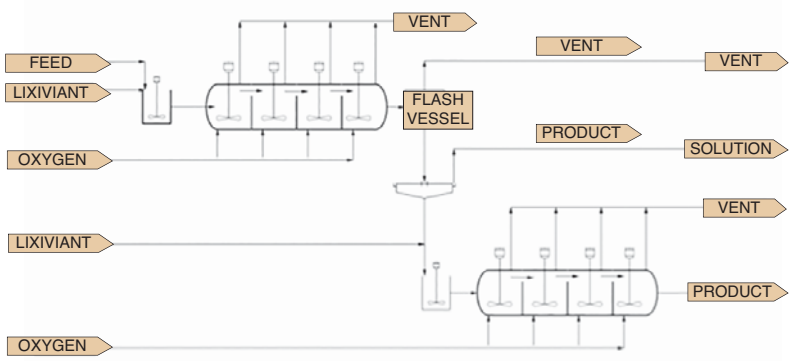

Figure 4—Series circuit with interstage thickening for pressure leaching

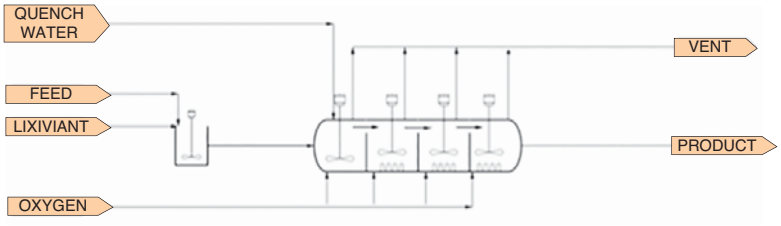

Figure 5—Quench cooling of the first compartment of an autoclave

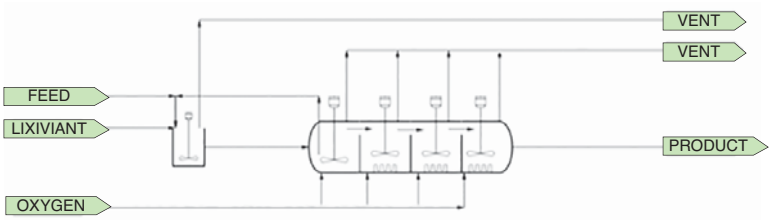

Figure 6—Flash recycling from the first compartment of an autoclave

The options for autoclave configuration and heat removal method are compared with the base case in terms of extraction and productivity.

Model framework

The autoclave model is a combination of mass balances, population balances, and energy balances. Each of these is discussed briefly in the sections below. Details of the model are available in the literature (Crundwell, 1994, 1995, 2000).

Inputs to the model include feed particle size, solids and solution throughput, reactor volume, retention time, reaction kinetics, gas mass transfer, and thermodynamic properties of the compounds. The mass balance, population balance, and energy balance equations are solved simultaneously in Cycad Process® software, resulting in product flows out of the reactor and cooling requirements.

Mass balance

The mass balance accounts for the conservation of mass. Mass balances for each component are included in the model. The mass balance equation for the solid and aqueous components is as follows:

$$Q C_{in}^{i} = Q C_{out}^{i} - rV \quad [4]$$

where Q is the volumetric flow rate of the slurry feeding the reactor, C^i is the concentration of component i, r is the rate of formation of component i, and V is the volume of the slurry in the reactor.

A mass balance for dissolved oxygen accounts for gas mass transfer, according to Equation [5] (Crundwell, 2005):

$$Q[O_2(aq)]_{in} = Q[O_2(aq)] - k_L a V([O_2(aq)]_{sat} - [O_2(aq)]) + rate\ of\ oxygen\ consumption \quad [5]$$

where k_La is the mass transfer coefficient and $[O_2(aq)]_{sat}$ is the saturation concentration of oxygen at the autoclave temperature.

Population balance

A characteristic that distinguishes the modelling of leaching reactors from other reactors is the change in particle size as the reaction proceeds. The population balance accounts for the change in particle size of the solids as they react. This is important because the rate of dissolution is higher for smaller particles than for larger particles. The population balance is

described by Rubisov and Papangelakis (1997) as a 'particle-counting' technique. The population balance equation is given in Equation [6]:

$$Qn(l)_{in} = Qn(l)_{out} - V\frac{dr_s n(l)_{out}}{dl} \quad [6]$$

where n_{in} and n_{out} are the particle size density functions of the inlet and outlet, respectively, on a number basis, r_s is the rate of shrinkage of particles in metres per second, and l is the particle diameter in metres.

The term $Qn(l)_{in}$ represents the material coming into the reactor with size l and the term $Qn(l)_{out}$ represents the material leaving the reactor with size l. The second term on the right-hand side represents the change in particle size due to reaction. This is made up of particles entering size class l due to shrinkage as well as particles leaving size class l due to shrinkage. The term $\frac{(drs\, n(l)out)}{dl}$ indicates that the reaction rate is dependent on particle size.

For a solid component i, the change in particle size distribution through the reactor represents the conversion of the component, as shown in Equation [7]:

$$X = 1 - \frac{\int_0^\infty l^3 n_{out}(l)dl}{\int_0^\infty l^3 n_{in}(l)dl} \quad [7]$$

Energy balance

The energy balance takes into account the heating or cooling requirements to maintain the reactor at the desired reaction temperature. The energy balance equation is:

$$\sum_i^n m_{in}^i H_{out}^i = \sum_i^n m_{out}^i H_{out}^i + Q + W \quad [8]$$

where m_{in} and m_{out} are the masses of each component in the system entering and exiting the reactor, respectively, H^i_{in} is the specific enthalpy of component i at the feed temperature, H^i_{out} is the specific enthalpy of component i at the exit temperature, n is the number of components in the system, Q is the heat addition to the system, and W is the shaft work done. For comparison purposes in this model, the term for shaft work, W, is not considered.

The value of H_i at temperature T is obtained from Equation [9]:

$$H^i = H_0^i + \int_{T_{ref}}^{T} CpdT \quad [9]$$

where H^i_0 is the enthalpy of formation at a reference temperature T_{ref}, and Cp is the heat capacity of component i.

The energy balance is solved by assuming that the reactor is maintained at a constant temperature. The cooling duty (Q), quench water requirements, or the flash recycle rate are adjusted so that the desired temperature is reached.

Evaluating the autoclave performance – the leaching number

The performance of leaching reactors depends on three factors: residence time, leaching kinetics, and particle size distribution. These factors are combined in the leaching number, defined by Crundwell (2005), according to Equation [10]:

$$N_L = \frac{r_s \bar{t}}{\bar{l}} \quad [10]$$

where r_s is the rate of shrinkage of particles, $\bar{t}$ is the mean residence time, and $\bar{l}$ is the mean particle size.

The leaching number can be interpreted as follows: in order to improve the performance of the reactor, the value of the leaching number must be increased. This can be achieved in three ways: increasing the intrinsic leaching rate, increasing the residence time, and decreasing the particle size. The value of the intrinsic leaching rate can be increased by increasing the temperature or the concentrations of reagents, or by adding a catalyst.

Model parameters

Process description

Sulphide concentrate is repulped in water to make up a slurry. The slurry is pumped to the first compartment of an autoclave. The autoclave has four compartments. Slurry flows from one compartment to the next over weirs which separate the compartments. Oxygen is fed to each compartment via gas nozzles. Unreacted oxygen is vented from the top of the vessel.

Operating conditions

The operating conditions of the autoclave are given in Table I.

Feed composition

The feed to the process is a concentrate containing chalcopyrite and pyrite. The composition is the same as that of a concentrate investigated by McDonald and Muir (2007). For modelling purposes, the gangue mineral is assumed to be quartz. The feed composition is shown in Table II.

Feed particle size distribution (PSD)

Particle size data was obtained for a chalcopyrite concentrate. The data was fitted to the Gaudin-Meloy model (Meloy and Gumtz, 1969), shown in Equation [11]:

$$P(\ell) = 1 - \left(1 - \frac{\ell}{L}\right)^{\alpha} \quad [11]$$

Table I

Operating conditions for pressure leaching of a chalcopyrite concentrate

Parameter	Unit	Value
Temperature	°C	200
Pressure	kPa	3000 (for autoclaves in series, the second autoclave will operate at slightly lower pressure)
Total volume	m^3	50
Head space	%	25
Live volume	m^3	40
Number of compartments		4
Live volume per compartment	m^3	10
Oxygen purity	%	98
Oxygen utilization per compartment	%	80
Approximate residence time	h	1
Feed solids content	%	15

Table II

Composition of solid feed to autoclave circuit

Mineral	Formula	Composition (mass %)
Chalcopyrite	$CuFeS_2$	80
Pyrite	FeS_2	6
Silica	SiO_2	14

where $P(\ell)$ is the mass fraction of particles, L is the maximum particle diameter, and α is a value indicating the spread of the distribution. The fitted values for L and α are given in Table III.

Lixiviant composition

The lixiviant for pressure leaching is usually made up of raffinate, with additional sulphuric acid to make up the desired concentration. The lixiviant composition used for the model is shown in Table IV. The lixiviant temperature is assumed to be 50°C.

Reaction kinetics

The dissolution of chalcopyrite and pyrite results in the formation of copper sulphate and ferric sulphate in solution. Pyrite dissolves to form ferrous sulphate in solution. It is assumed that these reactions follow the shrinking particle model with surface reaction control. The addition of oxygen results in the oxidation of ferrous iron to ferric iron. The ferric sulphate is hydrolysed to form haematite. The mass transfer of oxygen from the gas phase to the aqueous phase is also modelled as a reaction. Kinetic expressions for the dissolution and hydrolysis reactions were obtained from the literature (Langová and Matýsek, 2010; McDonald and Muir, 2007; Papangelakis and Demopoulos, 1991; Vračar and Cerović, 1997). The reactions and their rates are given in Table V.

In addition to these reactions, evaporation of water also occurs. The amount of water evaporated is calculated by assuming that the off-gas is saturated with water vapour. The saturation concentration of the gas stream is calculated from the temperature of the reactor.

Base case simulation results

Results from the simulation of the base case circuit are presented in this section

Particle size

The change in particle size of chalcopyrite down the reactor is shown in Figure 7 as a density function. Pyrite follows a similar trend.

According to Figure 7, the mean particle size increases down the autoclave. This is counter-intuitive since particles become smaller as they react. This phenomenon has been explained by Crundwell *et al.* (2013) as follows: If the spread of the feed PSD is narrow, the mean particle size decreases as the reaction proceeds, as expected. However, if the spread of the feed PSD is wide, the mean particle size will increase. The smaller particles react completely and thus no longer contribute to the PSD. The mean size therefore moves closer to the size of the larger particles.

The spread of the feed PSD can be quantified by the covariance, given in Equation [12]:

$$COVARIANCE = \frac{\sigma}{\mu} \quad [12]$$

where σ is the standard deviation of the particle size and μ is the mean particle size.

According to Crundwell *et al.* (2013), covariance values less than 0.5 result in a decrease in mean particle size, while values greater than 0.5 result in an increase.

Copper and sulphur extraction

The extraction of copper and sulphur in each compartment of the autoclave for the base case is shown in Figure 8. The overall copper extraction for the base case is 96.15%.

Energy balance

The energy requirements for cooling each compartment of the autoclave are shown in Table VI. The highest degree of sulphur oxidation occurs in the first compartment. However, the cooling duty is lower than that of the second compartment because the feed to the first compartment is at a

Table III

Gaudin-Meloy parameters for the particle size distribution of the autoclave feed

Parameter	Value
L (µm)	212
α	7.6

Table IV

Composition of lixiviant feed to autoclave circuit

Component	Concentration (g/L)
H_2SO_4	65
Cu	1
Fe	2

Table V

Reactions and reaction rates for the pressure leaching of chalcopyrite concentrate

Reaction	Kinetics
$O_2\,(g) \rightarrow O_2\,(aq)$	k_La = 1200 /h
$4CuFeS_2 + 17O_2 + 2H_2SO_4 \rightarrow 4CuSO_4 + 2Fe_2\,(SO_4)_3 + 2H_2O$	$r_{shrinkage} = 2623[O_2\,(aq)]$ µm/h
$2FeS_2 + 7O_2 + 2H_2O \rightarrow 2FeSO_4 + 2H_2SO_4$	$r_{shrinkage} = 10025[O_2\,(aq)]$ µm/h
$4FeSO_4 + 2H_2SO_4 + O_2 \rightarrow 2Fe_2\,(SO_4)_3 + 2H_2O$	$r = 1062[FeSO_4\,(aq)]^2$ M/h
$Fe_2\,(SO_4)_3 + 3H_2O \rightarrow Fe_2O_3 + 3H_2SO_4$	$r = 0.6[Fe_2(SO_4)_3\,(aq)]$ M/h

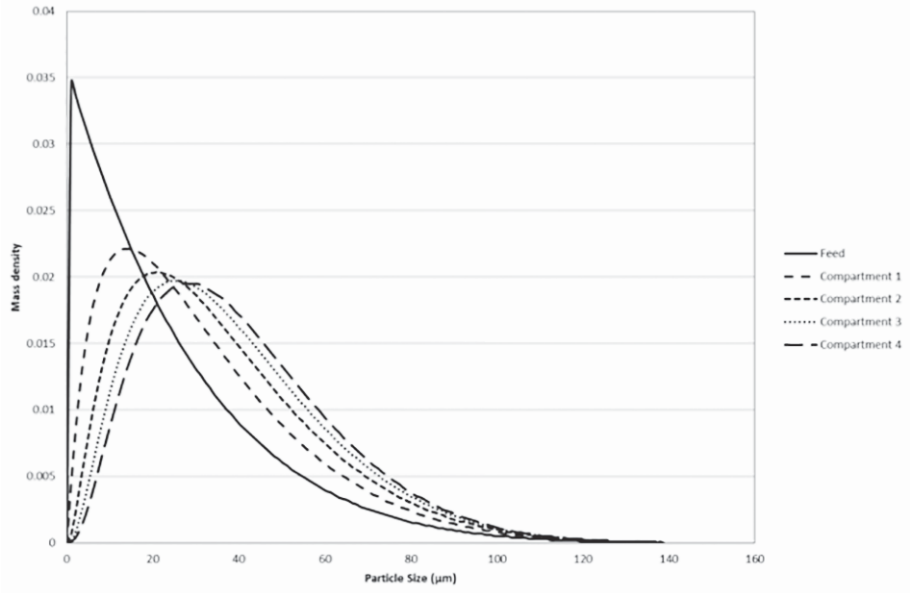

Figure 7—Particle size density of chalcopyrite in the feed and exit of each autoclave compartment

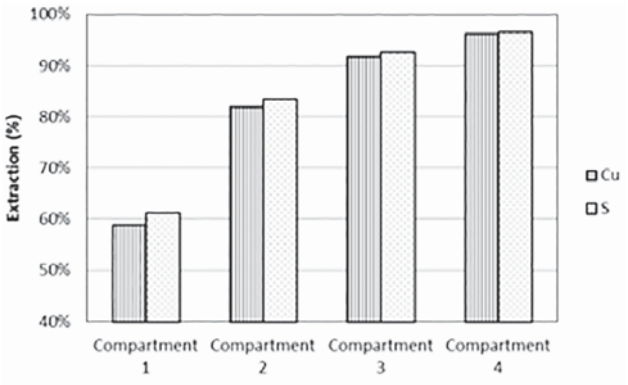

Figure 8—Extraction of copper and sulphur in each autoclave compartment in the base case circuit

temperature of 49°C. In the autoclave, this stream is heated to the operating temperature of 200°C, which results in a decrease in cooling requirements.

Effect of gas mass transfer

The effect of mass transfer of oxygen from the gas phase to the aqueous phase was investigated by varying the mass transfer coefficient and recording the resulting extractions of copper and sulphur. The same mass transfer coefficient was used in each compartment of the autoclave. The results are shown in Figure 9. Results show that higher values of k_La result in higher extractions of copper and sulphur.

Comparison of different autoclave configurations

In this section, the different circuit configurations are compared in terms of extraction, productivity, and energy requirements.

Copper and sulphur extraction

The overall extractions of copper and sulphur are shown in Figure 10. The base case and parallel circuits yield the same values for extraction. This is expected. The series circuits give slightly higher extractions of copper and sulphur. The highest extraction is achieved in the series circuit with interstage

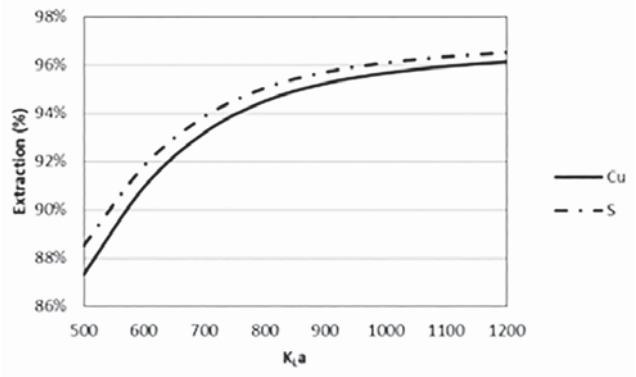

Figure 9—Effect of k_La on overall conversions of copper and sulphur for the base case

Table VI

Cooling duties in each autoclave compartment in the base case circuit

	Compartment 1	Compartment 2	Compartment 3	Compartment 4
Cooling duty (MW)	2.81	3.40	1.41	0.62

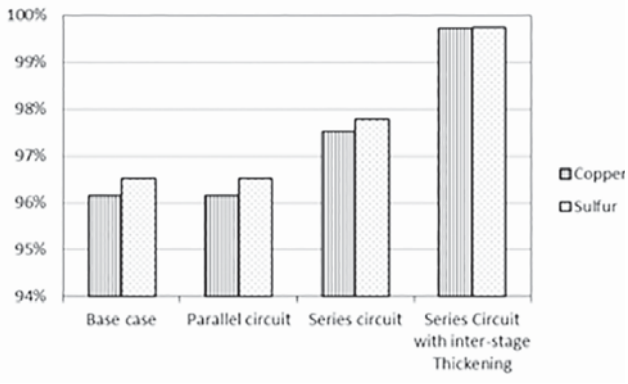

Figure 10—Overall extractions of copper and sulphur for all circuit options

thickening. This is because solution is removed after the first autoclave. A smaller volume of solution is added to make up a slurry with 30% solids. The residence time of the solids in the second autoclave is therefore significantly increased.

Productivity

The productivity of a reactor is a measure of the amount of material reacted per unit volume of the reactor, as given in Equation [13]:

$$Productivity = \frac{mass\ reacted/time}{reactor\ volume} \quad [13]$$

The productivity of sulphur leaching was measured. Results are shown in Table VII.

Energy balance

The cooling requirements for each compartment of the autoclave in the base case circuit were presented in Table VI. The cooling requirements for each autoclave compartment in the remaining circuits are presented in Table VIII.

Comparison of heat removal options

Copper extraction

The heat removal options are compared in terms of copper extraction down the autoclave. Results are shown in Figure 11. In the base case option, cooling coils are used. For the quench cooling option, copper conversion is lower than for the base case option. This is because the addition of quench water reduces the residence time in the autoclave.

The highest extraction of copper is achieved with the flash recycle option. This is because water is removed from the recycled material by evaporation. The residence time of the solids in the first compartment is therefore increased.

Conclusions

An autoclave model has been created to simulate the pressure leaching of a material containing chalcopyrite and pyrite. The model was used to compare different autoclave configurations and heat removal options.

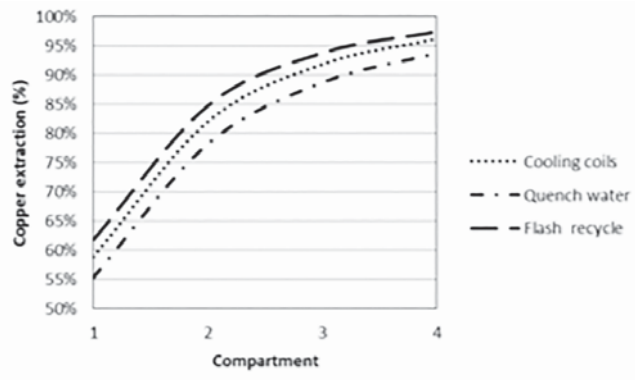

Figure 11—Overall copper extraction in each autoclave compartment for different heat removal options

Table VII

Sulphur extraction productivity for each circuit option

	Base case circuit	Parallel circuit	Series circuit	Series circuit with interstage thickening
Productivity (t/h/L)	54.14	54.14	55.85	55.95

Table VIII

Cooling requirements for each circuit option

	Cooling duty (MW)		
	Parallel circuit	Series circuit	Series circuit with interstage thickening
Autoclave 1			
Compartment 1	2.81	–0.28	–0.24
Compartment 2	3.40	7.14	7.14
Compartment 3	1.41	4.19	4.19
Compartment 4	0.62	2.49	2.49
Autoclave 2			
Compartment 1	2.81	1.51	–1.05
Compartment 2	3.40	0.94	0.91
Compartment 3	1.41	0.59	0.34
Compartment 4	0.62	0.38	0.11

The options for configuration of a circuit with two autoclaves are parallel, series, and series with interstage thickening. These options were compared in terms of copper extraction, productivity, and energy balance. The series circuit has higher copper extraction and productivity than the parallel circuit. The series circuit with interstage thickening has the highest extraction and productivity. This is because the thickening step removes solution and thus increases the residence time of solids in the second autoclave.

The downside of the two series circuits is the high cooling requirement in the first autoclave. The first compartment requires heat addition because of the increased feed rate. However, the second compartment requires 7 MW of cooling, which may not be practical. These options need to be compared in terms of capital costs.

The cooling options are cooling coils, flash recycling, and quench cooling. These were compared in terms of copper extraction and exit copper concentration. The quench cooling option results in the lowest copper extraction and concentration. This is because the quench water reduces the residence time in the autoclave. The flash recycle option gives the highest copper extraction and productivity. The reason is that flashing of the material from the first compartment increases the residence time of the solids in that compartment.

References

Crundwell, F.K. 1994. Mathematical modelling of batch and continuous bacterial leaching. *The Chemical Engineering Journal*, vol. 54. pp. 207–220.

Crundwell, F.K. 1995. Progress in the mathematical modelling of leaching reactors. *Hydrometallurgy*, vol. 39. pp. 321–335.

Crundwell, F.K. 2000. Modeling, simulation and optimization of bacterial leaching reactors. *Biotechnology and Bioengineering*, vol. 71, no. 4. pp. 255–265.

Crundwell, F K. 2005. The leaching number: its definition and use in determining the performance of leaching reactors and autoclaves. *Minerals Engineering*, vol. 18. pp. 1315–1324.

Crundwell, F.K. and Bryson, A.W. 1992. The modelling of particulate leaching reactors – the population balance approach. *Hydrometallurgy*, vol. 29. pp. 275–295.

Crundwell, F.K., du Preez, N., and Lloyd, J.M. 2013. Dynamics of particle size distribution in continuous leaching reactors and autoclaves. *Hydrometallurgy*, vol. 133. pp. 44–50.

Langová, S. and Matýsek, D. 2010. Zinc recovery from steel-making wastes by acid pressure leaching and hematite precipitation. *Hydrometallurgy*, vol. 101. pp. 171–173.

Meloy, T.P. and Gumtz, G.D. 1969. The fracture of single, brittle, heterogeneous particles–statistical derivation of the mass distribution equation. *Powder Technology*, vol. 2, no. 4. pp. 207–214.

McDonald, R.G. and Muir, D.M. 2007. Pressure oxidation leaching of chalcopyrite 1. Comparison of high and low temperature reaction kinetics and products. *Hydrometallurgy*, vol. 86. pp. 191–205.

Papangelakis, V.G. and Demopoulos, G.P. 1991. Acid pressure oxidation of pyrite: reaction kinetics. *Hydrometallurgy*, vol. 26. pp. 309–325.

Rubisov, D.H. and Papangelakis, V.G. 1997. Solution techniques for population balance equations as applied to heterogeneous aqueous processes in stirred tank reactors. *Computers in Chemical Engineering*, vol. 21, no. 9. pp. 1031–1042.

Schlesinger, M.E., King, M.J., Sole, K.C., and Davenport, W.G. 2011. Extractive Metallurgy of Copper. 5th edn. Elsevier.

Vračar, R.Ž. and Cerović, K.P. 1997. Kinetics of oxidation of Fe(II) ions by gaseous oxygen at high temperatures in an autoclave. *Hydrometallurgy*, vol. 44. pp. 113–124. ◆

http://dx.doi.org/10.17159/2411-9717/2016/v116n6a6

Understanding aqueous-in-organic entrainment in copper solvent extraction

by P. Cole*, T. Bednarski*, L. Thomas*, D. Muteba*, G. Banza*, and M. Soderstrom*

Synopsis

In copper solvent extraction, aqueous-in-organic entrainment results in the carry-over of unwanted species into the electrowinning process with negative cost implications. The need to bleed is increased and the purity of the copper cathode is potentially compromised, depending on the impurities being transferred (Cl, NO_3, Fe, Mn). In some cases, entrainment results in elevated levels of manganese in the electrolyte which can cause oxidative conditions to develop and degradation of the organic phase. Degraded organic phase detrimentally affects the physical performance of the copper solvent extraction process, contributing to even higher aqueous-in-organic entrainment. Aqueous entrainment may be minimized through good operating practices and maintenance of the organic quality, but the accurate measurement of entrainment remains a challenge. This paper presents coalescing devices designed to provide more exact measurements of aqueous-in-organic entrainment.

Keywords
copper solvent extraction, aqueous entrainment, measurement techniques, minimization.

Introduction

Many copper solvent extraction (SX) plants experience high aqueous-in-organic (A-in-O) entrainments but are unaware of the extent of the problem because entrainment is often not measured. Aqueous entrainment results in the carry-over of unwanted species into the electrowinning (EW) process and the need to bleed to maintain acceptable concentrations in the electrolyte. The costs associated with the bleed are exacerbated in copper plants where aqueous entrainment levels are high. Other than these direct costs, there are operational consequences of the build-up of certain species in the EW circuit that can have deleterious effects on plant performance.

Minimizing aqueous entrainment in operating plants requires an understanding of the factors that affect entrainment levels. Both chemical and operational influences are discussed in this paper. The difficulty of obtaining a representative sample makes it challenging to obtain an accurate measure of aqueous entrainment from a continuous process like SX. Coalescing devices used to get a more precise measurement of A-in-O entrainment are useful to complete mass balances around the SX circuits. Alternatively, mass balances can be used to estimate aqueous entrainments and are helpful as a tool to troubleshoot operations with a view to improving plant performance.

Coalescence and entrainment

The dispersion of two phases on mixing and the rate at which the dispersed phases disengage (coalescence) are integral steps in the SX process that govern the design and operation of a plant. Since the entrainment of one phase in another is essentially the result of retarded coalescence, a closer look at the coalescence of an organic-continuous mixture (aqueous droplets dispersed in an organic matrix) should assist in understanding of A-in-O entrainment. In the coalescence of aqueous droplets dispersed in an organic continuous phase, drop–interface and drop–drop coalescence are believed to proceed through a number of discrete stages, with the rate-limiting steps said to be the formation and drainage of the film of the continuous phase at the interface. Any factor that retards the formation and drainage of the interfacial film will influence the rate of coalescence and, by implication, aqueous entrainment (Ritcey, 2006).

Aqueous entrainment in copper SX operations

Both operational and chemical factors influence aqueous entrainment in copper SX operations. Probably the most important entrainment to minimize in operations is the aqueous entrained in the loaded organic (LO)

* *Cytec Solvay Group, Brussels, Belgium.*
 This paper was first presented at the, Copper Cobalt Africa Conference, *6–8 July 2015, Avani Victoria Falls Hotel, Victoria Falls, Livingstone, Zambia.*

phase that exits the E1 extraction stage because this solution, whether pre-settled in a LO tank or passing via a wash stage, will cause carry-over of undesired impurities from the pregnant leach solution (PLS) into the EW circuit.

Operating factors that influence aqueous entrainment

A number of factors related to the design of SX equipment are specifically focused on minimizing A-in-O entrainment. These include the following:

- LO tank designs that assist in the removal of A-in-O entrainment
- Coalescer devices such as the Chuquicamata LO coalescer and pace settlers
- Settler internals and picket fences directed at lowering aqueous entrainment.

In addition to settler and tank modifications, plants can also make changes to mixing equipment to achieve a more uniform droplet size and assist coalescence by a focus on low-shear and reduced mixing intensity.

Phase continuity

The preferred mode of continuity for a mixer-settler where LO exits the extraction circuit is aqueous continuity because coalescence from an organic-continuous dispersion will tend to leave aqueous droplets in the settled organic phase (Sole, 2008). However, in many operations, particularly in Africa where agitation leaching is common, the total suspended solids (TSS) content of the SX circuit is often high and stable operation is possible only in organic-continuous mode, which makes crud more compacted and stabilized at the interface, depending on the hydrophobicity of the crud solids. Managing crud in these plants is such a problem that organic-continuous operation is often mandatory, even at the expense of increased entrainment (Sole, 2008). Another reason for operating in organic-continuous mode is if dissolved silica is present in the PLS. If the levels of colloidal silica are high enough, a stable emulsion forms with aqueous-continuous mixing that fails to separate in the settler and can necessitate a shutdown of the SX plant.

Specific settler flux and organic bed depth

An important parameter in the design of gravity settlers is the specific settler flux, which is a function of the total flow rate of solution that enters a settler and defines the design settling area. Entrainment can be high in copper SX plants if operating specific settler fluxes are over the accepted range of 4 to 8 $m^3/m^2/h$ (Robinson *et al.*, 2008).

In the E1 mixer-settler units, the height of the organic phase in the settler is important to ensure low aqueous entrainment, especially for organic continuity where the aqueous is the dispersed phase. Because of the cost associated with the organic inventory, there is often a tendency to reduce the organic height in settlers. There is some debate on what is an optimum phase velocity or difference between the phases, but phase velocity has a clear impact on entrainment by affecting the amount of time available for the droplets to coalesce within the settler. Dependent on bed height and flow rate, the linear velocity (LV) for each phase is defined as:

$$LV_{ORGANIC} = Q_O/W.H_O \text{ and } LV_{AQUEOUS} = Q_A/W.H_A$$

where Q is the volumetric flow rate, W the settler width, H the height of the phase in the settler, and subscripts O and A refer to organic and aqueous phases respectively. Table I shows the diverging phase linear velocities for reduced organic heights in a settler.

Organic linear velocities typically fall in the range 100 to 200 m/h (3 to 6 cm/s) and it is generally recommended that an organic bed height of 25 to 35 cm be maintained (Sole, 2008). To put this into the context of a full-scale settler, 32 m wide and with an aqueous flow rate of 1000 m^3/h, the organic linear velocity for an organic height of 20 cm is 312 m/h, which is substantially higher than the typical accepted velocities. At 312 m/h and a settler length of 20 m, the organic takes 3.85 minutes to reach the overflow weir and, if the velocity is 200 m/h, the time to the weir is doubled to 6 minutes. It is not unreasonable to expect a substantial drop in aqueous entrainment simply by increasing the organic bed depth by 10 cm.

Chemical factors that influence aqueous entrainment

It is now accepted in the industry that the composition of the organic phase, *per se*, has little influence on the coalescing behaviour of dispersions. It is factors such as temperature and amount and type of solids present that result in crud formation and densities and viscosities of both the aqueous and organic phases that can significantly influence coalescence and aqueous and organic entrainment (Soto, 2012).

Organic quality

Organic quality can have a significant impact on the amount of A-in-O entrainment that is experienced at an operation (despite the steps taken to minimize the issue). Over time, the organic inventory accumulates contaminants from the PLS, electrolyte, or organic that are recovered and returned to the circuit from ponds and the EW circuit (Hutzler *et al.*, 2015). These contaminants can be interfacially active species and are indicated by a decrease in interfacial tension (IFT). The addition of surface-active components is found to generally retard coalescence as they accumulate at the interface and surface of droplets, resulting in a reduction in film drainage time. They are therefore a cause of increase in aqueous entrainment (Ritcey, 2006). Effective clay treatment with the correct dosage of acid-activated bentonite clay recovers the organic quality by removing the surface-active components (Hutzler *et al.*, 2015).

Side-by-side pilot plant trials

The results of side-by-side pilot plant trials conducted at two copper SX operations demonstrate the effect of organic quality on aqueous entrainment. In these trials, plant organic

Table I

Variation of linear velocity for solution bed depths in a gravity settler (internal O/A flow ratio of 2)

Height of organic (m)	0.4	0.3	0.2
$LV_{ORGANIC}$ $LV_{AQUEOUS}$	5 Q_A/W 1.7 Q_A/W	6.7 Q_A/W 1.4 Q_A/W	10 Q_A/W 1.25 Q_A/W

is compared with plant organic after clay treatment at a mass fraction of 5% clay. The operating parameters for the trials are given in Table II. All stages were operated in organic-continuous mode. The trials differed in both scale and duration of operation.

For Trial 1, entrained PLS in the loaded organic from stage E1 was periodically drained from the bottom of the two loaded organic drums. Entrainment was calculated by dividing the drained aqueous volume by the total volume of organic that had entered the loaded organic drum over the time period. The results given in Table III show that clay treatment significantly reduced the A-in-O entrainment by between 32% and 56% during normal operation. The time periods are for different days of operation.

For Trial 2, the A-in-O entrained in the loaded organic was accumulated in a coalescing device over the period of the trial. Figure 1 shows that the plant with untreated organic accumulated 65% more entrained aqueous than the plant with treated organic.

The cost of carry-over of species into electrolyte

Electrolyte bleed

Aqueous entrainment is the cause of impurity transfer of species like Cl, NO_3, and Mn into the electrolyte, while Fe transfer is due to a combination of entrainment and chemical extraction. Maintaining particular concentrations of species in the electrolyte is achieved principally through a bleed of the lean electrolyte (LE). Costs associated with the bleed are due to the following factors (discussed further in a later section):

- Loss of EW reagents, such as acid, cobalt, levelling aids, and mist suppressant from the electrolyte
- Re-extraction of copper
- Copper lost to the raffinate.

Table II

Operating parameters for side-by-side trials comparing untreated and clay-treated plant organic

	Trial 1	Trial 2
Circuit configuration	1E + 1S	2E + 2S +1W
Mixer volume	40 L	700 mL
Duration of operation	13 d	40 h
ΔIFT (clay treated – untreated)	6.5 dyne/cm	2.5 dyne/cm
PLS flow rate	3–4 L/min	0.1 L/min
Organic flow rate	8–9 L/min	0.1 L/min

Table III

Trial 1 – aqueous entrainment from E1 stage for side-by-side pilot trial

Time period	A-in-O entrainment (mL/m³)		Decrease (%)
	Untreated	Treated	
Period 1	2373	1038	56.2
Period 2	1963	1287	34.4
Period 3	1469	988	32.8

The quantity of bleed is dependent on the extent of contamination of the electrolyte, and the associated costs can be significant. For plants that are pushing copper production levels – common in the African operations – there is a resistance to bleeding electrolyte from the EW circuit, but such a practice has to be carefully managed to ensure good plant performance is maintained.

Deleterious effects of species build-up in electrolyte

Besides the need to bleed electrolyte, there are other possible consequences, listed in Table IV, of carry-over of chemical species from the PLS to the electrolyte. These consequences have associated costs, although they are primarily indirect in nature.

Chloride

Chloride entrainment is a concern at a number of operations, especially in Chile where elevated Cl levels in the PLS are not uncommon, originating from the chloride-containing atacamite ore and chloride-containing process water. Despite chloride concentrations as high as 50 g/L in the PLS of Latin American operations, chloride levels in the electrolyte are maintained at around 30 to 45 mg/L through a combination of wash stages, electrolyte bleed, and Cl_2 gas evolution in the tankhouse.

Nitrate

Nitrate is occasionally a cause for a bleed but this is largely limited to operations in the north of Chile. Some of the Latin

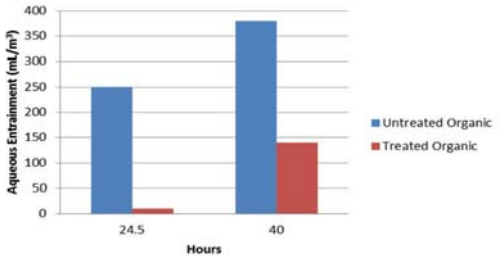

Figure 1—Trial 2 – aqueous entrainment accumulated from loaded organic for side-by-side pilot trial

Table IV

Consequences of carry-over of chemical species into the electrolyte

Chemical species transferred	Possible consequence
Cl	• Downgrade in cathode quality • Cl_2 gas generation in tankhouse • Corrosion of anode and pitting of cathodes
NO_3	• Nitration of organic phase and increased anode corrosion
Mn	• Oxidative degradation of organic • Precipitation of amorphous MnO_2 in electrolyte • Increased corrosion of anodes • Cl_2 gas generation in tankhouse (promoted) • Occlusion of Pb in cathode
Fe	• Decrease in EW current efficiency

American operations experience relatively high NO_3 levels in the plant PLS, the worst case reported being the Lomas Bayas plant (Zambra *et al.*, 2013). Transfer of nitrate from the PLS to the higher acid-containing LE can lead to operational problems. At specific conditions, nitration of the oxime in the plant organic occurs, resulting in decreased copper recoveries, and deteriorating phase separation efficiencies and Cu:Fe selectivity. In extreme cases, entrainment of high NO_3 PLS has impacted plant operability.

Manganese

Issues with manganese in the tankhouse have been reported in a number of regions, such as Australia, North America, and Latin America (Miller, 1995) and are a concern for many African operations. Elevated levels of manganese in the electrolyte are due to high concentrations of manganese in the PLS from the leaching of the manganese-containing cobalt mineral heterogenite and high aqueous entrainment. Under oxidative conditions, the manganese transferred into the EW circuit can result in the generation of higher oxidation state manganese species (up to Mn^{7+}), which when contacted with the organic phase cause degradation to occur (Bednarski, 2008; Bednarski *et al.*, 2011). Maintaining a Fe^{2+}/Mn ratio of at least 5 in the electrolyte is said to ensure that oxidizing conditions do not develop (Bednarski *et al.*, 2011). Miller (1995) reports that maintaining a Fe_{total}/Mn (Fe_{total} = Fe^{3+} + Fe^{2+} or total Fe) ratio of around 8 to 10 in the electrolyte prevents oxidative conditions from developing. However, there are plants in the African Copperbelt that operate the EW circuit with Fe/Mn ratios as low as 1 without developing oxidative conditions. Cobalt, which is also carried over into the electrolyte, is suspected to be the mitigating factor inhibiting the development of oxidative conditions (Miller, 2011). However, African operations are always at risk of developing oxidative conditions during start-up when the Fe and Co levels are still building up in the electrolyte. Monitoring the oxidation–reduction potential (ORP) of the electrolyte is the best way to ensure that oxidizing conditions are absent.

Oxidation of the oxime results in lower copper transfer. Oxidative degradation of the organic phase causes the formation of surface-active components that build up in the organic phase, affecting the IFT properties and resulting in an increase in phase separation times and entrainment, a decrease in kinetics that negatively impacts stage efficiencies, and a decrease in Cu:Fe selectivity (Bednarski *et al.*, 2011; Soderstrom *et al.*, 2010). Treatment of organic with acid-activated bentonite at the correct clay dosages recovers the quality and the performance properties of the plant organic.

Iron

Iron contamination of the electrolyte, both from chemical and physical transfer, is the most common factor requiring an electrolyte bleed. Elevated iron levels in the electrolyte reduce current efficiency, thereby increasing the power cost per unit of electrowon copper (Bednarski, 2008). Some African copper plants that have reduced or even eliminated electrolyte bleed to push production exhibit current efficiencies as low as 62%. It should be noted, however, that many other operational factors in the EW process, besides elevated iron levels, reduce current efficiency. These can be addressed by instituting judicious maintenance practices in the EW circuit.

Measuring aqueous entrainment

'Grab sample' method

It is generally difficult to obtain an accurate measurement of aqueous entrainment from a large continuous flow like an organic phase. Most commonly used in the industry, the 'grab sample' method typically consists of taking 100 mL samples from the organic overflow launder into an oil-in-water emulsion bottle and spinning them in a centrifuge (Figure 2). The method is highly dependent on the point of sample collection, reproducibility is extremely user-dependent, and accuracy requires the measurement of multiple samples. In addition, the volumes of entrained aqueous are extremely small, which can make measurements in a small container meaningless; 1000 mL/m^3, for example, is a mere 0.1 mL in the flask shown in Figure 2. Due to the deficiencies in the current methodology, in many plants A-in-O entrainment measurements are simply not recorded or recorded very infrequently.

Continuous measurement methods

Methods based on continuous measurement remove some of the variability in the sampling method and provide more representative data. They also collect larger samples, allowing for more meaningful entrainment measurements. The following section describes two relatively simple measurement techniques that have been used in commercial operations to assist in establishing a baseline measurement.

Equipment

Two continuously operated coalescing devices to provide more accurate aqueous entrainment measurements at copper SX plants are shown in Figure 3. One is a column design and the other is based on a mixer-settler design for conducting on-site continuous countercurrent pilot plant trials.

Figure 3a depicts the column coalescer. It is designed to coalesce entrained aqueous onto the packing from the organic exiting a mixer–settler unit (the overflow launder). Over time, the droplets of aqueous become large enough to settle into the aqueous collection pipe at the base of the coalescer. Based on this phenomenon, the unit will establish an equilibrium where the rate of coalescence onto the packing material matches the rate of settled aqueous such that measurements of the A-in-O entrainment can be made.

Figure 2—Centrifuge sample holder showing separated aqueous phase

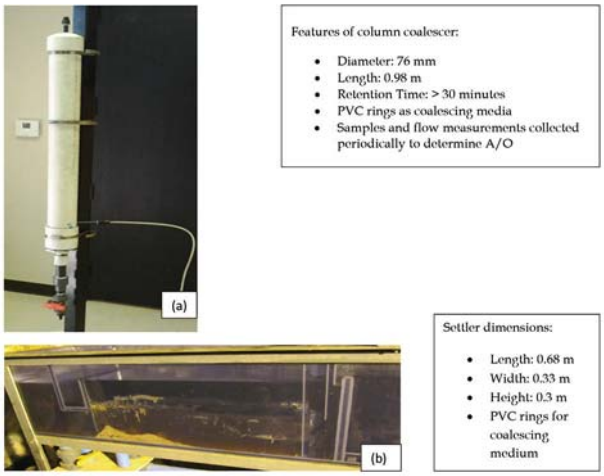

Figure 3—(a) Column and (b) settler-type coalescing device used for improved aqueous entrainment measurement

The coalescer should be placed in a location close to the organic advance line on the SX settler organic launder where samples for A-in-O entrainment measurements are taken. Sampling in the organic advance line will ensure the feed to coalescer is indicative of the entrainment across the length of the weir. An appropriately sized pump is used to meter organic into the column via the small-diameter pipe shown near the bottom of the column. Organic exits at the top of the column directly into the settler organic launder.

Figure 3b depicts the mixer–settler device. The coalescing chamber is filled with the polyvinyl chloride (PVC) coalescing media before use to measure the A-in-O entrainment. The device is placed adjacent to the overflow launder where LO exits the E1 settler. An appropriately sized metering pump is used to deliver LO from the launder into the settling chamber. Organic is pumped at a set flow rate over a 12-hour measurement period and exits directly into the organic overflow launder. The coalesced aqueous is drained from the bottom of the settling chamber to calculate an entrainment value.

Results

Figure 4 shows actual A-in-O entrainment levels measured in the loaded organic exiting the extraction circuit in a copper SX operation in Africa. Two observations appear from this data: (1) entrainment levels are relatively high, and (2) they are extremely variable.

In Figure 4, the graph on the left plots daily aqueous entrainment values collected over a one-month period. It shows values as low as 2341 mL/m³ and as high as 11 389 mL/m³, with an average value of 4176 mL/m³ and standard deviation of 1960 mL/m³. The histogram on the right indicates that 83% of the time, the measured aqueous entrainment was between 2000 and 5000 mL/m³.

The collection of this data assisted the operation in better recognizing the operational parameters that resulted in higher A-in-O entrainment from the LO stage to the LO tank. In particular, it re-emphasized the importance of operating the decant pump to capture the majority of the aqueous in the LO tank and return it to the extract circuit before contamination of the electrolyte occurred. The use of the coalescer allowed the operation to have a real-time measurement of aqueous entrainment and to better evaluate the impact of operational changes on the physical transfer. Among the operational changes that were considered, some of which were implemented, were modifications of the organic bed depth, organic quality, O/A ratio, and a picket-fence arrangement within the settler.

Using mass balances to calculate electrolyte bleed and costs

Once the average entrainment has been estimated, it is possible to validate these measurements utilizing mass balances. The mass balance also allows the operation to assess the bleed requirements and cost associated with the bleed. This assists the operation in prioritizing its efforts in addressing entrainment relative to other operational priorities. The mass balance stream flows are shown in Figure 5 for the EW tankhouse (TH).

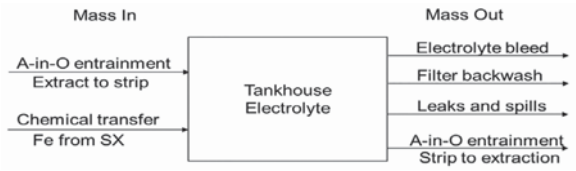

Figure 5—Mass balance streams for tankhouse electrolyte

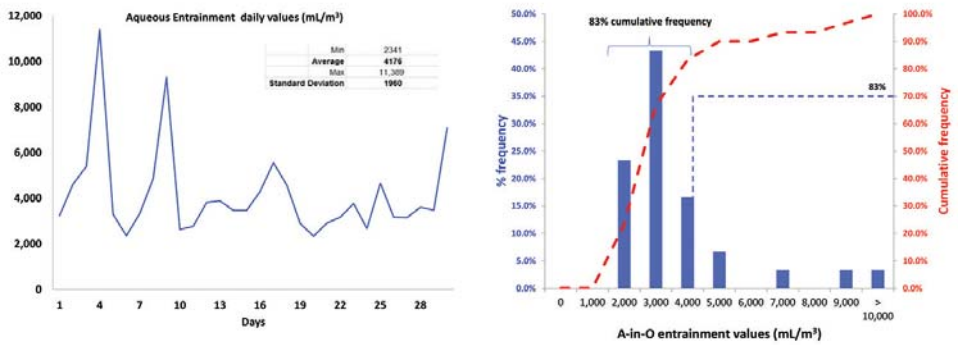

Figure 4—A-in-O measurements from an E1 settler organic launder

The mass balance calculation for one set of conditions, assuming an A-in-O in the LO of 4000 mL/m³ and an A-in-O entrainment of 1000 mL/m³ in the barren organic (BO), is shown in Table V.

As shown, the mass of impurities into the electrolyte exceeds the mass of impurities that would be lost due to 'natural' losses (A-in-O entrainment from strip to extract and filter backwash). Under these conditions, an additional intentional bleed would be required. Assuming the tankhouse impurity concentrations were allowed to reach the maximum target (3 g/L Fe and 0.3 g/L Mn), the amount of bleed required for each element X is: (Mass X in – Mass X out) / TH target LE X, which gives the values shown in Table VI.

The actual bleed would be based on the highest value. In this case, the plant would bleed for Fe at a flow rate of 10.05 m³/h. Based on an electrolyte composition of 35 g/L Cu and 190 g/L H_2SO_4, this would resut in the losses of copper and acid from the tankhouse summarized in Table VII.

Other than returning copper and acid back to the leaching circuit (the copper needing to be re-extracted), the bleed results in the loss of the other tankhouse reagents, such as cobalt sulphate, mist suppressant, and levelling aids. A cost breakdown associated with the bleed of 10.05 m³/h is given in Table VIII.

Electrolyte bleed requirements for various aqueous entrainment values are shown in Table IX. The cost of the bleed ranges from US$58.7 to US$86 8 per ton Cu recovered. As would be expected, any increase in A-in-O entrainment will have a significant impact on the bleed required. As shown, under these conditions (maintaining constant chemical iron transfer and constant A-in-O entrainment from strip), a change in the A-in-O entrainment from extract affects which element the plant would need to bleed to control. At an excessive A-in-O entrainment of 8 000 mL/m³, the plant would need to begin bleeding to maintain Mn instead of Fe.

Note: These entrainment values are considered very high – but are not unheard of in operations where operational controls to minimize entrainment are not implemented.

Table V

Mass balance around tankhouse to determine electrolyte bleed requirement

Mass in			Mass out (natural)		
Organic flow	m³/h	1 300	LE flow	m³/h	750
A-in-O entrainment extract	mL/m³	4 000	Filter backwash	m³/h	0.11
PLS Fe	g/L	1.23	A-in-O in BO	mL/m³	1 000
PS Mn	g/L	0.45	LE Fe	g/L	1.5
Fe from chemical transfer	mg/L	20	LE Mn	g/L	0.30
TH target LE Fe (max.)	g/L	3.0			
TH target LE Mn (max.)	g/L	0.30			
Mass Mn in entrainment	kg/h	2.34	Mass Mn out	kg/h	0.23
Mass Fe in entrainment	kg/h	6.40			
Mass Fe in transfer	kg/h	26.00			
Total Fe in	kg/h	32.40	Mass Fe out	kg/h	2.25

Table VI

Calculated tank house bleed (m³/h)

Bleed for Fe	10.05
Bleed for Mn	7.05

Table VII

Copper and acid loss associated with a 10.05 m³/h bleed from the tankhouse

LE Cu concentration	g/L	35
LE H_2SO_4 concencentration	g/L	190
Cu from tankhouse	kg/d	8441
Acid from tankhouse	kg/d	45 822

Table VIII

Cost breakdown of electrolyte bleed (10.05 m³/h) (assumptions: 6% of Cu lost, 94% of Cu re-extracted, reagent cost approx. 10% of total)

	t/a	US$/t	US$/a
Acid	16 725	250	4 181 250
Cu lost	185	6000	1 109 149
Cu re-extracted	2896	18	52 130
Reagents			530 000
Total ($ per annum)			5 872 529

Table IX

Electrolyte bleed requirements for various LO A-in-O entrainment values

A-in-O in LO	mL/m³	4000	6000	8000
Bleed for Fe	m³/h	10.05	11.11	12.11
Bleed for Mn	m³/h	7.05	10.95	14.85.25

Conclusions

A-in-O entrainment is an important parameter in SX operations, but is rarely measured accurately. Although plants allocate capital to minimize aqueous entrainment, there are also a number of operational adjustments that can be made, including organic quality adjustments, that can minimize entrainment costs. However, identifying the right parameters to optimize requires proper sampling and measurement procedures, which can be facilitated by relatively simple continuous measurement devices. In addition, operating copper SX plants should validate A-in-O measurements by conducting mass balances.

References

Bednarski, T. 2008. Behavior of iron and manganese in electrowinning solutions – a Hull cell study. *Tucson SME*, December 2008. Cytec Industries Inc.

Bednarski, T., Soderstrom, M., and Wiggett, S. 2011. Oxidation in copper SX processes. *Proceedings of the ALTA 2011 Copper-Nickel-Cobalt Conference*. ALTA Metallurgical Services, Melbourne, Australia. 9 pp.

Hutzler, B., Cole, P., Thomas, L., Bednarski, T., and Zambra, R. 2015. Clay treatment improvements using ACORGA® CB1000 clay binder. *Proceedings of Copper Cobalt Africa: in Association with the 8th Southern African Base Metal Conference*, Victoria Falls, Zambia, 6–8 July 2015. Southern African Institute of Mining and Metallurgy, Johannesburg.

Miller, G. 1995. The problems of manganese and its effects on copper SX-EW operations. *Proceedings of Copper 95-Cobre 95: Vol. 3. Electrorefining and Hydrometallurgy of Copper.* Cooper, W.C. (ed.). Canadian Institute of Mining, Metallurgy and Petroleum, Montreal, Canada. pp. 649–663.

Miller, G. 2010. Methods of managing manganese effects on copper SX-EW plants. *Proceedings of the ALTA 2010 Nickel Cobalt Copper Conference.* ALTA Metallurgical Services, Melbourne, Australia.

Ritcey, G.M. 2006. Solvent Extraction: Principles and Applications to Process Metallurgy. Chapter 5: Dispersion and Coalescence. Book 1, revised edition. Gordon Ritcey & Associates, Ottawa. pp. 208–228.

Robinson, T., Moats, M., Davenport, W., Karcas, G., Demetrio S., and Domic, E. 2008. Copper solvent extraction - 2007 world operating data. *Proceedings of ISEC 2008*. Volume I. Moyer, B.A. (ed.). Canadian Institute of Mining, Metallurgy and Petroleum, Montreal, Canada. pp. 435–440.

Soderstrom, M., Bednarski, T., and Villegas, E. 2010. Stage efficiency in copper solvent extraction plants. *Proceedings of the SME Annual Meeting*, Phoenix, AZ, February 2010. Society for Mining, Metallurgy & Exploration, Littleton, CO. Preprint 10–106.

Sole, K.C. 2008. Solvent extraction in the hydrometallurgical processing and purification of metals: process design and selected applications. *Solvent Extraction and Liquid Membranes: Fundamentals and Applications in New Materials*. Aguilar, M. and Cortina, J.L. (eds.). Taylor & Francis, Boca Raton, FL. pp. 141–200.

Soto, A. 2012. The impact of PLS viscosity on solvent extraction. *Cytec Solutions - For Solvent Extraction, Mineral Processing and Alumina Processing*, vol. 16, Cytec Industries Inc., USA.

Zambra, R., Quiladran, A., and Castro, O. 2013. The phenomenon of nitration in the Chilean copper hydrometallurgy. *Proceedings of Copper 2013: Hydrometallurgy*. Ugarte, G. (ed.). Chilean Institute of Mining Engineers, Santiago, Chile. 9 pp. ◆

SIBELCO

High Quality Magnesia for Hydromet Processes

Sibelco QMAG is one of the world's most trusted producers of high grade calcined (CCM), dead burned (DBM) and electrofused (EFM) magnesia for the global hydrometallurgical (Cu-Co, Ni-Co, RE and Uranium), agricultural, refractory and chemical markets. Our EMAG™45 CCM is recognised as a leading product for hydrometallurgical applications.

One of Sibelco's fundamental strengths is our application-focused research and technical centres which enable us to explore possibilities and focus on the needs of our customers. We have a team of experienced, highly qualified technical experts in the hydrometallurgical industry who work closely with our customers around the world to develop material solutions that add value to their business and give them a competitive advantage.

Mined and processed in Central Queensland, Australia, our QMAG magnesia products are sold and delivered to over 30 countries worldwide. Our QMAG mine has a resource in excess of 100 years producing superior cryptocrystalline magnesite and our QMAG plant is a modern production facility with an abundance of natural energy resources, including natural gas and electricity, and is in close proximity to road, rail and shipping facilities.

In Africa, our warehousing facilities are strategically located in Johannesburg, South Africa and Beira, Mozambique to service our various inland customers. Inventory at all locations is kept at levels so that customers can be assured of reliable, uninterrupted supply.

Talana Limited is engaged on Sibelco QMAG's behalf as our exclusive distributor and representative in Africa and controls all warehousing and distribution to our customers in the DRC, Zambia and other African countries. Talana has agreements in place with reputable hauliers to meet all of our clients' specific transport requirements.

Through our global network and our current and evolving QMAG product range, Sibelco is well positioned to support our magnesia customers long into the future.

About Sibelco

Sibelco is a global material solutions company. At Sibelco, we utilize nature's raw materials and all their variables to create high performance products that deliver consistent results for our customers and every day our materials work as essential components in the progress of society.

Founded in 1872, Sibelco has grown into a truly multinational business with more than 245 mining and production facilities worldwide and is one of the largest industrial minerals companies in the world.

In 2012, Sibelco acquired the Magnesia business, QMAG Limited in Queensland, Australia, which started operation in 1991.

For further information on Sibelco visit **www.sibelco.com**

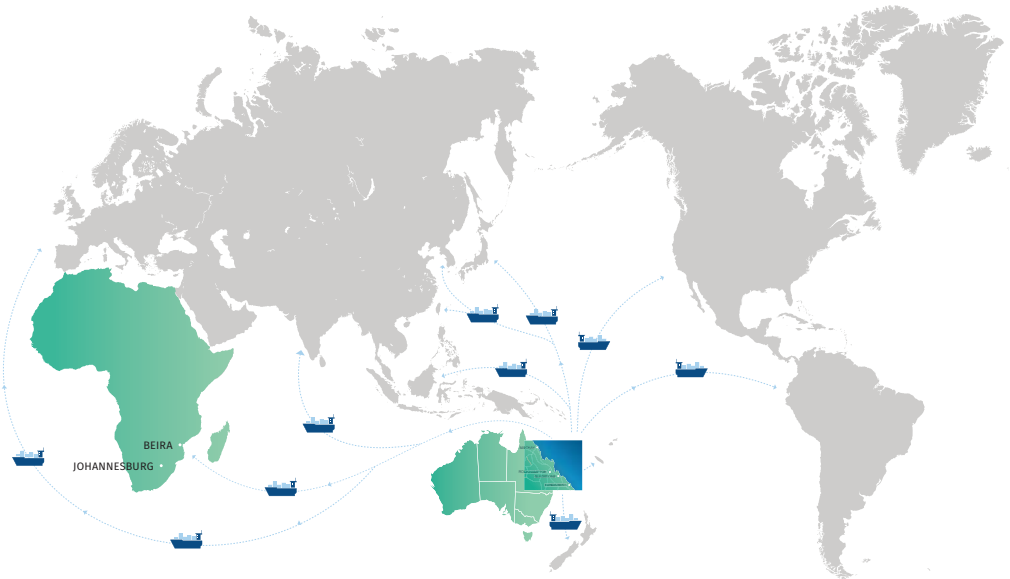

Material solutions advancing life

Sibelco QMAG
246 Boundary Road, PO Box 5798, Parkhurst Qld 4702
Tel: +61 7 4920 0200 | Fax: +61 7 4936 1380
Email: enquiries@qmag.com.au

Talana Limited
C2-402, 4th Floor Office, Block C, La Croisette, Grand Baie, 30517, Mauritius
Tel: +230 269 7370 | Fax: +230 269 7373
Email: office@talana.co

http://dx.doi.org/10.17159/2411-9717/2016/v116n6a7

Corrosion of lead anodes in base metals electrowinning

by A. Mirza*, M. Burr*, T. Ellis*, D. Evans†, D. Kakengela†, L. Webb‡, J. Gagnon‡, F. Leclercq§, and A. Johnston§

Synopsis

Lead-based alloys are used as the primary anodes for electrowinning from sulphate-based aqueous systems. Lead anode technology has evolved over the years, migrating from pure lead and lead-antimonial alloys to the present-day lead-calcium-tin alloys for copper electrowinning and lead-silver alloys for zinc electrowinning. Anode technology has also migrated from cast to rolled microstructures in search of improved mechanical properties and higher corrosion resistance. Although great strides have been made in the development of new alloys and production processes, the industry still has unresolved issues related to untimely corrosion, which limits anode life and may lead to higher contaminant levels in the metal being produced. Lead anodes corrode because of the difference in the chemical/electrochemical potential across the microstructural features of an anode. Given a very high purity material, we find that the grain boundary areas corrode significantly faster than the rest of the grain. A balance of alloying element selection and microstructural design allows the grain boundary area to be engineered, thus minimizing grain boundary corrosion. However, operational issues can lead to unexpected corrosion behaviours that we will discuss moving forward. The comments in this work, although directed toward copper electrowinning, can be extended to similar phenomena in other metals electrowon from sulphate media (*i.e.*, zinc, nickel, cobalt, manganese). The life cycle of electrowinning anodes depends on tankhouse operating conditions and maintenance of the anodes, including cleaning and straightening. This paper will focus on the operational aspects of maximizing the utilization of lead anodes for base metals electrowinning.

Keywords
electrowinning, base metals, anode corrosion, anode technology.

Introduction

Lead-based alloys are the primary anodes used in electrowinning from sulphate-based aqueous systems. Lead anode technology has evolved over the years, migrating from pure lead and lead-antimonial alloys to the present-day lead-calcium-tin alloys for copper electrowinning and lead-silver alloys for zinc electrowinning (Prengaman, Ellis, and Mirza, 2010). Anode technology has also migrated from cast microstructure to mechanically deformed, rolled microstructures in search of improved mechanical properties and higher corrosion resistance that results from the rapid production of a protective oxide coating (Prengaman, 1987; Prengaman and Morgan, 1992, 2001). Although great strides have been made in the development of new alloys and production processes (Prengaman, 2000), the industry still has unresolved issues related to untimely corrosion which limits anode life and may lead to higher contaminant levels in the metal being produced. The comments in this work, although directed towards copper electrowinning, can be extended to similar phenomena in other metals electrowon from sulphate media (*i.e.*, zinc, cobalt, nickel, manganese). The fundamental efficacy of lead-based anodes is dependent on the properties of PbO_2 (Prengaman and McDonald, 1980). In fact, lead anodes are used predominantly in sulphate-based electrolyte systems because of the protective ability of PbO_2. In particular, the protective adherent α-phase, which is the brown PbO_2 layer closest to the anode surface, isolates the lead from the corrosive electrolyte. It is composed of large, rhombic, closely packed crystals. The β-phase of PbO_2, which is black in colour, is the interface between the protective α-PbO_2 and the electrolyte, as shown in Figure 1. It is composed of tetragonal, fine, loosely adhering needle-shaped crystals. The transformation of α-PbO_2 to β-PbO_2 is marked by formation of PbO, $Pb(OH)_2$, $PbSO_4$, and other complex sulphates as reaction intermediates. The mechanism of electrochemical oxidation of lead to lead dioxide in sulphuric acid is discussed in detail by Pavlov and Dinev (1980).

The oxidation of a lead anode is therefore determined not by the reaction rate of lead with sulphuric acid but by mass transport of the ions participating in the reaction through

* *RSR Technologies, Dallas, TX, USA.*
† *Castle Lead Works, Krugersdorp, South Africa.*
‡ *Quemetco Metals Limited, Inc., Casa Grande, AZ, USA.*
§ *Le Plomb Francais, Estrees-Saint-Denis, France.*

 ISSN 2225-6253. This paper was first presented at the, Copper Cobalt Africa Conference, *6–8 July 2015, Avani Victoria Falls Hotel, Victoria Falls, Livingstone, Zambia.*

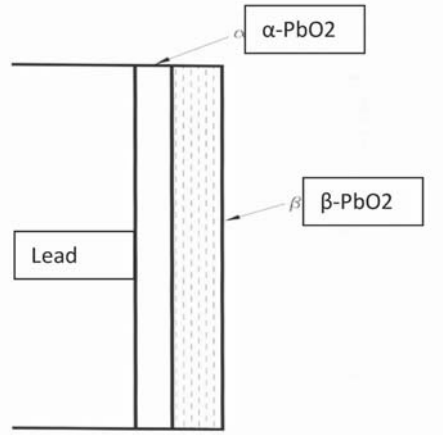

Figure 1—Lead anode corrosion in sulphuric acid

the electrochemical layer. The rate of oxidation decreases drastically with increasing thickness of the layer, and is prevented almost completely if the corrosion layer does not dissolve, flake off, or become porous (Hyvarinen, 1972). This mechanism renders the lead anode virtually inert in sulphate media, and the main reaction on the outer surface of the β-PbO_2 layer becomes the electrochemical decomposition of water into molecular oxygen (Equation [1]):

$$2H_2O \rightarrow O_2 + 4\,H^+ + 4\,e \qquad [1]$$

$$E_{(O2/H2O)} = 1.229 - (0.059/4)\,[4\,pH - \log\,(p_{O2})] \qquad [2]$$

The first stage in lead oxidation in the presence of oxygen is the formation of lead monoxide (PbO) and lead sulphate ($PbSO_4$). As the anode potential increases, the surface layer of PbO/$PbSO_4$ transforms to $Pb(OH)_2$, followed by conversion to the insulating tetragonal PbO, and then finally to PbO_2 at higher potentials. As evident in Figure 2, it is necessary to maintain an anode potential above 1.77 V to maintain the protective α-PbO_2. Unless the anode potential is consistently maintained above this value, the protective, adherent α-PbO_2 converts to the loosely adherent β-PbO_2 that flakes off and causes cathode contamination. This electrochemical layering effect explains the commercial success of lead-based anodes in sulphate media electrowinning in the last few decades.

Corrosion of lead anodes

A fundamental factor in anode corrosion is the difference in the chemical/electrochemical potential across the microstructural features of an anode. Given a very high purity material, we find that the grain boundary areas corrode significantly faster than the rest of the grain. Minimizing grain boundary corrosion by a balance of alloying element selection and microstructural design allows the grain boundary area to be engineered. However, operational issues can lead to unexpected corrosion behaviours, which we will discuss moving forward.

General corrosion

When a lead-based anode is exposed to a sulphate-based electrolyte, a thin film of $PbSO_4$ is formed instantly. As soon as power is switched on, oxygen is evolved at the anode. The thin film of lead sulphate is then converted to β-PbO_2. Upon further oxygen evolution, oxygen diffuses through β-PbO_2 to form α-PbO_2. The exact process during the oxidation of lead anode is determined by the structure and composition of the anode layer, which in turn is determined by the electrode potential as indicated in Figure 2. To produce the lowest lead content in the copper cathodes, lead anodes should be cleaned periodically to remove the loosely adherent portion of β-PbO_2. The objective is not to remove all the β-PbO_2 layers, but only the non-adhering layers with a pressure water wash. The typical surface of a cleaned lead anode in use with the adherent α-PbO_2 is shown in Figure 3.

In order to increase the functional life of the anodes, it is extremely important not to damage the adherent protective β-PbO_2 layer during anode cleaning by being overly aggressive.

Chloride corrosion

While 20–30 mg/L Cl^- in a copper electrowinning electrolyte is helpful for grain refining/levelling of the cathode deposits, higher chloride concentrations (>30 mg/L) increase corrosion of the Pb anodes due to the formation of soluble $PbCl_2$ and other Pb chloride complexes. Pb chlorides are more soluble than PbO_2 or $PbSO_4$. A steady-state concentration of 55–60 mg/L chloride in the electrolyte is too high, and a

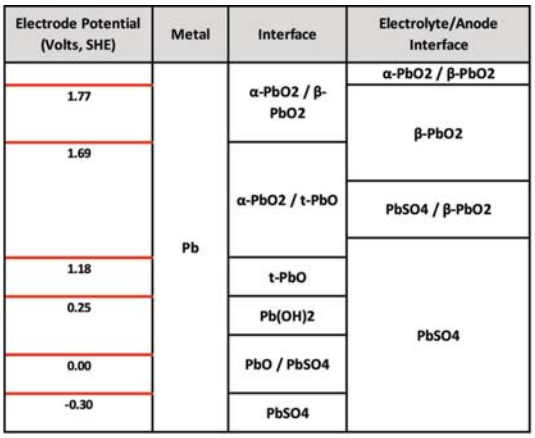

Figure 2—Schematic representation of lead corrosion films (after Burbank, 1956)

Figure 3—Hard, dense, adherent α-PbO_2 (brownish colour)

concentration above 100 mg/L Cl^- is highly deleterious for the anodes. Chloride also reacts with any MnO_2 on the anode surface to form $MnCl_2$. Higher levels of chloride (200–300 mg/L) are tolerated in zinc electrowinning because the much higher levels of manganese in the electrolyte form a thick protective layer of MnO_2. High chloride levels in the electrolyte also enhance the corrosion of stainless steel cathodes.

Chloride corrosion is highest at or above the solution line because the higher oxygen concentration at the surface enhances the formation of relatively soluble $PbCl_2$ by Equations [3] and [4]. The mechanism of formation of PbO and $PbSO_4$ in the presence of organics in the electrolyte *via* Equations [5] to [7] is explained in the section on Solution Line Corrosion.

$$PbO + 2HCl \rightarrow PbCl_2 + H_2O \quad [3]$$

$$PbSO_4 + 2HCl \rightarrow PbCl_2 + H_2SO_4 \quad [4]$$

$$O_2 + 4RH \rightarrow 4R^+ + 2H_2O + 4e \quad [5]$$

$$2R^+ + PbO_2 + H_2O \rightarrow PbO + 2R{=}O + 2H^+ \quad [6]$$

$$PbO + H_2SO_4 \rightarrow PbSO_4 + H_2O \quad [7]$$

In order to increase the functional life of lead anodes, it is imperative to keep chlorides levels in the copper electrowinning electrolyte below 20–30 mg/L.

Manganese-related corrosion

Copper electrowinning solutions often contain some manganese. It has been our customers' experience that at manganese concentrations above 40 mg/L in the electrolyte, manganese-related corrosion of lead anodes becomes significant. Problems related to manganese in the electrolyte have been discussed by Miller (1995) and Hughes *et al.* (1998). Cifuentes *et al.* (2005) investigated the effect of various impurities in a copper electrowinning electrolyte on the rate of corrosion of lead anodes and found that manganese increased the corrosion rate of lead anodes more significantly during normal tankhouse operation than during current interruptions.

Mechanism of manganese-related corrosion

The potential at the anode surface is high enough for Mn^{2+} in the electrolyte to oxidize to MnO_2 and MnO_4^- at the anode according to Equations [8] to [10]:

$$Mn^{2+} + 2H_2O = MnO_2 + 4H^+ + 2e;\ E^o = 1.21\ V \quad [8]$$

$$Mn^{2+} + 4\,H_2O = MnO_4^- + 8\,H^+ + 5e;\ E^o = 1.51\ V \quad [9]$$

The permanganate ion, MnO_4^-, attacks PbO_2 indirectly. It is first converted to MnO_2 by the following reaction:

$$MnO_4^- + 4H^+ + 3e = MnO_2 + 2H_2O;\ E^o = 1.68\ V \quad [10]$$

Equations [8] to [10] take place simultaneously on the anode, resulting in the formation of MnO_2. Manganese in solution also reacts directly with the stable PbO_2 corrosion layer on the anode surface to form MnO_2:

$$MnSO_4 + PbO_2 \rightarrow PbSO_4 + MnO_2 \quad [11]$$

$$\Delta G\ @\ 40\ ^\circ C = -24.84\ kcal/mol \quad [12]$$

The $PbSO_4$ formed in Equation [11] is also converted to PbO_2 at the anode but it will be in the form of loose, non-adherent flakes. Under such circumstances, MnO_2 and PbO_2 crystals will also grow together forming large, fluffy flakes that spall easily, as illustrated in Figure 4. This not only results in cathode contamination but can also contribute to the formation of dendrites on cathodes.

The best solution, of course, is to prevent manganese from getting into the electrolyte in the first place. However, if the manganese content of the electrolyte is greater than 40 mg/L, it is important to clean the anodes regularly to minimize cathode contamination and maintain low power consumption. The periodicity of cleaning is unique for each tankhouse and should be established by experience. If tankhouse parameters such as current density, temperature, and manganese, iron, or chloride concentrations change, then the frequency of anode cleaning will have to re-determined. Once determined, it should be followed conscientiously.

Addition of 100–200 mg/L cobalt to the electrolyte helps in minimizing the deleterious effects of manganese-related corrosion. By decreasing the oxygen overpotential on the lead anode, cobalt in the electrolyte promotes oxygen evolution in preference to manganese oxidation. Above 200 mg/L, the cost/benefit ratio of adding cobalt decreases. Other measures to control manganese in copper electrowinning electrolyte are discussed in detail by Miller (1995). The literature alludes to using Fe/Mn ratios between 5 and 10 to alleviate manganese attack of Pb anodes. The extent to which iron helps depends on the relative rates of reaction of Fe^{2+} to Fe^{3+} and of Mn^{2+} to MnO_2. This is determined by several factors, such as temperature, mass transport, acid concentration, *etc.*

Permanganate, MnO_4^-, being a powerful oxidant, degrades the solvent extraction reagents. Therefore, copper tankhouses have to sometimes add iron deliberately to decrease the formation of MnO_4^-.

Hanger bar corrosion

The main reasons for hanger bar corrosion are:

- Electrolyte–hanger bar contact
- Corrosion by copper sulphate
- Electrolyte penetration
- Ineffective anode design.

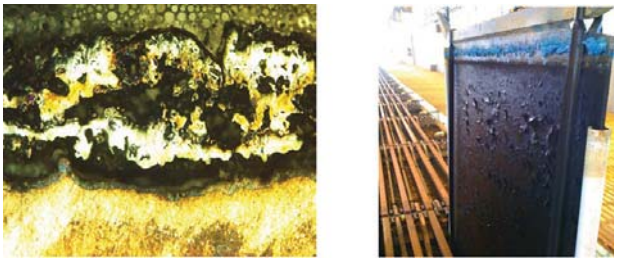

Figure 4—Disruption of PbO_2 by MnO_2 and formation of large, soft, loosely adherent layers

Electrolyte–hanger bar contact

The electrolyte level is sometimes raised to overflow the electrolyte in order to float off the entrained organics. Electrolyte can also seep up to the hanger bars through the mist control foam or plastic balls by capillary action. If electrolyte is allowed to come in intimate contact with the hanger bars, as shown in Figure 5, copper will react spontaneously with H_2SO_4 to form $CuSO_4.5H_2O$. The exposed portion of the copper hanger bar between the end of the lead covering and the attachment to the busbar is corroded rapidly. To increase the functional life of lead anodes, it is therefore important not to immerse the hanger bars in the electrolyte and not to allow the level of plastic balls or the mist suppressant foam to be within 8–10 mm of the hanger bars.

When the hanger bar corrodes rapidly, it becomes weak and is no longer structurally sound. This is a safety issue during anode lifting and transport by crane for cleaning. It also causes the anodes to tilt, changing the anode–cathode spacing across the cell, with several ramifications as discussed in the section on Uneven Electrode Spacing.

Corrosion by copper sulphate

In covered copper tankhouses, acid rains down constantly on the anodes. As shown in Figure 5, copper reacts with sulphuric acid to form cupric sulphate ($CuSO_4.5H_2O$). However, what is not obvious is that cupric sulphate reacts spontaneously with lead to form cuprous sulphate [$Cu_2(SO_4)_2$]:

$$2CuSO_4{:}5H_2O\ (\text{Blue}) + Pb \rightarrow Cu_2SO_4\ (\text{Green}) + PbSO_4\ (\text{White}) + 10\ H_2O \quad [13]$$

$$\Delta G\ @\ 40\ ^\circ C = -21.72\ \text{kcal/mol} \quad [14]$$

Electrolyte penetration

This type of corrosion is illustrated in Figure 6 and is most prevalent in covered copper tankhouses. Corrosion of lead by copper sulphate could weaken the integrity of the lead coating and allow penetration of the acid into the area between the protective lead encapsulation and the copper bar. This results in the formation of a significant amount of copper sulphate underneath the lead covering the hanger bar. Expansion upon crystallization of copper sulphate forces the lead away from the copper bar. This process becomes iterative, resulting in an eventual splitting of the lead castaround, as shown in Figure 6. Local and independent concentration cells are also set up in the region between the lead castaround and copper hanger bar, causing the copper to be corroded rapidly.

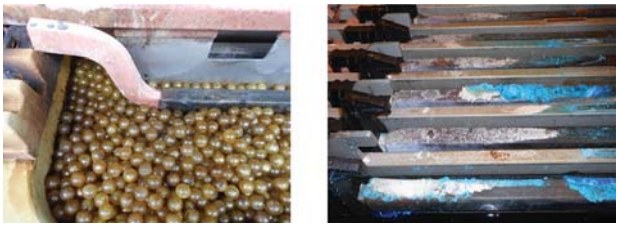

Figure 5—Corrosion of hanger bar due to immersion or seepage and corrosion of lead by $CuSO_4$

Ineffective anode design

Anode design is a crucial yet often overlooked or undervalued aspect of anode life optimization. Anode design is an important consideration in cathode plating efficiency. If the anode hanger bar is moved closer to the solution line in an effort to minimize the size of the lead anode, various modes of anode damage follow, owing to both electrochemical and mechanical reasons.

Corrosion stems from the exposed copper bar's proximity to the electrolyte level and from the presence of hoods for acid mist control. The captured acid mist runs down the hood and drops onto the exposed copper bar. With effective design, protection is extended to such vulnerable areas of the hanger bar. Figure 7 demonstrates the 'evolution' of anode hanger bar encapsulation design (from left to right).

In order to combat hanger bar corrosion in covered tankhouses and prolong anode life, the hanger bar needs to be completely coated with lead and the hanger bars must be washed often to prevent build-up of copper sulphate.

Solution line corrosion

Solution line corrosion is often mistaken for weld corrosion where the weld line in welded anodes corresponds with the solution level. However, solution line corrosion, such as shown in Figure 8, is sometimes observed on rolled/slotted and cast anodes where a weld line is absent. If there is carryover of organics into the electrolyte from the solvent extraction process, the organics can cause solution line corrosion and can sometimes literally burn at the solution line.

Mechanism of solution line corrosion

Formation of free radicals:

$$O_2 + 4RH \rightarrow 4R^+ + 2H_2O + 4e \quad [15]$$

Figure 6—Corrosion of hanger bar by acid penetration

Figure 7—Progressive evolution in hanger bar design

Figure 8—Corrosion at solution line by organics

These surface-active polar molecules concentrate at the aqueous–organic interface at the solution line and react with the protective PbO_2 as follows.

Free radical attack on protective α-PbO_2 to form unprotective PbO:

$$2R^+ + PbO_2 + H_2O \rightarrow PbO + 2R{=}O + 2H^+ \quad [16]$$

Reaction of PbO with H_2SO_4 to form $PbSO_4$:

$$PbO + H_2SO_4 \rightarrow PbSO_4 + H_2O \quad [17]$$

The $PbSO_4$ formed is converted to PbO_2 at the anode but it will be in the form of loose, non-adherent flakes. Since no alloy currently exists that can protect the anode, the only suitable action is to prevent organics from entering the tankhouse. To minimize solution line corrosion, the organics from the solvent extraction process must be removed from the electrolyte before it reaches the tankhouse. Column flotation, sand filters, or scavenger cells can be used for this purpose (Kordosky, 2002). Electrowinning cells should be split into scavenger and production cells to minimize organic carryover from the solvent extraction plant (Beukes and Badenhorst, 2009). Improved mixer–settler design enhances the distribution of the dispersion exiting the mixer and minimizes organic entrainment. In the case of settlers, it is essential to provide for sufficient flotation time to float the organics. Other means employed in the tankhouses include scrubbing and surface vacuuming. None of these methods are ideal because anodes will be exposed to organic attack, even if only the anodes in the scavenging section of the tankhouse.

Miscellaneous tankhouse issues

Uneven electrode spacing

The electrode spacing should be as consistent as possible. Figure 9 indicates that this is not always the case in a tankhouse. The inter-electrode spacing in copper tankhouses is usually about 10 cm. Below this spacing, the risk of shorts due to electrode alignment and dendritic growth of nodules becomes unacceptably high. If a dendrite touches the anode, the protective PbO_2 becomes overheated, is softened, and spalls off under conditions of intense turbulence caused by oxygen evolution. This process is autocatalytic and blows holes through the anode. Therefore, to increase the useful life of lead anodes and to decrease power consumption, it is important to maintain uniform anode–cathode spacing and monitor and eliminate the shorts as soon as they are formed.

The potential of the electrowinning cell is the sum of respective half-cell reaction potentials as well as the ohmic drop in the electrolyte, busbars, and other competing electrochemical reactions. The ohmic drop in the electrolyte is a function of the electrode spacing, ionic mobility, concentration of the species in solution, and current density. Non-uniform electrode spacing adversely affects current distribution, power consumption, current efficiency, cathode contamination, and plating quality.

Copper plating on lead anodes

Strangely enough, copper sometimes deposits on lead anodes, as shown in Figure 10. This happens due to two reasons:

- Dendrites
- Power outage.

Dendrites

The local area where the dendrite touches the anode will become cathodic and copper will therefore deposit on the anode in this area. More importantly however, the protective α-PbO_2 in the region around the dendrite will be reduced to $PbSO_4$ which will flake off under conditions of intense oxygen evolution in the surrounding areas. This autocatalytic process will continue unabated until the dendrite blows a hole through the anode.

Power outage

Copper also plates on the lead anode if there is a power outage and if the anodes and cathodes are left electrically connected in the tankhouse electrolyte. This is also found to be a very common problem in cast Pb-Sb anodes compared with rolled Pb-Ca-Sn anodes. This is because cast anodes

Figure 9—Uneven electrode spacing

Figure 10—Copper plating on lead anode (courtesy of Nikkelwerk)

have segregation and casting defects, such as porosities and inclusions, which lead to non-uniform electrochemistry. As a result, there are areas in a cast anode that become relatively anodic to other areas more easily. On the other hand, rolled microstructure is very uniform with no casting defects, which results in uniform electrochemical behaviour across its surface.

Temperature fluctuations

Lead anodes should be protected from temperature fluctuations of the electrolyte. Due to differences in the coefficients of thermal expansion between the lead anode and PbO_2 on the surface of the anode, a rapid drop in electrolyte temperature of about 10°C may result in spalling of the PbO_2 layer from all the anodes in a tankhouse simultaneously. Electrolyte temperature fluctuations of a few degrees are not uncommon in tankhouses, but a sudden cold weather front can result in the electrolyte temperature dropping 10°C or more, especially in open tankhouses. An electrolyte heating system will prevent rapid fluctuations in temperature.

Addition of cobalt

The main purpose of cobalt addition to copper electrowinning electrolyte is to depolarize the oxygen evolution reaction on a lead anode. This decreases the oxygen evolution overpotential and results in power savings. In other words, cobalt promotes the evolution of oxygen from the anode surface rather than corrosion of lead. Cobalt also protects the lead anode from corrosion and cathode copper from lead contamination. The adsorbed CO^{2+} ions on the lead anode hinder the penetration of oxygen into the PbO_2 lattice, thus decreasing the rate of PbO_2 formation and making the oxide layer thin and dense. The adsorbed cobalt ions also harden the oxide layer and make it less subject to spalling. Cobalt concentrations of 100–200 mg/L are common in copper tankhouses around the world. The exact level of cobalt is dependent on the manganese content, current density, and the electrolyte bleed rate, and has to be determined experimentally for each tankhouse. If any of these tankhouse parameters change significantly, then a new optimum cobalt concentration would have to be established, and once determined, maintained at this level. Cobalt is also lost from the system with the bleed stream. A drop in the cobalt content for several days may cause the cobalt to desorb from the anode surface, softening the flakes and increasing the likelihood of lead contamination of the cathode. Therefore, cobalt must be metered in continuously to the electrolyte to replace the cobalt that is lost through the bleed. Cobalt is a significant operating cost to copper solvent extraction–electrowinning operations.

Summary

The different types of corrosion processes described that effect lead anodes are by no means exhaustive but typical of those encountered in practice. Lead alloys are the preferred material for electrowinning anodes from acidic sulphate solution because they are insoluble and have the ability to form a protective PbO_2 layer. They are corrosion resistant, economical, and have an acceptable operating voltage. There are alternative anode technologies, but none can compete economically with lead anodes. Moreover, limited long-term industrial test work has been carried out with the alternative anodes to prove their technical, practical, and commercial viability. Rolled Pb-Ca-Sn anodes are used widely in copper electrowinning. They are strong, have a particularly high corrosion resistance, good form stability, and have a low potential drop between the hanger bar and the lead sheet. The electrochemical performance of lead anodes is independent of whether they are made from primary or secondary lead. If the anodes are maintained properly according to the broad guidelines discussed in this paper, we can expect an optimum functional life.

References

Beukes, N.T. and Badenhorst, J. 2009. Copper electrowinning: theoretical and practical design, *Proceedings of Southern African Hydrometallurgy 2009*. Southern African Institute of Mining and Metallurgy, Johannesburg. pp. 213–240.

Burbank, J. 1956. Anodization of lead in sulphuric acid. *Journal of the Electrochemical Society*, vol. 103, no. 2. pp. 87–91.

Cifuentes, L., Astete, E., Crisostomo, G., Simpson, J., Cifuentes, G., and Pilleux, M. 2005. Corrosion and protection of lead anodes in acidic copper sulphate solutions. *Corrosion Engineering Science and Technology*, vol. 40, no. 4. pp. 321–327.

Hughes, C., Barnard, K., Cheng, C.Y., and Larcombe, K. 1998. The role of contaminants in phase separation during copper solvent extraction. *Proceedings of the ALTA Copper Hydrometallurgy Forum*, Brisbane, Australia.

Hyvarinen, O. 1972. The effect of silver and cobalt on the oxygen evolution at lead anodes. Laboratory of Process Metallurgy, Helsinki University of Technology, Otaniemi, Finland.

Kordosky, G.A. 2002. Copper recovery using leach/solvent extraction/electrowinning technology: forty years of innovation, 2.2 million tonnes of copper annually. *Journal of the South African Institute of Mining and Metallurgy*, vol. 102. pp. 445–450.

Miller, G. 2010. Methods of managing manganese effects on copper SX-EW operations. *Proceedings of ALTA 2010 Ni-Co-Cu Conference*, Perth, Australia.

Miller, G. 1995. The problems of manganese and its effects on copper SX-EW operations. *Copper 95 - Cobre 95, Electrorefining and Hydrometallurgy of Copper*, vol. 3. Cooper, W.C., Dreisinger, D.B., Dutrizac, J.E., Hein, H., and Ugarte, G. (eds.). Canadian Institute of Mining, Metallurgy and Petroleum, Montreal. pp. 649–663.

Pavlov, D. and Dinev, Z. 1980. Mechanism of the electrochemical oxidation of lead to lead dioxide electrode in H_2SO_4 solution. *Journal of the Electrochemical Society*, vol. 127, no. 4. pp. 855–863.

Prengaman, R.D. 1987. New insoluble lead anodes for copper electrowinning. *The Electrorefining and Winning of* Copper. *Proceedings of the TMS 116th Annual Meeting*. Hoffman, J.E., Bautista, R.G., Ettel, V.A., Kudryk, V., and Wesely, R.J. (eds). The Minerals, Metals and Materials Society, Warrendale, PA. pp. 387–401.

Prengaman, R.D. 2000. Electrowinning anode. US patent 6,131798. RSR Technologies, Dallas, TX.

Prengaman, R.D., Ellis, T., and Mirza, A. 2010. 10 years' experience with rolled lead-calcium-silver anodes. *Proceedings of Lead-Zinc 2010*. Siegmund, A., Centomo, I., Geenen, C., Piret, N., Richards G., and Stephens, R. (eds.). The Minerals, Metals and Materials Society, Warrendale, PA. pp. 819–837.

Prengaman, R.D. and McDonald, H.B. 1980. Stable lead dioxide anode and method for production. US patent 4,236,978. RSR Corporation, Dallas, TX.

Prengaman, R.D. and Morgan, C.E. 1992. Electrowinning anode and method of manufacture. US patent 5, 172,850. RSR Corporation, Dallas, TX.

Prengaman, R.D. and Morgan C.E. 2001. Electrowinning anodes which rapidly produce a protective oxide coating. US patent 6,224,723 B1. RSR Technologies, Dallas, TX. ◆

http://dx.doi.org/10.17159/2411-9717/2016/v116n6a8

Development of a geometallurgical model for a copper concentrator

by M. Valenta* and B. Mulcahy*

Synopsis

The purpose of executing a project in a stagewise fashion is to evaluate all potential options in a cost-effective manner and develop an understanding of the project drivers, thereby minimizing overall project risk to the client. Among the more valuable tools for this exercise are production and financial models that can be used to quantify the sensitivity of the project to the critical parameters.

The mine and concentrator used in this case study are located on the Kalahari Copper Belt, which extends from Zambia through northern Botswana into Namibia. This area of Africa has seen very little industrial development and the project will create much-needed employment and development in the region.

The success of this project thus far can be attributed to the close cooperation between the geological, mining, and metallurgical disciplines. Regular updates of projected capital and operating cost estimates coupled with project outputs guided the teams in optimizing their various discipline models, ultimately delivering a compelling argument for the execution of the project. Key to the success was the development of a geometallurgical model for the prediction of concentrate tonnage, grade, and recovery for the life of the mine from the mining plan.

This paper summarizes the metallurgical findings and the outcome of the various project stages. The development of the model is discussed, as are the challenges faced in developing a suitable metallurgical process route.

Keywords
geometallurgy, Kalahari Copper Belt, modelling, copper, circuit design, stagewise project execution.

Introduction

The Kalahari Copper Belt

The Kalahari Copperbelt, which extends from Zambia across northwest Botswana into Namibia, is considered to be a broad time equivalent of the Central African Copperbelt, with a similar style of mineralization. However, at shallower depths (<25 m), chrysocolla and malachite exist in significant proportions in certain geological areas.

As illustrated in Figure 1, the project is located in the Ghanzi-Chobe Fold Belt which forms part of the Kalahari Copper Belt. The Ghanzi Group, which overlies the lowest stratigraphic unit (the Kwebe Formation), consists of three formations, namely the Ngwako Pan, the D'Kar, and the Mamuno Formation (Hall, 2012).

Mineralization already occurs in the first 10 m of the D'Kar Formation and is characterized by low-sulphur, low-iron copper sulphides (chalcocite and bornite). The overall genesis of the mineralization resulted from hydrothermal convection cells generated by the high heat flow associated with the thinning, extended continental crust during basin formation. The fluids circulating in these hydrothermal convection cells leached base metals from the underlying Kgwebe formation and produced large volumes of metal-enriched calcareous and siliceous fluids. These fluids then percolated upwards into the highly permeable Ngwako Pan Formation sediments and through them into the base of the less permeable D'Kar Formation, depositing the base metals in disseminated blebs or within thin parallel calcareous and siliceous veins.

Two major areas (Area 1 and Area 2) have been identified in the project that are parallel in a southwest—northeast orientation and are approximately 1 km apart. The degree of mineral oxidation in Area 1 is significantly higher than in Area 2, and this is attributed to an observed difference in bedding orientation within the deposits (Hall, 2012).

The geologists initially defined three zones in the orebody based on the occurrence of various copper-bearing minerals: the upper zone (0–25 m), middle zone (25–35 m), and the lower zone (>35 m). This definition served its purpose in planning the test work that was required and predicting the relative copper grades and recoveries that could be expected from each zone. On completion of the variability test work the definitions became less relevant when the predictive models were developed based on the mineral content of the ore.

* *Metallicon Process Consulting (Pty) Ltd, Ifafi, South Africa.*
 ISSN 2225-6253. This paper was first presented at the, Copper Cobalt Africa Conference, *6–8 July 2015, Avani Victoria Falls Hotel, Victoria Falls, Livingstone, Zambia.*

Development of a geometallurgical model for a copper concentrator

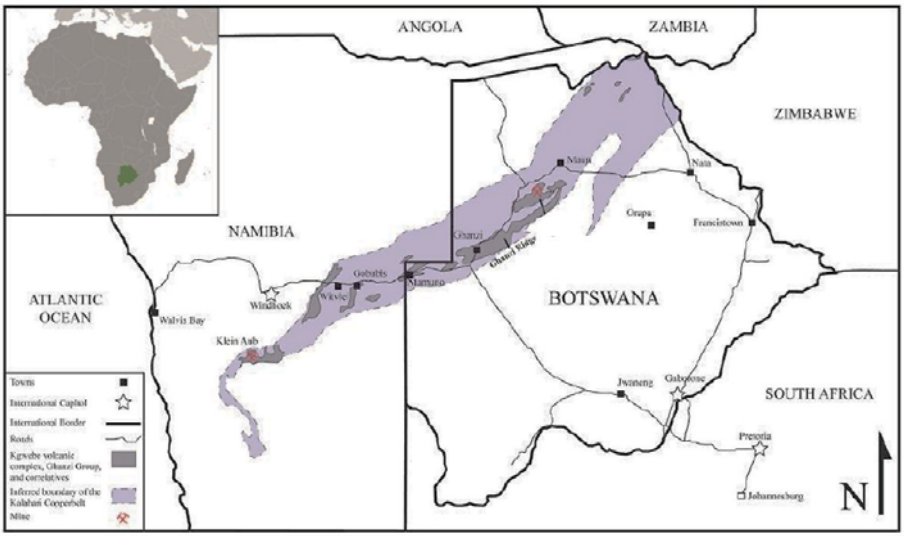

Figure 1—The Kalahari Copper Belt

Country background

The project area is within 200 km of the Central Kalahari Nature Reserve and it is not uncommon for game such as lion and elephant to be reported in the region. The project is also in close proximity to Maun, which is regarded as the gateway to the Okavango Delta and is of significant value to Botswana as an ecological gem and a tourist destination.

Furthermore, the project is in an arid region where water is more precious to the local population than the diamonds from the nearby Orapa diamond mine. Throughout the development of the project the team considered all avenues to minimize the consumption of water. Botswana is also dependent on other countries, particularly South Africa, for the supply of electricity. Developments in the resource market have put strain on the supply of electricity throughout the Southern African Development Community (SADC) and for this reason the team had to consider technology that would minimize the consumption of electricity.

Project development

From the outset the project team planned to use a tollgating approach and develop the project in stages as illustrated in Figure 2.

The objective of such a strategy is to establish formal reporting deadlines, thus allowing the three major project disciplines (geology, mining, and metallurgical) to share information and update the project database. The metallurgical engineers required updates from the geological and mining teams on the latest geological and mining models to refine their metallurgical test work. The mining engineers could then optimize their mining plans to focus on high-yielding areas based on the head grades and the associated metallurgical response for each defined geological area.

Furthermore, as illustrated in Table I, the early stages of the project are conducted to a low degree of accuracy and do not normally involve all the engineering disciplines (mechanical, electrical, civil, and structural). This results in a significant reduction in cost for these stages and the time taken to complete the work.

This allowed the metallurgical engineers the freedom to consider a variety of options early in the project with little or no input from the other engineering disciplines. The capital and operating cost estimates are, however, sufficiently accurate to allow for a comparison of the different process options. Options could be carried forward to the next stage if further resolution was required.

Metallurgical test work

Throughout the test programme, qualitative and quantitative mineralogical analysis was conducted on all of the samples. The results were related to the flotation results and provided valuable information for understanding the metallurgical response.

Initially, two composite samples were produced from drill cores. These samples were used to conduct the preliminary tests to develop the process design criteria for the order-of-magnitude study. The test work included milling, gravity concentration, flotation, and leach tests.

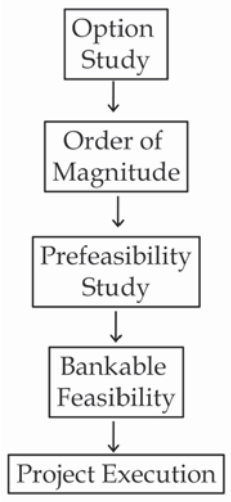

Figure 2—Stages in the development of the project

The preliminary results provided valuable information for the geologists and defined the criteria for characterizing the samples. The subsequent reports from the geologists confirmed the varying oxidation highlighted in the literature (Hall, 2012), and three composites were generated for each of the two geological areas relative to sample depth, as discussed above. Milling and flotation tests were conducted on the composites and the results of the flotation tests related to the quantitative mineralogical analysis. This provided adequate information for the development of the fundamental processing flow sheet.

Variability flotation tests were carried out as per the proposed flow sheet on individual core samples to determine the variability in the flotation response and concentrate grades produced.

Results and discussion

Mineralogy

Qualitative mineralogy

Qualitative mineralogical analysis on various drill cores from the two deposits confirmed the geological observations. The predominant copper mineral observed in samples from depth (>35 m) was chalcocite with small amounts of bornite. Trace amounts of malachite were also observed in these samples. Liberation of the copper-bearing minerals did not appear to be a challenge.

Shallower samples contained increasing amounts of malachite, with samples shallower than 25 m containing varying concentrations of chrysocolla. The chrysocolla appeared to be associated with the malachite and liberation of the copper-bearing minerals would not pose a challenge.

Quartz was identified as the predominant gangue mineral, while plagioclase, mica, chlorite, and calcite were also identified. Calcite seemed to be more abundant in the upper zones than in the lower zones. Clay minerals occur in minor to trace amounts in some of the upper and middle samples. Calcite and chlorite are both high acid consumers, indicating that acid leaching may not be a process option.

Quantitative mineralogy

Following the initial qualitative mineralogy on the earlier drill cores, more detailed quantitative mineralogical investigations were carried out on the composite-by-depth samples and the variability samples.

The copper deportment in the two deposits is illustrated in Figure 3. It is clear that a large amount of chrysocolla is present in shallower samples that were submitted for test work. The middle zone appears to show a mixture of copper sulphide and oxide minerals, while negligible malachite and chrysocolla are evident in the lower zone.

Preconcentration

To allow for an informed choice with regard to the inclusion

Table I

Level of engineering and degree of accuracy

Stage	Option study	Order of magnitude	Pre-feasibility	Bankable feasibility
Duration	Workshop	2 weeks	6 weeks	6 months
Expected accuracy	None	30–40%	25–30%	5–10%
Typically quoted accuracy	None	-15% +30%	-10% +25%	-5% +10%
Process engineering	Block flow diagrams	Preliminary Process Flow Diagrams (PFD's)	Decided PFD's	Final PFD's
Civil and structural engineering	None	Factored cost	General Arrangement Drawings (GA's)	GA's and detail
Mechanical enginering	None	Factored cost	General arrangement	GA's, detail and tender process
Electrical and control engineering	None	Factored cost	Factored cost	Detailed take-off

N/A: Not applicable

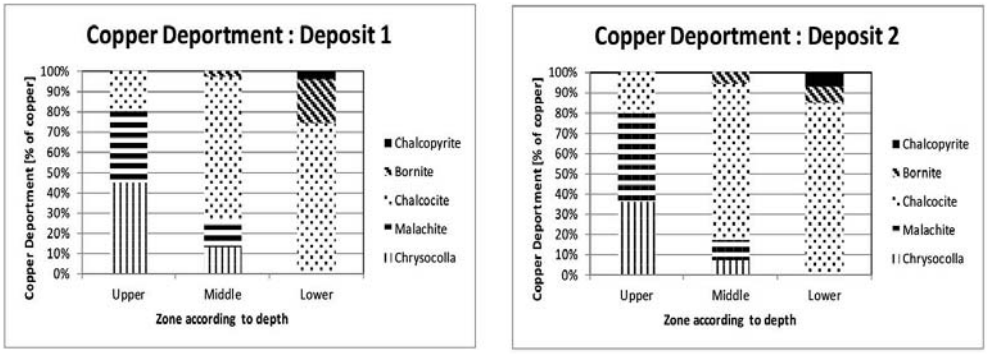

Figure 3—Copper deportment in the two deposits

of a dense media separation (DMS) plant in the main process flow sheet, some heavy liquid separation (HLS) test work was carried out on the –6 mm to +1 mm fraction of the reef material.

Results showed that a DMS plant operating at a cut density of 2.7 t/m^3 would theoretically reject 30% of the mass, with a loss of 9% of the copper to waste at a grade of 0.4% copper.

The DMS simulation indicated that due to the large amount of near density material, unstable operation of the DMS plant could be expected. The inclusion of a DMS plant in the flow sheet was therefore not recommended.

Comminution

Flotation tests were conducted at various grinds. The optimal grind was found to be 55% passing 75 µm. Comminution test work included the characterization of the ore through the determination of the crusher work index, rod and ball mill Bond Work indices, and drop weight tests to determine the fully/semi-autogenous (FAG/SAG) mill parameters.

Regrinding the sulphide concentrate to a P_{80} of 38 µm did not improve the recovery, but resulted in a significant improvement in copper grade. It was, however, noted that finer grinding of ores containing oxides resulted in a decrease in recovery, and this was attributed to the liberation and subsequent loss of chrysocolla that was originally associated with floatable species. This was confirmed in the qualitative mineralogical analysis.

Flotation and leaching

The initial test work on the composites of the two drill cores indicated that the recovery of the predominant copper-bearing mineral (chalcocite) did not pose a challenge and that recoveries in excess of 90% could be achieved at relatively high copper grades of up to 45%. These results were achieved using a classical sulphide flotation reagent suite of potassium amyl xanthate (PAX) and a common water-soluble polyglycol ether (DOW 200) as frother.

Flotation tests on the shallower samples yielded a lower recovery. The mineralogical analysis revealed the presence of other copper minerals, particularly malachite and chrysocolla, in the flotation tailing.

The gangue acid consumption of the oxide ore was found to be excessively high, making it uneconomical to recover the oxide copper by acid leaching. It was decided to utilize a sulphidization step in the flotation circuit with the addition of NaHS to make the specific oxide minerals more susceptible to sulphide flotation (Kongolo *et al.*, 2003; Newell *et al.*, 2006; Raghavan *et al.*, 1984).

In principle, the sulphidization flotation method is attractive, but the major disadvantages include potential depression of the sulphide minerals when sulphidization is used in excess, difficulty in controlling optimum dosage, and the fact that different oxide minerals respond differently to the addition of the sulphidizer.

Since sulphidization may result in depression of the sulphide minerals, and the sulphide and oxide minerals reacted differently to fine grinding of the rougher concentrate, it was decided to process the ore in two rougher-cleaner circuits in series, *i.e.* a sulphide circuit and an oxide circuit.

The chrysocolla was found to respond poorly to flotation, even with the addition of a sulphidizer. The mineralogical analysis revealed that the majority of the chrysocolla is recovered to a flotation concentrate through association with floatable species, *e.g.* malachite, that is recoverable under sulphidizing conditions.

Solid–liquid separation

Test work was done to determine the thickening and filtration characteristics of the tailings and concentrate.

It was found that the tailing was not difficult to filter and that high thickener underflow densities of up to 69% solids by mass could be achieved. Paste thickening tests showed that paste could be generated at 72% solids by mass.

Process design

Option study

The option study took the form of a one-day workshop that included a number of industry experts in the processing of copper. Presentations were given by geologists, mining engineers, minerals processing engineers, and hydrometallurgists on the status of the project and the findings of other studies on similar ores. Various options were considered and the most viable options compiled in an option study report for future reference. It was the opinion of the group that the most viable option, given the available data, would be a classical flotation plant utilizing a conventional crushing and grinding circuit.

Order-of-magnitude estimate

The process flow sheet recommended in the option study was considered and a capital and operating cost estimate generated.

The procedure required the development of the process engineering deliverables, *i.e.* the process flow diagrams, mass balance, and equipment sizing. Prices for major items of equipment were sourced from selected vendors and the team's database of prices. The direct capital cost of the concentrator was generated through a process of factorization by assuming that the cost of the mechanical equipment would make up 40% of the overall direct capital cost. At the time of compiling the estimate this assumption was proven valid for six similar flotation plants. The operating cost was compiled from first principles utilizing the team's experience and database, and where necessary input from the client project team.

This information was used by the mining engineers as an input to optimize the mine design, which in turn provided a revised input to the metallurgical team for the next stage.

Pre-Feasibility Study

The first set of test work confirmed earlier assumptions and it was decided that a flotation plant would be the most suitable process option. The geological and mineralogical data available at the time of the study indicated the presence of oxidized copper minerals, although the relative amount was negligible. A conventional sulphide copper circuit in a rougher, cleaner, and recleaner configuration was therefore selected for the flotation circuit.

Test work did, however, indicate a benefit for a sulphide rougher concentrate regrind to a P_{80} of 38 µm and this was therefore included in the design.

Various plant circuit configurations were considered with the focus on the comminution and tailings dewatering circuits. A large difference between the rod mill Bond Work index (21 kWh/t) and the ball mill Bond Work index (15 kWh/t) at a limiting screen size of 150 µm indicated the potential for a critical size build-up in a conventional SAG mill. Three scenarios were considered for the milling circuit, namely:

- Conventional three-stage crushing circuit followed by two-stage ball milling
- A conventional SABC circuit with a pebble crusher
- A top-size crusher and a high-pressure grinding roll (HPGR) followed by a conventional ball mill.

A cost analysis was conducted, and although the cost of the first two options were very close the first option was selected as the option of least risk. This would be reconsidered during the next phase of the project.

Given the shortage of water in the region, three options were considered for the processing of the flotation tailings. In each case the mode of tailings deposition was also considered in the generation of the capital and operating cost.

- Belt filtration
- High-density thickened tailing (non-paste)
- Paste thickening.

The cost of belt filtration and the associated material handling requirements for the filter cake eliminated this option. The negligible improvement in water consumption using paste thickening did not justify the high capital and operating cost associated with the pumping of paste. Therefore, high-density thickened tailings with a conventional tailings dam was selected.

The capital and operating costs were generated using a factorized approach as discussed under order-of-magnitude-estimate.

Feasibility Study

A large proportion of the metallurgical test work conducted during the Feasibility Study, concentrated on variability test work and locked cycle test work on the various ore types to confirm and support the assumptions made throughout the previous study. Extensive mineralogical analyses were included, which revealed the presence of varying amounts of oxidized copper minerals (malachite and chrysocolla).

Various alternatives were considered and an oxide flotation circuit employing a sulphidizing agent was then included in the design.

Based on the findings of the test work the comminution circuit in Figure 4 was proposed. The run-of-mine ore is processed through a primary crusher followed by a coarse ore stockpile. Coarse ore from the coarse ore stockpile is processed through a secondary and tertiary crusher circuit and proceeds to a fine ore stockpile ahead of the primary ball mill.

The primary and secondary ball mill discharge are combined in a common cyclone feed sump. The secondary ball mill is in closed circuit with a cyclone producing a cyclone overflow of 55% passing 75 µm.

The cyclone overflow is gravitated to the surge tank/conditioner ahead of the sulphide rougher flotation bank as illustrated in Figure 5. Sulphide rougher concentrate is re-milled to 80% passing 38 µm prior to cleaner flotation. Sulphide recleaner concentrate is thickened prior to filtration. Sulphide cleaner tailings are pumped to the head of the oxide cleaner bank.

The sulphidization agent (NaHS) is added to the sulphide rougher tailing ahead of the oxide rougher bank. The oxide rougher concentrate is not re-milled and is processed in the oxide cleaner and recleaner bank. The oxide recleaner concentrate is thickened prior to filtration.

The oxide rougher tailing is thickened in a high density thickener to 68% solids by mass before being pumped to the tailing dam.

Geometallurgical models

The metallurgical inputs are critical in determining the viability of a new mining venture. The value of this data is important from two aspects:

- Determining the amount of valuable mineral that will be produced as a direct input into the financial model
- Providing inputs in terms of metal recovery and associated costs into the mining plan and financial model in order to optimize the mining plan.

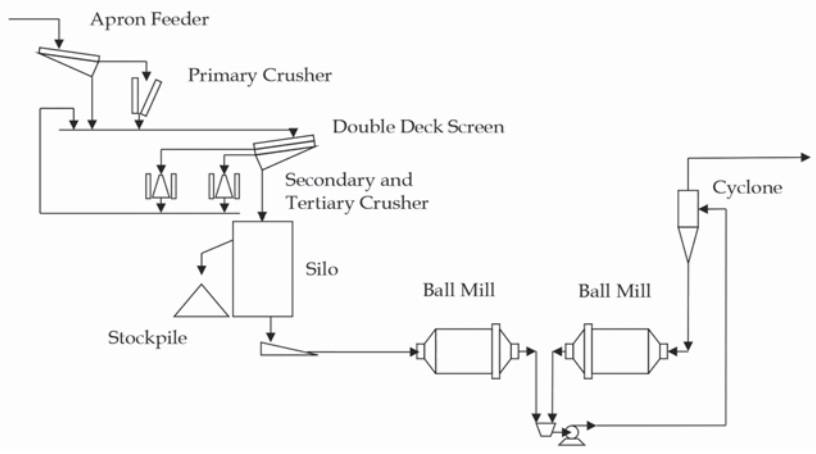

Figure 4—Proposed milling circuit

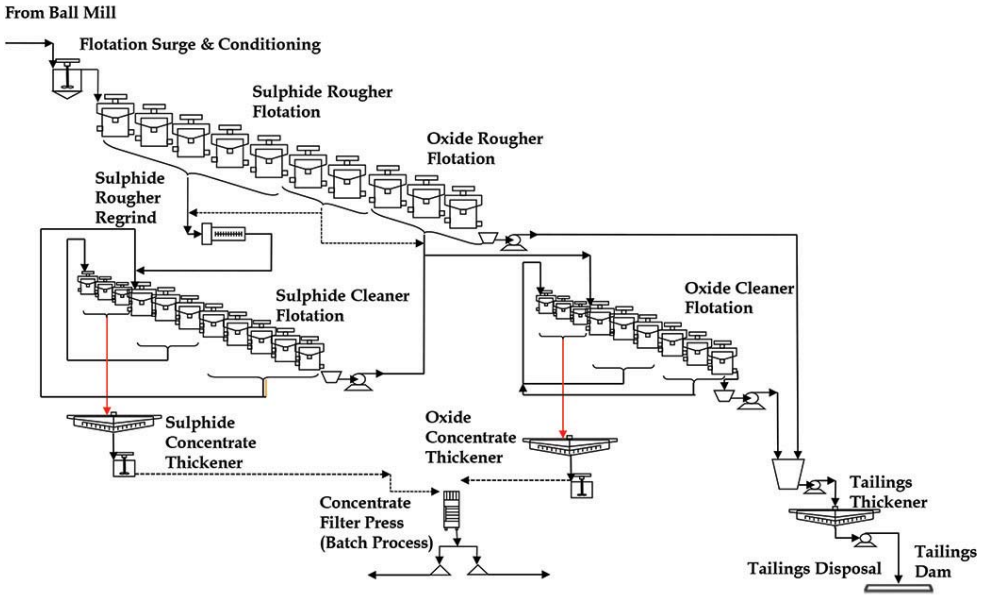

Figure 5—Proposed flotation circuit

In the initial phases of the project, discrete recovery predictions for each mining area, based on the initial batch test work, were used to estimate overall recovery for the mining plan and financial model. As more flotation and mineralogical data became available, a more detailed model forecasting the recovery, concentrate grade, and concentrate tonnage was developed.

Development of the models

A relationship between the sulphur-to-copper ratio and copper recovery became evident from test work on samples from the different zones. It became necessary to further investigate this relationship by conducting tests on individual samples within the range of sulphur-to-copper ratios for these zones (typically between zero and 30%).

The relationship illustrated in Figure 6 was observed and a linear regression of the data generated. It is interesting to note that for the lower sulphur-to-copper ratios the recoveries for Area 2 are significantly higher than the corresponding recoveries for Area 1. This supports the observation that the copper minerals in Area 1 tend to exhibit a higher degree of oxidation compared to Area 2.

A similar relationship was observed between the mass ratio reporting to the sulphide concentrate and the sulphur-to-copper ratio. This relationship was important in determining the overall grade of the concentrate produced.

A comprehensive analysis was done of the sulphide and oxide concentrates for the upper, middle, and lower zones for each mining area. Based on the zone that was being considered in the mining plan, a sulphide concentrate grade and oxide concentrate grade could be derived. This overall concentrate grade could then be calculated from the mass ratio reporting to sulphide or oxide concentrate discussed above.

Concentrate production model

The mining plan compiled by the geologists and mining engineers was used to generate a forecast of the metal production and associated cost. The algorithm derived from the above relationships was included in the mining plan and the financial model, together with the capital and operating costs.

The algorithm can be summarized as follows:

- Calculate the mass of copper recovered to concentrate using the mining head grade and tonnage, and the recovery from the recovery model
- Calculate the fraction of concentrate reporting to the sulphide concentrate using the linear relationship with the sulphur-to-copper ratio
- Apply the copper concentrate grade based on the sulphur-to-copper ratio to determine the grade of the sulphide and the oxide concentrate
- Calculate the masses of sulphide and oxide concentrate produced.

This algorithm was used to predict the copper production and the concentrate grade for the life of mine. The copper production and copper grade for the first 24 months of operation are illustrated in Figure 7.

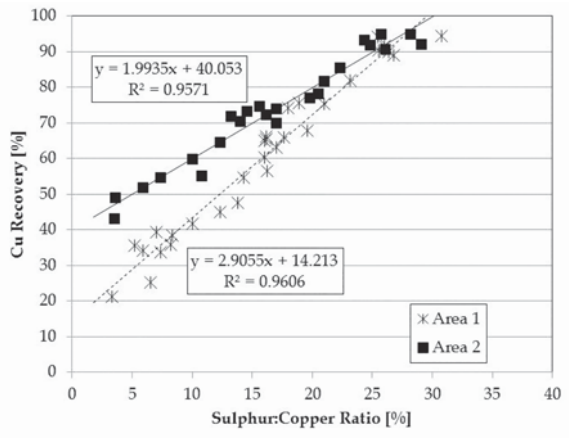

Figure 6—Relationship between Cu recovery and sulphur-to-copper ratio

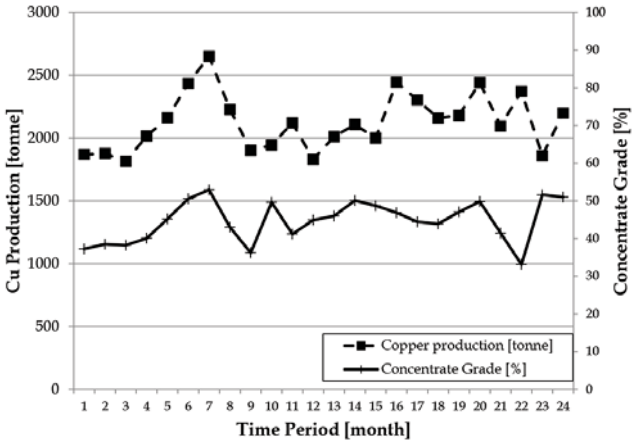

Figure 7—Forecast concentrate grade and production

Use of the metallurgical model in the integrated mining plan yielded an additional 1.2 Mt of mineable ore from an overall 19.5 Mt reserve. This is equivalent to an increase of 6% in the mineable reserves.

Quality of the metallurgical test work

Comparison of assays

Assaying of the drill cores had begun well before the metallurgical test work commenced at Mintek in Randburg, South Africa. As the client was based in Australia, it was decided to submit the geological samples to the Genalysis laboratory in Australia.

A comparison was completed on the head assays for each of the drill core samples for the Mintek assays and the Genalysis assays. Applying the paired t-test analysis confirmed that the two data-sets were not significantly different at a 95% confidence level. This finding was significant as it indicated that the model developed using the Mintek analyses could be applied to the mining model developed in Australia using results from Genalysis.

Quality of flotation test work

A number of routine checks were completed to determine the quality of the flotation test work, *e.g.* comparison of the reconstituted head grades and the assayed head grades of the samples for the various flotation tests as illustrated in Figure 8. The paired t-test analysis of the two data-sets found that there was no significant difference at a 95% confidence level.

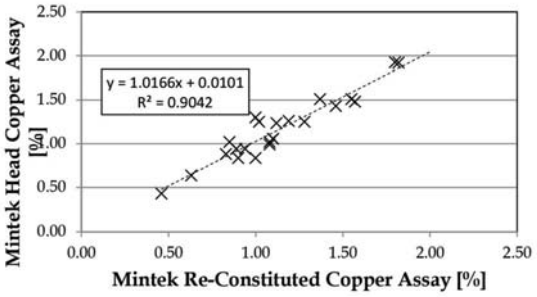

Figure 8—Comparison between Mintek and Genalysis assays

Conclusions

The mineralogy of the Kalahari Copper Belt is interesting and presents challenges, particularly in the recovery of copper in the form of copper oxides, where recoveries can be as low as 30%. Further fundamental test work needs to be completed to identify more efficient means of recovering the copper, particularly in the presence of high acid-consuming species.

Detailed mineralogical analysis prior to and during the metallurgical test work added a significant amount of value in that it allowed the metallurgists to relate the results of the test work to the mineralogical observations. Furthermore, the mode of occurrence of the copper lost to tailings could be identified and addressed in the process design.

Variability test work proved to be critical in accurately defining the metallurgical characteristics of the deposit, thereby ensuring that ore variability was recognized in the mining plan.

Cooperation and regular communication between the various disciplines on the project proved to be critical in ensuring the success of the project and minimizing the risk to the client. As illustrated in this case study, the combination of the discipline models resulted in ore previously classified as 'uneconomical' being reclassified and deemed mineable, making the project a more viable proposition.

References

Hall, W.S. 2012. Geology and paragenesis of the Boseto copper deposits, Kalahari Copper Belt, North West Botswana. MS thesis, Colorado School of Mines.

Kongolo, K., Kipok,a M., Minanga, K., and Mpoyo, M. 2003. Improving efficiency of oxide-cobalt ores flotation by combination of sulphidisers. *Minerals Engineering*, vol. 16. pp. 1023–1026.

Newell, A.J., Skinner, W.M., and Bradshaw, D.J. 2006. Restoring the floatability of oxidized sulfides using sulfidisation. *International Journal of Mineral Processing*, vol. 84. pp. 98–107.

Raghavan S., Adamec E., and Lee L. 1984. Sulfidisation and flotation of chrysocolla and brochantite. *International Journal of Mineral Processing*, vol. 12. pp. 173–191. ◆

First choice for the sand and aggregate industry

We supply:
Trio® crushers
Trio® vibrating screens
Enduron® vibrating screens
Trio® feeders
Trio® washers
Trio® conveyors

Contact us on +27 (0)11 9292600 for more information.

Minerals
weirminerals.com

http://dx.doi.org/10.17159/2411-9717/2016/v116n6a9

Ivanhoe Mines' giant Kamoa copper discovery in the DRC – a metallurgical perspective

by V.L. Nkuna*, T. Naidoo*, and S.R. Amos*

Synopsis

Ivanhoe Mines' Kamoa copper project is a recently discovered high-grade copper sulphide deposit in the Katanga Province of the Democratic Republic of Congo. The mineralization identified to date within the resource is typical of sedimentary-hosted stratiform copper deposits and comprises three distinct units: supergene, mixed, and hypogene mineralization. Since 2010, various metallurgical test work campaigns have been conducted on drill core from different areas within the deposit in line with resource expansion. The most recent bench-scale flotation test work has shown positive repeatable results. The work was conducted on a composite sample of drill core from the southern part of the Kamoa resource. The sample is representative of the first four to five years of planned production, when Ivanhoe Mines intends to produce clean, high-grade copper flotation concentrate. A detailed test work roadmap developed from first principles for the campaign led to an optimum flow sheet for treating the Kamoa mineralization. Copper recoveries of 88.3%, at a concentrate grade of 39.0% copper, were achieved using a composite sample — an improvement on the previously published 85.9% life-of-mine average copper recovery indicated in the November 2013 Kamoa Preliminary Economic Assessment.

Keywords

Kamoa copper project, copper, sulphide, mineralogy, mill-float, hypogene, supergene, circuit development, integrated flow sheet, copper recovery, fine grained, bornite, chalcopyrite, chalcocite.

Introduction

The Kamoa project is a newly discovered, very large, stratiform copper deposit with adjacent prospective exploration areas within the Central African Copperbelt, approximately 25 km west of the town of Kolwezi in the Democratic Republic of the Congo (DRC) and about 270 kilometres west of the provincial capital of Lubumbashi. Ivanhoe Mines holds its 95% interest in the Kamoa copper project through a subsidiary company, Kamoa Copper SA Limited SPRL, and DRC government owns 5%. The project location is indicated in Figure 1.

In January 2013, a new independent mineral resource estimate ranked Kamoa as Africa's largest high-grade copper discovery and the world's largest undeveloped high-grade copper discovery. At this time, Ivanhoe Mines had estimated discovered Indicated Mineral Resources of 739 Mt grading 2.67% copper, containing 43.5 billion pounds of copper, and Inferred Mineral Resources of 227 Mt grading 1.96% copper, containing 9.8 billion pounds of copper, as demonstrated in the Preliminary Economic Assessment (PEA) (AMC, 2013). A 1% copper cut-off grade and a minimum vertical mining thickness of 3 m were applied in each classification.

The project execution is planned in two phases, the first phase being a 3 Mt/a mine and concentrator producing approximately 100 000 t/a copper in concentrate for sale, while the second includes a mine and concentrator expansion and the construction of a smelter producing approximately 300 000 t/a of blister copper.

A series of metallurgical test work campaigns (comminution and flotation) on the Kamoa mineralization has been carried out since 2010 using drill cores from different areas within the deposit in line with the resource development and expansion. Figure 2 represents a grade-thickness map of the Kamoa resource with the underground mining areas included; grade-thickness refers to copper grade in per cent multiplied by the thickness of the mineralization in metres.

The Kamoa deposit differs from other copper deposits in the DRC as it is predominately a copper sulphide deposit with negligible cobalt and copper oxide mineralization. The copper sulphide mineralization consists predominantly of bornite (Cu_5FeS_4), chalcopyrite ($CuFeS_2$), and chalcocite (Cu_2S). The copper minerals are fine-grained with average grain sizes ranging from 6 μm to 14 μm. The flow sheet development incorporates finer than normal primary grind targets and extensive re-grinding in order to

* *Ivanhoe Mines, Johannesburg, South Africa.*
 ISSN 2225-6253. This paper was first presented at the, Copper Cobalt Africa Conference, *6–8 July 2015, Avani Victoria Falls Hotel, Victoria Falls, Livingstone, Zambia.*

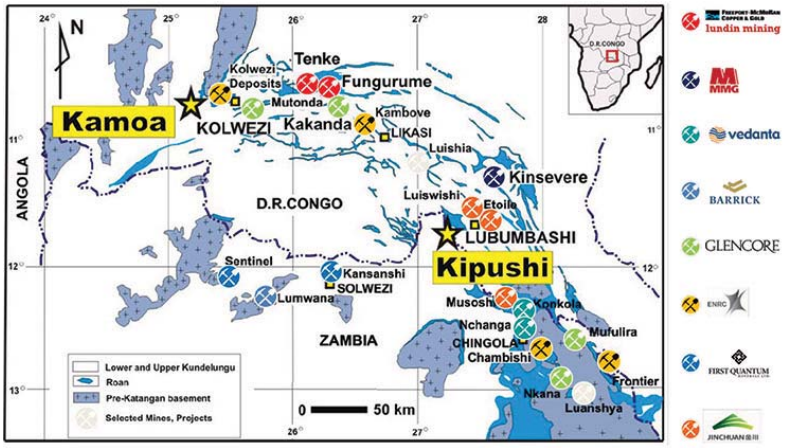

Figure 1—Locality of the Kamoa copper project

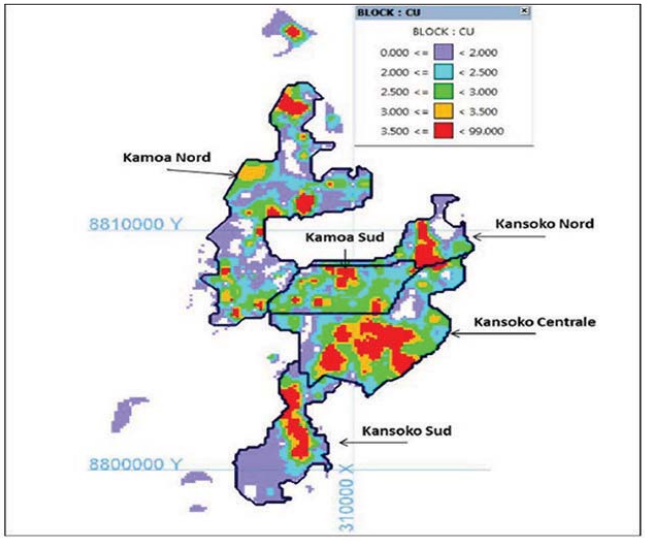

Figure 2—Resource map

sufficiently liberate the copper sulphide minerals and achieve acceptable copper recoveries and concentrate grades. The flow sheet development, based on first principles, resulted in a mill-float (MF1) circuit which yielded positive results, with copper recoveries of 88.3% at a concentrate grade of 39.0% copper. The concentrate produced is generally low-energy with Fe/SiO_2 ratios in the region of 1.1 and is suitable for processing using the Outotec Direct to Blister technology or blending with higher Fe/SiO_2 concentrates. The concentrate contains very low arsenic levels of around 0.01%, which makes it suitable for toll smelting.

Metallurgical test work background

A total of six test work phases have been completed to date on mineralized material from the Kamoa deposit. All test work was conducted at the Mintek laboratory in Johannesburg and the Xstrata Process Support (XPS) Laboratory in Sudbury, Ontario.

The previously developed mill-float mill-float (MF2) circuit achieved good performance, as reported in Table I. The circuit was developed to partially liberate the coarse copper sulphide minerals at 80% passing 75 μm and subject the material to primary rougher flotation. The primary rougher tailings were milled in a secondary ball mill to a finer grind of 80% passing 38 μm. The secondary mill product was then floated in the secondary rougher flotation. Further regrinding of primary and secondary rougher concentrate to 15 and 10 μm, respectively was required to liberate copper-bearing minerals to achieve the desired copper concentrate grade. This circuit, known as the 'Frozen Flowsheet', became the benchmark and was published in the 2013 PEA.

Phase 6 circuit development

With the development of the mine production schedule published in the November 2013 PEA, high-grade, shallow copper areas that had been discovered further south in the resource were targeted for early production. A sampling campaign was carried out in line with the new developments to include the high-grade Kansoko Sud and Kamoa Centrale areas, which represent the initial mining areas.

Table I

Phase 2 flotation results

Ore type	Cu feed (%)	Mass pull (%)	Cu recovery (%)	Cu grade (%)	SiO_2 grade (%)	Fe grade (%)	S grade (%)	As grade (%)
Phase 2 supergene	3.73	6.9	83.2	45.1	26.0	5.02	9.25	
Phase 2 hypogene	3.31	7.7	86.7	37	13.1	18.3	24.6	0.005

The test work was separated into two phases.

- Phase 6A – A master composite sample (23% supergene and 77% hypogene) and reference supergene and hypogene representing the first four years of mining and two preproduction years was tested. Kansoko Sud and Kansoko Centrale are predominantly mined during this time. This phase of the project assumes the sale of copper concentrate to a third-party smelter and represents the project payback period
- Phase 6B – This composite sample represents years 5 to 15 of mining and involves owner-smelting. Kansoko Centrale. Kamoa Sud. and Kansoko Sud are predominantly mined during this time. Reference supergene and hypogene samples were also composited from these areas.

Material from the different areas could potentially be metallurgically different and it is thus important to characterize and test both composite samples. The majority of this paper is assigned to the flow sheet development associated with the Phase 6 sample.

Flotation test work sample selection and composition

Intersections from 16 drill core wedges (8 for Phase 6A and 8 for Phase 6B) were selected and sent to XPS for the Phase 6 test work programme. Samples were selected incorporating the following criteria:

- The average copper head grade from the mine schedule
- The average ratio of hypogene to supergene
- The required mining cut
- Spatial considerations to cover specific mining zones
- The average mass ratio from the various mining areas.

Feed mineralogy

Mineralogical investigations were conducted on the Phase 6A and 6B composite samples, together with their respective hypogene and supergene reference composite samples. Test charges of 2 kg were milled to a product *P*80 size of 212 μm and prepared for mineralogical investigations, *i.e.* bulk mineralogy, copper deportment and association, as well as *in situ* grain size.

The Phase 6A and 6B composite bulk mineralogy was found to be similar to previous metallurgical samples from Phases 2, 3, and 5, with feldspar, mica, quartz, and chlorite being the dominant gangue minerals.

The copper deportment analysis indicated that the major copper minerals present in the Phase 6A master composite were bornite (38%), chalcopyrite (29%), and chalcocite (20%), with minor amounts of covellite (6%) and copper oxides with some native copper (3%). For the Phase 6B composite, the major copper minerals were chalcopyrite (41%), bornite (38%), and chalcocite (16%), with minor amounts of covellite (0.8%) and copper oxides with some native copper (0.6%).

In situ grain size distributions were measured at a feed grind size *P*80 of 212 μm and indicate a combined copper sulphide *P*80 of approximately 50 μm for both the 6A and 6B master composites. Chalcopyrite tends to be coarser grained, while bornite and chalcocite are finer grained.

MF1 versus MF2 circuit

Two sets of MF2 flotation tests using the Phase 6A sample with grinds set at 75/38 μm and 106/38 μm, respectively, were performed and results compared to the MF1 rougher kinetic test with the primary grind set at 38 μm (Figure 3).

The MF1 test resulted in superior performance compared with the MF2 tests for both copper recovery and grade, at a lower mass pull. The MF1 circuit was thus carried through to the cleaner circuit development, with no further development of the MF2 circuit.

Rougher kinetics on Phase 6 composites

Rougher rate tests were performed on the Phase 6A master composite at various primary *P*80 grind sizes; *viz.*, 150, 106, 75, 53, and 38 μm at up to 40 minutes' rougher flotation time. The results are summarized in Figure 4.

There is a clear benefit in grinding finer with respect to the grade and recovery of the rougher concentrate. Overall recoveries from the MF1 platform ranged from 82.9% for the 150 μm grind to 92.7% for the 38 μm grind.

On the basis of the MF1 results, the 38 and 53 μm tests were selected for further development. The concentrate and tailings samples were analysed using Quantitative Evaluation of Minerals by Scanning Electron Microscopy (QEMSCAN) to inform the cleaner circuit development. Rougher kinetics tests were also performed on the 6B composite, which similarly indicated a clear benefit in grinding finer with respect to the copper grade and recovery to rougher concentrate.

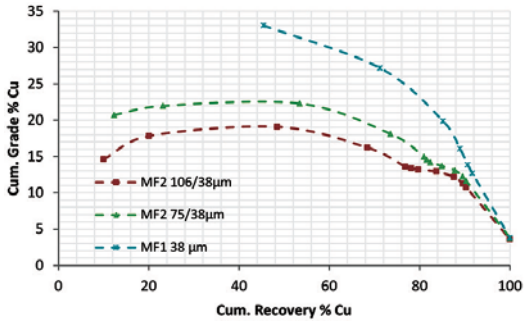

Figure 3—MF1 and MF2 grade-recovery curve for Phase 6A master composite (6A MC)

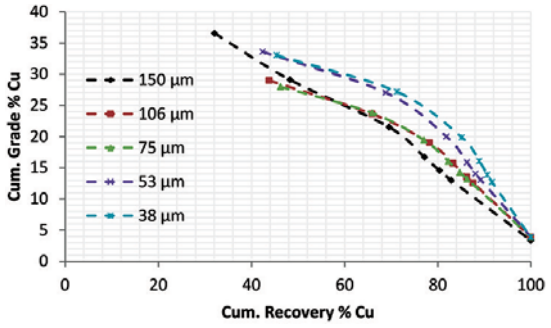

Figure 4—Rougher rate grade-recovery curves for Phase 6A master composite

Rougher concentrate and tailings mineralogy

Mineralogical test work was performed on timed rougher concentrates (five samples taken at different intervals) and tailings from the Phase 6A master composite (38 and 53 µm grinds) and also the Phase 6B master composite (38 µm grind) to determine copper mineral liberation, grain size, and silica association.

The liberation distribution of copper sulphides with respect to total copper sulphides in the feed indicated that, regardless of primary grind for both composites, almost all liberated material had floated after approximately 10 minutes (R1 to R3 in Figure 6). The implication of this is that a portion of this rougher concentrate could report directly to final concentrate and achieve saleable concentrate grades. This is referred to as the 'high-grade flash cleaner circuit'.

Mineralogy results (XPS, 2014a) demonstrated that from approximately 10 minutes onwards, there is a switch from liberated sulphide flotation to middlings sulphide flotation (R4 to R6 in Figure 5). These concentrates require fine re-grinding to liberate the copper sulphides and reduce gangue, mainly silica, content in final concentrate.

The rougher tailings mineralogy for the different primary grind tests consistently indicates that locked copper sulphides are present in the coarse size fraction, as shown in Figure 6. This highlighted an opportunity in that the rougher tailings could be scalped/screened and the coarse fraction re-ground and re-floated.

The class sizes used in Figure 6 are illustrated in Table II.

Cleaner circuit development

Based on mineralogical results from the Phase 6A timed rougher concentrates and tailings, cleaner circuit development was carried out on both the 53 µm and 38 µm grinds in the three areas detailed below:

- High-grade flash cleaners. This section upgrades the fast-floating high-grade rougher concentrate collected during the first few minutes of rougher flotation into saleable concentrate and bypasses the concentrate re-grind circuit. A 5- to 7-minute rougher concentrate was upgraded in two cleaning stages and consistently achieved copper recoveries of between 65% and 75% at copper grades above 36% for both primary grinds (38 and 53 µm)
- Medium-grade cleaners. This section treats the subsequent partially liberated middlings rougher concentrate and recycled high-grade cleaner tailings. The circuit consists of a concentrate re-grind to further liberate the copper sulphides locked in gangue minerals to a *P*80 of between 10 µm and 15 µm prior to a dedicated cleaner flotation circuit to produce increments of saleable concentrate. Cleaner kinetics were also investigated to determine the optimum residence time with minimal gangue recovery
- Tailings scalp circuit. The relatively high-grade coarse size fraction of the tailings was treated by scalping and re-grinding prior to flotation. This achieved between 3% and 5% additional copper recovery to saleable concentrate, depending on the primary grind.

The inclusion of the tailings scalping circuit was further investigated and a number of integrated flow sheet configurations were successfully tested for both the 53 µm and 38 µm primary grinds. These flow sheets are discussed below.

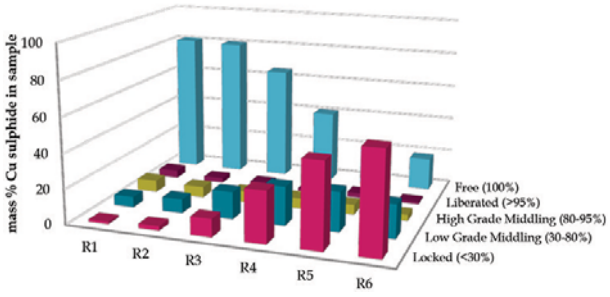

Figure 5—Phase 6A master composite combined Cu sulphide liberation (surface area %)

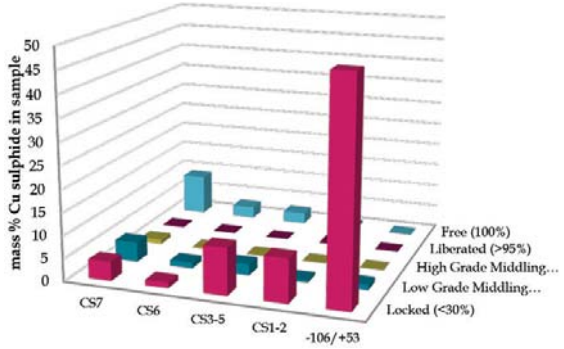

Figure 6—Phase 6A MC kinetic test 53 µm rougher tail combined Cu sulphide liberation (surface area %)

Table II

Class sizes definition table

Description	CS7	CS6	CS3-5	CS1-2	-106/+53
Minimum size (µm)	0	3	8	20	53
Maximum size (µm)	3	10	25	53	106
Average particle size (µm)	2	5	14	29	55

Integrated flow sheet 1 (IFS 1)

This circuit configuration is an MF1 platform with a mainstream target grind of 38 μm. Milled slurry is subjected to the 40-minute rougher flotation residence time; high-grade (HG), or fast-floating and medium-grade (MG), or slower floating concentrates are collected separately. HG rougher concentrate is upgraded in two HG cleaning stages without further re-grinding to produce a HG increment to final concentrate. The MG rougher concentrate is combined with the HG cleaner tailings and re-ground to a *P*80 of 15 μm before being cleaned in two stages. Rougher tailings are scalped and the oversize (+38 μm) is re-ground to a *P*80 size of 15 μm, and then scavenged in a 5-minute float to produce a discard tail and a scavenger concentrates. The latter is re-treated in the MG re-cleaner bank together with the MG cleaner concentrate.

Integrated Flow sheet 2 (IFS 2)

The IFS 2 is identical to the IFS 1 circuit, with the exception that the MG rougher concentrate and HG cleaner tails are combined with scalped tailings oversize as feed to the re-grind mill.

Integrated Flow sheet 3 (IFS 3)

This circuit is the same as IFS 1, with the exception being that the primary grind is 53 μm.

Integrated Flow sheet 4 (IFS 4)

This circuit is the same as IFS 2, with the exception being that the primary grind is 53 μm.

Integrated Flow sheet 5 (IFS 5)

The circuit configuration is an MF1 platform with a mainstream target grind of 53 μm. Milled slurry is subjected to the 40-minute rougher flotation residence time; high-grade (HG), or fast-floating and medium-grade (MG), or slower floating concentrates are collected separately. HG rougher concentrate is upgraded in two HG cleaning stages without further re-grinding to produce a HG increment to final concentrate. The MG rougher concentrate is re-ground to a *P*80 of 10 μm before being cleaned in two stages. Rougher tailings are scalped and the oversize (+53 μm) is combined with the MG rougher concentrate and re-ground to a *P*80 of 15 μm. It is then cleaned in two stages with the MG rougher concentrate.

The grade-recovery curve comparison for these flow sheets is presented in Figure 7.

From Figure 7, it is clear that IFS 2 and IFS 4 perform the best. IFS 4 achieved the best results at 88.3% copper recovery and 39% copper concentrate grade. Upon further investigation of the results from IFS 4 and IFS 2, it was determined that the re-grind mill produced a *P*80 of 12 and 10 μm, respectively, *i.e.*, finer than the target size of 15 μm. This finer grind translates to better liberation, which improved the MG cleaner flotation performance. Based on these results, it was concluded that a target re-grind *P*80 of 10 μm was required to improve the copper grade for improved transport costs.

A mainstream target grind of 38 μm (IFS 2) was deemed risky compared to a target grind of 53 μm (IFS 4). An alternative technology to ball milling is required to achieve the finer grind, *viz.*, tower mills. Thus, IFS 4 in Figure 8 was selected as the preferred circuit as it was deemed a lower risk circuit and produced marginally better performance than IFS 2.

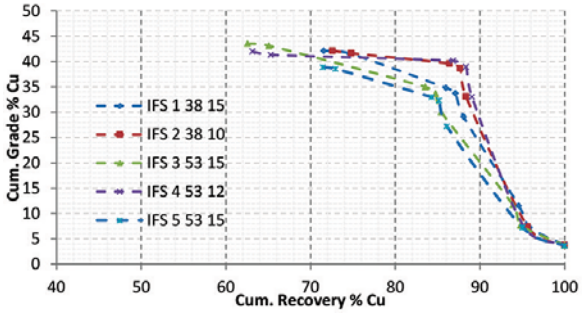

Figure 7—Comparison of Phase 6A integrated flow sheet grade-recovery curves (XPS, 2014b

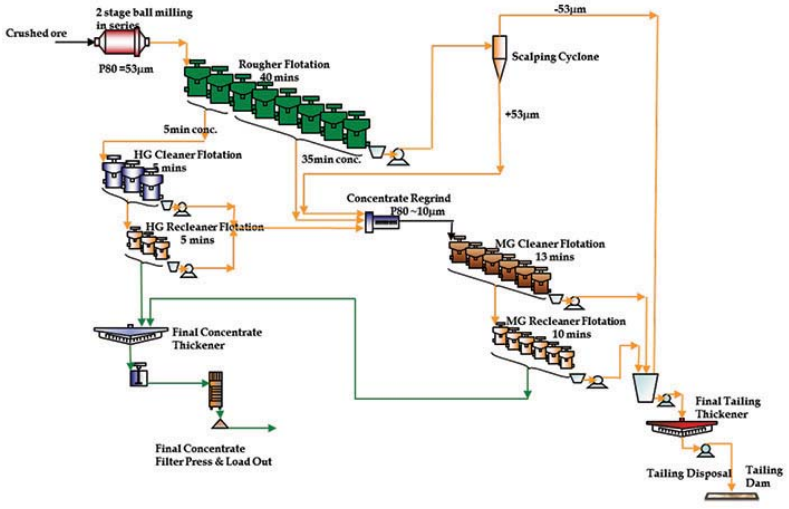

Figure 8—Phase 6 integrated flow sheet (IFS 4)

Further tests were conducted with the IFS 4 flow sheet with a target grind of 10 μm, which provided similar results, indicating that the results are repeatable.

Baseline flotation test (Phase 2 'Frozen Flowsheet')

Phase 6A development master composite was tested with the published PEA MF2 'Frozen Flowsheet'. The result is compared with the Phase 6 integrated IFS 4 circuit in Figure 9.

The 6A development composite achieved 88.3% copper recovery at a concentrate grade of 39.0% copper using the integrated Phase 6 flow sheet, an improvement from 85.9% copper recovery and 30.0% copper grade from the 'Frozen Flowsheet'. The 6B development composite (not shown) achieved 92.3% copper recovery at a concentrate grade of 37.0% copper through the integrated Phase 6 flow sheet, an improvement from 89.7% copper recovery and 27.5% Cu concentrate grade through the 'Frozen Flowsheet'. The Phase 6 integrated circuit, IFS 4, achieved superior results for both composites compared with the 'Frozen Flowsheet' circuit.

Preliminary variability

Preliminary variability flotation tests on the Phase 6 hypogene and supergene composites, representing up to year 15 of the PEA mine production schedule, have been conducted using the Phase 6 'integrated flow sheet', IFS 4 (10 μm target re-grind). The results in Table III indicate that the copper recoveries and concentrate grades are in line with the copper feed mineralogical compositions for each composite.

This illustrates that the IFS 4 (10 μm) flow sheet developed using the 6A master composite is suitable for treating the various composites up to year 15 of the PEA mine production schedule. Possibly, blending of supergene and hypogene may be required to achieve a concentrate specification for offtake agreements.

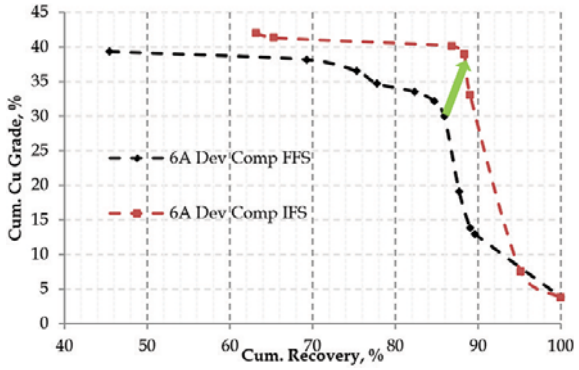

Figure 9—Grade-recovery curve comparison of the PEA FFS and Phase 6 IFS4 results of 6A MC

Conclusions

A viable circuit has been developed for the Kamoa resource to successfully treat composites representing different project phases (payback period and up to 15 years of mine life) and the different mineralization; *i.e.*, hypogene and supergene composites. The IFS 4 circuit developed with 6A master composite has proven suitable for treating the various composites and individual geometallurgical units. The Kamoa copper minerals are finely grained, hence the flow sheet development incorporated finer than typical primary grinding to a mainstream product size *P*80 of 53 μm and intensive re-grinding to a target size *P*80 of 10 μm to sufficiently liberate the copper sulphide minerals and achieve optimal copper recoveries and concentrate grade. The integration of the coarse copper-containing tailings fraction provided an additional recovery benefit of 3 to 5% Cu.

Acknowledgements

The authors would like to thank the senior management at Ivanhoe Mines for permission to publish this work. We sincerely thank Dr N.O. Lotter and the team at Xstrata Process Support for the diligent work and input throughout the test work campaigns. We also thank Mintek's team for the contribution to the comminution and flotation test work. Their efforts, interpretations, and input are highly appreciated.

References

AMC Consultants Pty Ltd. 2013. Kamoa Preliminary Economic Assessment.

XPS. 2014a. Rougher kinetic flotation tests: Phase 6A1 development composite. Internal report from XPS to Ivanhoe Mines, 15 May 2014.

XPS. 2014b. Kamoa Phase 6 flow sheet development composite. Internal report from XPS to Ivanhoe Mines, 14 November 2014. ◆

Table III

Summary of saleable concentrate produced by IFS 4 with a 10 μm regrind size

Sample	Head grade (% Cu)	Mass pull (%)	Copper		Cu sulphide recovery (%)	S grade (%)	Fe grade (%)	SiO_2 grade (%)	Fe:SiO_2	Dominant CuS mineral
			Grade (%)	Rec. (%)						
6AMC	3.67	8.53	39.0	88.3	94.4	24.8	16.3	14.6	1.12	Bornite
6A hypogene	3.57	8.98	35.7	89.9	92.6	31.7	23.4	4.92	4.76	Chalcopyrite
6A supergene	3.68	5.62	48.5	75.3	91.6	16.7	8.47	14.51	0.58	Chalcocite
6B MC	3.27	8.13	37.0	92.3	96.8	29.2	22.7	7.62	2.98	Chalcopyrite
6B hypogene	2.99	6.29	44.5	91.9	96.0	25.2	15.4	10.6	1.45	Bornite
6B supergene	3.87	5.96	46.6	69.4	>100	18.4	10.6	15.8	0.67	Chalcocite

http://dx.doi.org/10.17159/2411-9717/2016/v116n6a10

Copper solvent extraction: status, operating practices, and challenges in the African Copperbelt

by K.C. Sole* and O.S. Tinkler†

Synopsis

Although the first large-scale application of copper recovery by solvent extraction took place in Zambia in the early 1970s, it is only in the last decade that this technology has become widely employed in this part of the world and is now a mainstay unit operation in copper hydrometallurgical flow sheets. The mineralogy of the ores of the African Copperbelt, and hence the characteristics of African leach liquors, differs significantly from those in Chile and the southwestern USA, where copper solvent extraction has had a long and successful history. These differences provide operators, metallurgists, reagent vendors, and engineers with many challenges: new approaches are needed to adapt solvent-extraction technology for successful implementation in this region. This paper examines typical operating practice in the African Copperbelt, discusses differences compared with other parts of the world, and looks at some of the challenges and opportunities presented by these flow sheets.

Keywords
copper, solvent extraction, African Copperbelt, operations, review.

Introduction

Following the success of the Rancher's Bluebird and Bagdad solvent extraction and electrowinning (SX–EW) operations in Arizona in the late 1960s, the Tailings Leach Plant at Chingola, Zambia, became the first large-scale copper SX plant in the world, commissioned in 1974. Despite the equipment design now being outdated, this plant still continues to operate successfully, indicating the versatility and adaptability of this technology. Today, there are some 75 copper SX operations worldwide with cathode production above 10 kt/a. The top ten producers currently account for about 40% of the global 4.3 Mt/a SX–EW copper production. South America (predominantly Chile and Peru) is the largest copper cathode-producing region, with annual production of some 2 Mt. The Central African Copperbelt (Zambia and the Democratic Republic of Congo (DRC)) is second, with cathode production of 1.2 Mt/a, and North America (USA and Mexico) third, producing close to 0.8 Mt/a Cu (Solvay Cytec data, 2014). The remaining 0.35 Mt/a comes from all other regions combined (referred to as 'Rest-of-World').

Current operations in Zambia and the DRC are summarized in Figure 1. The industry in this region is characterized by a few very large (>200 kt/a) operations, owned by major multinational corporations, and a large number of small (3 to 20 kt/a) plants, mainly Chinese-owned.

This paper examines typical SX operating practice in the African Copperbelt, discusses differences compared with other parts of the world, and looks at some of the challenges presented by the conditions, as well as innovations in flow sheets, reagents, and operating conditions that have been introduced in these circuits.

Copper SX: a truly adaptable process

Distinct characteristics emerge when one examines copper SX on a regional basis. Table I compares characteristics of the pregnant leach solutions (PLS) in Central Africa with those of North America, South America, and other parts of the world where copper SX is practiced. The nature of the PLS varies considerably (0.23 to 43 g/L Cu), depending largely on the type of process and geographic location (Sole *et al.*, 2013). The versatility of this technology is indicated by its ability to cope with large variations in copper grade as well as selectively recover copper from widely varying PLS compositions. Extreme examples include Mexicana de Cananea (Mexico), which processes a feed containing 2 g/L Cu and 45 g/L Fe, and Cobre Las Cruces (Spain), which recovers >40 g/L Cu from a PLS background of >50 g/L Fe.

Copper grades are typically lowest in the southwestern USA, where the industry is mature and many operations have been in production since the mid-1980s. The ores are mainly lower-grade mixed oxide and

* *Consulting Hydrometallurgist, Johannesburg, South Africa.*
† *Cytec Solvay Group, Tempe, AZ, USA.*

 ISSN 2225-6253. This paper was first presented at the, Copper Cobalt Africa Conference, *6–8 July 2015, Avani Victoria Falls Hotel, Victoria Falls, Livingstone, Zambia.*

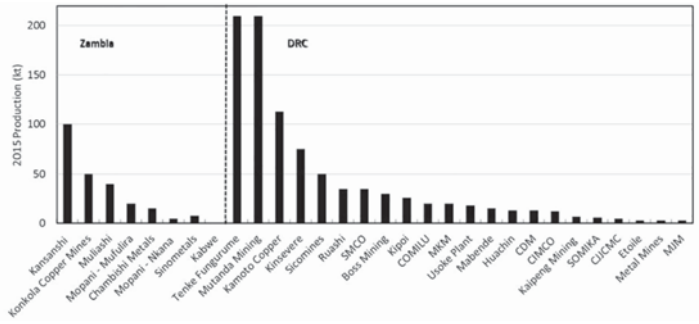

Figure 1—2015 production of operating copper SX–EW plants in the Copperbelt

Table I

Variation of average PLS composition with location

Location	Cu (g/L)	pH	Fe (g/L)	Mn (g/L)	Co (g/L)	Cl (mg/L)	TSS (mg/L)
North America	0.3–3	1.5–2.5	3–45	1–3	—	70	30
South America	1.0–6.5	1.1–2.5	0.3–31	0.3–12	0.06	870	44
Africa	3.0–43	1.5–2	3.4	0.9	6.7	—	137
Rest-of-World	1.0–40	1.0–2.5	—	—	—	—	—

secondary sulphide, containing 0.2 to 0.3% acid-soluble copper. The operations are typically heap and dump leaching, with permanent pads (rather than on–off pads) to minimize operational costs. The SX circuits are often configured for series–parallel or all-parallel operation, as this maximizes copper production by treating high volumes of low-grade PLS. At most sites, the high PLS flow rates give extraction organic-to-aqueous (O:A) flow rate ratios well below 1:1, so extraction stages operate in aqueous-phase continuity—a feature that is unusual in other parts of the world. These operations are characterized by efforts to minimize operating costs and extend the profitable life of mine for as long as possible. There is an emphasis on minimizing organic losses and maximizing organic recovery (*e.g.*, by increased retention time in the raffinate pond and use of equipment such as Pacesetter coalescers, Jameson cells, and pond skimmers).

Chilean operations process mainly oxides with an acid-soluble copper grade of 0.4 to 0.8%. Many of these are located in the Atacama Desert, where the predominant mineral, atacamite ($Cu_2Cl(OH)_3$), gives levels of chloride in the PLS as high as 40 g/L. The presence of >30 mg/L Cl is detrimental to copper EW (Lakshmanan *et al.*, 1977), so SX circuits usually have a wash stage to limit chloride transfer to the electrolyte. Several sites also have high levels of nitrates in the PLS. Nitrate is a strong oxidizing agent, which presents severe challenges associated with accelerated reagent degradation. Processing is mainly by heap, dump, and run-of-mine (ROM) leaching. An acid cure is common to increase leach recovery. Heap leaching of primary and secondary sulphides is becoming more common; primary sulphides frequently give elevated levels of Fe in the PLS so reagent selectivity is particularly important.

The majority of Australian leach–SX–EW operations have come to the end of their operating lives, so the Rest-of-World region is now characterized by expansion in countries such as Laos, Myanmar, Kazakhstan, and China. Olympic Dam, one of the last remaining Australian operations, has complex metallurgy (copper is produced as a byproduct of uranium) and a life-of-mine of at least 200 years (Russell, 2014). The Rest-of-World locations are often very remote, with difficult logistics. Some of the flow sheets are complex, comprising pressure leaching as well as agitated tank leaching, and there is a wide variation in the types of leach solutions that are processed by SX.

The African operations have the advantage of high ore grades (3 to 5% acid-soluble Cu), and consequently significantly higher PLS copper grades than found in other regions (43 g/L Cu design at Kamoto Copper Company, for example). Although the predominant oxide minerals, such as malachite, chrysocolla, and heterogenite, are easily leachable, acid consumption varies considerably from site to site and even within orebodies—in some cases, rendering even high-grade orebodies uneconomical. After crushing and grinding, leaching is usually carried out at slightly elevated temperature (35 to 45°C) in agitated tanks, which results in dissolution of almost all the acid-soluble copper in a matter of hours, rather than months or even years in the case of heap leaching. The feed to leaching can be whole ore, oxide concentrates, roasted sulphide concentrates, or tailings.

An additional feature of DRC operations is that the orebodies often contain significant quantities of cobalt, usually produced as an intermediate cobalt hydroxide product that is further refined in Europe or China. A few operations produce cobalt cathode after solution purification. Logistics in this region remain very difficult, with most reagents having to be transported by road from South Africa, Namibia, or Tanzania. Many sites have therefore installed sulphur-burning plants to produce their own sulphuric acid on site from elemental sulphur.

It is evident from the above discussion that copper SX is practiced very differently in different parts of the world and that each region has its own unique challenges that require innovation and adaptability to ensure the consistent and profitable production of high-quality copper cathode.

Copper solvent extraction: status, operating practices, and challenges

The copper SX–EW landscape in Central Africa

Zambia

The first large-scale copper SX plant in the world was commissioned at the Nchanga Tailings Leach Plant (TLP) in Zambia in 1974, with a daily production of 200 t Cu cathode (Holmes *et al.*, 1976). The mixer–settlers, configured as four trains each comprising three extraction and two stripping (3E–2S) stages, are long and narrow (aspect ratio of 2.9:1) and the mixers have a design residence time of 3 minutes. Given the constraints of the extractants at the time that TLP was designed, multiple stages of extraction and stripping were necessary to achieve the desired copper recovery. With advances in equipment design and extractant formulations, the largest modern-day mixer–settlers could process about 85% of the TLP's total PLS flow in a *single* 2E–1S circuit!

Largely unknown in the history of African metallurgy is that the first aldoxime reagents (the ACORGA P-5000 Series) were developed by ACORGA Ltd, which was a joint venture between Anglo American Corporation of South Africa and the UK's Imperial Chemicals Industries (ICI) (a forerunner of what is today the multinational company, Cytec Solvay) (Tumilty *et al.*, 1977). The first commercial aldoxime extractants were produced for use in copper SX and exhibited many advantages in extracting power, kinetics, and selectivity over then-existing reagents. Although extractant chemistry, stability, and performance have improved significantly since that time, aldoximes (with a stripping modifier) still form the basis of some 66% of copper cathode production today.

Development of the industry and current operations

Located 10 km from Ndola, the Bwana Mkubwa SX–EW plant (BMML) was established by First Quantum Minerals (FQM) in 1998 to process oxide tailings from dams in the area. In 2003, the plant was redesigned and expanded to process oxide ore from the Lonshi deposit, located some 35 km away in the DRC. At its peak in 2005, BMML produced just under 50 kt cathode (FQM, 2006). First Quantum halted operations at BMML between 2008 and 2010 and reopened for about a year in 2010. Although this plant no longer operates, it provided a pioneering example to the industry of how rapidly, inexpensively, and simply copper SX flow sheets could be installed and run profitably.

Kansanshi Mine, 80% owned by FQM subsidiary Kansanshi Mining plc, reached commercial production in April 2005. It is the largest copper mine in Africa and the eighth-largest in the world, with capacity of 400 kt/a Cu (210 kt/a by SX–EW) and, unusually for this region, 130 000 oz/a Au (FQM, 2015). Ore treatment is flexible to allow for variation in ore type, with processing possible through an oxide circuit, a sulphide circuit, and a transitional ore 'mixed float' circuit. Sulphide ore is concentrated by crushing, milling, and flotation (Chongo and Ngulube, 2015). Oxide ore is treated via crushing, milling, flotation, leaching, and SX–EW to produce sulphidic and gold-bearing flotation concentrates, as well as electrowon cathode copper (FQM, 2015). The hydrometallurgical circuit employs both pressure and atmospheric leaching steps, and has five SX circuits and three tankhouses. The site also has its own dedicated acid plants. The autoclave leach results in relatively high levels of iron(III) reporting to the PLS. It is well known that ferric iron deteriorates current efficiency in EW and this plant has battled with transfer of iron to the electrolyte (Mwale and Megaw, 2011).

Mopani Copper Mines (MCM) produced 212 kt of copper (including refined copper from third parties) in 2013, representing a 13% year-on-year increase. The Nkana site has two SX circuits: one treats the PLS from an oxide leach; the other was used to remove copper in the cobalt circuit until the cobalt plant was closed in 2014. The Mufulira site has three SX circuits that treat a blend of heap- and vat-leaching solutions. Vat leaching is unusual in modern flow sheets—Mantos Blancos in Chile is the only other plant currently employing this technology (Schlesinger *et al.*, 2011). Although Glencore halted production at Mopani in September 2015, pending improved copper prices, several mining capital projects (Synclinorium Shaft at Nkana, Mufulira Deeps, Mindola Deeps) remain in progress and will ultimately extend mine life by 20 to 25 years (Mining Technology, 2016a).

Chambishi Metals, located near Chambishi, is one of the oldest plants in the region. It was commissioned in 1978 and privatized in 1998. In one of the more interesting flow sheets, the plant treats Cu/Co sulphide concentrates imported from DRC via a roast–leach–SX–EW process. The newly built SX circuit ensures the delivery of a low-copper feed solution to the cobalt refining circuit and the production of high-purity copper cathode. The cobalt purification process involves lime precipitation followed by SX and ion-exchange processes for zinc and nickel removal, respectively, before cobalt is electrowon, degassed, and crushed to produce London Metal Exchange (LME)-grade cobalt metal.

China Non-Ferrous Metals Company (CNMC) started the Sinometals leach plant in 2008. Located near Kitwe, this plant processes a variety of copper-containing raw materials. Through its subsidiary Luanshya Copper Mines (LCM), CNMC also operates the Muliashi SX–EW operation that was commissioned in 2012. Muliashi produces cathode (approximately 40 kt/a) from both agitated and heap-leach circuits.

Challenges and future prospects

Until 2012, Zambia was the largest copper producer in Africa, but it has since been overtaken by the DRC, particularly with respect to cathode copper (Figure 2). Zambian mining policy has travelled the path from assets being held by privately owned companies, through nationalization during the 1960s, and back to private ownership again in 2000 (Limpitlaw, 2011; Sikamo *et al.*, 2015). The lack of success of the nationalization policies has been strongly articulated by the Minister of Mines (Kapembwa, 2014): it is now well accepted that the economy, productivity, and health and safety performance fare far better under corporate management. Today, the Zambian government retains a minority interest in most of the large projects and mines through its holding company, Zambia Consolidated Copper Mines Investment Holdings plc (ZCCM-IH). Under a law passed in January 2015, Zambia's mining royalty rate increased more than threefold, which put enormous pressure on operating copper mines (Hill, 2014a). With the depressed commodity price, the new law was revised in early 2016 to prevent multiple mine closures and mass layoffs (Hill, 2016).

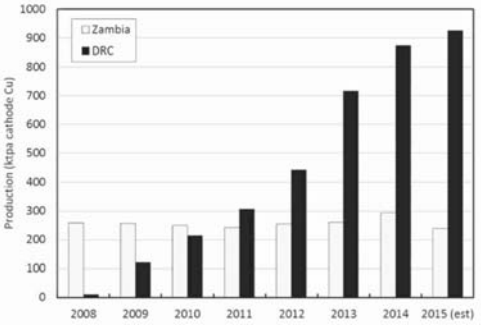

Figure 2—SX-EW cathode copper production of Zambia and DRC from 2008 to 2015

As in many Southern African countries, electricity supply is an increasing source of concern. The national producer, ZESCO, has 2200 MW capacity and produces some 90% of demand, but is increasingly under pressure as additional mining projects come online. In particular, commissioning of FQM's Sentinel mine and smelter in 2015 has significantly constrained supply. This Kansanshi smelter is more recently exacerbated by a two-thirds drop in hydroelectric output as a consequence of the regional drought. The national regulator granted an electricity tariff increase of 28% in 2014 (Hill, 2014b) and a further tariff increase of 26% was implemented in 2016 (Mining Technology, 2016b).

Democratic Republic of Congo

Development of the industry and current operations

The DRC is widely considered to be one of the richest countries in the world with respect to natural resources. It contains commercially viable quantities of some 50 commodities, including one-third of the world's cobalt and 10% of the world's copper.

Although hydrometallurgy had been employed in the DRC by Union Minière du Haut Katanga and its successor company, Gecamines, since the 1950s, it is only very recently that SX–EW has become commonplace. Some of the first companies to move back into the country in the early 2000s operated furnaces that produced 97 to 99% blister copper from high-grade copper oxide ores while others built leach–direct EW operations. In both cases, the intention was to minimize capital costs and recoup their investments as fast as possible by producing copper on a short lead time. Cathode produced by direct EW was of poor quality, but facilitated cash flow for further expansions and upgrading. The first large-scale modern SX–EW facility was commissioned in 2008. Since then, the industry has expanded rapidly and there are now over 20 operations producing copper via this route and almost as many projects in development.

One of the world's largest SX–EW operations is Tenke Fungurume Mining (TFM), located between the two rural towns of these names. TFM has one of the richest orebodies in the world and huge effort and resources were poured into the development of a flow sheet for this project in the 1970s. At that time, the project was far advanced and the emerging technology of SX was a crucial component. With the outbreak of a series of civil wars in (then) Zaire, all mining projects ceased from the mid-1970s. It is only since about 2004 that the political situation in DRC has stabilized sufficiently for adventurous multinational companies to start reinvestment in this region. Tenke, which started operation in 2009 and expanded in 2013, is today considered the flagship operation of the Copperbelt, with 2014 production of 203 kt Cu and 13.2 kt Co as $Co(OH)_2$. Under the management of US-based Freeport McMoRan, it also boasts amongst the best safety records in the region and lowest cash operating costs (US$1.15 per pound net of cobalt credits) (Freeport McMoRan, 2014). In May 2016, Freeport announced the sale of this asset to China Molybdenum (Wilson, 2016).

Two other major DRC operations are Glencore-owned Kamoto Copper Company (KCC) and Mutanda Mining, both located near Kolwezi at the far end of the Copperbelt. KCC's Luilu plant started production in the 1950s under Union Minière du Haut Katanga and was considered a world-class operation at that time. It fell into disuse and disrepair during the war years, but was restarted in 2008 using the original flow sheet. The process comprised agitated leaching of oxide concentrate and roasted sulphide concentrate followed by precipitation separations and direct EW. The first of three SX circuits was brought online in December 2012 and production today is entirely by SX–EW. The plant now has a design capacity of 300 kt/a Cu and produced 200 kt Cu and 2.78 kt Co cathode in 2014 (Katanga Mining, 2014). Glencore placed this operation on care and maintenance in September 2015, pending improved commodity prices.

Mutanda Mining started as a greenfield project in 2010. It is located on one of the richest deposits in this country and has gone through several expansions since start-up. Today, this operation, which treats whole ore by agitated leaching and heap leaching, boasts four SX circuits and seven EW tankhouses, with a design capacity of 200 kt/a Cu. Production in 2014 was reported as 197 kt Cu cathode and 14.4 kt Co as $Co(OH)_2$ (Fleurette Group, 2015).

Located near KCC, Sicomines is the first large Chinese operation in DRC. Commissioning started in mid-2015, and the first phase of the project will produce 35 kt/a Cu cathode. The second phase, starting in mid-2016, will increase this to 150 kt/a. The plant will also produce $Co(OH)_2$. As shown in Figure 3, there are numerous other small Chinese operations in DRC, most producing 12 to 20 kt/a Cu cathode. MKM (La Minière de Kalumbwe Myunga) produces 20 kt/a Cu cathode and 600 t/a $Co(OH)_2$. Comilu (Compagnie Minière de Luisha) started production in 2015 with a design capacity of 14 kt/a

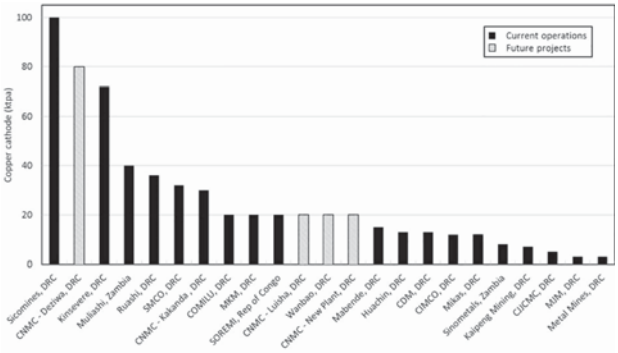

Figure 3—Current and future Chinese-owned copper operations in Central Africa

cathode using a heap leaching–SX–EW flow sheet and is currently operating at about 50% of design. CIMCO (Congo International Mining Company) currently produces 500 to 1000 t/month cathode, also via heap leaching–SX–EW. Shituru Mining Company (SMCO), located outside Likasi, was commissioned in 2012 and produces 35 kt/a copper cathode by agitated leach–SX–EW.

The Chinese-owned Mineral & Metals Group (MMG) operates Kinsevere, located near Lubumbashi. This started as a dense medium separation plant producing concentrate, but today the flow sheet comprises SX and EW, producing above 70 kt/a copper cathode. The available oxide ore is depleting and feasibility studies are currently underway to process sulphide material in the future.

Ruashi Mining, owned by China's Jinchuan Group (following the 2011 acquisition of Metorex), is located on the outskirts of Lubumbashi. The operation has a long history of copper and cobalt mining, going as far back as 1911. The modern operations have been in production since 2005. These comprise three open pits and copper is produced by leach–SX–EW following flotation concentration of the oxide ore—an unusual unit operation, but one that is employed in a few DRC flow sheets. Copper recovery is maximized by operating high- and low-grade SX circuits. Ruashi produces its own sulphuric acid and SO_2 to reduce the need to purchase acid and sodium metabisulphite (SMBS) that is required to reductively leach cobalt (III) from heterogenite. Cobalt is produced as $Co(OH)_2$ by precipitation with MgO. Ruashi currently produces 38 kt/a Cu and 4.4 kt/a Co (Metorex, 2015).

Chemaf's Usoke plant in Lubumbashi produced 15.2 kt Cu and 2.0 t Co in 2014 (Shalina Resources, 2015). The SX–EW equipment was brought from the old Mount Gordon site in Australia in 2007 when that plant closed and has considerable capacity available (31.5 kt/a). Chemaf originally produced cobalt as $CoCO_3$, but today cobalt is mainly sold as $Co(OH)_2$, produced by precipitation with MgO. A cobalt EW pilot facility produces 50 t/a cobalt cathode of 99.9% purity. Their nearby Etoile plant is nearing completion and is designed to produce 20 kt/a Cu and 3.8 kt/a Co.

Tiger Resources' Kipoi project is located between Lubumbashi and Likasi and currently produces 25 kt/a copper cathode by heap leach–SX–EW. Following several years of operating a heavy-media separation plant, the SX–EW plant was successfully commissioned in May 2014.

The Roan Tailings Reclamation (RTR) project is currently under construction near Kolwezi and will produce 77 kt/a cathode copper during its first phase of operation, currently targeting Q4 2016 for first metal production. The flow sheet is an agitated leach followed by SX–EW. The plant will also produce 14 kt/a Co as $Co(OH)_2$. In contrast to most other DRC operations, this tailings material contains significant qualities of zinc. Because tailings are treated, mining costs are negligible for this project and operating costs are expected to be very low, providing resilience for the operation in times of depressed commodity prices.

Challenges and future prospects

Electrowinning of copper is very energy-intensive (approx. 2.1 MWh/t Cu). Decades of infrastructure decay in DRC have left an electricity supply that is unreliable, both from the viewpoints of availability and stability. Power failures up to six times per day are not uncommon. Many operations supplement their power requirements using diesel generators, which adds significantly to operating costs. Fortunately, this situation should improve steadily, as mining companies make investments in the regional power grid. The Congo River is estimated by the United Nations to be able to supply the electricity needs of the entire continent by hydroelectric power (International Rivers, 2015a). The proposed Grand Inga scheme, if all seven phases are eventually implemented, will supply 40 000 MW—twice the generating capacity of the world's largest hydroelectric plant, the Three Gorges in China (Pearce, 2013). In 2013, Inga produced 115 MW DC, which increased to 250 MW in 2014. The Inga-3 project is expected to start by 2020 and will eventually supply a further 4800 MW (of which South Africa will take 2500 MW) (International Rivers, 2015b). Reliable and sufficient electricity supply is vital to the successful revitalization of the economy, and particularly the mining industry.

Transport infrastructure also creates huge challenges in this region. Almost all capital equipment and operating consumables must come in by road transport, either from Namibia, South Africa, or Tanzania, a distance of 2200 to 3000 km. Typical overland transit times range from 10 to 20 days. As a comparison of the impact of transport on operating costs, MMG report that the cost of sulphuric acid at Kinsevere is almost double that at their Sepon operation, which is situated in a remote location in Laos. There are no operating railways in the DRC Copperbelt, but initiatives are underway to bring in rail transport from the deep-water port at Walvis Bay, Namibia (Njini, 2014), and from Dar es Salaam, Tanzania (The Guardian, 2013). Onerous and expensive visa requirements, excessive landing fees (leading to expensive airfares), and difficult travelling conditions are also an impediment to foreign investment and expertise.

The economic and political stability of the country still presents unacceptable risk for many investors. The DRC has the near-lowest nominal gross domestic product (GDP) per capita in the world. In 2014, DRC had the second-lowest Human Development Index of 187 ranked countries (UNDP, 2014) and is also one of the lowest-ranked countries on the Corruption Perception Index (Transparency International, 2014).

On the positive side, the Copperbelt orebodies are incredibly rich by global standards: tailings sent to waste are typically of much higher grade than the feeds of many older operations in North and South America—which, nevertheless, are able to operate profitably. There is enormous potential for improved productivity, recovery, and throughput in these operations. The lowest labour costs of all copper-producing countries (World Salaries, 2015) give ample opportunities for operations to drive themselves down the cost curve and become competitive in global terms. Mutanda is already one of the five lowest-cost producers in the world.

Significant opportunities also exist to capitalize on the large-scale production of cobalt. The demand for cobalt is increasing because its main applications are technology-based and in high-temperature alloys. The price of cobalt is likely to increase more than that of copper in the short to medium term.

Central African copper SX–EW technical characteristics and challenges

Agitated leach flow sheets

Because of the high grade of the Central African ores and their readily acid-leachable minerals, leaching is generally carried out in agitated tanks, in contrast to the percolation (heap, dump, and ROM) leaching of most North and South American operations. The upside of agitated leaching is that the residence time required is of the order of hours (rather than months or years) and high PLS tenors can be achieved. The downside, however, is that extensive washing of the leach residue is required to minimize copper (and cobalt) losses to the tailings solids. Multiple countercurrent decantation (CCD) units are required, with the associated need to introduce flocculants and other settling-enhancing chemicals into the PLS, which may detrimentally impact the physical behaviour of the SX organic phase. A further disadvantage of solid–liquid separation by CCD is the high levels of total suspended solids (TSS) that report to the PLS and which greatly increase crud formation and the associated losses of extractant and diluent. In percolation leaching systems, the ore bed itself acts as a filtration medium, so TSS values are much lower (see Table I).

A unique flow sheet configuration, developed as a consequence of agitated leaching and the large washing requirements, is the so-called Split Circuit, the patent for which is held by BASF (Kordosky and Nisbett, 2005; Nisbett *et al.*, 2008). The relatively high-copper tenor PLS generated from the leaching circuit is passed through several stages of CCD for solid–liquid separation. The overflow from the first thickener reports to a high-grade SX circuit, which is operated to maximize copper throughput. The acid-containing raffinate is returned to the leach. The diluted PLS generated by washing through the remaining CCD stages reports to a low-grade SX circuit, which is operated to maximize copper recovery and minimize the amount of copper reporting to the final raffinate. This raffinate is used for washing, which allows some further copper recovery from any incompletely leached solids and utilization of the 'free' acid that has been generated by SX. In some flow sheets, a portion of the low-grade raffinate is neutralized and discarded, so any associated copper represents a loss to tailings.

Extractant choices and consumptions

The most widely used extractants are modified and non-modified aldoxime–ketoxime blends, *e.g.* LIX 984N from BASF Corporation and ACORGA OPT5510 and OPT5540 from Cytec Solvay Group. Some plants in Zambia also use modified aldoxime reagents successfully.

The extractant concentration employed (Table II) obviously bears a direct relationship to the copper tenor of the PLS (Table I) and extraction efficiency required. Most of the African operations use significantly higher extractant concentrations than elsewhere: for example, Mutanda employs 35 vol.% extractant to process a PLS containing 22.5 g/L Cu, while KCC uses 33 vol.% for a PLS of 26 g/L Cu.

The high TSS levels in an agitated leaching PLS are responsible for crud formation in SX circuits. A consequence is that extractant consumption is much higher than would typically be expected for the processing of high-grade copper liquors. To illustrate this, Table III compares the reagent consumptions of three hypothetical, well-operated, mid-sized operations in Chile, the USA, and the DRC. In this comparison, the assumption is made that annual production is 46 kt and organic losses are the same (50 mg/L). Clearly, extractant usage in the African case should be significantly lower than in Chile or the USA. Actual usages are more in the 3 to 6 kg/t range: the difference is attributable to both higher entrained losses of organic and the significant organic losses associated with crud.

Interestingly, although several operations have mixer temperatures in the 35–45°C range, hydrolytic degradation of the extractant is seldom an issue. This can be attributed to the relatively high replacement or 'make-up' rate, as discussed above.

Table II

Variation of average extractant and diluent parameters with location (Sole *et al.*, 2013)

Location	Extractant			Diluent		
	Concn. (vol.%)	Net transfer (g/L Cu/vol.%)	Usage (kg/t Cu)	Aromatics (vol.%)	Flash point (°C)	Usage (kg/t Cu)
N. America	8.7	0.19	3.9	12	79	31.4
S. America	15.4	0.28	2.7	10	80	22.9
Africa	30.3	0.23	4.1	18	87	12.4

Table III

Comparison of expected and actual extractant consumptions for well-operated plants

Location	Circuit config.	PLS		Extract	ΔCu	Extractant	Extractant usage (kg/t cathode)	
		Cu (g/L)	Flow (m^3/h)	O/A	(PLS–Raff, g/L)	(vol.%)	Calculated	Actual
USA	2E+1S	1.55	3500	0.6	1.5	12	3.9	3–5
Chile	2E+2S	5.5	1050	1.0	5	15	1.5	1–3
DRC	2E+2S	12	477	1.5	11	25	1.1	3–6

Diluent choice and consumption

Safety considerations, particularly flash point, dominate diluent selection. Despite the growing global tendency to minimize carbon footprint and use aliphatic diluents, in Africa, diluents containing higher aromatic content (8 to 25 vol.%) have been traditionally preferred for the enhanced solvating capacity that this offers for the higher extractant concentrations (Table II). A recent study, however, indicates that aliphatic diluents may potentially be used for these applications (Brown, 2015).

Of increasing concern to the regional industry is diluent availability. Until recently, all diluent has been supplied from the South African Petroleum Refinery (SAPRef); however, with advancing age, this refinery is suffering increasingly frequent and lengthy shutdowns (137 days of lost production in 2014), which is aggravating diluent supply. The other South African and Zambian refineries do not currently produce suitable products for this application and there is an increasing need to import alternatives. Although these offer suitable safety and chemical properties, imports obviously command a significant price premium and add to ever-increasing operating costs and lead times on orders. This issue will not be resolved in the short term and innovative solutions are required to ensure that the increasing diluent demands of Copperbelt users can be consistently and reliably met.

Suspended solids and crud management

The rate of build-up of crud, both at the settler interface and on the bottom of the settlers, is by far the most significant operational issue facing the African agitated leach–SX operations. To put it in perspective, heap leach operations typically deliver PLS containing <30 mg/L TSS, while—even after clarification—most agitated leach PLS will contain upwards of 50 mg/L and frequently over 100 mg/L TSS. If not actively managed, the crud will literally fill up the settlers over a six- to twelve-month period. Most agitated leach–SX operations regularly take individual settlers off-line to remove bottom crud. Minimizing the entry of solids into SX is obviously the best approach, although this is difficult to accomplish in practice. Several operations have installed pinned-bed clarifiers on the PLS streams; these have seldom been effective, although there are examples where TSS are consistently reduced to <20 mg/L.

Crud exacerbates losses of the organic phase and crud treatment systems are required to reclaim as much of these expensive reagents as possible. It is usually necessary to clay-treat any recovered organic phase before returning it to the circuit to avoid introducing organic degradation products or other detrimental compounds into the SX circuit. Although expensive, three-phase centrifuges and plate-and-frame filters have become standard equipment both to separate the organic phase from the solids and aqueous phase and to separate organic from clay. The solid component of crud ultimately reports to tailings disposal.

Impact of up- and downstream additives

Flocculants, coagulants, flotation chemicals, and similar reagents are surfactants. If the addition of these chemicals to upstream unit operations is not properly controlled, they can have severe detrimental impacts on the SX circuit. Because the SX process is interfacial—involving the transfer of Cu^{2+} ions across an aqueous–organic interface—its chemical and physical performances are strongly influenced by the presence of any foreign species that interfere with the interfacial characteristics. It is critical to evaluate the potential impact that the upstream introduction of a new reagent may have on the downstream SX performance.

The transfer of organics, such as mist suppressants and smoothing agents, from EW to SX via the return spent electrolyte can also have unintended consequences if not properly managed.

Impact of dissolved and hydrated silica species

African PLS often contain very high levels of dissolved or hydrated silica species. As is well known, silica can form polymeric structures under appropriate conditions of temperature and aging. These can significantly alter the viscosity of the solutions in the SX circuit, which impedes the transfer of copper ions across the aqueous–organic interface. Silica is usually also a major component of crud.

Coagulants can be used to remove colloidal silica and fine particles (less than 0.5 μm diameter). Coagulants are surface-active agents, so it is important to ensure that these do not interfere with the interfacial behaviour in the SX circuit. Neutral (uncharged) coagulants, which cannot be overdosed, are generally preferred. Liquid coagulants, rather than common powder-based solids, are safer to use (no inhalation hazard) and can be used directly without prior dilution. Chambishi has employed silica coagulants ahead of both their copper and zinc SX circuits to remove silica from the PLS and avoid severe clogging of their filters.

Impact of high PLS and spent electrolyte temperatures on degradation

Agitated leaching systems, particularly those processing secondary sulphides, often operate above ambient temperature. As oxide deposits reach the end of their life and the processing of primary sulphides increases, an increasing prevalence of autoclave leaching is expected to be seen in this part of the world. The temperatures of autoclave-generated PLS are typically higher than those of atmospheric percolation leaching operations. Spent electrolyte is also typically at 40°C due to resistive heating of the electrolyte during electrodeposition. The effect of elevated temperature manifests in two ways. The main mechanism of diluent loss is via evaporation: the rate of evaporation increases with increasing temperature, leading to increased diluent consumption per ton of cathode produced. Elevated temperature also increases the rate of hydrolytic degradation of both extractant and diluent.

Aqueous and organic entrainment

One positive aspect of aqueous-in-organic entrainment—unique to Africa—is the transfer of cobalt from the PLS to the advance electrolyte. Copper EW typically requires 150 to 200 mg/L Co to be present in the electrolyte to assist with passivation of the anode and minimizing lead contamination of the cathode. This is usually added as cobalt sulphate salt and comprises a significant operating cost (US$3.50–4.00 per ton Cu) in North and South American operations. In Africa, the electrolyte typically contains some 2000 mg/L Co as a result of entrainment from the PLS (Sole *et al.*, 2013) and no further cobalt addition is required.

Organic-in-aqueous entrainment represents the main source of extractant losses in these circuits. This is caused by crud formation and inefficient phase disengagement in settlers. Methods to recover organic include the installation of an after-settler, flotation columns, activated carbon columns, or other coalescing systems. The use of coalescence packs in loaded organic tanks assists with removal of entrained PLS ahead of the strip circuit. It is critically important to minimize the organic contamination of the advance electrolyte (target <30 mg/L entrained organic): not only does the presence of organic ruin the cathode appearance, but it has been responsible for several tankhouse fires in DRC in recent years.

Conclusions

As indicated in the discussions above, copper SX in Central Africa faces many challenges, but offers many significant opportunities in return. The current and planned expansions of existing operations and the proliferation of projects in various stages of development in the Copperbelt suggest that this region will become the dominant copper producer of the world within the next decade. The rich, extensive, and easily leachable orebodies, coupled with low labour costs, provide conditions for large operators to become among the lowest global cost producers. Hampering the rapid development of the industry are the ongoing (albeit improving) power supply situation, expensive and difficult logistics, lack of capacity in technical and management skills, corruption, and unhelpful government regulation and legislation. The many unique issues presented by this region are promoting innovation and the development of new and interesting flow sheets, all of which enhance the use of SX technology. Provided that the political environment remains stable, the long-term outlook for the copper industry in this part of the world is extremely positive for operators, suppliers, and engineering companies.

References

Brown, C.W. 2015. Physical property-performance relationships of commercial diluents in African copper solvent extraction conditions. *Proceedings of the Copper Cobalt Africa Conference.* Southern African Institute of Mining and Metallurgy, Johannesburg. pp. 269–280.

Chongo, C. and Ngulube, C. 2015. Development and optimisation of Kansanshi ore treatment. *Proceedings of the Copper Cobalt Africa Conference.* Southern African Institute of Mining and Metallurgy, Johannesburg. pp. 69–80.

First Quantum Minerals. 2006. First Quantum reports operational and financial results for three months and twelve months ended December 31, 2005. *Press Release*, 9 March 2006.

First Quantum Minerals. 2015. Kansanshi. http://www.first-quantum.com/Our-Business/ operating-mines/Kansanshi/default.aspx

Fleurette Group. 2015. Fourth quarter and 2014 calendar year production report. http://www.prnewswire.co.uk/news-releases/fleurette-group-mutanda-mining -sarl-fourth-quarter-and-2014-calendar-year-production-report-291499461.html

Freeport McMoRan. 2014. Annual Report 2014. http://investors.fcx.com/files/doc_financials/ annual/10_K2014.pdf

Hill, M. 2014a. Zambian mine royalty rise to cost 12,000 jobs, Chamber says. *Bloomberg Business*, 19 Dec. 2014. http://www.bloomberg.com/news/articles/2014-12-19/zambia-mining-royalty-increase-to-cost-12-000-jobs-chamber-says

Hill, M. 2014b. Zambian power surplus to shrink as copper mining expands. *Bloomberg Business*, 25 Nov. 2014. http://www.bloomberg.com/news/articles/2014-11-25/zambian-power-surplus-to-shrink-as-copper-mining-expands-1-

Hill, M. 2016. Zambia plans price-based royalty for ailing copper mines. *Bloomberg Business*, 17 Feb. 2016. http://www.bloomberg.com/news/articles/2016-02-17/zambian-cabinet-approves-lower-variable-copper-royalties

Holmes, J.A. Deuchar, A.D. Stewart, L.N., and Parker, J.D. 1976. Design, construction and commissioning of the Nchanga Tailings Leach Plant. *Extraction Metallurgy of Copper*, vol. II. AIME, New York. pp. 907–925.

International Rivers. 2015a. Grand Inga dam, DR Congo. http://www.internationalrivers.org/ campaigns/grand-inga-dam-dr-congo

International Rivers. 2015b. The Inga-3 hydropower project. http://www.internationalrivers.org/ campaigns/the-inga-3-hydropower-project

Kapembwa, J. 2014. Zambia has no intention of nationalising its mines – NOT AGAIN. *The Southern Times Online*, 28 Feb. 2014. http://www.southern-timesafrica.com/articles/9516/Zambia-has-no-intention-of-nationalising-its-mines---NOT-AGAIN--/#.VRUpGeGBdcA

Katanga Mining. 2015. Financial results Q4 2014. http://www.katangamining.com/~/media/ Files/K/Katanga-mining-v2/investor_relations/financialresults/res2014/q4-2014/mda-q4-2014.pdf

Kordosky, G.A. and Nisbett, A. 2005. Methods for improving the recovery of metal leaching agents. World Patent WO 2005012581 A2.

Lakshmanan, V.I. Mackinnon, D.J., and Brannen, J. M. 1977. The effect of chloride ion in the electrowinning of copper. *Journal of Applied Electrochemistry*, vol. 7, no. 1. pp. 81–90. http://rd.springer.com/article/10.1007/BF00615534#

Limpitlaw, D. 2011. Nationalisation and mining: lessons from Zambia. *Journal of the Southern African Institute of Mining and Metallurgy*, vol. 111. pp. 737–739.

Metorex Group. 2015. Ruashi Mining. http://www.metorexgroup.com

Mining Technology. 2016a. Glencore to invest $1.1bn to develop Mopani mine shafts in Zambia. *Mining Technology*, 31 Mar. 2016. http://www.mining-technology.com/news/newsglencore-to-invest-11bn-to-develop-mopani-mine-shafts-in-zambia-4852541

Mining Technology. 2016b. Zambia increases power tariffs for mining companies. *Mining Technology*, 1 Feb. 2016. http://www.mining-technology.com/news/newszambia-increases-power-tariffs-for-mining-companies-4798074

Mwale, M. and Megaw, D. 2011. Development of effective solvent-extration process control – low cost implementation value-addition to hydrometallurgical copper operations. *Proceedings of the Sixth Southern African Base Metals Conference.* Southern African Institute of Mining and Metallurgy, Johannesburg. pp. 353–365.

Nisbett, A., Peabody, S., and Kordosky, G.A. 2008. Developing high-performing copper solvent-extraction circuits: strategies, concepts, and implementation. *Solvent Extraction: Fundamentals to Industrial Applications. International Solvent Extraction Conference ISEC 2008*, vol. 1, Moyer, B.A. (ed.). Canadian Institute of Mining, Metallurgy and Petroleum, Montreal, Canada. pp. 93–100.

Njini, F. 2014. Namibia may seek investors for DRC, Zambia rail to port. *Bloomberg Business*, 8 Oct. 2014. http://www.bloomberg.com/news/articles/2014-10-08/namibia-may-seek-investors-for-drc-zambia-rail-to-port

Pearce, F. 2013. Hydropower megaproject to dam Congo River. *New Scientist*. http:// www.newscientist.com/article/dn23589-hydropower-megaproject-to-dam-river-congo.html#

Russell, C. 2014. BHP Billiton chief Andrew Mackenzie says Olympic Dam in South Australia will be mined for 200 years at least. *The Advertiser*, 20 Aug. http://www.adelaidenow.com.au/ business/bhp-billiton-chief-andrew-mackenzie-says-olympic-dam-in-south-australia-will-be-mined-for-200-years-at-least/story-fni6uma6-1227029973661?nk=74bbba54dfd3216aa2ba705c4 5276353

Schlesinger, M.E., King, M., Sole, K.C., and Davenport, W.E. 2011. Extractive Metallurgy of Copper, 5th edn. Elsevier.

Shalina Resources. 2015. Processing operations. http://www.shalinaresources.com

Sikamo, J., Mwanza, A., and Mweemba, C. 2015. Copper mining in Zambia–History and future. *Proceedings of the Copper Cobalt Africa Conference.* Southern African Institute of Mining and Metallurgy, Johannesburg. pp. 1–10.

Sole, K.C., Zarate, G., Steeples J., Tinkler, O., and Robinson, T.G. 2013. Global survey of copper solvent extraction operations and practices. *Proceedings of Copper-Cobre 2013 Conference*, vol. IV. Gecamin, Santiago, Chile. pp. 137–148.

The Guardian. 2013. DRC, Burundi and Tanzania discuss air, rail, water links. *The Guardian*, 28 Nov. 2013. http://www.ippmedia.com/frontend/?l=62051

Transparency International. 2014. Corruption Perceptions Index 2014. https://www. transparency.org/cpi2014

Tumilty, J., Seward, G., and Massam, J.P. 1977. The ACORGA P-5000 Series: A novel range of solvent-extraction reagents for copper. *Advances in Extractive Metallurgy*. Institution of Mining and Metallurgy, London.

United Nations Development Program. 2014. Human Development Report 2014. http://hdr. undp.org/sites/default/files/hdr14-report-en-1.pdf

Wilson, J. 2016. Freeport sells key copper mine for $2.7bn to China Molybdenum. *Financial Times*, 9 May 2016. http://www.ft.com/intl/cms/s/0/f222487c-15d3-11e6-b197-a4af20d5575e.html#axzz496ZDm8YK

World Salaries. 2015. Miner salaries – international comparison. http://www.worldsalaries.org/ miner.shtml. ◆

http://dx.doi.org/10.17159/2411-9717/2016/v116n6a11

Review, evolution, and optimization of the treatment of Kansanshi mixed copper ore

by C. Ngulube*, C. Chongo*, and F.X. Paquot*

Synopsis

Over the last six years, the Kansanshi copper-gold mine has continued to process significant quantities of complex transitional mixed ores. Initially, the ore treated came predominantly from accumulated stockpiles. Subsequently, the feed source shifted primarily to freshly mined ore that generally showed less tarnish with better flotation kinetics, but with the downside of lower concentrate grades. A number of changes were made to improve the efficiency of the rougher circuit and quality of concentrate produced. These changes were as a result of initial mineralogical studies and laboratory flotation test work that were discussed at length in a previous paper[1]. Salient among the recommendations adopted as a result of previous work were increased circuit capacity and a modified configuration to increase the residence time and the number of sulphidization stages. These modifications were completed and commissioned in 2011. This, however, resulted in significantly low rougher concentrate grades and a below-specification final concentrate product. This was due primarily to higher mass pulls from the extended rougher bank with multiple concentrate discharge streams, and which necessitated an enlarged cleaning capability. The extra cleaning capacity came on stream in 2014. Of note was the development of a recovery model, based on the strong correlation between the total copper and acid-soluble copper ratio, as a tool for monitoring plant performance.

Keywords
copper, flotation, optimization, mixed ore, sulphidization, modelling.

Introduction

The Kansanshi mine, the largest copper mine in Africa, is 80% owned by Kansanshi Mining plc, a subsidiary of First Quantum Minerals. The remaining 20% is owned by the state through the parastatal Zambia Consolidated Copper Mines Ltd (ZCCM). The mine is located approximately 10 km north of the town of Solwezi and 180 km to the northwest of the Copperbelt town of Chingola. The mine has been in commercial operation since 2005.

Prior to June 2009, Kansanshi mine treated only two ore types: oxide and sulphide. All transitional ores mined during the period leading up to 2009 was stockpiled. The treatment of the minerologically complex transitional ores through a third train commenced in June 2009, but entailed numerous metallurgical challenges. This transitional ore (called 'mixed ore') could not previously be treated economically due to the high content of high acid-consuming (GAC) minerals. This made it unsuitable for the oxide float–leach circuit, and poor flotation response ruled out the conventional sulphide float circuit. The novel circuit involved a conventional sulphide pre-float followed by flotation involving staged-controlled potential sulphidization (CPS).

All the copper minerals constituting the alteration sequence from primary sulphides to carbonates or silicates are present in various proportions in the Kansanshi transitional ores (Table I). The alteration of primary sulphides starts with an impoverishment in iron to form covellite. Further oxidation results in an impoverishment in sulphur and enrichment in copper to form digenite, then chalcocite (Dunn and Muzenda, 2001). The final steps of alteration, leading to the formation of copper oxide minerals such as malachite or chrysocolla (a silicate) depend mainly on the composition of the gangue or fluid. The iron liberated during the alteration sequence can remobilize to form goethite or limonite. These iron oxides and hydroxides are particularly prejudicial for flotation if they precipitate on the surface of the copper minerals because they are not collectable with xanthates (Woods, 2003).

The traditional method applied for the flotation of copper oxide or mixed ores is sulphidization, which was first developed with industrial success on Pb–Zn oxide ores in

1Paquot, F.X. and Ngulube, C. 2012. Development and optimization of mixed sulphide/oxide copper ore treatment at Kansanshi *Journal of the Southern African Institute of Mining and Metallurgy*, vol. 115, no. 12.

* *First Quantum Minerals Ltd, Kansanshi Mine, Solwezi, Zambia.*

Table I

Copper minerals present at Kansanshi mine

Mineral	Formula	Mineral	Formula
Chalcopyrite	$CuFeS_2$	Azurite	$Cu_2(CO_3)_2.Cu(OH)_2$
Bornite	Cu_5FeS_4	Cuprite	Cu_2O
Covellite	CuS	Tenorite	CuO
Digenite	Cu_9S_5	Chrysocolla	$(Cu,Al)_2H_2Si_2O_5(OH)_4.nH_2O$
Chalcocite	Cu_2S	Native copper	Cu
Malachite	$CuCO_3(OH)_2$		

Australia (Crozier, 1991). The method involves multistage addition of sodium sulphide (Na_2S), sodium hydrogen sulphide (NaHS), or ammonium sulphide $(NH_4)_2S$ as a sulphidizing agent, together with xanthate collectors such as potassium amyl xanthate (PAX) (Kongolo *et al.*, 2003; Mwema and Mpoyo, 2001). The effectiveness of sulphidization for flotation of oxidized sulphides has also been demonstrated (Newell *et al.*, 2006). When introduced in the slurry, the sulphidizer dissociates into the species H_2S, H_S^- or S_2^-, depending on the pH. These ions react with the copper oxide minerals to form a sulphide layer on the surface of the oxide minerals (Zhou and Chander, 1992). The sulphidizer concentration can be controlled by measuring the E_S potential of the pulp using a sulphide ion-selective electrode. The reaction between the sulphidizer and malachite is optimum at a potential of –500 mV (Jones and Woodcock, 1978). However, xanthate flotation is depressed at this potential. Oxidation of sulphide ions in excess is then necessary to reach the optimal potential of –300 mV (Ferron and Manu, 1994). This leads to the formation of reducing agents such as thiosulphates, which are not necessarily indifferent in the flotation process (Castro *et al.*, 1974; Soto and Laskowski, 1973).

Direct collectors, such as fatty acids and hydroxamates, have also been developed for the flotation of oxide minerals (Lee *et al.*, 1998, 2009). The fatty acids have the drawback of being unselective over the carbonated gangue minerals and are therefore unsuitable for the Kansanshi mixed ores. Paquot *et al.* (2009) demonstrated the advantage of the sulphidization route over direct hydroxamates flotation.

The original Kansanshi mixed circuit configuration had six 150 m³ flotation cells. With this configuration, the first pair of cells was designated as a sulphide pre-flotation stage (referred to as a rougher stage). Sequentially, two sulphidization stages, each comprising two 150 m³ flotation cells, immediately followed the rougher stage. These were referred to as CPS 1 and 2. Two series of sulphidization conditioning tanks, to control sulphidizer addition against an Es/Eh potential and collector, preceded each sulphidization stage. The sulphidizer used was sodium hydrogen sulphide (NaHS).

Foremost among the metallurgical challenges with the mixed float was the loss of a certain class of copper minerals to the tails, despite indications that these minerals were fully liberated and floatable (Table II.). Paquot *et al.* (2009) and Ngulube *et al.* (2011) conducted several investigations to investigate this copper loss to tails, collecting samples across the whole circuit to assess liberation and mineral classes. Hundreds of laboratory flotation tests were also simultaneously conducted on flotation feed and final tails, under various plant conditions, in order to compare the performance of the plant with the ideal conditions in the laboratory.

The salient points from these studies were as follows.

- During the sulphide pre-flotation (roughers), recoveries were generally predominantly in the particle size range –150 μm to +38 μm and, despite the fairly good mineral liberation, recovery was poor for the coarse (+150 μm) and fines (–38 μm) fractions. In the acid-insoluble copper range (sulphide mineralization), chalcocite and chalcopyrite showed the best flotation response (64 to 65% recovery) while covellite had the worst response among both primary and secondary sulphides. However, 'porous' chalcocite also had poor recoveries, mainly attributable to higher the amount of reagents required to activate surfaces that hardly contribute to hydrophobicity. Less than half of the liberated chalcopyrite (45%) was recovered in the rougher stage, mostly due to partial transformation of chalcopyrite to iron oxyhydroxides. These oxyhydroxide rims decreased the floatability of normally floatable mineral species. Even after sulphidization, liberated chalcopyrite and covellite were the sulphide species that displayed lower recovery
- In the first sulphidization stage (CPS 1), the best recoveries were observed in the size range –150 μm to +75 μm. There was, however, very low recovery of the fines fraction (–38 μm). Compared with the roughers, there was better flotation response in CPS 1 with regard to sulphide recovery compared with the oxides. This was attributed mainly to the sulphidizer (NaHS) activating the tarnished or rimmed sulphide components. Secondary sulphides also showed a superior response to sulphidization
- Malachite recovery started to become significant only in the second sulphidizing stage (CPS 2). Additionally, the coarse fraction sulphides were activated and recovered at this stage. However, only 50% of the liberated malachite was recovered. Malachite associated with iron oxides and hydroxides was not recovered
- Major losses of the coarse but prior-activated particles in the CPS stages occurred in the cleaning circuit. However, chalcopyrite recovery was better than that of other secondary sulphides, malachite, and oxidized native copper in the cleaning section

Table II

Contribution of each mineralogical class to the copper losses in the final tails

Mineralogical class	Contribution to final Cu losses (%)
Chalcopyrite (Cp)	14.5
Chalcocite (Cc)	3.86
Covellite (Cv)	7.33
Cp+Cv+Cc+Dg (digenite)	3.30
Cp+Cv+Dg+Cc+FeOx (iron oxyhydroxides)	6.02
Cp+gangue	9.75
Malachite (Mal)	28.03
Mal+FeOx	19.98
Chrysocolla (Ch)	6.16
Total	99

- The main copper losses in the final tails were attributed to liberated chalcopyrite and malachite (16% and 28%, respectively) that should be recovered if properly sulphidized. Malachite associated with iron oxides and hydroxides also contributed to a significant proportion of losses (20%). These losses are attributed mainly to poor sulphidization efficiency. Even lower recoveries were noticed for malachite stained by iron oxyhydroxides. Chalcopyrite had slow-floating tendencies as well. With the exception of covellite, the remainder of secondary sulphides had the best flotation responses. There was no evidence of chrysocolla floating
- The average recovery difference between the laboratory experiments performed on the flotation feed and the plant results was around 9%. When floating the flotation tails in the laboratory without any additional reagents, the recovery was seen to improve by an average of 5%, while floating the tails with additional reagents resulted in improvements of up to 10% (Figure 1)
- The higher the acid-soluble copper feed grade, the higher the observed improvement (Figure 2). The additional recovery was only around 2% when the acid-soluble copper feed grade was lower than 0.2%, but was as high as 15% when the acid-soluble copper feed grade was higher than 0.6% (Figure 3).

In this paper, we review the subsequent circuit changes and modifications that resulted from the findings of the work undertaken up to 2011, and the various challenges that these changes introduced. Relevant points from the above work were:

- The need for increased residence time and stages for both the roughers and the CPS stages to capture more of the slow-activating mineral species and size fractions. Findings of the mineralogical studies, coupled with test work, pointed to insufficient residence time and less- than-efficient sulphidization. The slow-floating chalcopyrite needed more residence time and the fully liberated but lost malachite needed more sulphidization stages and residence time
- The need to divert the mixed cleaner scavenger tails out of the mixed circuit because recirculating oxide minerals were increasing the possibility of this being lost to tails.

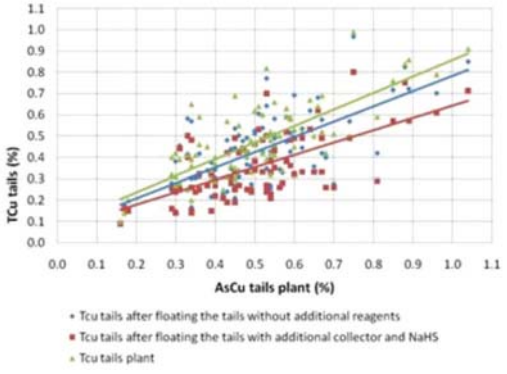

Figure 1—Reflotation of tails with and without reagent addition

Plant expansions and results

Rougher/CPS expansions

The results of the plant and laboratory test work and mineralogy analysis were used to justify the extension of the mixed ore flotation plant, with the total changes costing approximately US$19 million. A more conservative recovery improvement of 5% was considered to justify this expenditure.

In mid-2011, six 300 m³ float cells were commissioned: four cells dedicated to the sulphide flotation circuit and the other two being flexible between mixed and sulphide ore flotation, depending on milling circuit configuration. The volume capacity of the mixed ore flotation plant increased from 900 m³ to 1500 m³ or 2100 m³, depending on whether the 300 m³ cells were used for mixed ore flotation. In late 2011, an extension of the CPS plant was commissioned to increase the number of sulphidization intervals to the current four stages. From an initial 900 m³ total capacity and two sulphidization stages, by the end of 2011 there was a total capacity of 2100 m³ and four sulphidization stages available. Subsequently, residence time increased from an average 20 minutes to between 30 and 60 minutes, depending on the milling circuit configurations.

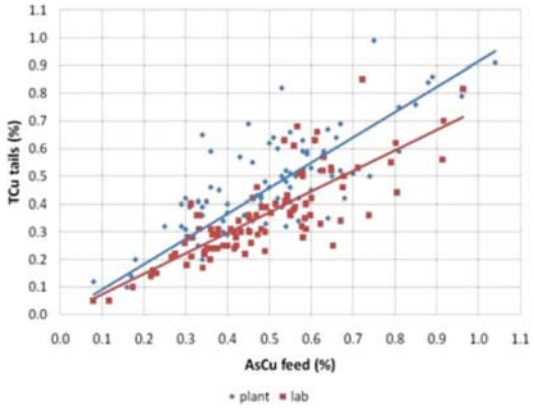

Figure 2—Plant tailings compared with laboratory tailings analysis for acid-soluble copper minerals

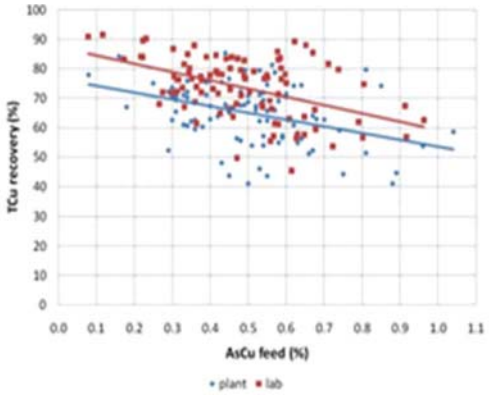

Figure 3—Plant recovery compared with laboratory recovery for acid-soluble copper minerals

Notably, during the same period in 2011, due to a shortfall of sulphide ore from the pit, it was decided that more of the mixed ores would be treated, utilizing the larger sulphide mills. This resulted in an 80% increase in daily throughput, effectively reducing the residence time through the mixed float circuit from 45 minutes to about 30 minutes.

Figure 4 depict the flow sheets before and after the expansion. Figure 5 shows the effect of the additional float cells on the recovery from mixed ore.

Results from mixed circuit expansions

From the results obtained after the mixed circuit expansions, it could at first glance (Figure 5) be deduced that there was an immediate improvement, especially if the two periods of running the same mills on mixed ore (before June 2011 and after June 2012) are considered. However, as can be seen from Figure 6, recovery from the mixed ore through the Kansanshi circuit also has a very strong correlation with the total Cu/acid-soluble Cu ratio. The period 2011 and 2012 also coincided with the shift from treating predominantly stockpiled transitional ores to predominantly freshly mined ore from the pit. This ore was better grade-controlled for quality (acid-soluble Cu grade which was found to be the best approximation of the weathering profile). Initially, classification of mixed ores was based purely on the amount of acid-soluble Cu and GAC minerals in the material. Freshly mined material also showed less tarnishing. Figure 7 shows the progressive drop in sulphidizer consumption, especially during this same period of the circuit expansion.

Clearly, a rigorous statistical approach was required to prove the benefits of the expanded circuit and the increased number of sulphidization stages.

The F-test result

As shown in Table III, two sets of recovery data were subjected to F-tests. The first set of data was for 192 days

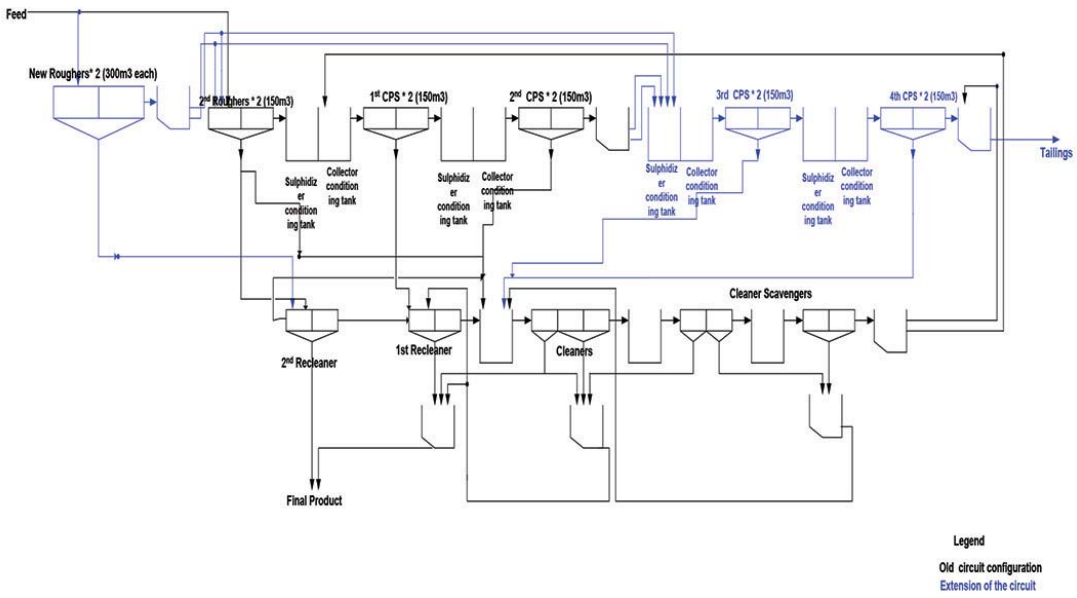

Figure 4—New and old circuit configurations

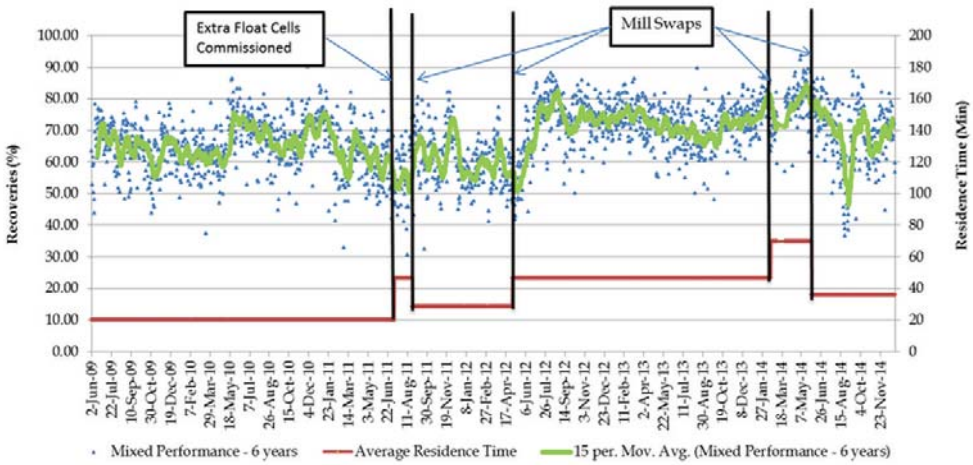

Figure 5—Effect of flotation residence time on mixed recovery

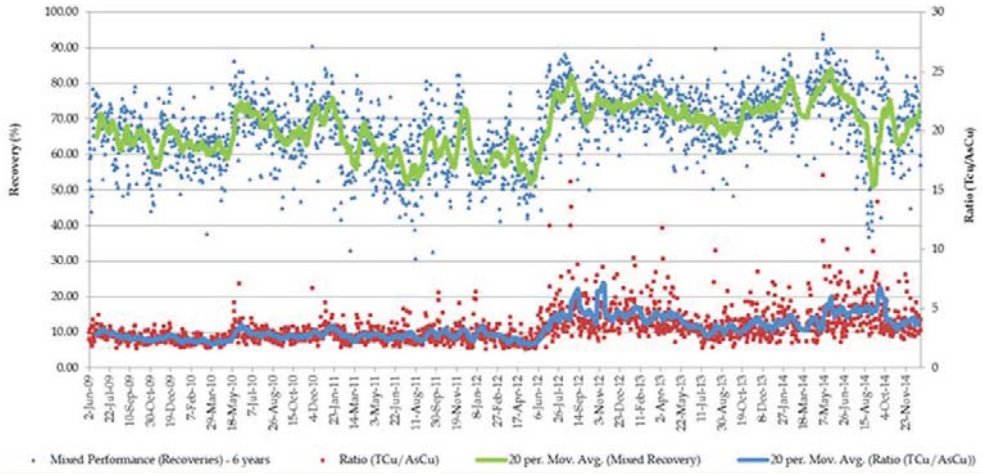

Figure 6—Relationship between total Cu/acid-soluble Cu ratio and mixed recovery

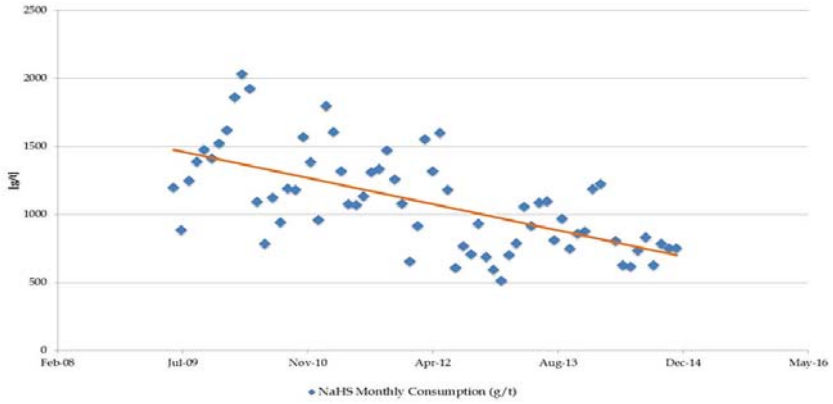

Figure 7—NaHS consumption over the six-year period

Table III

F-test results

Parameter	F-test results		F-test two-sample for variance	
	Low residence time 1 (20 min)	High residence time 1 (45 min)	Low residence time 1 (20 min)	High residence time 1 (45 min)
Mean	68.43603		60.23057	
Variance	113.6457		63.02303	
Observations	204	75.88294	192	70.30985
Df	203	46.3551	191	117.5439
F	2.451632	204	0.536166	192
P(F<=f) one-tail	1.65E-10	203	9.88E-06	191
F Critical one-tail	1.260095		0.787708	

(192 data points) taken from on either side of the mill swap, which resulted in major changes in residence time. The new residence time was around 45 minutes on average, compared with 20 minutes before the extension. A recovery difference of 7.45% (higher at a residence time of 45 minutes) was noted with 100% confidence limit. Similarly, 204 data points were picked for before and after the mill swap in 2011/2012. This data-set showed a 10% recovery drop at a residence time of 30 minures, again with 100% confidence limit.

Cleaner/recleaner flotation

The increase in rougher and CPS stages on the mixed circuit was therefore successful in reducing copper losses. However, the resulting multiple sub-concentrate discharge points caused a drop in final product (final concentrate) quality. The higher mass pulls, and consequently increased volume reporting to the limited cleaner/recleaner flotation bank of only 288 m^3 total volume, subdivided into nine float cells of 32 m^3 each, led to higher insoluble components (silicates,

aluminates, *etc.*) in the final combined concentrates. This resulted in significant smelter penalties. Figure 8 shows the trend of insolubles in the mixed ore final product, the recleaner concentrate. In August 2014, the cleaner/recleaner capacity was increased to ameliorate this problem, to great effect (Figure 8). Volumetrically, the capacity increased from a restricted 288 m^3 to a substantial 1220 m^3, consisting of three banks: 6 × 150 m^3 cleaners, 8 × 30 m^3 recleaners, and a further 5 ×16 m^3 re-recleaners.

Comparative recovery models

The variation in mineralogy and TCu/AsCu contents in the feed causes significant fluctuations in recovery (Table IV). Flotation recovery from mixed ore generally varies between 50–90%. The NaHS consumption varies between 300 g/t and 3000 g/t. Robust multilinear regressions using iteratively reweighted least squares was used for modelling the plant flotation final tails and NaHS consumption. Performance of the plant is compared with the model on a daily basis. This also serves to highlight the variability in the results and reagent consumption. The correlation coefficients between the total Cu tails grade or NaHS dosage and the total Cu feed grade and acid-soluble Cu feed grade are given in Table V. The equations are of the form:

$$TCu_{(tail)} = a_1 * TCu_{(feed)} + a_2 * AsCu_{(feed)} \quad [1]$$

$$NaHS = \beta_1 * TCu_{(feed)} + \beta_2 * AsCu_{(feed)} \quad [2]$$

Figure 9 shows the models obtained for the total Cu grade of the tails, the corresponding recovery, and the model obtained for the NaHS consumption. Table VI gives the correlation coefficients between the models and the actual plant daily results.

The main parameter affecting the total Cu recovery or the total Cu of the tails is the acid-soluble Cu feed grade. Because the oxide minerals are more difficult to recover than the sulphides, a lower recovery (higher tails grade) can be expected when the acid-soluble Cu feed grade increases. It is thus not possible to set a fixed recovery target for the mixed ore flotation. However it is possible to set a tails grade target depending on the acid-soluble Cu feed grade. As a general rule, if the total Cu tails grade is lower than the acid-soluble feed grade, an average plant performance is achieved. The NaHS consumption depends mainly on the acid-soluble Cu feed grade. The fit for the model of the NaHS consumption is poor because it is calculated based on the variations in stock inventory levels. The model of the total Cu tails grade is not much different from the one obtained with the daily results, but the model of the NaHS consumption is very different, and the fit is much better; however, the application range has been reduced. Because the NaHS consumption is very variable, the stocks must be controlled carefully to avoid running out of reagents and to avoid holding excessive stock that would degrade. The model of the NaHS consumption can be used for monitoring the NaHS stocks, depending on the forecast for feed grades coming from the mine.

Conclusions

The envisaged recovery improvements from plant extensions and increasing the stagewise addition of sulphidizer were achieved. The increased residence time increased the recovery of slow-floating (tarnished) chalcopyrite. The probability of recovery of previously fully liberated but unrecovered malachite was increased by the addition of a further two stages of sulphidization at the tailings end of the old circuit. The mineralogical results showed that most chalcopyrite was recoverable only after being activated by sulphidizer in the

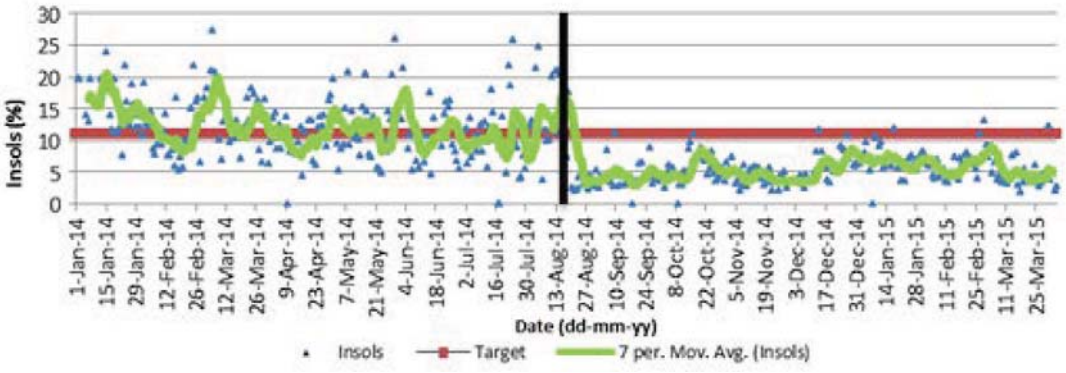

Figure 8—Proportion of insoluble material in the concentrates

Table IV

Range of data used for the model

	Total Cu (%)	Acid-soluble Cu (%)	NaHS (g/t)
Min.	0.50	0.17	282
Max.	2.48	0.93	3800

Table V

Correlation coefficients

	Total Cu feed	Acid-soluble Cu feed
Total Cu tails	0.62	0.86
NaHS	0.35	0.64

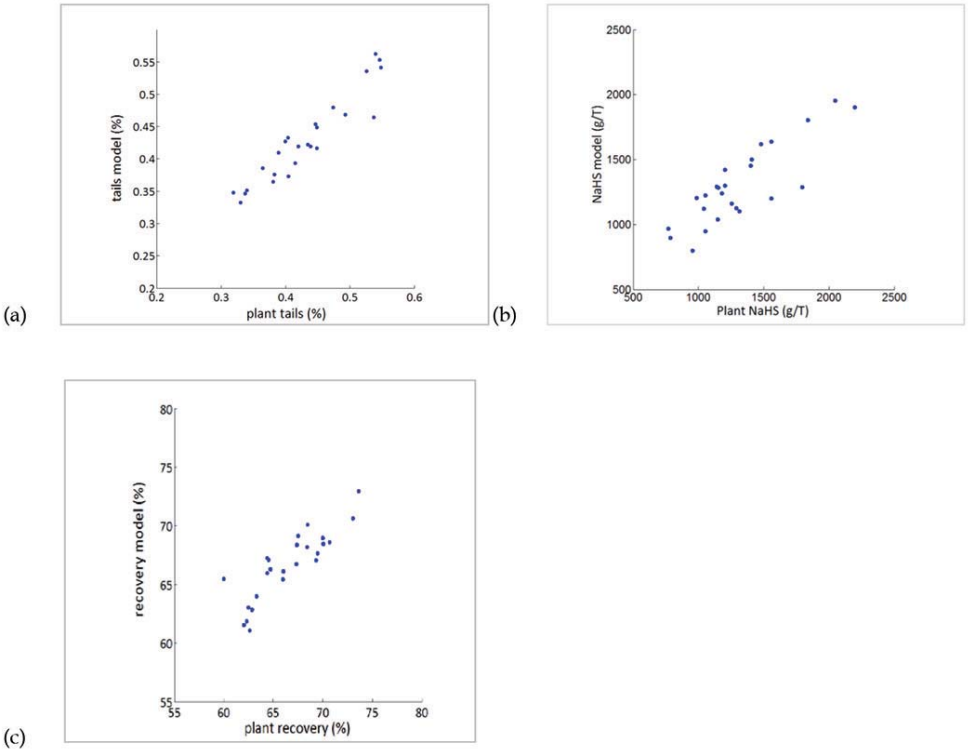

Figure 9—(a) Actual plant tails *versus* model, (b) actual NaHS consumption *versus* model, and (c) actual plant recovery *versus* model

Table VI

Correlation coefficients between the models and the actual results

Parameter	Correlation coefficient
Total Cu tails	0.86
Recovery	0.75
NaHS consumption	0.64

first stage of sulphidization. Similarly, malachite recovery was achieved only in the second stage of sulphidization. Another gain in increasing the number of sulphidization stages is the recovery of liberated coarse-grained minerals.

References

Castro, S., Soto, H., Goldfarb, J., and Laskowski, J. 1973. Sulphidizing reactions in the flotation of oxidized copper mineral II. Role of the adsorption and oxidation of sodium sulphide in the flotation of chrysocolla and malachite. *International Journal of Mineral Processing*, vol. 1. pp. 151–161.

Crozier, R.D. 1991. Flotation, Theory, Reagents and Ore Testing. Pergamon Press.

Dunn, J.G. and Muzenda, C. 2001. Thermal oxidation of covellite (CuS). *Thermochimica Acta*, vol. 369, no. 1–2. pp. 117–123.

Ferron, C.J. and Manu, N.N. 1994. Recovery of copper oxide minerals by sulfidization flotation. Lakefield Research, Canada. 11 pp.

Lee, J.S., Nagaraj, D.R., and Coe, J.E. 1998. Practical aspects of oxide copper recovery with alkyl hydroxamates. *Minerals Engineering*, vol. 11, no. 10. pp. 929–939.

Lee, K., Archibald, D., Mclean, J., and Reuter, M.A. 2009. Flotation of mixed ore copper and sulphide minerals with xanthate and hydroxamate collectors. *Minerals Engineering*, vol. 22. pp. 395–401.

Jones, M.H. and Woodcock, J.T. 1978. Optimization and control of laboratory sulphidization of oxidized copper ores with an ion selective electrode. *Proceedings of the Australasian Institute of Mining and Metallurgy*, vol. 266. pp. 11–17.

Kongolo, K., Kipoka, M., Minanga, K. and Mpoyo, M. 2003. Improving efficiency of oxide-cobalt ores flotation by combination of sulphidisers. *Minerals Engineering*, vol. 16. pp. 1023–1026.

Mwena, M.D. and Mpoyo, M. 2001. Improvements of cobalt recovery in flotation of curo-cobaltiferous ore at Gecamines. *Proceedings of Copper Cobalt Nickel and Zinc Recovery*, Victoria Falls, Zimbabwe, 16–18 July 2001. Southern African Institute of Mining and Metallurgy, Johannesburg. pp. 1–9.

Paquot, F.X. and Ngulube, C. 2012. Development and optimization of mixed sulphide/oxide copper ore treatment at Kansanshi. *Journal of the Southern African Institute of Mining and Metallurgy*, vol. 115, no. 12. pp. 1253–1258. http://dx.doi.org/10.17159/24119717/2015/v115n12a15

Paquot, F.X., Bastin, D., Mukutuma, A., and Delaney, A. 2009. Metallurgical performances of the sulphidization route and the direct alkyl hydroxamates flotation of mixed carbonated copper-gold ores of the Kansanshi deposit. *Proceedings of Flotation 2009*, Cape Town, South Africa, 9–12 November 2009. Minerals Engineering International, Falmouth, UK. ◆

MATRIX REFERENCE MATERIALS

A Part of Torre Industries

QUALITY CRMs
FOR MINING AND EXPLORATION

BUY AMIS MATRIX CRMs
ASSAY STANDARDS PRICED FOR ROUTINE LABORATORY QUALITY CONTROL

- Affordable multi-element "Matrix CRMs"
- Choose from a wide range of AMIS product groups, grades and matrices
- Strong technical support

CREATE CRMs
FROM YOUR OWN ORE

- Improve assay with custom CRMs made from your own ore
- Any batch size from .5 to 5 tonnes
- Shipments accepted from anywhere in the world
- Made according to ISO Guide 34 requirements (for RM producers)
- An ISO 9001:2008 Certified Producer

ROUND ROBINS
JOIN THE AMIS INTER-LABORATORY TESTING SCHEMES

- Assessing mineral laboratory performance against global peers
- For continuous laboratory improvement
- Approximately 50 AMIS proficiency testing schemes (AITS) per year
- According to ISO Guide 43 requirements (for PT schemes)

www.amis.co.za

TÜVRheinland® CERT ISO 9001

ISO 9001:2008 CERTIFIED COMPANY

http://dx.doi.org/10.17159/2411-9717/2016/v116n6a12

Unlocking Rustenburg Base Metals Refiners sulphur removal section

by J. Hagemann* and M. Pelser†

Synopsis

The Anglo American Platinum Rustenburg Base Metals Refiners (RBMR) is the largest producer of nickel cathode in South Africa. It treats slow-cooled matte to recover a platinum group metal-containing magnetic fraction for downstream processing and a nonmagnetic fraction to produce nickel and copper cathode, cobalt sulphate, and sodium sulphate. The refinery was recently expanded from 21 to 33 kt/a nickel. During the ramp-up phase, the sulphur removal section was found to be a constraint to throughput. Nickel hydroxide is precipitated from nickel spent electrolyte by addition of sodium hydroxide, and filtration of the nickel precipitate allows sulphur to be removed from the circuit as aqueous sodium sulphate in the filtrate. The filtration fluxes were found to be limiting the circuit's capacity. An obvious solution would have been to install additional filtration capacity at significant capital cost and long lead times. RBMR chose rather to first initiate a collaborative project with Anglo American Technical Solutions to better understand the impact of process conditions on filtration characteristics and to evaluate whether the filtration flux could be increased by improving the quality of the nickel precipitate.

A deeper understanding of nickel hydroxide precipitation chemistry and kinetics in the context of high nickel and sodium hydroxide concentrations was developed, guided by precipitation theory and confirmed by laboratory tests and plant observations. It was found that the filtration rate could be significantly improved by modifying the precipitate characteristics. A new precipitation process was engineered and retrofitted into the existing plant. Since start-up of the new precipitation system, the available capacity of the sulphur removal section has more than doubled, and control of the process has improved with the better agitation. This paper describes the theory and results used to design the new agitation system, as well as the impact of the change on capital investment, operability, and process efficiency.

Keywords

base metal refining, nickel hydroxide, precipitation, filtration, agitation, sulphur removal.

Introduction

The Anglo American Platinum Rustenburg Base Metal Refiners (RBMR) forms part of the company's smelting and refining complex in Rustenburg for separating and recovering platinum group metals (PGMs) as well as base metals. The hydrometallurgical route for treating converter matte was adopted by Anglo American Platinum in 1966. Since its inception the refinery has undergone a number of expansions, including the commissioning of a new refinery in 1981 and an expansion to 33 kt/a nickel in 2011. The process has evolved to increase throughput, increase recovery, and improve the safety, health, and environment aspects of the operation. The 2011 brownfield expansion entailed changes to the process chemistry and technology using the existing assets with minimal additional equipment. The major new equipment included a new tankhouse for nickel electrowinning. The changes are described in detail by Bryson *et al.* (2008). The expansion project proceeded in a capital-constrained environment following the 2008 financial crisis. The project itself was deferred for a year in 2009 and the plant started plating cathode from the new tankhouse only in 2011. Technical difficulties in integrating certain of the new processes and equipment prolonged the ramp-up phase for the plant (Anglo American Platinum Limited Annual Report, 2012). The sulphur removal section in the BMR was found to be a constraint to throughput in 2013, preventing the plant from reaching its nameplate capacity.

Nickel hydroxide is precipitated from nickel spent electrolyte by addition of sodium hydroxide, and filtration of the nickel precipitate removes sulphur from the circuit as aqueous sodium sulphate in the filtrate. The hydroxide is retained within the circuit by redissolution using additional nickel spent electrolyte. This section was identified as a bottleneck by the frequent build-up of solution ahead of the processing step to a point where the plant needed to turn down or stop. The rate of flow is dictated by the flux achievable during the filtration of the hydroxide precipitate. The nominal throughput capacity of the section was estimated to be equivalent to 21 kt/a (the original plant capacity, even though additional filtration capacity had been installed as part of the expansion project) and needed to be increased by more than 50% to reach 33 kt/a.

* *Anglo American Platinum Ltd, Rustenburg, South Africa.*

† *Anglo American Technical Solutions, Johannesburg, South Africa.*

The obvious solution to increase throughput was to install additional filtration capacity at significant additional capital expenditure. The capital requirement for expanding the filtration capacity was estimated to be in excess of R60 million with a lead time of 9 months for the first filter. RBMR chose rather to initiate a collaborative project with Anglo American Technical Solutions (ATS) to better understand the impact of process conditions on filtration characteristics and to evaluate whether the filtration flux could be increased by improving the quality of the nickel precipitate. Underpinning the project are the fundamentals of precipitation (nucleation and growth mechanisms), which are constrained by the desired chemistry of the overall circuit. The scope of the investigation included generating a deeper understanding of the processes involved during nickel hydroxide precipitation in the context of high nickel and sodium hydroxide concentrations; quantifying the extent to which filtration flux can be improved by manipulating the precipitation conditions; and engineering of the process equipment capable of delivering the desired precipitate.

Sulphur deportment

The RBMR flow sheet can be simplified as shown in Figure 1 for purposes of discussing the sulphur balance. The slow-cooled matte, better known as Waterfall Converter Matte (WCM), is received by RBMR where it undergoes a number of milling and magnetic separation steps to produce a nonmagnetic nickel-copper matte (NCM) and a magnetic-enriched concentrate (MEC). The sulphur associated with the matte accounts for 70% of the total sulphur input into the refinery. The MEC is subjected to a number of oxidative pressure leaching and atmospheric leaching steps targeting the base metal phases to produce a PGM-rich residue. Sulphuric acid is used as lixiviant in these leaching steps, accounting for the additional sulphur input.

The NCM undergoes a series of metathetic and oxidative leaching steps in the leach and purification section to solubilize and separate nickel from copper. Sulphur is solubilized by the oxidation of sulphides to sulphate. The liquors undergo further purification, including the recovery of cobalt as well as the removal of selenium, tellurium, iron, lead, and zinc. The sulphur-based reagents used in this section add to the total sulphur input into the refinery.

Not all of the sulphur in the matte is solubilized and the remaining sulphur is rejected in the copper pressure leach residue (CPLR). The amount of sulphur rejected with the residue depends on the extent of sulphur oxidation during copper leaching. The solubilized sulphur passes through the copper electrowinning tankhouse to produce copper spent electrolyte. It is used to replace fresh acid addition into the leach and purification section and migrates through the circuit to form part of the feed stream to nickel electrowinning. Some sulphur is rejected from the circuit during the various purification steps, while the remaining bulk of the sulphur passes through the nickel electrowinning tankhouse to be rejected in the sulphur removal section. Nickel is returned to the leach and purification section as nickel dissolution solution (NDS). The sodium sulphate produced from the sulphur removal section is transferred to the sodium sulphate crystallization section for recovery. This results in the removal of an estimated 60 kt/a sodium sulphate through the sulphur removal section at an equivalent production rate of 33 kt/a nickel cathode.

Sulphur removal

Soluble sulphur is rejected by the filtration of nickel hydroxide from neutralized nickel spent electrolyte. The sulphur removal section (Figures 2 and 3) draws spent electrolyte from storage into the leading reactor, neutralizing free acid using sodium hydroxide. The nickel hydroxide is precipitated in the second reactor by raising the pH, again using sodium hydroxide. The reactors operate at 80°C. The volume of the reactors results in a mean residence time of approximately 30 minutes per reactor. The precipitated slurry is transferred through a pumpbox to a bank of six rotary vacuum drum filters (Eimco filters). The resultant filtrate passes through a polishing filtration stage, raising the pH value to ensure the nickel concentration is below 10 mg/L before it is transferred to the crystallization plant. The hydroxide cake is repulped and transferred to the dissolution reactors where it is dissolved using additional spent electrolyte. The net result of precipitation and dissolution is the neutralization of free acid produced during electrowinning. The sodium hydroxide consumption therefore reflects nickel production. The dissolution solution is finally returned to the leach and purification section.

The titration curve of nickel spent electrolyte (Figure 4) indicates the initial neutralization of free acid followed by the precipitation of nickel hydroxide. The prominent pH increase between acid neutralization and nickel precipitation allows the two reactions to be segregated into the leading and precipitation reactors, respectively. The ratio of sodium hydroxide used for the two reaction steps depends on tankhouse operation (advance electrolyte tenor and bite) and is reflected in the split of spent electrolyte to precipitation and dissolution. This split ratio is not explicitly set during the operation of the plant. The operator sets the flow to precipitation and allows the controller to draw the spent required for dissolution based on a fixed pH set-point. The reactions are therefore inherently balanced.

Ideally, the operator would control the flow to sulphur removal to balance nickel spent volume. This is, however, not possible in a system that is constrained by filtration capacity. The plant assumes the characteristics of a 'pull' system. The rotary vacuum drum filters operate at maximum capacity and the operator adjusts the throughput in discrete increments to the number of filters online. The pumpbox acts as a small

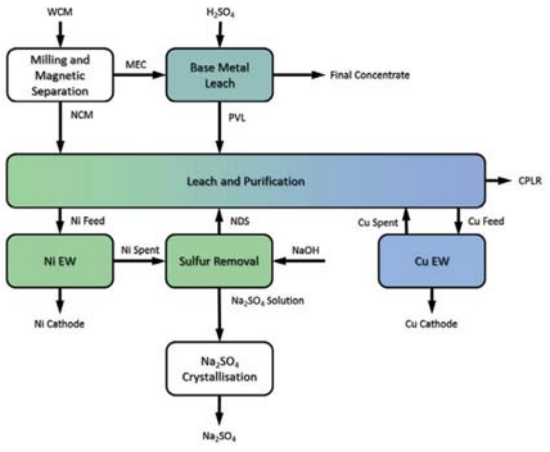

Figure 1—Simplified block flow diagram illustrating sulphur deportment through RBMR

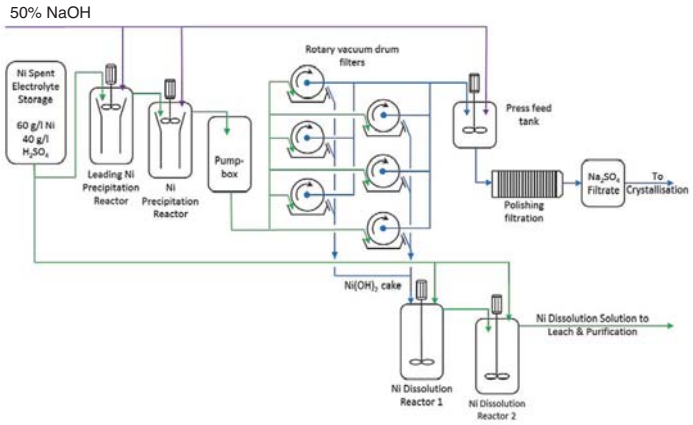

Figure 2—Process flow diagram of the sulphur removal section

Figure 3—Photograph of the sulphur removal section showing the rotary vacuum drum filters in the foreground and the polishing filters, precipitation, and dissolution reactors in the background

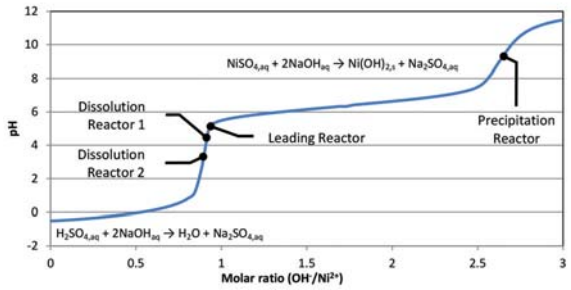

Figure 4—Titration curve of nickel spent electrolyte using sodium hydroxide

buffer, allowing the operator to balance the flows. The flow is subject to fluctuations, causing instability in pH control which will be shown later in the paper to be severely detrimental to the filtration characteristics of the precipitate produced. This further aggravates the problem, causing the throughput to drop below that required to balance the spent electrolyte volume and for the storage tanks to fill. The last resort available to the operator is to drain the boots of the filters to the dissolution reactors, sustaining flow through the plant at the cost of retaining sodium sulphate in the circuit. This causes the sodium sulphate concentration to rise and solution storage in other parts of the plant to fill. Inevitably, the plant needs to be turned down or even stopped to allow the sulphur removal section to recover. The obvious solution to this problem is to increase the filtration capacity of the section through further capital investment. A more challenging solution involves re-evaluating the fundamental filtration characteristics of the nickel hydroxide precipitate, however unlikely this may seem since the existing circuit had operated for more than 30 years.

Methods of improving precipitate quality

Supersaturation is the extent by which a compound exceeds its theoretical solubility in solution, and impacts the properties of solids produced. As an example, Söhnel and Garside (1992) discuss the relationship between supersaturation and precipitation. The control of supersaturation is not easy, given the low solubility levels and fast reaction kinetics involved during precipitation. The kinetics can exceed the rate of mixing, causing the precipitation reaction to be localized within the reactor volume. The concentration of the reactants and method of mixing play pivotal roles in the level of supersaturation generated and hence the quality of the precipitate produced.

Demopoulos (2009), in his review paper on precipitation in hydrometallurgy, suggests the following methods for controlling supersaturation:

- pH control
- Metal complexation and dissociation
- Dilution
- Redox reactions
- Dissolution reactions.

The latter two options are not applicable to the large-scale production of nickel hydroxide. The redox method can be used only in multivalent systems such as Fe^{2+}/Fe^{3+}, while the dissolution method is complicated by the requirement to form a precursor compound from which the final precipitate is produced.

The method of supersaturation control via pH control was studied by Sist and Demopoulos (2003) on synthetic nickel laterite leach solutions (6 g/L Ni). It entails a semi-batch stepwise precipitation procedure, keeping the pH value below the point where the onset of homogeneous nucleation is observed. The method requires seed material to promote heterogeneous nucleation. According to the authors, the method can be translated to a continuous process where each step represents a reactor in series and the final product is

recycled as seed. Application of this method at RBMR would require more than the suggested four stages, given the higher nickel concentration (60 g/L Ni).

The control of supersaturation via complexation during nickel hydroxide precipitation is achieved using ammonia, as described by Mubarok and Lieberto (2013) and E *et al.* (2015). The ammonia complex ($(Ni(NH_3)_6)^{2+}$ lowers the concentration of free nickel, limiting the supersaturation level. A molar ratio NH_4^+:Ni^{2+} in excess of three is required for this method to work. The high ammonia concentration required excludes this method from being applied to RBMR.

Dilution of the reagent streams using barren solutions is a guaranteed method of reducing supersaturation, but it may not always be practical to apply. The extent of dilution achieved by addition of water or recycling of filtrate within the constraints of the process would be insufficient to alter the dominating precipitation mechanism. It is, however, possible to internally dilute the feed streams using the reactor's content, depending on the reactor's operating parameters and mixing. This proved to be the optimum solution for RBMR and will be discussed in more detail.

Investigation

A plant survey was conducted in September 2013 to characterize the circuit. The filtration flux rates (flow of filtrate per unit filtration area) of samples from different points in the circuit were measured using a standardized filtration test (Figure 5). The filtration test was designed to simulate the rotary vacuum drum filters, targeting a similar cake thickness at the same vacuum pressure. Some solids were observed in the leading reactor and, in spite of the low solids loading, presented a high filtration resistance. The highest flux rates were observed at the precipitation reactor, decreasing to half of that value in the pumpbox and ending at one-third of the original value at the boot of the filters. This was interpreted to be indicative of a fragile precipitate and seems to have been considered in the design of the original plant. The reactors are fitted with low-intensity agitators (<0.07 kW/m^3) and draught tubes with no agitation in the pumpbox. At the time of the survey, the initial laboratory results indicated that an improved precipitate could be produced under high-intensity agitation (approx. 0.7 kW/m^3) leading to better dispersion of the reactants. The immediate action taken was to lower the NaOH addition point from the surface to a point close to the impeller in the precipitation reactor. This resulted in an increase in nominal throughput capacity from an estimated equivalent of 21 kt/a to 24 kt/a nickel.

Investigation of the process continued at the hydrometallurgy facilities of ATS. A laboratory reactor (Figure 6) was operated as a mixed suspension mixed product removal (MSMPR) reactor by continuously feeding plant solution and sodium hydroxide, and overflowing the nickel hydroxide product slurry. The reactor was baffled and agitated using a variable-speed overhead stirrer fitted with a double pitch-blade turbine impeller. The reactor was heated using thermal fluid to control the contents at 80±0.1°C. All feed and product vessels were placed on load cell platforms for mass balance purposes. A pressurized pH probe was used and the pH value was maintained within 0.05 pH units of the set-point by the controlled addition of 45% sodium hydroxide. All the equipment (pumps, stirrer, heating circulator, pH transmitter, and weight transmitters) were connected to a process controller for data logging and control purposes. The majority of the test work was conducted in a 2 L laboratory reactor. The effect of scale was evaluated in a 7.5 L laboratory reactor and a 50 L pilot plant reactor train. Scale-up was constrained by available equipment and mixing conditions could not be replicated in full.

The initial programme evaluated reaction conditions (agitation intensity, pH set-point, and residence time), reactor configuration (pre-neutralization, reagent dilution, reagent addition point, and seed recycle) and scale (2 L, 7.5 L, and 50 L). All the tests yield precipitates characterized by filtration flux rates more than double what was achieved under stable plant conditions. The results showed that the reaction condition had the most profound effect on the filtration characteristics of the precipitate. Little benefit was derived from changing the reactor configuration and the different scales evaluated showed the results to be scalable.

The improved results from the tests were explained as follows. The low solubility of nickel hydroxide and high concentrations of reactants (60 g/L Ni in spent electrolyte and 45–50% NaOH) can easily generate high supersaturation levels, pushing the system deep into the homogeneous nucleation region. Mixing in a continuous precipitation reactor involves contacting three fluids, consisting of the two reactant streams and the bulk solution. The combined concentration of the reactants (Ni and OH) in the bulk is kept at its lowest value by controlling the reactor close to the stoichiometric ratio. Supersaturation levels are then limited when mixing the feed streams with the bulk, effectively diluting the reactants prior to the reaction. This is easily achieved in a laboratory-scale reactor with high circulation rates promoting mixing of the inlet streams with the bulk.

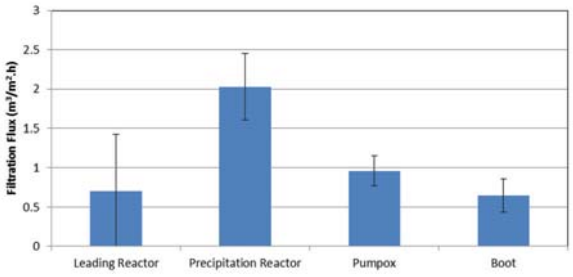

Figure 5—Filtration flux rates measured during plant survey

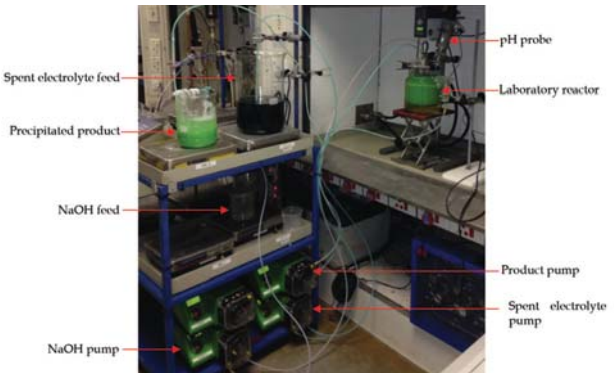

Figure 6—Continuous test work set-up for nickel hydroxide precipitation

The mechanism can be further explained with reference to Figure 7. The black diagonal lines represent increasing levels of supersaturation starting from solubility (S = 1). The blue and red lines represent the mixing lines of spent electrolyte and sodium hydroxide with the bulk solution, respectively. The solid mixing lines represent the optimum pH value (approx. 8.5) with similar supersaturation levels generated while mixing the two reactants with the bulk. With a lower bulk pH value (7.0, dotted lines) the supersaturation level decreases for mixing the spent electrolyte, but increases for mixing sodium hydroxide. The opposite is true with a higher bulk pH value (10, dashed lines). The mixing line with the highest supersaturation level dominates, suggesting deteriorating filtration characteristics on both sides of the optimum.

The explanation was tested against an expanded set of runs evaluating the pH set-point (Figure 8). The extents of precipitation in all of the tests were greater than 98%. The highest flux rate was achieved at the point of lowest combined reactant concentration. At pH set-points below this optimum point, the nickel concentration rises in the bulk solution, likely causing high supersaturation levels around the sodium hydroxide inlet. Again, at pH set-points above this optimum point, the hydroxide concentration rises in the bulk solution, likely causing high supersaturation levels around the nickel spent electrolyte inlet. The explanation held up to the extended test work and was used to develop the design intent of a new reactor.

Field-emission gun scanning electron microscope (FEG-SEM) micrographs indicate a change in the habit of the precipitate formed (Figure 9). The shape of the precipitates produced at both high and low pH set-points tends to be highly irregular, forming loose agglomerates with some fine particles present. The precipitate produced at the optimum pH set-point is spherical in shape and more regular in size. The particle size distributions of the precipitates were measured using a laser diffraction instrument (Malvern Mastersizer). The Sauter mean diameters, d_{32}, of the particles produced at both high (pH 9.5, 6.45 μm) and low (pH 7.5, 9.14 μm) set-points were lower than at the optimum set-point (pH 8.5, 20.2 μm). Flux through a packed bed is proportional to the Sauter mean diameter of the particles, corroborating the results from the filtration tests.

Implementation

A new agitator was engineered and installed into the standby reactor in the precipitation train. The following design intent was used:

- Single-stage precipitation of nickel hydroxide at optimum pH set-point
- Promotion of mixing of feed streams with bulk solution
- Increased circulation of the bulk to promote homogeneity.

The resulting design was a quad-impeller agitator with the feed streams added to the top and bottom of the reactor. Bulk mixing was realized through the multi-impeller arrangement while mixing of the feeds was realized at the individual top and bottom impellers. Offtake from the reactor is from the middle, which is also the pH measurement point. The installed cost of the new agitation system was less than R1 million.

The agitator was commissioned in June 2014. Mixing in the reactor was characterized prior to hot commissioning to confirm that it met the design intent. At the time of installation, there was still some uncertainty regarding the optimum agitation speed and the agitator was therefore fitted with a variable-speed drive. As part of commissioning, the circulation time of the reactor was measured at varying agitation speeds using the methods described by Bourne (1997). The agitation speed was selected to yield the design circulation time (6 seconds). Performance of the section has since been satisfactory, negating the need for further optimization. The measured residence time distribution approximated an ideal CSTR (continuous stirred tank reactor) while the circulation time was significantly lower compared to the old configuration (66 seconds).

Plant operation

One of the immediate effects observed during commissioning was the lower boot levels in the rotary vacuum drum filters. The filtration characteristics of the precipitate improved to

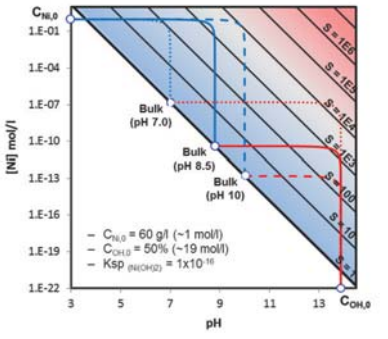

Figure 7—Precipitation diagram for single-stage continuous precipitation of nickel hydroxide. Diagonal lines represents increasing levels of supersaturation

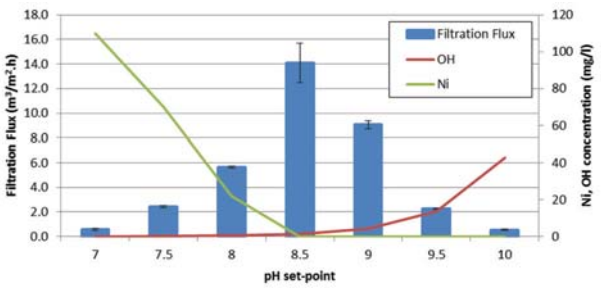

Figure 8—Extended tests evaluating the filtration flux as a function of pH set-point. Nickel concentrations were measured using inductively coupled plasma optical emission spectroscopy (ICP-OES) and hydroxide concentrations were calculated from pH measurements and the water dissociation constant at 80°C

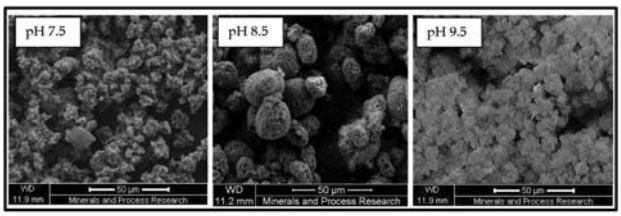

Figure 9—FEG-SEM micrographs of precipitate produced at various pH set-points

such an extent that the filtration rate exceeded the feed rate of the individual filters. Spot filtration tests suggest an improved, robust precipitate being produced, with filtration flux rates measuring up to 12.4 $m^3/m^2.h$ at the reactor and decreasing by only 20% at the drum filter (67% historic). FEG-SEM micrographs (Figure 10) indicate that the habit of the precipitate had changed to match that observed in the optimum laboratory tests.

Operability and efficiency of the plant were assessed using process data for the period prior to the investigation, after the change in the NaOH addition point, and after the installation of the new agitation system. pH control in the reactor benefited from the improved dispersion of NaOH, resulting in a faster-responding signal. An advanced process controller was deployed with the new agitation system to help control pH. The overall result was a decrease in the standard deviation in the pH signal from 0.86 to 0.63 with the changed feed point, and finally to 0.48 with the new agitation system. The improved pH control is essential to consistently produce a good-quality precipitate, as was shown during the investigation.

Operability of the sulphur removal section is reflected in the storage levels of the spent electrolyte. The capacity of the storage is 670 m^3, with intervention required as soon as the level reaches 600 m^3. The frequency of spent storage exceeding 600 m^3 has decreased from 9.1% to 4.8% with the changed feed point to 1.1% with the new agitation system at continually increasing throughputs. The typical number of filters online decreased from five to four with the new agitation system, while the mean boot levels dropped from 85% to 45%. The requirement to drain the filter boots has fallen away, resulting in the average sodium sulphate concentration of the nickel electrolyte decreasing from 170 g/L to 150 g/L. The sulphur removal section is no longer considered to be a constraint to throughput.

The sulphur removal section has consistently been able to match the plant production rate since the installation of the new agitation system. Two capacity runs were conducted to establish the new maximum capacity of the section. This was done by building spent electrolyte volume in storage tanks and then operating the plant with a reduced number of filters. The flow of spent electrolyte was systematically increased to the point where the pumpbox stabilized, indicating the filtration limit. The plant was maintained at this point until the spent volume was depleted. The equivalent nickel production rate was then calculated from the caustic consumption and extrapolated to an equivalent of five filters being online (five online, one standby). The two runs, first with one filter and the second with two filters, indicated an equivalent capacity of 49 and 55 kt/a, respectively. The section has sufficient filtration capacity to reach 33 kt/a, provided that the precipitate's filtration characteristics can be maintained during ramp-up.

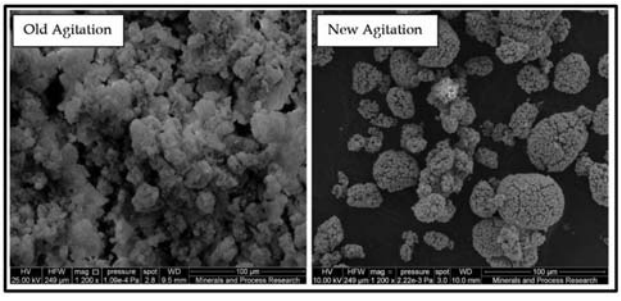

Figure 10—FEG-SEM micrographs of the precipitate produced from the plant before and after installing the new agitation system

Conclusions

The Anglo American Platinum Rustenburg Base Metal Refiners was recently expanded to 33 kt/a nickel cathode capacity and is in the process of ramping up. The sulphur removal section was found to be a constraint to throughput, limiting plant capacity. Through a collaborative effort with Anglo American Technical Solutions the sulphur removal section was unlocked from an equivalent capacity of 21 kt/a Ni to initially 24 kt/a Ni by moving the caustic addition point, and finally to a capacity well in excess of 33 kt/a Ni by installing a new agitation system. The new agitation system changed the habit of the precipitate to match that observed in the laboratory trials. The project was delivered from initialization through investigation and design to implementation in 12 months. The cost of installing the new agitation system was less than R1 million. This obviated the need of the fall-back option, which would have required increasing filtration capacity by installing three additional rotary vacuum drum filters at an estimated cost of R60 million and with a lead time of 9 months for the first filter.

Acknowledgements

The authors would like to thank the management of Anglo American Platinum for permission to present this paper. This was a collaborative project with numerous individuals involved from ATS and RBMR. In particular, the authors would like to acknowledge the contributions of Nico Groenewald and Chandon Bezuidenhout on the test work; Gerhard van Wyk and the RBMR Engineering Department for the implementation of the agitation system; Shaun Johnson for the implementation of the advanced process controller; Eugene Els for the design of the agitation system; and Les Bryson for his support of the project.

References

Anglo American Platinum Ltd. 2012. Annual Report 2012. 276 pp.

Bourne, J.R. 1997. Mixing in single-phase chemical reactors. *Mixing in the Process Industries*. Harnby, N., Edwards, M.F., and Nienow, A.W. (eds.). Butterworth-Heinemann, Oxford. pp. 184–199.

Bryson, L.J., Hofrik, Z., Collins, M.J., Stiksma, J., and Berezowsky, R.M. 2008. New matte leaching developments at Anglo Platinum's base metal refinery. *Hydrometallurgy 2008, Proceedings of the Sixth International Symposium*. Young, C.A., Taylor, C.A., and Choi, Y. (eds.). Society for Mining, Metallurgy and Exploration, Inc., Littleton, CO, USA. pp. 570–579.

Demopoulos, G.P. 2009. Aqueous precipitation and crystallisation for the production of particulate solids with desired properties. *Hydrometallurgy*, vol. 69. pp. 199–214.

Weiwei, E., Jingcai, C., Chao, Y., and Zai-Sha, M. 2015. Experimental study by online measurement of the precipitation of nickel hydroxide: Effects of operating conditions. *Chinese Journal of Chemical Engineering*, vol. 23. pp. 860–867.

Mubarok, M.Z. and Lieberto, J. 2013. Precipitation of nickel hydroxide from simulated and atmospheric-leach solution of nickel laterite ore. *Procedia Earth and Planetary Science*, vol. 6. pp. 457–464.

Sist, C. and Demopoulos, G.P. 2003. Nickel hydroxide precipitation from aqueous sulfate media. *Journal of Metals*, vol. 55, no. 8. pp. 42–46.

Söhnel, O. and Garside, J. 1992. Precipitation: Basic Principles and Industrial Applications. Butterworth-Heinemann, Oxford. ◆

http://dx.doi.org/10.17159/2411-9717/2016/v116n6a13

A modification of the zeta potential of copper sulphide by the application of a magnetic field in order to improve particle settling

by S. Gqebe*, M. Rodriguez-Pascual*, and A. Lewis*

Synopsis

Gravitational sedimentation of suspensions in various precipitation processes is hindered by colloidal stability. This is due to the high surface charge of the suspension and results in strong attraction/interaction between the ions on the particle surface and counter-ions in solution. Moreover, this strong interaction results in a charge build-up that renders the suspension stable. In order to induce gravitational sedimentation of these particles, a redistribution of ions close to the particle surface is required. We therefore sought to redistribute ions close to the particle surface by applying a magnetic field. This results in the reduction of interparticle electrostatic repulsive forces and a subsequent increase in the zeta potential of a suspension. For the purpose of this study, a copper sulphide suspension was used. Copper sulphide particles were exposed to a range of field strengths for set exposure times and their zeta potential was measured before and after exposure. All particles had an initial zeta potential value equal to or less than –40 mV prior to magnetic field exposure. A significant increase in zeta potential was observed, with values reaching a maximum of –16.5 mV when exposed to a 2 T field strength for 40 minutes. This is due to Lorentz ion shifts resulting from the Lorentz force exerted by the magnetic field on the particle surface.

Keywords
precipitation, sedimentation, copper sulphide, zeta potential, colloidal stability, electric double layer, charge destabilization.

Introduction

Metal sulphide precipitation is a process for treating industrial waste streams with high residual concentration of mixed metal ions and acid mine drainage. This process has been reported to achieve higher metal removal compared with the industrially prevalent lime precipitation, due to the sparingly soluble nature of the metal sulphide precipitates formed. However, precipitation is governed by high levels of supersaturation which favour the formation of fine particles (Lewis, 2010). Consequently, some of the metal sulphide fines formed exhibit slow settling dynamics and thus tend to remain suspended in solution.

The formation of fines, which reduces the efficiency of gravitational solid-liquid separation, is encountered in the mining industry. As a result, in most mining processes, large tanks to which chemical flocculant is added are required. Improving the settling characteristics of such fines without the addition of chemical flocculant would reduce both the settling time and volume required for settling. As a result, there is a need to investigate post-precipitation techniques that may improve the settling characteristics of such fines.

Commonly, fines suspended in solution are referred to as stable colloids. Colloidal stability may be attributed to strong interparticle electrostatic repulsive forces that hinder aggregation (Park *et al.*, 2010).

When an electrolyte solution is in contact with another phase, such as a solid, gas, or another liquid immiscible with the electrolyte, a spontaneous redistribution of ions between the two phases takes place (Derjaguin, Churaev, and Muller, 1987). It follows that surfaces acquire a surface electric charge when brought into contact with a polar medium such as water. According to Derjaguin, Churaev, and Muller (1987) and Shiebl, Babick, and Stintz 2012), this charge may be acquired through surface ionization, ion adsorption, and ion dissolution.

The mechanism behind this acquisition of charge is as follows: a cloud of counter-ions forms around the charged particle in solution, creating an electro-neutral counter-ion complex (Haung *et al.*, 1999; Velev and Bhatt, 2006). The ions in the fluid layer closest to the particle surface are strongly attracted to the substrate and are hence immobile. This is known as the Stern layer. Co-ions are repelled by the particle surface. However, they exist in the diffuse layer where both co-ions and counter-ions are found as mobile ions that are adsorbed in equilibrium with one another.

Collectively, the particle surface, Stern layer, and diffuse layer make up the electric double layer (Derjaguin, Churaev, and Muller, 1987). Within the electric double layer, the

* *University of Cape Town, Cape Town, South Africa.*
 ISSN 2225-6253. Paper received Nov. 2014; revised paper received Apr. 2015.

concentration profile of ions gives rise to an electrostatic potential that decays exponentially with increasing distance from the charged particle surface. Along this electrostatic decay, various electrostatic potential points can be found that correspond to the surface, Stern, and zeta potentials.

In a colloidal dispersion, each particle possesses this electric double layer. It follows that the electric double layers of neighbouring particles interact with one another as a result of electrostatic and osmotic forces between the ions and the surfaces (Shiebl, Babick, and Stintz, 2012). This interaction results in changes in the ionic concentration and thus changes in the electrostatic potential distribution. These changes translate to a disturbance of the dissociation and adsorption equilibria within the diffuse layer and therefore change the surface distribution (Chan, 1976; Carnie, Chan, and Gunning, 1995; Chan *et al.*, 2006). A strong overlap may even result in a change in the surface charge sign.

As a result of interacting double layers, an overall interaction energy between particles can be determined. This takes into account the interplay between the attractive van der Waals forces and the electrostatic repulsive forces between particles and can be used to determine whether the particles will attract or repel one another. The ionic concentration strongly affects the electric double layer. This is due to the Debye length, which is a characteristic of the electric double layer thickness and is inversely proportional to the square root of the ionic concentration of a solution. At high ionic strengths, colloids aggregate due to the screening of the charge on the colloids by the electric double layer. The converse is also true: at low electrolyte concentrations the colloids remain dispersed (Attard, 2001). This makes the ionic concentration a key parameter in determining the interaction energy between particles as the electric double layer is the sole contributor to the electrostatic repulsive force between particles. As a result, the balance between the van der Waals attractive force and the electric double layer repulsive force determines the stability of colloidal dispersions (Attard, 2001; Ohshima, 1995).

Colloidal stability is generally indicated by a high absolute magnitude of the zeta potential value, which is usually measured by micro-electrophoresis. This is in accordance with work conducted by Mokone, van Hille, and Lewis (2010) and Nduna, Rodriguez-Pascual, and Lewis (2013). By changing the zeta potential, one can influence the stability of a suspension and thus alter its settling characteristics. This zeta potential is defined as the potential difference between the particle surface and the bulk liquid (Velev and Bhatt, 2006). According to Lipus, Krope, and Crepinsek (2001) and Velev and Bhatt (2006) the zeta potential of a particle can be altered by the application of an external field. The reason for this is that when the colloids in solution are exposed to a magnetic field, a Lorentz force is created which acts on every charged particle moving through the field as shown in Equation [1]:

$$F = qv\mathrm{B} \qquad [1]$$

where F is the Lorentz force [N], q is the electric charge [C], v is the velocity [m.s^{-1}], and B is the magnetic field strength [N.s.C^{-1}.m^{-1}].

The Lorentz force effect on ions in the bulk of the solution can only be determined by Equation [1]. This Lorentz force results in the shifting of ions both in the bulk solution and close to the particle surface (Lipus, Krope, and Crepinsek 2001). However, this ion shift is retarded by the liquid viscosity force. The viscosity force is equal to the Lorentz force in accordance with Newton's law for force balance. As a result, the Lorentz ion shift Δx_i is derived from this relationship via Equations [1] and [2]:

$$F_{vis} = \frac{-6\Pi\eta r_i \Delta x_i}{T} \qquad [2]$$

where F_{vis} is the liquid viscosity force [N], η is the fluid viscosity [kg.s^{-1}.m^{-1}], B is the magnetic field strength [N.s.C-1.m-1], t is the exposure time [s], r_i is the ion radius [m], and Δx_i is the Lorentz ion shift [m].

$$\Delta x_i = \frac{q}{6\Pi\eta r_i} Btv \qquad [3]$$

Calculation of the Lorentz ion shift for ions in the bulk solution revealed that the Lorentz force has very little or no effect on the collision probability of these ions. However, the Lorentz ion shifts become significant close to the particle surface. Lipus, Krope, and Crepinsek (2001) reported that shifted counter-ions in the Stern layer will remain absorbed for a longer time according to desorption time estimations for bivalent ions of natural waters. This is because these bivalent ions have high desorption energies. Without strong adsorption of the shifted counter-ions in the Stern layer and electrostatic attractions, this desorption time would be much shorter. The ion shifts by Lorentz force translate into successful charge destabilization close to the particle surface and alter the zeta potential of particles.

Consequently, the focus of this research was to study the effect of a magnetic field on the interparticle electrostatic repulsive forces by measuring the zeta potential of a copper sulphide suspension.

Previous researchers showed that the application of a magnetic field to ferromagnetic particles, which are particles with a high magnetic susceptibility, increased the settled weight of these particles with time (Higashitani *et al.*, 1994; Wang, Pugh, and Forssberg, 1994). Due to this susceptibility, ferromagnetic particles will strongly attract each other when exposed to a magnetic field as a result of applied magnetic forces. Wang, Pugh, and Forssberg (1994) observed an increase in the settled weight of chromite particles that were previously stabilized in solution with increasing magnetic field strength. In contrast, copper sulphide is diamagnetic and therefore has no magnetic properties. When copper sulphide particles are exposed to a magnetic field, aggregation is not achieved because of magnetic forces. Instead, the magnetic field exerts a Lorentz force on the particle surface and causes a redistribution of ions close to the particle surface, which results in the reduction in the interparticle electrostatic repulsive force. It is this reduction in the electrostatic repulsive force between particles that induces aggregation.

Materials and methods

There are two main steps involved in this study: (1) the precipitation of a copper sulphide suspension and (2) application of a magnetic field to this suspension. Experiments were conducted at atmospheric pressure and 23°C ± 2°C. A metal ion solution with a concentration of

500 mg/L was made by dissolving copper sulphate pentahydrate in de-ionized water and an equimolar sulphide solution was made by dissolving sodium sulphide nonahydrate in de-ionized water. Both solutions were stored in 4 L closed vessels as bulk solutions.

For a single experimental run, 500 mL of each solution was poured into separate beakers. 2 mL of sodium hydroxide was poured into the beaker containing the sodium sulphide solution in order to maintain the pH of the final copper sulphide suspension at a value above 6. This was done in order to avoid the formation of hydrogen sulphide gas, which may result from the reaction at pH values below 6. 2 mL of sodium hydroxide was also added to maintain a constant pH for each experimental run. The beakers were then sealed using parafilm. A 4 mm diameter hole was made in each parafilm layer in order to provide access via tubes to the solution inside each beaker. Nitrogen was sparged into each beaker for 20 minutes in order to minimize reactant oxidation. After sparging, the reaction proceeded in a T-mixing device supplied with reactants by a magnetic gear pump. For effective mixing in a T-mixer, a Reynolds number in the turbulent region must be maintained (Weigl, Bardell, and Cabrera, 2003). This corresponds to a pump speed equal to or greater than 1427 r/min. Consequently, for each experimental run, a pump speed greater than 1427 r/min was used. Due to equipment limitations, a constant pump speed for each experimental could not be maintained and the speed varied between 1650 r/min and 2885 r/min. A 1 L glass vessel was placed at the output end of the T-mixer to collect the formed copper sulphide suspension. From this vessel, a sample of the suspension was taken in order to measure the zeta potential immediately after precipitation. Figure 1 illustrates the set-up used for the precipitation step.

For sampling, a 10 mL syringe was filled with the copper sulphide suspension. This was then dispensed into a 42 mL sample bottle already containing 32 mL of sodium chloride spectator ions with an ionic strength of 0.01 M. The zeta potential of the sample was then measured using a Malvern Zetasizer Nano. Once the zeta potential had been measured, the copper sulphide suspension was exposed to a magnetic field.

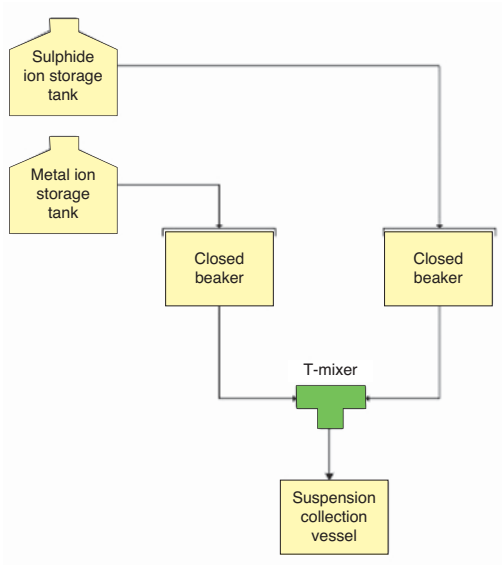

Figure 1—Experimental diagram for the precipitation of a copper sulphide suspension

For this step, a cuvette with a volume of 2 mL was filled with the suspension. The cuvette was then placed in the middle of a 30 cm long stainless steel cylindrical sample holder with a diameter of 1.27 cm. At this midpoint, the cuvette is exposed and not encased by the sample holder as there is a rectangular cutout. The sample holder was then placed between the two magnetic poles. This was a fixed position as the sample holder was screwed into the same position each time. Once the sample was in place, the magnet was switched on to the desired field strength for a set exposure time. For oscillating sample tests, the sample holder motor was switched on. The motor had a fixed speed of 2 Hz. The field strengths and exposure times in Tables I and II were tested:

Subsequent to magnetic field exposure, the zeta potential of the suspension was measured once again.

Results and discussion

Each precipitated copper sulphide suspension had an initial zeta potential equal to or less than –40 mV. Mokone, van Hille, and Lewis (2010) and Nduna, Rodriguez-Pascual, and Lewis (2013) reported that the zeta potential value of a copper sulphide suspension becomes more negative with increasing pH. Furthermore, Nduna, Rodriguez-Pascual, and Lewis (2013) attained a zeta potential value of –50.1 mV for

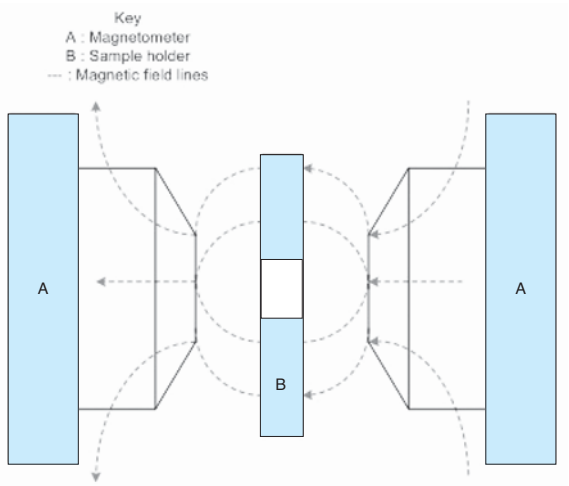

Figure 2—Schematic of magnetometer

Table I

First set of experiments conducted

Sample type	Magnetic field strength [T]	Exposure time [min]
Non-oscillating sample	0.5	40
	0.6	
	0.7	
	0.8	
	0.9	
	1	

Table II

Operating conditions for magnetic exposure

Sample type	Magnetic field strength [T]	Exposure time [min]
Non-oscillating sample	1	10
		20
		40
	1.5	10
		20
		40
	2	10
		20
		40
Oscillating sample	1	10
		20
		40
	1.5	10
		20
		40
	2	10
		20
		40

a copper sulphide suspension precipitated at pH 9. Accordingly, this result was anticipated as each suspension was precipitated at a pH value of 6.3.

Results from the first set of experiments listed in Table I revealed that a magnetic field had negligible effect on the change in the zeta potential of copper sulphide suspensions at field strength values less than 1 T at the exposure time used (Figure 3). At 1 T, there is a noticeable change in the zeta potential of a copper sulphide suspension, from an initial value of –40 mV to –36 mV. This resulted in a less negative zeta potential value. This increase in zeta potential translates to a decrease in the electrostatic repulsive force between colloids. However, the change in zeta potential observed at 1 T will not significantly increase the settling rate of the suspension. This is because a suspension with a zeta potential value of –36 mV is still within the stable colloid range, with a positive net interaction energy which indicates that repulsive electrostatic forces dominate.

A substantial change in the zeta potential of a copper sulphide suspension was seen at field strengths equal to or greater than 1 T when exposed for at least 40 minutes. As can be seen on Figure 4, at 1.5 T, a negligible effect on particle zeta potential was observed for exposure times of 10 and 20 minutes. However, for an increased exposure time of 40 minutes, the zeta potential value of the copper sulphide suspension became less negative and increased from –42.9 mV to –28 mV. The final zeta potential of this suspension is within the range for fast settling rates. This increase in zeta potential is due to a reduction in the interparticle repulsive forces, which favours aggregation as attractive forces now dominate.

At 2 T, an insignificant effect on the zeta potential of a copper sulphide suspension was seen for an exposure time of 10 minutes. However, at this field strength, increasing the exposure time had an observable effect on the zeta potential of a copper sulphide suspension with a maximum of –19.5 mV being reached for an exposure time of 40 minutes. The zeta potential of this suspension increased from –40 mV to –19.5 mV. A comparison of the DLVO plots in Figure 5 for the initial and final zeta potential values for the 2 T suspension showed a decrease in the net interaction energy between colloids. This decrease is due to complete elimination of the electrostatic repulsive forces and thus an overall negative interaction energy with solely attractive van der Waals forces present. This favours aggregation and, by extension, improved settling rates.

The following equations were used to calculate the net interaction energy:

$$V_T = V_R + V_{vdW} \quad [4]$$

where V_T is the net interaction energy [J], V_R is the electrostatic repulsive force [J], and V_{vdW} is the attractive van der Waals force [J].

$$V_R = \varepsilon a \psi_o^2 \exp\frac{-r(s-2)}{s} \quad [5]$$

where ε is the dielectric constant [C.V^{-1}.m^{-1}], a is the particle radius [m], ψ_0 is the surface potential [V], r is interparticle distance [m], and s is the normalized interparticle distance [m].

$$V_{vdW} = -\frac{A}{6}\left[\frac{2}{s^2-4} + \frac{2}{s^2} + \ln\frac{s^2-4}{s^2}\right] \quad [6]$$

where A is the Hamaker constant [J].

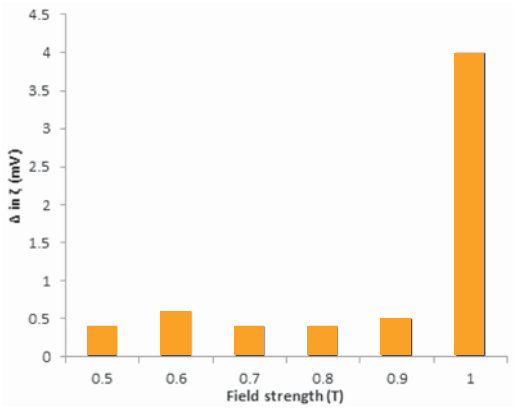

Figure 3—Change in zeta potential for a constant exposure time at various magnetic field strengths

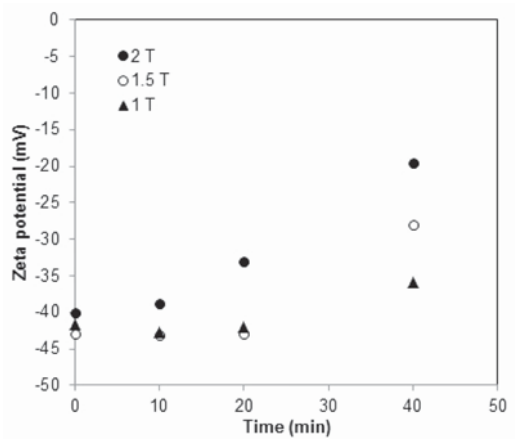

Figure 4—Zeta potential of copper sulphide as a function of exposure time at constant field strength

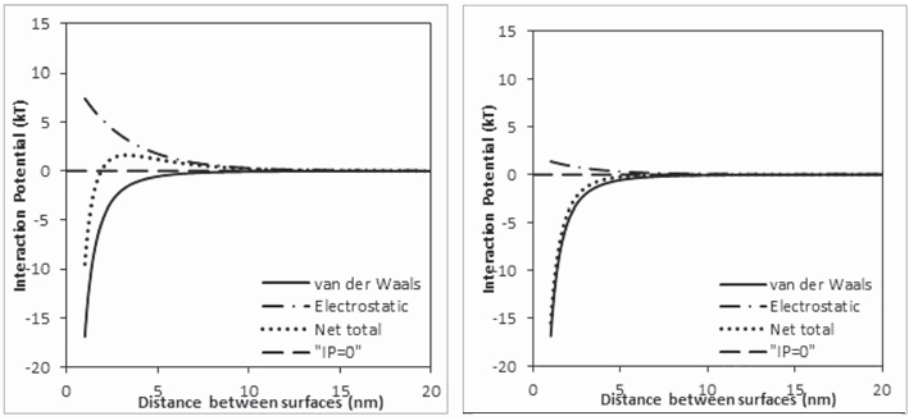

Figure 5—Net interaction energy plots for a suspension with an initial zeta potential of -40 mV (left) and final zeta potential of –19.5 mV (right)

Changes in zeta potential observed when suspensions are exposed to a magnetic field are due to the Lorentz force effect on ions close to the copper sulphide particle surface (Lipus, Krope, and Crepinse k, 2001). This effect is commonly known as the Lorentz ion shift and is solely responsible for the changes in zeta potential observed in this study.

According to Equation [1], the Lorentz force increases with increasing magnetic field strength at constant charge and particle velocity. This is why larger changes in the zeta potential of copper sulphide suspensions at higher field strengths are observed. It is imperative to note that although magnetic exposure destabilizes charge close to the particle surface, the overall system charge remains electro-neutral.

From the results obtained, it can be deduced that the application of a magnetic field improves the settleability of diamagnetic suspensions by eliminating interparticle electrostatic repulsive forces.

In the last set of tests (see Table II), copper sulphide particles were oscillated in a homogeneous magnetic field. Lipus, Krope, and Crepinsek (2001) reported that the most successful magnetic water treatment devices are of dynamic type, with an oscillating dispersion through a static magnetic field. It follows that the results obtained by oscillating copper sulphide in a homogeneous field showed improved results. A maximum zeta potential of –16.5 mV was obtained for an exposure time of 40 minutes. Zeta potential values of –22.3 mV and –20.9 mV were obtained for 1 T and 1.5 T respectively for a 40-minute exposure period.

A comparison of the results shown in Figures 4 and 6 reveals that the zeta potential of copper sulphide particles can be increased to within the range for fast settling rates at lower field strengths when the particles are oscillated in the magnetic field. This is because, for dynamic magnetic treatment, there is a significant reduction in the interparticle repulsive forces on each particle surface due to an increased Lorentz force. This results from an increase in the particle velocity and thus a greater Lorentz counter-ion ion shift in the Stern layer (Lipus, Krope, and Crepinsek, 2001). A comparison of Figures 4 and 6 also shows that an increase in field strength reduces the retention time required for increasing the zeta potential of a suspension to within the range for fast settling rates.

Conclusions

This study shows that there is significant potential in the application of a magnetic field to precipitation processes aimed at treating industrial waste streams with high residual metal ion concentrations, such as acid mine drainage, where the size and charge of the precipitates formed hinder gravitational solid-liquid separation. The technique used in this study not only improves the settling kinetics of a suspension, but does so without the addition of a chemical flocculant and therefore has an added advantage of reducing the volume required for settling. The zero additional chemical additives approach also reduces the environmental impact of industrial waste streams. This study has shown promising results on a laboratory scale; however, further investigation is required before it moves towards industrial application.

From the results, it can also be concluded that the zeta potential of a copper sulphide suspension may be modified by the application of a magnetic field. This is due to the ion redistribution on the particle surface as a result of the Lorentz force. However, this result is achievable only once a threshold magnetic field strength value of 1 T with a minimum exposure time of 40 minutes has been reached. In

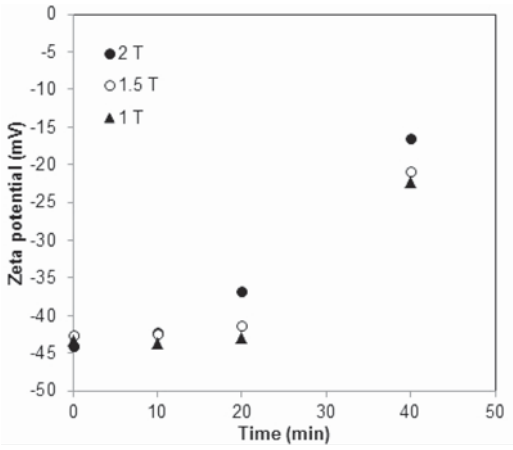

Figure 6—Zeta potential of copper sulphide as a function of exposure time at constant field strengths with a pulsating sample

addition, it can be concluded that as the magnetic field strength is increased, a shorter exposure time is required to eliminate interparticle repulsive forces. This effect is amplified in the case where the suspension is oscillated in the magnetic field. As zeta potential is related to colloidal stability, a change in zeta potential can alter the settling characteristics of a suspension. An increase in zeta potential translates to a decrease in interparticle electrostatic repulsive forces and promotes aggregation. Consequently, shorter settling times are achieved.

Recommendations

Although the effect of a magnetic field on zeta potential has been shown, it is important to verify how long this effect lasts. It follows that determining the magnetic memory of the system is the first recommendation.

The effect of suspension speed on zeta potential could be tested only at a fixed speed of 2 Hz due to equipment limitations. Testing the effect of a range of speed values on zeta potential would provide a broad spectrum of results.

Although zeta potential may be used as a proxy to indicate the settleability of a suspension, further settleability tests may be done if there is interest in quantifying the settleability of the suspension.

The recommendations mentioned above can be achieved only with a magnet that possesses the following functions:

1. Multiple sample holder oscillating speed values
2. Increased sample volume for magnetic exposure
3. Higher magnetic field strengths.

Unfortunately, the magnetometer used in this study did not support these functions. As a result, these tests could not be conducted.

References

Attard, P. 2001. Recent advances in the electric double layer in colloid science. *Current Opinion in Colloid and Interface Science*, vol. 6, no. 4. pp. 366–371.

Carnie, S.L., Chan, D., and Gunning, J.S. 1995. Electric double layer between dissimilar spherical colloidal particles and between a sphere and a plate. *Langmuir*, vol. 10, no. 1. pp. 2993–3009.

Chan, D. 1976. Electrical double layer interactions under regulation by surface ionization equilibria--dissimilar amphoteric surfaces. *Journal of the Royal Society of Chemistry*, vol. 72, no. 1. pp. 2844–2865.

Chan, D., Healy, T.W., Supasiti, T., and Usui, S. 2006. Electrical double layer interactions between dissimilar oxide surfaces with charge regulation and Stern–Grahame layers. *Journal of Colloid and Interface Science*, vol. 296, no. 1. pp.150–158.

Derjaguin, B.V., Churaev, N.V., and Muller, V.M. 1987. Surface Forces. Consultants Bureau, New York.

Higashitani, K., Iseri, H., Okuhara, K., Kage, A., and Hatade, S. 1994. Magnetic effects on zeta potential and diffusivity of nonmagnetic colloidal particles. *Journal of Colloid and Interface Science*, vol. 172, no. 2. pp. 383–388.

Huang, Q.R., Dubin, P.L., Moorefield, C.N., and Newkome, G.R. 1999. Counterion binding on charged spheres: effect of pH and ionic strength on the mobility of carboxyl terminated dendrimers. *Journal of Physical Chemistry B*, vol. 104, no. 5. pp. 898–904.

Lewis, A.E. 2010. Review of metal sulphide precipitation. *Hydrometallurgy*, vol. 104, no. 2. pp. 222–234.

Lipus, L.C., Krope, J., and Crepinsek, L. 2001. Dispersion destabilization in magnetic water treatment. *Journal of Colloid and Interface Science*, vol. 236, no. 1. pp. 60–66.

Mokone, T.P., Van Hille, R.P., and Lewis, A.E. 2010. Effect of solution chemistry on particle characteristics during metal sulfide precipitation. *Journal of Colloid and Interface Science*, vol. 351, no. 1. pp. 10–18.

Nduna, M., Rodriguez-Pascual, M., and Lewis, A.E. 2013. Effect of dissolved precipitating ions on the settling characteristics of copper sulphide. *Journal of the Southern African Institute of Mining and Metallurgy*. vol. 113, no. 5. pp. 435–439

Ohshima, H. 1995. Effective surface potential and double-layer interaction of colloidal particles. *Journal of Colloid and Interface Science*, vol. 174, no. 1. pp. 45–52.

Park, Y., Huang, R., Corti, D.S., and Franses, I. 2010. Colloidal dispersion stability of unilamellar DPPC vesicles in aqueous electrolyte solutions and comparisons to predictions of the DLVO theory. *Journal of Colloid and Interface Science*, vol. 342, no. 2. pp. 300–310.

Shiebl, B., Babick, F., and Stintz, M. 2012. Calculation of double layer interaction between aggregates. *Advanced Powder Technology*, vol. 23, no. 2. pp. 139–147.

Velev, O.D. and Bhatt, K.H. 2006. On chip manipulation and assembly of colloidal particles by electric fields. *Journal of the Royal Society of Chemistry*, vol. 100, no. 27. pp. 38–750.

Wang, Y., Pugh, R.J., and Forssberg, E. 1994. The influence of interparticle surface forces on the coagulation of weakly magnetic mineral ultrafines in a magnetic field. *Colloids and Surfaces*, vol. 90, no. 2–3. pp. 117–133.

Weigl, B.H., Bardell, R.L., and Cabrera, C.R. 2003. Lab on a chip for drug development. *Advanced Drug Delivery Reviews*, vol. 55, no. 3. pp. 349–377. ◆

http://dx.doi.org/10.17159/2411-9717/2016/v116n6a14

Experimental study on phosphorus distribution ratio and capacity of environment-friendly dephosphorization slag for high-phosphorus hot metal pretreatment

by F. Yang*, X.G. Bi*, and J.D. Zhou*

Synopsis

In this investigation, the phosphorus distribution ratios in the CaF_2 system and B_2O_3 system dephosphorization slags for high-phosphorus hot metal pretreatment were measured by an indirect method under laboratory conditions. Firstly, the phosphorus distribution ratio between liquid slag and solid iron was measured, and then the phosphorus distribution ratio between liquid slag and hot metal was calculated. Phosphorus capacity was calculated in terms of the composition and optical basicity of the slag. Dephosphorization slag was also studied by scanning electron microscopy, energy dispersive analysis, and X-ray diffraction analysis. The experimental results show that the phosphorus capacity of the B_2O_3 slag system is much greater than that of the CaF_2 system. It is demonstrated thatB_2O_3 can completely replace CaF_2 as fluxing agent for high-phosphorus hot metal pretreatment. With CaF_2 as fluxing agent, the phosphorus capacity increases with increasing CaO content in the slag, but the phosphorus distribution ratio decreases. B_2O_3, when used as fluxing agent, can react with high melting point phases such as $2CaO{\cdot}SiO_2$ and $3CaO{\cdot}P_2O_5$ in the slag to form new phases with low melting points such as $11CaO{\cdot}B_2O_3{.}4SiO_2$, $2CaO{\cdot}B_2O_3{.}SiO_2$, and $Ca_{9.93}(P_{5.84}B_{0.16}O_{24})$ $(B_{0.67}O_{1.79})$, thereby acting as a fluxing agent. When the ratio of $w(B_2O_3)/w(CaO)$ is 0.16, the phosphorus distribution ratio reaches its maximum value, that is, the dephosphorization ability of the slag is at its maximum.

Keywords
hot metal pretreatment; dephosphorization; phosphorus distribution ratio; phosphorus capacity.

Introduction

As international iron ore prices continue to rise, the development of China's steel industry is facing a lot of pressure. Against this background, development and utilization of domestic high-phosphorus iron ore resources is particularly important. When high-phosphorus iron ore is used in ironmaking, the phosphorus content in the hot metal can reach 0.35% or more, and the hot metal must be pretreated. For hot metal with 0.08–0.10% dissolved phosphorus, the traditional hot metal dephosphorization pretreatment technologies are relatively mature. However, when using these methods to dephosphorize hot metal containing 0.35% P or more, the amount of dephosphorization slag can reach 100–150 kg per ton of hot metal. Furthermore, the traditional dephosphorization methods require the addition of large amounts of CaF_2 as fluxing agent, and this results in high fluoride levels in the dephosphorization slag. The fluorine in the slag can partially dissolve in water and thereby causes high fluoride concentration in the water and soil. Once the fluoride is absorbed by humans or animals, it can result in toxic effects on the central nervous system and myocardium. In addition, fluoride can accumulate in the environment, and thereby pose a health risk to animals and humans through the food chain (Li, 2007; Liu, Wang, and Dong, 2011, Diao, 2013). The objective of this research is to replace CaF_2 with B_2O_3 as fluxing agent while achieving the expected goals of hot metal pretreatment.

The melting point of B_2O_3 (450°C) is much lower than that of CaF_2 (1419°C). B_2O_3 can interact with FeO, CaO, MgO, and other oxides to form compounds with low melting points such as $CaO{\cdot}B_2O_3$ (m.p. 1154°C). Compared with CaF_2, B_2O_3 has a greater advantage in rapid slagging (Hamano and Horibe, 2004). The purpose of this article is to investigate the influence of environment-friendly dephosphorizing slag composition on the dephosphorization process, and to provide a theoretical basis for the preparation of an environment-friendly dephosphorization agent that has strong dephosphorization ability. The phosphorus distribution ratio and phosphorus capacity of the CaF_2 slag system were also determined.

Experimental method

The phosphorus distribution ratio and the phosphorus capacity of B_2O_3 dephosphorization slag for high-phosphorus hot metal pretreatment were determined under

* *Key Laboratory for Ferrous Metallurgy and Resources Utilization of Ministry of Education, Wuhan University of Science and Technology, Wuhan, China.*

 ISSN 2225-6253. Paper received May 2015; revised paper received Nov. 2015.

laboratory conditions using a thermodynamic equilibrium furnace. The interior structure of the furnace is shown in Figure 1. The compositions of the CaF_2 and B_2O_3 slag systems are shown in Table I and Table II, respectively. The compositions of the pure iron crucible and iron foil are shown in Tables III and IV, respectively. In the experiments, 99.999% high-purity argon gas was purged to provide an inert furnace atmosphere. Slag samples were thoroughly mixed and placed into pure iron crucibles. The crucibles were then loaded into the furnace, and the furnace was heated to 1400°C. The temperature was kept constant for 1 hour, and then lowered to 1350°C, before being kept constant at 1350°C for 11 hours. Finally, the crucibles were removed from the furnace and immediately quenched with water to avoid oxidation reactions that would drive the reactions of Fe_2O_3-FeO-Fe to equilibrium. The pre-melted slag from the equilibrium experiments was crushed, and placed again in pure iron crucibles, together with pure iron flakes of about 1 g weight and 0.1 mm thickness. The crucibles containing the pre-melted slag and iron flakes were then loaded into the furnace, and the temperature was raised to 1300°C and kept constant for 12 hours under argon gas protection to obtain a full equilibrium between the slag and iron flakes. Finally, the crucibles were removed and quenched with water to avoid oxidation that would drive the reaction of P-P_2O_5 to equilibrium. The samples obtained from the experiments were treated as follows.

(1) The slag that had adhered on the iron flakes was ground and cleaned up with supersonic waves in an acetone solution

(2) The phosphorus dissolved in the iron flakes was measured with the molybdenum blue light absorption method. The microstructure and elemental composition of the slag were analysed with scanning electron microscopy using energy-dispersive X-ray spectroscopy (SEM-EDS). The minerals in the slag were characterized by X-ray diffraction.

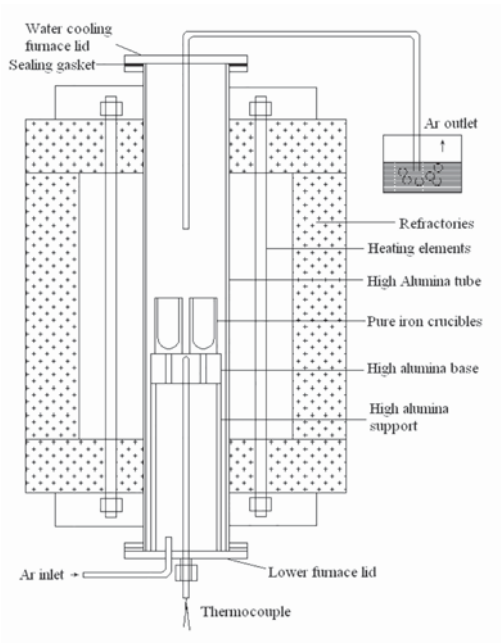

Figure 1—Interior structure of the thermodynamic equilibrium furnace

Calculation of the phosphorus capacity and phosphorus distribution ratio

According to the composition of the slag obtained from the equilibrium experiment, phosphorus capacity is calculated by the following formula (Wei, Yang, and Sommerville, 2002).

$$\lg C_{PO_4^{3-}} = (-\frac{36412}{T} + 37)\Lambda + \frac{71493}{T} - 30.8 \quad [1]$$

where $C_{PO_4^{3-}}$ is the phosphorus capacity, T the reaction temperature (K), and Λ the optical basicity. The Λ is the weighted average of the optical basicity of all components in slag, and is calculated using the formula:

$$\Lambda = \sum_{B=1}^{n} x_B \Lambda_B \quad [2]$$

where Λ_B is the optical basicity of oxide, and x_B is the molar fraction of cations in oxide.

Table I

Composition (mass %) of CaF_2 slag system

No.	FeO	SiO_2	P_2O_5	CaO	CaF_2
1-0-1	11.32	7.06	13.44	51.73	16.45
1-0-2	10.24	9.12	16.12	48.75	15.77
1-0-3	10.50	10.79	18.50	46.10	14.31
1-0-4	10.37	12.03	19.65	43.72	14.23

Table II

Composition (mass %) of B_2O_3 slag system

No.	$w(B_2O_3)/w(CaO)$	FeO	SiO_2	P_2O_5	CaO	B_2O_3
3-0-1	0.08	8.14	9.93	15.28	61.71	4.94
3-0-2	0.10	5.37	9.71	15.78	62.85	6.29
3-0-3	0.12	5.85	9.81	15.43	61.53	7.38
3-0-4	0.14	6.66	7.24	15.41	62.01	8.68
3-0-5	0.16	6.34	7.30	14.65	61.82	9.89
3-0-6	0.18	5.68	7.15	14.36	61.79	11.12

Table III

Composition of pure iron crucible (mass %)

C	Si	P	Mn	S	N
0.008	0.002	0.006	0.017	0.005	0.008

Table IV

Composition of iron foil (mass %)

C	Si	Mn	P	S	Cr	Cu
0.07	0.0032	0.036	0.021	0.001	0.006	0.032
Ti	**V**	**As**	**B**	**Zn**	**Fe**	
0.0012	0.0001	0.005	0.001	0.011	99.8	

x_B also denotes the molar fraction of oxygen of oxide in the slag, and is calculated by formula:

$$x_B = \frac{n_O x_B'}{\sum n_O x_B'} \quad [3]$$

where x_B' is molar fraction of oxide, n_O is the number of oxygen atoms in the oxide molecule. It is specified that one fluorine atom in the fluoride molecule is equal to 1/2 oxygen atoms. x_B' can be calculated by:

$$x_B' = \frac{w_B / M_B}{\sum \frac{w_B}{M_B}} \quad [4]$$

where w_B is the percentage of oxide and M_B is the molar mass of oxide.

In this paper, the measured value of the phosphorus distribution ratio is not between liquid slag and carbon-saturated hot metal but between liquid slag and solid iron flake, thus a conversion is needed. Im, Morita, and Sano (1996) calculated the phosphorus distribution ratio between liquid slag and solid pure iron flakes (Tsukihashi, Nakamura, and Orimoto, 1990; Knacke, Kubaschewski, and Heselmann, 1991; Im, Morita, and Sano, 1996; Zhou *et al.*, 2011). The expression of phosphorus distribution ratio is as follows:

$$L_P^{Fe\text{-}\alpha,\gamma} = \frac{(\%P)}{[\%P]^{Fe-\alpha,\gamma}} \quad [5]$$

where $\alpha L_P^{Fe-\alpha}$ is the phosphorus distribution ratio between liquid slag and α iron, $L_P^{Fe-\gamma}$ the phosphorus distribution ratio between liquid slag and γ iron, %P the mass percentage of P in liquid slag, $[\%\ P]^{Fe\text{-}\alpha}$ the mass percentage of P in α iron, and $[\%\ P]^{Fe\text{-}\gamma}$ is the mass percentage of P in γ iron.

After thermodynamic conversion, the distribution of phosphorus between carbon-saturated iron and α iron and γ iron is obtained by:

$$\frac{[\%P]^{Fe-\alpha}}{[\%P]^{Fe-C}} = 0.779 \quad [6]$$

([P] in solid iron is larger than 0.41%)

$$\frac{[\%P]^{Fe-\gamma}}{[\%P]^{Fe-C}} = 0.413 \quad [7]$$

([P] in solid iron is smaller than 0.41%)

where $[\%\ P]^{Fe\text{-}C}$ is the mass percentage of P in carbon-saturated hot metal.

Results and discussion

Phosphorus capacity and phosphorus distribution ratio of CaF_2 slag system

Equilibrium compositions and phosphorus capacity calculated for the CaF_2 slag system are shown in Table V.

The phosphorus contents in the CaF_2 slag system and solid iron flake, and the phosphorus distribution ratio between liquid slag and carbon-saturated hot metal are also shown in Table VI. The relationship between phosphorus distribution ratio and CaO content is depicted in Figure 2.

It can be clearly seen from Table V that when the CaO content in the slag is the highest, the phosphorus capacity of the CaF_2 slag system reaches the maximum value. That is, at a CaO content in slag of 49.72%, the phosphorus capacity is 11.66×10^{22}. At a CaO content in slag of about 44%, the change in phosphorus capacity is small. As can be seen from

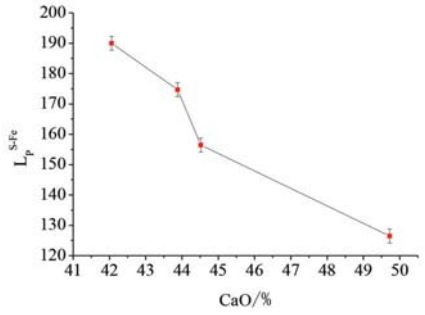

Figure 2—Relationship between phosphorus distribution ratio and CaO content

Table V

Equilibrium composition (mass %) and phosphorus capacity of CaF_2 slag system

Test number	FeO	Fe_2O_3	CaO	SiO_2	P	CaF_2	$C_{PO_4^{3-}}$ x 10^{22}
1-0-1	7.64	3.2	49.72	6.91	5.39	16.06	11.66
1-0-2	5.63	3.14	44.52	8.99	6.44	15.12	3.274
1-0-3	5.78	2.3	43.88	10.51	7.19	14.60	2.948
1-0-4	6.52	2.86	42.06	11.72	8.28	13.61	2.331

Table VI

Phosphorus distribution ratio of CaF_2 slag system

Test number	(FeO) (mass %)	(P) (mass %)	$[P]_{Fe}$ (mass %)	$LP^{s\text{-}Fe}$
1-0-1	7.64	5.39	0.0176	126.48
1-0-2	9.63	6.44	0.0172	156.45
1-0-3	5.78	7.19	0.0176	174.67
1-0-4	6.52	8.28	0.0179	189.98

Experimental study on phosphorus distribution

Table VI and Figure 2, $L_p^{s\text{-}Fe}$ increases with decreasing CaO content. For example, as the CaO content decreases from 49.72% to 42.06%, the $L_p^{s\text{-}Fe}$ increases from 126.84 to 189.98. $L_p^{s\text{-}Fe}$ is influenced synthetically by slag basicity, fluxing agent content (effect of slag melting), and FeO content, among other factors. $L_p^{s\text{-}Fe}$ of the slag in test 1-0-4 is 189.98, the maximum value. The basicity of 1-0-4 slag is 3.76. However, $L_p^{s\text{-}Fe}$ of 1-0-1 slag reaches the minimum value, with a basicity of 17.20. When the basicity is too high, the dephosphorizing slag contains solid CaO particles deposited from the bath. The higher the basicity, the more CaO particles are deposited. Figures 3 and 4 show elemental analyses and a micrograph of CaO solid particles in melted slags from tests 1-0-2 and 1-0-3, respectively. It can be clearly seen that the quantity and size of CaO particles in melted slag with 44.52% CaO are much greater than in slag with 43.88% CaO. This explains why $L_p^{s\text{-}Fe}$ bears an inverse relationship to CaO content. More CaO particles increase the viscosity of slag, which in turn decreases $L_p^{s\text{-}Fe}$. In this condition, it is required to decrease the basicity of the slag, increase the amount of fluxing agent, or increase the FeO content of the slag.

Phosphorus capacity and phosphorus distribution ratio of B_2O_3 slag system

Equilibrium compositions and phosphorus capacity calculated for the B_2O_3 slag system are shown in Table VII.

Phosphorus distribution ratios obtained for the B_2O_3 slag system between liquid slag and carbon-saturated hot metal are shown in Table VIII. The relationship between phosphorus distribution ratio and $w(B_2O_3)/w(CaO)$ is depicted in Figure 5.

As can be seen from Table VII, the phosphorus capacity of all B_2O_3 slag system is generally higher. The highest value is as high as 57.54×10^{23}. It can be seen from Table VIII and Figure 5 that at a $w(B_2O_3)$ to w(CaO) ratio of 0.16, the phosphorus distribution ratio reaches the highest value of 156.12. As the B_2O_3 content continues to increase, the phosphorus distribution ratio begins to decrease. As such, this kind of slag system (test number 3-0-5) has the highest dephosphorization ability.

When the quantity of B_2O_3 is appropriate, during the dephosphorization reaction, B_2O_3 reacts with $2CaO{\cdot}SiO_2$ to form $11CaO{\cdot}B_2O_3{\cdot}4SiO_2$ and $2CaO{\cdot}B_2O_3{\cdot}SiO_2$. Moreover, B_2O_3

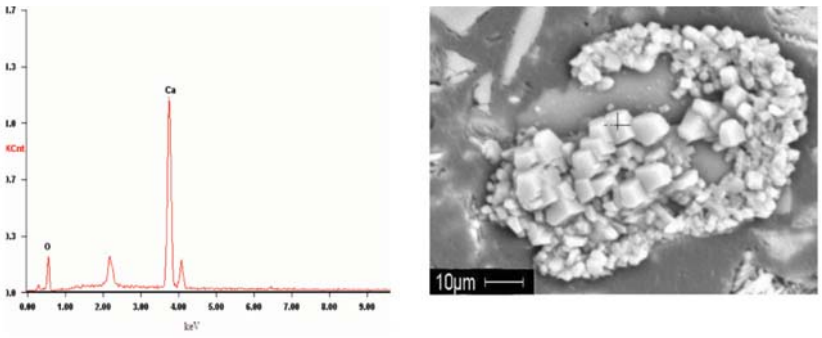

Figure 3—Elemental analysis and micrograph of CaO particles in slag, test 1-0-2

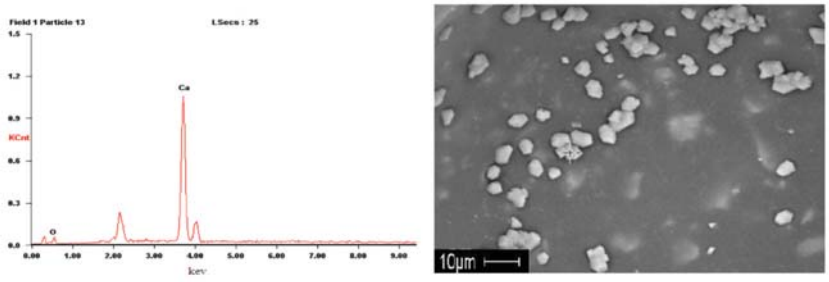

Figure 4—Elemental analysis and micrograph of CaO particles in slag, test 1-0-3

Table VII

Equilibrium composition (mass %) and phosphorus capacity of CaF_2 slag system

Test number	$w(B_2O_3)/w(CaO)$	FeO	Fe_2O_3	CaO	SiO_2	P	B_2O_3	$C_{PO_4^{3-}}$ x 10^{23}
3-0-1	0.08	6.55	1.58	60.91	8.23	4.83	4.87	6.46
3-0-2	0.10	4.15	1.30	60.86	5.62	5.79	6.47	57.54
3-0-3	0.12	5.58	1.13	59.41	8.29	5.69	7.02	2.95
3-0-4	0.14	4.54	2.76	60.81	5.53	5.63	8.12	5.62
3-0-5	0.16	5.30	1.39	59.58	8.26	6.88	9.48	1.41
3-0-6	0.18	4.54	1.43	60.85	5.40	5.68	10.95	3.09

Experimental study on phosphorus distribution

Table VIII

Phosphorus distribution ratios of B_2O_3 slag system

Test number	(FeO) (mass %)	(P) (mass %)	$[P]_{Fe}$ (mass %)	$LP^{s\text{-}Fe}$
3-0-1	6.55	4.83	0.0179	111.44
3-0-2	4.15	5.79	0.0184	129.96
3-0-3	5.58	5.69	0.0173	135.83
3-0-4	4.54	5.63	0.0183	147.06
3-0-5	5.30	6.88	0.0182	156.12
3-0-6	4.54	5.68	0.0183	128.19

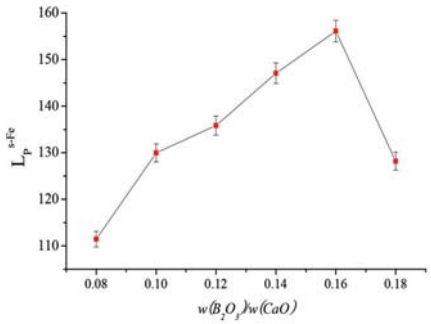

Figure 5—Relationship between phosphorus distribution ratio and $w(B_2O_3)/w(CaO)$

continues to react with $3CaO{\cdot}P_2O_5$, which is formed by reaction between CaO and P_2O_5, to form $Ca_{9.93}(P_{5.84}B_{0.16}O_{24})(B_{0.67}O_{1.79})$, which has a low melting point. Thus B_2O_3 acts as a fluxing agent and is beneficial for dephosphorization reactions. In this case, the phosphorus distribution ratio and capacity are the highest. The XRD pattern from test 3-0-5 is shown in Figure 6.

Conclusions

With CaF_2 as fluxing agent, the phosphorus capacity of dephosphorization slag for high-phosphorus hot metal is between 2.331×10^{22} and 11.66×10^{22}. Phosphorus capacity increases with increasing slag basicity. However, too high a CaO content adversely affects the phosphorus distribution ratio because the melting of the dephosphorization slag becomes difficult, and this reduces the fluidity of the slag, hindering diffusion and decreasing the dephosphorization rate.

The phosphorus capacity of the B_2O_3 slag system is between 1.41×10^{23} and 57.54×10^{23}, which is one order of magnitude higher than CaF_2 system. It has been demonstrated that B_2O_3 can completely replace CaF_2 as fluxing agent for high-phosphorus hot metal pretreatment.

The phosphorus distribution ratio of the B_2O_3 system is 111.44–156.12. At a $w(B_2O_3)$ to $w(CaO)$ ratio of 0.16, the phosphorus distribution ratio reaches its highest value. The dephosphorization ability of this slag system is therefore the strongest.

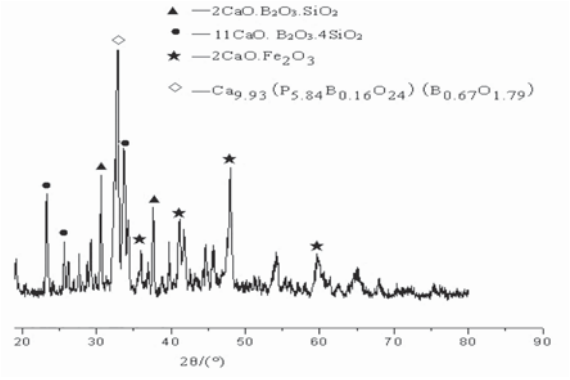

Figure 6—XRD pattern of $w(B_2O_3)/w(CaO)=0.164$

References

Diao, J. 2013. Effect of Al_2O_3 and Na_2O on dephosphorization of high phosphorus hot metal. *Journal of Iron and Steel Research*, vol. 25, no. 2. pp. 9–10.

Hamano, T. and Horibe, M. 2004. The dissolution rate of solid lime into molten slag used for hot-metal dephosphorization. *ISIJ International*, vol. 44, no. 2. pp. 263–267.

Im, J., Morita, K., and Sano, N. 1996. Phosphorus distribution ratios between $CaO\text{-}SiO_2\text{-}Fe_tO$ slags and carbon-saturated iron at 1573K. *ISIJ International*, vol. 36, no. 5. pp. 517–521.

Li, C. 2007. Fluoride pollution sources, control technology and its source. *Iron & Steel Technology*, no. 3. pp. 5–153.

Knacke, O., Kubaschewski, O., and Heselmann, K. 1991. Thermochemical Properties of Inorganic Substance. Springer-Verlag, Berlin.

Liu, L., Wang, S., and Dong, Y. 2011. Performance of low fluoride dephosphorization slag of hot metal. *Journal of Iron and Steel Research International*, vol. 18, no. 1. pp. 11–15.

Tsukihashi, F., Nakamura, M., and Orimoto, T. 1990. Thermodynamics of phosphorus for the $CaO\text{-}FetO\text{-}CaF_2\text{-}SiO_2$ and $CaO\text{-}Al_2O_3$ systems. *Tetsu-to Hagane*, vol. 76, no. 10. pp. 1664–1671.

Wei, E. Yang, Y., and Sommerville, I.D. 2002. The fundamentals of using custom-designed slags to remove impurities from liquid steel. *Proceedings of the 60th Electric Furnace Conference*, San Antonio, TX, 10–13 November 2002. Kanagy, D.L. and Baker, M.A. (eds.). Iron & Steel Society, Warrendale, PA. pp. 761–771.

Zhou, J. Bi , X, Huang, Z., and Jin, Y. 2011. Phosphorus distribution equilibrium between $CaO\text{-}FeO^*\text{-}SiO_2\text{-}P_2O_5(15\%)\text{-}CaF_2(B_2O_3)$ slag system and carbon-saturated hot metal at 1573K. *Proceedings of the International Conference on Chemical, Material and Metallurgical Engineering*, Beihai, China 23-25 December, 2011. Trans Tech Publications, Zurich. pp. 369–372. ◆

http://dx.doi.org/10.17159/2411-9717/2016/v116n6a15

Tiger's eye in the Northern Cape Province, South Africa – grading, distribution, small-scale mining, and beneficiation potential

by S. Rasmeni*, D. Chetty*, P. Sebola*, and K. Seripe*

Synopsis

South Africa's Northern Cape Province hosts semi-precious and gemstone occurrences that are sporadically mined on a small scale by local communities. Tiger's eye, a gemstone known for its chatoyancy properties, is found in important deposits located near the town of Prieska, where is it intermittently mined. Challenges faced by small-scale and informal mining include mining without proper permits, risky mining practice in dangerous terrain, and illegal export of raw material without concerted effort at domestic beneficiation. As part of a study aimed at job creation and social upliftment in the region, tiger's eye deposits in the Prieska area were assessed to assist small-scale miners to understand tiger's eye grades and their distribution. This will allow not only more efficient and safer mining of these deposits, but also beneficiation of the raw product into tumbled stones, cabochons, jewellery, and other small artefacts for sale. A hub established in Prieska by Mintek trains locals in the beneficiation of tiger's eye. Supply to the hub must make use of a consistent grading system, which is discussed in this paper. Together with proper mine licensing, such an approach will develop mining and beneficiation skills, and create and sustain employment for the local community.

Keywords
Tiger's eye, grading, beneficiation, small-scale mining.

Introduction

Tiger's eye is a semi-precious stone known for its chatoyancy property, which is caused by parallel, silicified asbestos fibres that impart a silky lustre to specimens. Deposits of tiger's eye in the surrounds of the town of Prieska, Northern Cape Province, formed the focus of a study aimed at small-scale mining and beneficiation of this commodity. The Prieska tiger's eye deposits are located along the N10 route to Upington (Figure 1). Tiger's eye is unevenly distributed and occurs as lenses of various sizes, interbedded in gently folded metasedimentary rocks of mostly banded iron formation (BIF). The tiger's eye occurrence in the Northern Cape Province, especially in the Prieska area, has not been extensively researched. There is thus limited information available in the public domain. The lack of knowledge on tiger's eye distribution has resulted in local small-scale miners adopting a trial-and-error method of mining. Basic geological mapping and field evaluation of the deposit, coupled with professional judgement, are important aspects of any small-scale mining operation and can contribute significantly to the formulation of various acceptable and equally viable mining methods and practices.

A recent study by Ledwaba (2014) was aimed at documenting brief introductory details on tiger's eye mining and its potential for employment creation and poverty alleviation in the Prieska area. In the past, studies were undertaken by Mintek with the aim of grading tiger's eye in the Northern Cape (Kleyenstüber, 1990; Pillay and Thompson, 2008). This was after Mintek realized that a proper grading and pricing system for raw tiger's eye was lacking. According to information from local miners, the grades and prices remain dictated by foreign buyers, who export the material to countries like China, the UK, and Italy to be beneficiated.

This paper provides outcomes from fieldwork that was designed to evaluate and map tiger's eye deposits located in areas to the west and northwest of Prieska, and to explore artisanal mining activities in the area, with a view to understanding the geology, mining methods, distribution of mineralization, and ultimately, the sustainability of the operations in terms of tiger's eye supply. Furthermore, a standard grading system based on scientific observations has been refined, based on samples sourced from various suppliers in the Prieska area. These samples are graded based on bench-scale tumbling and polishing tests in order to match the *in situ* estimation of grade with tumbled product quality. In the absence of an international standardized grading system, a consistent grading system that is fully understood by suppliers, miners, and buyers is recommended.

* *Mineralogy Division, Mintek, Randburg, South Africa.*
 ISSN 2225-6253. Paper received Aug. 2015; revised paper received Nov. 2015.

Tiger's eye in the Northern Cape Province, South Africa

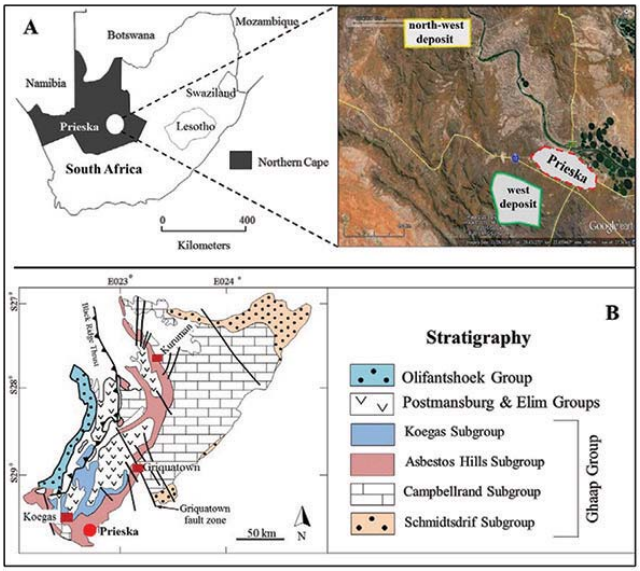

Figure 1—(A) Locality map of South Africa, showing the Northern Cape Province and the Prieska area. The Google Earth image shows the locality of the two mapped tiger's eye deposits. (B) Geological map and stratigraphic column showing the Asbestos Hills Subgroup, which hosts the tiger's eye deposits (modified from Schröder *et al.*, 2011)

Geological setting and occurrence

The deposits are hosted in BIF of the Asbestos Hills Subgroup within the the Ghaap Group, which is overlain by the Postmasburg and Elim Groups, and Olifantshoek Group of the Transvaal Supergroup. The Asbestos Hills Subgroup within the Ghaap Group is underlain by the Schmidtsdrif and Campbellrand subgroups and is overlain by the Koegas Subgroup (Figure 1A). The surface geomorphology is characterized by mountainous terrain. The surface geology is largely dominated by unconsolidated aeolian sands and calcretes. Together, they mantle the BIF, which is distributed in patchy erosional remnants rather than in large continuous units.

Associated with the tiger's eye seams are pockets containing crocidolite asbestos (unsilicified material) that could pose a health risk to miners trying to dislodge the tiger's eye from the seams. The Prieska tiger's eye deposits are characterized by numerous active and abandoned diggings, some of which have been abandoned due to lack of proper mining equipment and technology to expose and extract the seams. If the tiger's eye seam dips steeply, the miners are forced to abandon the area as they cannot remove the thick overburden.

Tiger's eye distribution

Although other tiger's eye occurrences have been reported on numerous private farms in the Prieska area, two major deposits occur on communal land. The first deposit is located west of Prieska, and the second deposit is located towards the northwest (Figure 1B). The BIF units that host tiger's eye are separated by a pediment surface covered by vegetation and, in some places, unconsolidated, reddish-brown to grey aeolian sands and gravel. Three types of tiger's eye occur in the area. These are blue tiger's eye (silicified crocidolite); yellow tiger's eye, and variegated tiger's eye (a mixture or intergrowth of yellow and blue tiger's eye with sharp contacts between them). The yellow type is the more sought-after variety, although the silicified blue (crocidolite) and variegated material are also required by the world market. Additionally, fibrous tiger's eye is encountered in the outcrops, where unsilicified asbestiform fibres are present. A more systematic method of grading the yellow variety of tiger's eye according to its thickness, lustre, and non-deformity of the fibres has been investigated by Mintek in the past and a refinement of this method is presented later in this paper.

Prieska west deposit

The study area, which covers an area of approximately 32 km^2, is located between 5 km and 15 km west of Prieska with a boundary along the N10 highway to Upington (Figure 1B). This is the more intensively exploited deposit of the two studied, and occurs at elevations between 980 m and 1280 m with thickness varying between 2 cm and 5 cm. Mineralization is hosted in fold-related structures that are associated with faulting. Folds and fold-related veins strongly control the location of these deposits. The weathered and calcretized BIF is well exposed in most excavations studied and occurs interbedded mostly with tiger's eye and calcretized sandy soil and gravel. Therefore, the geology throughout the study area, especially the low-lying areas, is dominated by alternations of calcareous and calcified soil and gravels, deeply weathered and calcretized BIF, and calcrete hardpan.

Mining in weathered and calcretized BIF is relatively easy, but also risky, since the overburden is prone to collapse. Weathered BIF is relatively soft, whereas sandy, calcareous soils that have an open voided grain structure, with the individual grains being separated by a bridging material (such as loose powder calcrete or calcite) possess a collapsible fabric (Figure 2). This bridging material loses strength and rapid settlement may take place if such soils are exposed to increased moisture content under load. On the other hand, mining in calcrete hardpan (hardened calcareous soils) areas using simple equipment such as picks and shovels could be a futile exercise since the ground is rigid and compacted.

The occurrence of various types of tiger's eye in the Prieska west area is presented in the form of a geological map in Figure 3. The information on the map is based on the tiger's eye seams exposed on the surface and the distribution of previous mining activities. Seventy-five excavations/trenches measuring 1.5–70 m × 2–2.5 m × 0.5–3 m were evaluated. The various BIF units hosting tiger's eye are categorized as follows: high-grade zones (approx. 80% yellow, 18% blue/variegated, and 2% fibrous tiger's eye occurrences); low-grade zones (approx. 40% yellow, 50% blue/variegated, and 10% fibrous tiger's eye), and fibrous zones (approx. 10% yellow, 60% blue/variegated, and 30% fibrous tiger's eye). The fibrous type is restricted to the south to southwest portion, in the vicinity of the abandoned asbestos mine.

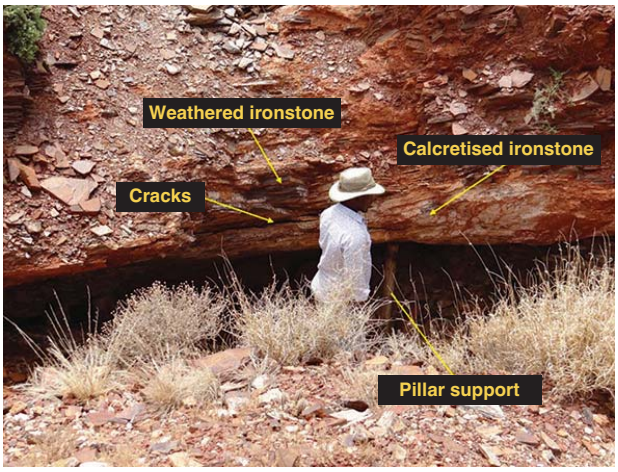

Figure 2—Hanging overburden resulting from tiger's eye mining, with poor support

Prieska northwest deposit

The Prieska northwest deposit is located about 35 km northwest of the Prieska community area. The total claim area, which comprises the Geduld farm, covers an extent of between 15 km² and 18 km² and is set in mountainous and faulted terrain. The deposit is accessed through a single-track road, with sandy and rocky driving conditions due to high and uneven terrain.

The geology of the Prieska northwest area is presented in the form of a geological map in Figure 4. In the northern sections of the claim area, two abandoned asbestos mines are located about a kilometre from dilapidated farmhouses. Loose

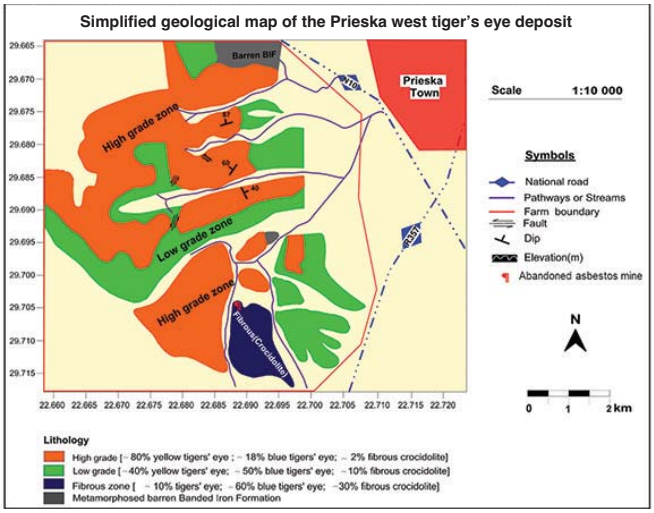

Figure 3—Geological map of the Prieska west tiger's eye deposit, showing zones of high- and low-grade tiger's eye, and asbestos-rich and barren areas

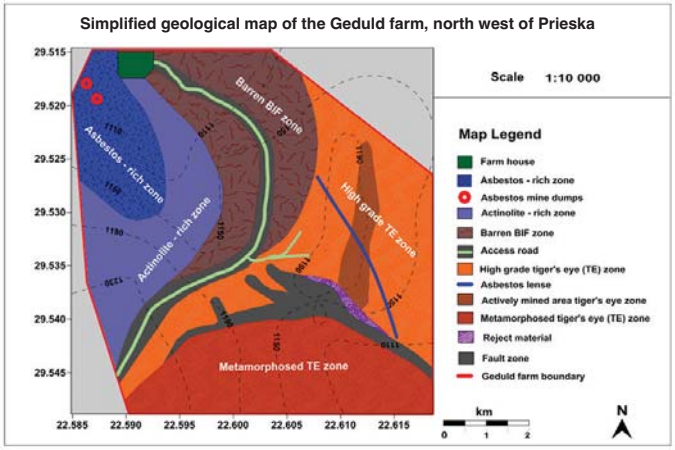

Figure 4—Geological map of the Prieska northwest tiger's eye deposit, showing zones of high-grade tiger's eye, and asbestos-rich, actinolite-rich, and metamorphosed tiger's eye zones, as well as barren areas

chert and dolomite can also be observed around the abandoned asbestos mines. The south and southeastern sections consist of approximately 25 diggings or trenches with intensely metamorphosed BIF and quartzite outcrops hosting tiger's eye.

Visible trenches and some untapped surface exposures show that two grades of tiger's eye occur in the area: high grade, which is restricted to the centre and eastern portion, and reject material towards the southern portion of the farm boundary. The reject material observed in this area is unique, in that it resembles the high-grade material but lacks chatoyancy, which is the main feature of tiger's eye. The absence of the chatoyancy effect can be attributed to intense metamorphism. Fibre bundles are distorted, resulting in difficulty in separation from the country rock, and this renders reject material unusable in the gemstone industry. Folds and vein-related structures strongly control the location of the tiger's eye deposits in this area.

Tiger's eye grading

Grading of tiger's eye is focused mainly on the yellow or golden yellow variety since this is most sought-after. Although a systematic grading method based on physical and mineralogical characteristic has been developed by Mintek in the past (Kleyenstüber, 1990), ambiguous tiger's eye grading systems still exist among various small-scale miners. Their grading system is based on the individual's experience. In a normal situation, the price of each product should be influenced by grade. However, circumstances such as market supply *vs*. demand, the financial situations of the seller and buyer, and their relationship often play a role in the pricing. Various grades of tiger's eye were sourced from different suppliers in the Prieska area. The main aim was to compare the quality of various stones purchased, as per local grading, with the Mintek grading system.

Currently, yellow tiger's eye material from the Prieska area is graded based on physical appearance into three grades, in order of decreasing quality: A, B, or C. The A grade is further categorized into A1 (lowest quality), A2, A3, and A4 (highest quality), and B grade is subdivided into B1, B2, B3, and B4, based on the thickness of the seam, as shown in Table I. The A4 and B4 grades are reportedly rare.

Table I

Grades and standardized prices of tiger's eye from Prieska suppliers

Description	Thickness (mm)	Price per kg (rands)
A1 or (A medium)	10–19	25
A2	20–24	30
A3	25–32	35
A4*	> 32	40–50
B1 or B medium	10–19	15
B2	20–24	18
B3	25–32	20
B4*	> 32	22–25

*Rare/uncommon in this area.

Criteria for tiger's eye grading

Chatoyancy creates the attractive visual effect for which tiger's eye is known. However, this effect can be altered by the slightest orientation change of a single fibre, incomplete silicification, and the grain size and orientation of the replacing mineral, quartz. In low-grade tiger's eye specimens, thick fibres, incomplete silicification, and size and orientation of quartz replacement can be easily observed. In a high-grade material, such characteristics are observed under the petrographic microscope, as they occur on a very limited scale. Microscopic features do not have a major impact on the price or quality of tiger's eye and many of them do not directly affect the chatoyancy.

The following characteristics are used during tiger's eye grading (Kleyenstüber, 1990; Pillay and Thompson, 2008):

- *Colour*—the golden or honey yellow and light brown colours are the most valuable and are also more prized than blue or variegated material
- *Length of fibre*—thin seams <10 mm are generally considered as reject material, and the fibres that are >100 mm are the most valuable
- *Chatoyancy lines*—graded according to frequency and sharpness. Material with sharp lines is more valuable than that with diffuse lines. High-quality tiger's eye should have numerous straight and sharp chatoyancy lines, whereas lower quality specimens will have broken or wavy lines
- *Fibre orientation in relation to the host rock*—fibre orientation affects the cutting of the gemstone. The fibres should be oriented perpendicular to the bedding in the host rock, otherwise chatoyancy is reduced. For high-quality material, the fibre length orientation should not be greater than 5° to the bedding. Kinks and bends also decrease the quality of specimens
- *Macro inclusions*—macro and micro inclusions are also considered during tiger's eye grading. Macro inclusions are cracks, holes, and pit marks, which will have a definite detrimental effect on the beneficiated product. Such inclusions on the micro scale are best viewed under the optical microscope
- *Silicification*—silicification should be complete, with no asbestos fibre remaining
- *Texture*—fine-textured fibre bundles show the best play of light, whereas coarse-textured material, as well as incomplete silicification, will cause problems during cutting and polishing.

Prieska suppliers vs. Mintek's grading system for tiger's eye

Table II summarizes Mintek's grading of tiger's eye using the A, B, C, and reject material classifications. This was the benchmark against which raw material purchased from different local suppliers was compared. The various categories of A-grade tiger's eye material (as per supplier classifications), consisting of A1, A2, and A3, were cut and polished, with some tumbled (Figure 5), to observe the consistency of the appearance of the final product. Based on the polished and tumbled pieces, the physical characteristics of the A-grade categories are all similar to that of the Mintek A-grade classification. The only difference is the thickness of

Table II

Mintek's grading system for tiger's eye (Kleyenstüber, 1990; Pillay and Thompson, 2008; present study)

Grade	Colour	Fibre properties			Appearance		Inclusions		Mass
		Fibre length (mm)	Fibre orientation	Chatoyancy lines	Lustre	Texture	Inclusions	Types of inclusions	pieces (g)
A	Yellow	10–20	Perpendicular	1*	Silky	Fine	None	–	100–200
	Light brown, yellow brown	10–20	Perpendicular to 50° off vertical	>2 (straight)	Silky	Medium	None	–	100–250
B	Yellow brown, light brown, brown, khaki	15–25	Angular – single kink	1* – >2 (straight)	Silky to dull	Fine or medium	Few	Pitting marks, fracture, lines, holes or minerals*	200–350
C	Light brown/ light yellow, brown, khaki	20–30 S=S-shaped	Z=Strong kinks	> 2 broken, wavy and Straight	Silky, glassd or Dull	Medium or coarse	Plenty	Veins, spots, fracture, host rock, holes or minerals*	400–500
Reject	Yellow, brown, blue, green	<10	Perpendicular	1*	Silky	Coarse	Plenty	Various or crocidolite	100–200

1* = Strong visual effect
Minerals* Mineral inclusions include quartz, magnetite, and goethite

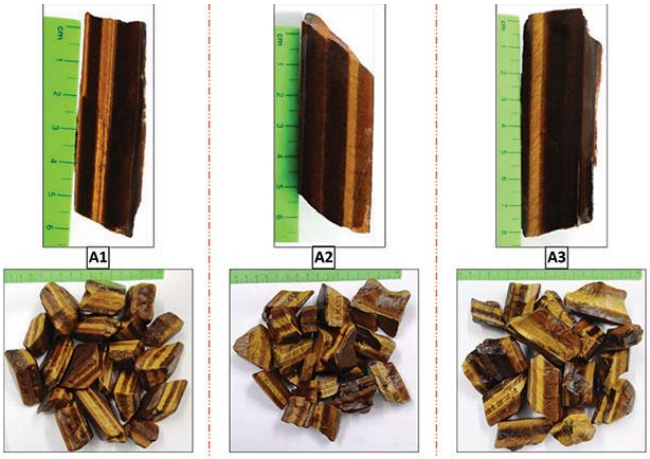

Figure 5—Polished pieces of tiger's eye (top) and tumbled products (bottom) of A-grade sub-types

the seam in each category. The A1 grade varies in thickness from 1 cm to 1.9 cm, whereas the A2 grade has a thickness of about 2 cm to 2.4 cm, and A3 varies from 2.5 cm to 3.2 cm in thickness. Except for seam thickness, there is no observable distinction between the A-grade sub-categories.

The B-grade material is subdivided into B1 and B2 (Figure 6) based on the thickness. The physical characteristics of the B1 material are equivalent to the Mintek B-grade classification, and the seam thickness varies from 1 cm to 1.9 cm. On the other hand, the B2 grade varies in thickness from 2 cm to 2.4 cm and the physical characteristics do not meet the Mintek classification for B-grade material. These samples are characterized by numerous black lines and inclusions of iron oxide, hydroxide, and quartz. Furthermore, they polish poorly due to the presence of coarse fibre bundles. Apart from that, veins cut across the material and possess wavy fibre bundles. Therefore, the above characteristics for B2-grade material are equivalent to those of C-grade material in the Mintek grading scheme.

Beneficiation potential

A beneficiation hub was commissioned in Prieska by Mintek and the National Youth Development agency in June 2014. This hub currently trains unemployed youths from the area in a structured programme. Mintek and the Siyathemba Municipality are responsible for running the facility, with the Municipality to take over responsibilities in future. The facility is managed through a local entrepreneur in consultation with both responsible parties. Current training, done via Mintek, focuses on jewellery-making using tiger's eye sourced from the Prieska area, and finished pieces have been successfully marketed (Figure 7), typically for between R300 and R500 a piece. Training on pottery and glass bead making has been included as a value addition to the tiger's eye jewellery making. Additionally, stone cutting and jewellery production utilize other semi-precious stones sourced locally.

Marketing models are under development to promote the sale of the beneficiated products, which will range from

Figure 6—Polished pieces of tiger's eye (top) and tumbled products (bottom) of B-grade subtypes

Figure 7 – Jewellery produced at the Prieska beneficiation centre, making use of tiger's eye

jewellery to small artefacts and novelties. Once in full production, the hub will bring much-needed relief and avoid exploitation of the small-scale miners by intermediate and foreign buyers. The miners will be able to sell their raw material directly to the Prieska beneficiation hub at competitive prices, through a consistent grading system understood by all. This will also ensure proper quality control of the products brought to market, and hence consistent and competitive pricing of finished products, all of which will be managed by the local learners currently in training. Ultimately, the community will thus take responsibility for the sustainability of the hub activities. If correctly managed, the Prieska tiger's eye deposit is expected to remain in production for the next 15–20 years. This, together with other tiger's eye deposits in the surrounding areas such as Niekerkshoop, will ensure a sustainable supply to, and viability of, the Prieska beneficiation hub.

Conclusion

Tiger's eye mining operations in the Prieska area continue to spread due to the increased demand for this commodity and the preference for mining over other means of livelihood such as farming in the area. While the majority of the miners continue living in extreme poverty with little or no formal education, their situation is expected to change.

The present study successfully delineated zones of high, low, and reject grades of tiger's eye in the two field areas near Prieska. The information, together with identified asbestos zones, will assist the miners to effectively and safely mine the tiger's eye. Furthermore, the refined grading scheme can be used for consistent quality assessment and pricing, and thus reduce exploitation of miners, as they will understand, and work using, the uniform system. Pricing can then be competitively done to alleviate illegal export.

Local beneficiation opportunities established through the hub in Prieska will promote skills development and job creation in the community. Training programmes will ensure that miners are regulated, and thoroughly trained in marketing, mining methods, and financial management. In this way, improved small-scale mining of these deposits can supply the beneficiation centre, and help sustain domestic beneficiation and marketing of this semi-precious stone.

Acknowledgements

The authors would like to that the following organizations and agencies for their support.

Department of Mineral Resources (DMR)
Council for Geosciences (CGS) – Upington Office
National Youth Development Agency (NYDA)
Siyathemba Municipality.

References

LEDWABA, P.F. 2014. Tiger's eye in the Northern Cape Province – potential for employment creation and poverty alleviation. *Journal of the Southern African Institute of Mining and Metallurgy*, vol. 114. pp. 881-885.

KLEYENSTÜBER, A.S.E. 1990. A proposed grading system for raw tiger's eye. *Mintek report* no. M406D. Randburg. 11 pp.

PILLAY, K. and THOMPSON, W. 2008. IM3 – mineralogy and grading of tiger's eye from the Northern Cape, South Africa. *Mintek report* no. 40332. Randburg.

SCHRÖDER, S., BEDORF, D., BEUKES, N.J., and GUTZMER, J. 2011. From BIF to red beds: Sedimentology and sequence stratigraphy of the Paleoproterozoic Koegas Subgroup (South Africa). *Sedimentary Geology*, vol. 236, no. 1–2, 15 April 2011. pp. 25–44. ◆

http://dx.doi.org/10.17159/2411-9717/2016/v116n6a16

Selenium minerals and the recovery of selenium from copper refinery anode slimes

by C. Wang*, S. Li*, H. Wang*, and J. Fu*

Synopsis

Since it was first identified in 1817, selenium has received considerable interest. Native selenium and a few selenium minerals were discovered several decades later. With the increasing number of selenium minerals, the occurrence of selenium minerals became the focus of much research. A great number of selenium deposits were reported all over the world, although few independent selenium deposits were discovered. Selenium is obtained mainly as a byproduct of other metals, and is produced primarily from the anode mud of copper refineries. This paper presents a comprehensive review of selenium minerals, as well as the treatment of copper refinery anode slimes for the recovery of selenium. Our focus is on the selenium minerals, including their discovery and occurrence, and the distribution of selenium resources. In addition, the main methods of recovering selenium from copper anode slimes are summarized.

Keywords
selenium, selenium minerals, anode slimes.

Introduction

Selenium (Se) was first observed in 1817 in a laboratory (Greenwood *et al.*, 1984). The discovery of selenium was made by the Swedish chemist J.J. Berzelius and J.G. Gahn, who isolated selenium from a red residue in sulphuric acid from pyrite mined at Fahlun, Sweden. Selenium was named from the Greek word selene (moon), since it resembled tellurium, which had been discovered a few years earlier and named from the Latin word *tellus* (Earth).

After the first observation of selenium in the laboratory, selenium received considerable interest. In 1954, E.P. Kaiser pointed out that Se is enriched in sulphide ores and often associated with Bi, Co, Sn *etc.* (Kaiser 1954). In 1959, Hawley and Nichol investigated selenium in Canadian sulphide minerals, and presented the content of selenium in sulphide from several deposits of different types. They also proposed that Se is enriched in low-temperature hydrothermal pyrite (Hawley and Nichol, 1959). The thermodynamic conditions for forming native selenium and selenium minerals in sedimentary rocks were discussed, as well as geochemical behaviour of selenium near the oxidation zones of sulphides in the 1970s (Howard III, 1977; Zhu *et al.*, 2003). Zhu *et al.* examined the morphology, features, and genesis of native selenium from Yutangba, Enshi City, Hubei Province, China in 2004, and pointed out, from the different forms of native Se, that selenium can be activated,transformed, remobilized, and enriched at sites such as in the unsaturated subsurface zone or in the saturated zone (Zhu *et al.*, 2005). The transport and deposition of selenium in felsic volcanic-hosted massive sulphide deposits of the Yukon Territory, Canada was studied and reported by Layton-Matthews *et al.* (2005).

Selenium is a comparatively rare and greatly dispersed element. The average selenium content in the Earth's crust is considered to vary between 0.05 and 0.09 μg/g (Lakin 1972; Greenwood *et al.*, 1984; Jiajun *et al.*, 1997). Elemental selenium is seldom found in nature; industrially, selenium is obtained as a by-product of mining other metals such as copper, iron, and lead (Fishbein 1983; Wen and Qiu 1999). It is produced primarily from the anode slimes of copper refineries (Butterman *et al.*, 2004). There are various reports in the literature on the treatment of copper anode slimes to recover selenium (Hoffmann 1989; Cooper 1990).

In this paper, we provide an overview of selenium minerals, as well as the recovery of selenium from copper refinery anode slimes. Our focus is on the occurrence of selenium minerals and selenium deposits. We also examined the research work reported in the literature on the treatment of copper refinery anode slimes for the recovery of selenium.

Selenium minerals

In 1956, Thompson *et al.* discovered felty

* *School of Mining Engineering, University of the Witwatersrand, Johannesburg, South Africa.*
 ISSN 2225-6253. Paper received Dec. 2012; revised paper received Feb. 2016.

native selenium, which is violet acicular crystal. Coleman and Delevaux (1957) investigated the occurrence of selenium in sulphide from sandstone-type uranium ores in the western USA, and discovered trigonal and monoclinic native selenium, as well as clausthalite and ferroselite (Thompson *et al*,. 1956; Coleman and Delevaux, 1957). The occurrence of large particle of native selenium up to 20–30 mm in length in coal seams was reported by Zhu *et al.* (2005). In 1990, spherical and tubular native selenium was discovered in a hydrothermal U-Se-Re polymetallic deposit (Zhu *et al.*, 2003).

The selenide deposits in the eastern Harz Mountains, Germany were intensively studied. The selenide-bearing deposits at Tilkerode, Lerbach, Clausthal, Zorge, St. Andreasberg, and Trogthal, are recognized as typical selenide vein deposits of telethermal origin (Simon *et al.*, 1997). The polymetallic selenide mineralization at Tilkerode, Zorge, Lerbach, and Trogthal occurs mainly as small deposits not associated with larger base-metal deposits, while the selenide minerals at Clausthal and St. Andreasberg are associated with larger deposits mined primarily for silver, lead, zinc, and copper. The series of selenides from Tilkerode was identified mainly by Tischendorf: clausthalite (PbSe), naumannite (Ag_2Se), tiemannite (HgSe), eskebornite ($CuFeSe_2$), trogtalite ($CoSe_2$), hastite ($CoSe_2$), freboldite (CoSe), bornhardtite (Co_3Se_4), berzelianite (Cu_2Se), umangite (Cu_3Se_2), klockmannite (CuSe), and stibiopalladinite (Pd_5Sb_2) (Davis *et al.*, 1977; Stanley *et al.*, 2002). Two unidentified minerals, noted by Tischendorf in 1958, represented two new species: chrisstanleyite ($Ag_2Pd_3Se_4$) and tischendorfite ($Pd_8Hg_3Se_9$) (Stanley *et al.*, 1990, 2002). Wallis described a number of additional mineral species in the Tilkerode selenide assemblage: krŭtaite ($CuSe_2$), athabascaite (Cu_5Se_4), temagamite (Pd_3HgTe_3), eucairite (CuAgSe), trüstedtite (Ni_3Se_4), penroseite ($(Ni,Co,Cu)Se_2$), and geffroyite ($(Ag,Cu,Fe)_9(S,Se)_8$) (Stanley *et al.*, 2002).

Davis *et al.* (1977) reported a new selenide of palladium, palladseite ($Pd_{17}Se_{15}$), which occurs in the residual concentrates from gold washing at Itabira, Minas Gerais, Brazil and is associated with arsenopalladinite, isomertieite, and atheneite.

Selenian miargyrite ($AgSb(Se_{0.6}S_{1.4})_2$), a new variety of miargyrite, was found in gold-bearing quartz veins in middle-lower Silurian quartzite of the Ailaoshan metamorphic belt, Yunnan province, China. It is intimately associated with freibergite, stibnite, ullmannite, and native gold and occurs as grains from 0.1 to 0.02 mm in diameter (Yunfen *et al.*, 1990).

Stanley *et al.* (1990) examined the precious and base metal selenide mineralization at Hope's Nose, Torquay, Devon, England. The selenide assemblage consists of clausthalite (PbSe), tiemannite (HgSe), klockmannite (CuSe), umangite (Cu_3Se_2), tyrrellite ($(Cu,Co,Ni)_3Se_4$), trustedtite (Ni_3Se_4), penroseite ($NiSe_2$), naumannite (Ag_2Se), eucairite (AgCuSe), and fischesserite (Ag_3AuSe_2). A new mineral, chrisstanleyite ($Ag_2Pd_3Se_4$), was discovered in gold-bearing carbonate veins in Middle Devonian limestones at Hope's Nose. It is associated with palladian and argentian gold, fischesserite, clausthalite, eucairite, tiemannite, umangite, cerussite, calcite, and bromian chlorargyrite (Paar *et al.*, 1998).

Selenio-sulfantimonide was discovered in the Laerma gold-copper-uranium deposit in China in 1993. It is associated with native gold, tiemannite, clasthalite, lautite, aurostibite, gersdorffite, quartz, barite, *etc.* and occurs as fine grains, about 0.01–0.5 mm (Minghua *et al.*, 1993).

As many selenium minerals were identified and discovered, numerous investigators conducted imvestigations on selenium minerals. More than 90 selenium minerals had been identified by 1998. Wen and co-workers reviewed the selenium minerals and their occurrence (Huayun, 1998).

Recently, a new series of selenium minerals was discovered. Stanley *et al.* (2002) reported a new mineral species from the Eskaborner Stollen at Tilkerode, Harz Mountains, Germany. Tischendorfite occurs as aggregates in a carbonate matrix, together with the associated metallic minerals clausthalite, tiemannite, chrisstanleyite, stibiopalladinite, and gold.

Schlemaite, a new mineral species from the Niederschlema–Alberoda vein-type uranium deposit, was discovered at Hartenstein, Erzgebirge, Germany. It occurs in aggregates of up to several hundred micrometres across, with berzelianite, eucairite, and clausthalite in a dolomite-ankerite matrix. Of the three vein-type uranium deposits in the Schneeberg-Schlema-Alberoda ore district, Niederschlema-Alberoda is considered the major occurrence of selenides in the Erzgebirge of Germany. In addition, rare selenides of Cu, Bi, Hg, Ni, and other elements were reported (Förster *et al.*, 2003).

Jaguéite, the copper analogue of chrisstanleyite, was discovered in a telethermal selenide vein-type deposit at the El Chire prospect, Los Llantenes District of La Rioja Province, Argentina. The new species is generally associated with chrisstanleyite, particularly in intimate intergrowths, clausthalite, naumannite, tiemannite, klockmannite, berzelianite, umangite, and aguilarite. In addition, two unnamed compounds, chemically $(Ag, Cu)_6Hg_2Pb_2Se_3$ and $(Ag, Cu)_8Hg_3(S, Se)_7$, occur as rare constituents (Paar *et al.*, 2004).

Jolliffeite, previously known only from Lake Athabasca, Saskatchewan, Canad was reported from the Niederschlema–Alberoda uranium deposit in the Erzgebirge region of Germany. Jolliffeite, an exotic mineral, is associated with haematite, Ni–Co–Se-bearing löllingite, clausthalite, tiemannite, mercurian hakite–giraudite solid solutions, sulphurian berzelianite, sulphurian umangite, hessite, Ni-Co-As-bearing pyrite, and Se-rich chalcopyrite (Förster *et al.*, 2004).

Three occurrences of clausthalite were reported in Poland, in abandoned polymetallic deposits at Kowary and Kletno and the Fore-Sudetic copper deposits (Thompson *et al.*, 1956; Kucha, 1982). A new occurrence of clausthalite, together with uraninite, was reported in the Sudetes, southwest Poland. Clausthalite forms veinlets in a breccia comprising <50% calc-silicate rock fragments (Thompson *et al.*, 1956).

Plumboselite, a new selenite from the Tsumeb mine, Namibia, occurs as fibres on clausthalite and is associated with smithsonite, mimetite, and vaterite. It occurs in subparallel to divergent clusters of thin, flattened, colourless fibres up to 0.3 mm in length (Kampf *et al.*, 2011).

All the reported selenium minerals are shown in Tables I–III. The minerals are mainly selenides, selenium sulphides

Table I

Selenide minerals (Huayun, 1998; Zhu *et al.*, 2003)

Name	Chemical formula	Name	Chemical formula
Antimonselite	Sb_2Se_3	Athabascaite	Cu_5Se_4
Bambollaite	$Cu(Se, Te)_2$	Bellidoite	Cu_2Se
Berzelianite	Cu_2Se	Bohdanowiczite	$AgBiSe_2$
Bornhardtite	$Co^{+2}Co_2^{+3}Se_4$	Bukovite	$Tl_2Cu_3FeSe_4$
Cadmoselite	CdSe	Clausthalite	PbSe
Crookesite	$Cu_7(Tl, Ag)\ Se_4$	Dzharkenite	$FeSe_2$
Eskebornite	$CuFeSe_2$	Eucairite	CuAgSe
Ferroselite	$FeSe_2$	Fischesserite	Ag_3AuSe_2
Freboldite	CoSe	Guanajuatite	Bi_2Se_3
Hastite	$CoSe_2$	Jolliffeite	(Ni, Co) AsSe
Kitkaite	NiTeSe	Klockmannite	CuSe
Kullerudite	$NiSe_2$	Luberoite	Pt_5Se_4
Makinenite	γ-NiSe	Mgriite	Cu_3AsSe_3
Merenskyite	$(Pd, Pt)\ (Te, Se, Bi)_2$	Naumannite	Ag_2Se
Oosterboschite	$(Pd, Cu)_7Se_3$	Padmaite	PdBiSe
Palladseite	$Pd_{17}Se_{15}$	Penroseite	$(Ni, Co,Cu)\ Se_2$
Permingeatite	Cu_3SbSe_4	Petrovicite	$PbHgCu_3BiSe_5$
Sabatierite	Cu_4TlSe_3	Sederholmite	β-NiSe
Selen-tellurium	(Se, Te)	Stilleite	ZnSe
Tiemannite	HgSe	Trogtalite	$CoSe_2$
Trustedtite	Ni_3Se_4	Tyrrellite	$(Cu, Co, Ni)_3Se_4$
Umangite	Cu_3Se_2	Wilkmanite	Ni_3Se_4
Schlemaite	$(Cu, ?)_6\ (Pb, Bi)Se_4$	(IMA99. 023)	Cu_2HgSe_2
Krutaite	$CuSe_2$	Achavalite	FeSe
Sudovikovite	$PtSe_2$	Chrisstanleyite	$Ag_2Pd_3Se_4$
Jaguéite	$Cu_2Pd_3Se_4$	Tischendorfite	$Pd_8Hg_3Se_9$
Plumboselite	$Pb_3O_2(SeO_3)$,		

Table II

Selenium sulphides (Huayun, 1998; Zhu *et al.*, 2003)

Name	Chemical formula	Name	Chemical formula
Aguilarite	Ag_4SeS	Chameanite	$(Cu, Fe)_4\ As(Se, S)_4$
Csiklovaite	$Bi_2Te(S, Se)_2$	Drysdallite	$Mo(Se, S)_2$
Geffroyite	$(Ag, Cu, Fe)_9\ (Se, S)_8$	Giraudite	$(Cu, Zn, Ag)_{12}\ (As, Sb)_4\ (Se, S)_{13}$
Hakite	$(Cu, Hg)_3\ (Sb, As)\ (Se, S)_3$	Ikunolite	$Bi_4(S, Se)_3$
Jeromite	$As(S, Se)_2$	Junoite	$Pb_3Cu_2Bi_8\ (S, Se)_{16}$
Kawazulite	$Bi_2\ (Te, Se, S)_3$	Kurilite	$(Au, Ag)_2\ (Te, Se, S)$
Laitakarite	$Bi_4(Se, S)_3$	Laphamite	$As_2(Se, S)_3$
Nevskite	Bi(Se, S)	Nordstromite	$Pb_3CuBi_7S_{10}Se_4$
Paraguanajuatite	$Bi_2(Se, S)_3$	Pekoite	$PbCuBi_{11}(S,Se)_{18}$
Penzhinite	$(Ag, Cu)_4Au(S, Se)_4$	Petrovskaite	AuAg(S, Se)
Platynite	$(Pb, Bi)_3\ (Se, S)_4$	Poubaite	$PbBi_2Se_2(Te, S)_2$
Proudite	$Cu_{0\sim1}Pb_{7.5}Bi_{9.3\sim9.7}(S,Se)_{22}$	Selenostephanite	$Ag_5Sb(Se, S)_4$
Skippenite	$Bi_2Se_2(Te, S)$	Soucekite	$PbCuBi(S, Se)_3$
Tsnigriite	$Ag_9SbTe_3\ (S, Se)_3$	Watkinsonite	$PbCu_2Bi_4\ (Se, S, Te)_8$
Weibullite	$Pb_6Bi_8(S, Se)_{18}$	Wittite	$Pb_3Bi_4\ (S, Se)_9$
Crerarite	$(Pt, Pb)\ Bi_3(S, Se)_{4-X\ (X\sim0.7)}$	Vihorlatite	$Bi_{8+X}\ (Se, Te, S)_{11-X}$
Babkinite	$Pb_2Bi_2\ (S, Se)_3$	Mozgovaite	$PbBi_4\ (S, Se)_7$

Table III

Oxygen-containing selenides (Huayun, 1998; Zhu *et al.*, 2003)

Name	Chemical formula	Name	Chemical formula
Ahlfeldite	$(Ni,Co)SeO_3 \cdot 2H_2O$	Carlosruizite	$K_6\ (Na, K)_4\ Na_6\ Mg_{10}\ (Se_6O_4)_{12}\ (IO_3)_{12} \cdot 12H_2O$
Chalcomenite	$CuSeO_3 \cdot 2H_2O$	Chloromenite	$Cu_9O_2\ (SeO_3)_4Cl_6$
Clinochalcomenite	$CuSeO_3 \cdot 2H_2O$	Cobaltomenite	$CoSeO_3 \cdot 2H_2O$
Demesmaekerite	$Pb_2Cu_5(UO_2)_2(SeO_3)_6(OH)_6 \cdot 2H_2O$	Derriksite	$Cu4(UO_2)(SeO_3)_2(OH)_6$
Downeyite	SeO_2	Francisite	$Cu_3Bi\ (SeO_3)_2O_2Cl$
Georgbokiite	$Cu5O_2\ (SeO_3)_2Cl_2$	Guilleminite	$Ba(UO_2)_3(SeO_3)_2(OH)_4 \cdot 3H_2O$
Haynesite	$(UO_2)_3(SeO_3)_2(OH)_2 \cdot 5H_2O$	Ilinskite	$NaCu_5O_2\ (SeO_3)_2\ Cl$
Kerstenite	$PbSeO_4$ (?)	Mandarinoite	$Fe_2Se_3O_9 \cdot 6H_2O$
Marthozite	$Cu(UO_2)_3(SeO_3)_3(OH)_2 \cdot 7H_2O$	Molybdomenite	$PbSeO_3$
Olsacherite	$Pb_2(SeO_4)(SO_4)$	Orlandiite	$Pb_3\ (Cl, OH)_4\ (SeO_3) \cdot H_2O$
Piretite	$Ca(UO_2)_3(SeO_3)_2\ (OH)_4 \cdot 4H_2O$	Schmiederite	$Pb_2Cu_2(SeO_3)(SeO_4)(OH)_4$
Selenolite	SeO_2	Sophiite	$Zn_2(SeO_3)Cl_2$
(IMA2000-050)	$KCdCu_7O_2\ (SeO_3)_2Cl_9$	(IMA96.002)	$Ca_{0.75}\ (H_3O)_{0.25}\ (UO_2)_3\ (SeO_3)_2\ (OH)_{3.75} \cdot 2.5H_2O$

Table IV

Mode of occurrence of some selenium minerals (Zuomin, 1997)

Modes of occurrence		Typical combination of selenium minerals
Placer deposits		Clausthalite, makinenite, ferroselite, cadmoselite, selenium
Tin deposits		Laitakarite, clausthalite, guanajuatite
Kustelite deposits		Fischesserite, naumannite, clausthalite, berzelianite, guanajuatite, paraguanajuatite
Uranium deposits		Demesmaekerite, derriksite, guilleminite, haynesite, marthozite, antimonselite, umangite, dzharkenite, berzelianite
Contact metasomatic deposits		Clausthalite, guanajuatite, paraguanajuatite
Oxidation zone of copper-cobalt sulphide deposits		Eucairite, trogtalite
Carbonate gangue	Calcite veins	Clausthalite, guanajuatite, paraguanajuatite, tiemannite, naumannite, bellidoite, berzelianite, umangite, crookesite, dzharkenite, antimonselite, aguilarite, athabascaite
	Dolomitic gangue	Clausthalite, hastite, trogtalite, bornhardtite
	Siderite veins	Clausthalite, penroseite, naumannite, tiemannite
Quartz vein		Kawazulite, laitakarite
Carbonate –albite veins		Clausthalite, kitkaite, paraguanajuatite, penroseite, Ni-selenide
Quartz-anthophyllite veins		Laitakarite

and oxygen-containing selenides (Huayun, 1998). There are a few native selenium minerals, selenium oxides, as well as intermetallic compounds between selenium and metals.

Selenium is chemically very similar to sulphur, and sulphur is the primary accompanying element in selenium minerals. Many of its compounds are analogues of sulphur compounds, and selenium substitutes for sulphur in minerals and other compounds.

Cu, Bi, Pb, Ag, and Te are the main element in selenium minerals, followed by Co, Ni, Fe, and Sb. Based on the content of selenium in sulphides, Yang (Huayun, 1998) described the affinity between Se and related elements, which can be divided into three categories (with decreasing affinity): (1) Pb, Ag, Bi, Hg, Cu; (2) Co, Ni; (3) Fe, Zn. Se forms a few minerals with precious metals, *e.g.* Au, Ag, Pt, Pb.

Mineralogical studies of numerous selenium minerals have not been fully conducted due to their restricted occurrence, small particle size, and experimental limitations. For instance, there are five selenides of nickel: kullerudite, makinenite, sederholmite, trustedtite, and wilkmanite, but no information has been reported about reflectivity or color index (Huayun, 1998).

Occurrence of selenium minerals

Selenium minerals occur in various forms, which can be divided primarily into three categories: independent minerals; isomorphism; adsorbed on clay minerals. Although there are about 100 selenium minerals, the metal rarely occurs in commercial concentrations. Selenium occurs mainly in sulphides or sulphosalt minerals in the form of isomorphism; there are rare selenium deposits that are commercially viable (Brown Jr, 1998; Huayun, 1998).

Selenium deposits can be divided into independent deposits and accompanying deposits. The occurrence of some selenium minerals is shown in Table IV. As regards independent selenium deposits, hydrothermal deposits are dominating type, and the Pakarharkar deposit in Bolivia is typical, while the Yutangba Se deposit in China, a sedimentary deposit, is an exception.

Selenium resources occur mainly in combined deposit, which can be divided into several industrial types, *i.e.* magmatic, porphyry, skarn, hydrothermal, volcanogenic-sedimentary, and sedimentary. Among these, magmatic, porphyry, hydrothermal, and sedimentary type deposits are dominant.

Selenium minerals are often closely associated with other minerals in very fine particles. For example, clausthalite occurs mainly as finer particles in the size range from 0.005 mm to 0.01 mm in the Wolverine deposit, Yukon Territory, Canada. It occurs with sulphides and is often associated with tetrahedrite or silver stibnic clausthalite in the same grain (Figure 1).

The mechanism of selenium mineral formation remains unclear. Selenium minerals are often associated with gold, but no selenium-gold minerals have been discovered. Furthermore, the relationship between selenium and sulphur in minerals is still indistinct, *e.g.* the replacement of selenium is ordered or disordered.

Distribution of selenium resources

According to the US Bureau of Mines (USBM), the world's selenium reserve base is 1.34×10^5 t, and the proved reserves amount to 7.1×10^4 t (Brown Jr, 1998). The reserves are dominated by America with 52.7% of the total reserves; Asia, Africa, Europe, and Oceania account for 15.4%, 15.4%, 12.2%, and 4.4%, respectively (Feng and Jiajun, 2002). Chile, America, Canada, China, Zambia, Zaire, Peru, the Philippines, Australia, and Papua New Guinea account for about 76.9% of the proved reserves. There are about 40 countries that lack selenium resources.

Independent industrial deposits of selenium are rare. No independent selenium deposits were reported until the discovery of the Pakarharkar deposit in Bolivia in the 1980s. Since then, a series of associated deposits have been discovered in Canada, America, Chile, Zambia, Zaire, *etc.* (Daming, 1996). The main Se deposits of the world are shown in Table V.

Recently, selenium resources were reported at the Wolverine and KZK deposits in the Finlayson Lake District (FLD) of the Yukon, Canada. In the mid-1990s, three polymetallic volcanic-hosted massive sulphide deposits were discovered in the FLD with a combined resource of 21.5 Mt. Elevated selenium levels in the Wolverine and KZK massive sulphide ores were recognized during metallurgical testing and in the pre-feasibility stages of exploration. Selenium concentrations up to 3420 g/t are reported, with a mean value of approximate 700 g/t (Layton-Matthews *et al.*, 2005). The selenium in the Wolverine deposit occurs mainly as fine particles of clausthalite and silver stibnic clausthalite between 0.005–0.05 mm in diameter.

China is one of the major countries that hold selenium resources, with the fourth-largest recoverable reserves after Canada, America, and Belgium (Brown Jr, 1998). There are 10 ascertained Se deposits, including Jinshan gold deposit,

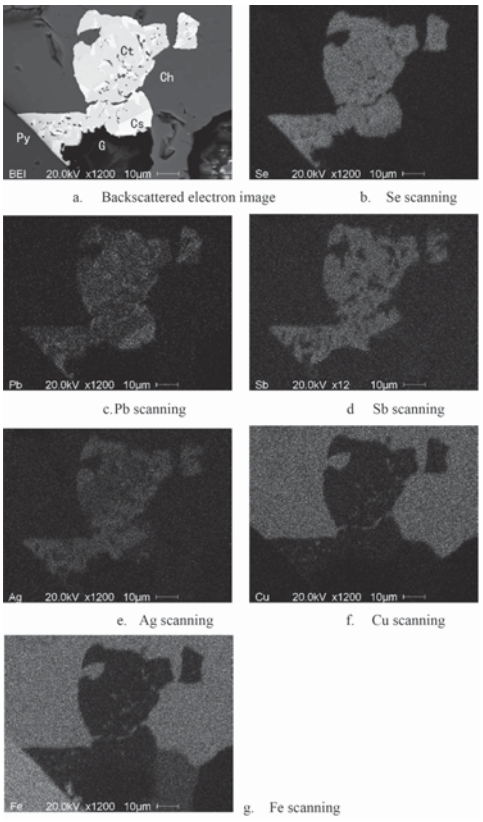

Figure 1—Scanning electron micrograph of clausthalite and silver stibnic clausthalite. Ct – silver stibnic clausthalite, contains Se, Ag, Sb, Pb; Cs – clausthalite, contains Se, Pb; Ch – chalcopyrite; Py – pyrite; G – gangue

Table V

The main Se deposits of the world (Daming 1996)

Country	Name	Types	Mineral elements	Grade (10^{-6})	Scale
America	Bingham	Magmatic	Se, Cu	21.5	Large
	Twin Buttes	Magmatic	Se, Cu	21.5	Large
Bolivia	Pakarharkar	Alteration	Se	>10	Small
Canada	Noranda	Volcanic hydrothermal	Se, Cu, Ni	64	Oversize
	Flin Flon	Volcanic hydrothermal	Se, Cu, Ni	64	Oversize
Chile	Escondida	Magmatic	Se, Cu	>10	Large
	Chuquicamata	Magmatic	Se, Cu	>10	Large
The Philippines	Atlas	Magmatic	Se, Cu	>10	Large
Zaire	Kolwezi	Clastic sedimentary	Se	>10	Large
Zambia	Mufulira	Clastic sedimentary	Se	>10	Large
	Nchanga	Clastic sedimentary	Se	>10	Large

Table VI

The main Se deposits of China (Daming 1996)

Province	Name	Types	Mineral elements	Grade (10-6)	Scale
An'hui	Tongguanshan		Se, Au, Cu		Large
Gansu	Baijiazuizi	Magmatic	Se, Au, Ni	>10	Oversize
Guangdong	Dabaoshan	Hydrothermal		>30	Large
Gansu	Laerma	Hydrothermal	U, Hg, Se, Au	29.4	Large
Hubei	Baiguoyuan		Ag, Se, V	67~79	Large
Hu'nan	Qibaoshan		Au, Ag, Se, S	>10	Large
Hubei	Shuanghe	Clastic sedimentary	Se	84.12	Medium
Hubei	Yutangba	Clastic sedimentary	Se	84.12	Medium
Jiangxi	Chengmenshan	Skarn	Polymetallic		Oversize
Jiangxi	Jinshan	Porphyry	Se, Cu, Au	15.4	Oversize
Qinghai	De'erni	Hydrothermal	Cu, Co, Au, Se, S		Large
Shanxi	Jinduicheng	Porphyry	Au, Se, Mo		Medium
Shanxi	Dashigou	Magmatic	Se, Mo	>10	Medium
Shanxi	Huayangchuan	Magmatic	Sr, Pb, Nb, Ag, Se, tombarthite	>10	Medium

Baijiazuizi Cu-Ni deposit, and Chengmenshan copper deposit (Zuomin, 1997). In addition, some independent selenium deposits have been discovered in China, *i.e.* the Yutangba Se deposit and Laerma Se-Au deposit (Wen and Qiu, 1999). Proven reserves of selenium occur mainly with copper and nickel ores, and are distributed in the northwest of China and the Lower Yangtze region. The main Se deposits of China are shown in Table VI.

The recovery of selenium from copper anode slimes

The largest source of selenium is the anode slimes formed during the electrolytic refining of copper (Elkin and Margrave, 1982). Production usually begins by oxidation to produce selenium dioxide at an appropriate temperature. The selenium dioxide is then dissolved in water and the solution is acidified to form selenous acid (oxidation step). Selenous acid is sparged with sulphur dioxide (reduction step) to yield elemental selenium. In South Africa, Se is mostly removed to about 1 mg/L before the leach solution is sent to copper electrowinning. In South African refineries, Se is recovered mostly by precipitation using sulphurous acid. Different approaches to treating anode slimes are shown in Figure 2.

Sulphatizing roast

In the sulphatizing roast, sulphuric acid is used as an oxidant in the presence of air for the conversion of selenium or selenides to their tetravalent oxides (Hoffmann *et al.*, 1976; Hoffmann, 1989). Selenium is volatilized as selenium dioxide and passes into the scrubbers. The scrubbing of the off-gases results in complete recovery of the selenium from the gas stream. The process is shown in Figure 3.

Although the process entails an advantage in that the sulphur dioxide produced in the roasting step reduces the selenious acid to elemental selenium and the sulphuric acid consumed in the roast is regenerated, this process is a net consumer of sulphuric acid. In addition, the rather long reaction times required for the oxidation of the selenium, extensive foaming due to sulphur dioxide liberation, as well as the cumbersome equipment due to large allowances for freeboard add difficulties to the process.

Soda roast

Slimes are mixed with sodium carbonate, a binder clay, and water to form a stiff paste, and then pelletized, dried, and roasted at a low temperature (530–650°C) to convert all selenium and tellurium to the soluble hexavalent state. The roasted pellets are ground and leached in water. Selenium

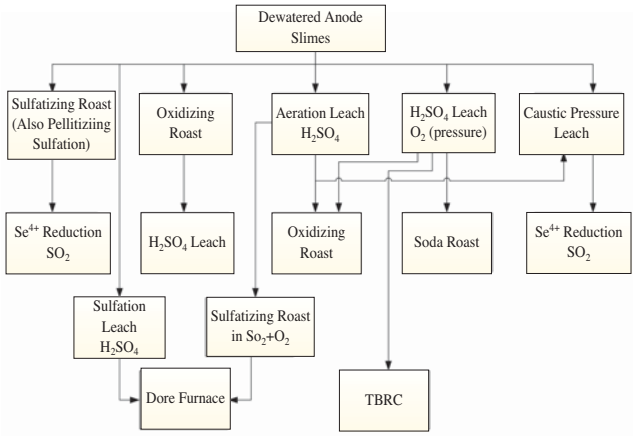

Figure 2—Flow sheet of different approaches to the treatment of copper anode slimes (Cooper, 1990)

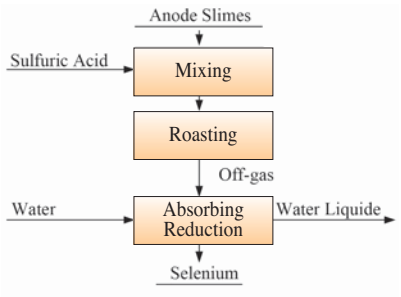

Figure 3—Flow sheet for anode slimes treatment with sulphation roasting (Yang *et al.*, 2005)

goes into solution (as the selenate Na_2SeO_4), while tellurium is insoluble in the alkaline solution; thus the two elements are separated in this stage (Figure 4).

Two processes are commonly employed for the reduction of hexavalent selenium from solution (Figure 5) (Hoffman 1997; Yang *et al.* 2005). In the first process, selenium is leached from the slimes and recovered from solution by crystallization. The crystalline sodium selenate is mixed with charcoal and reduced to sodium selenide under controlled conditions of heating. The sodium selenide cake is leached with water, and the dissolved sodium selenide is readily oxidized to the elemental form by blowing air through the solution. The recycling of much of the solution is a significant advantage considering the severe restrictions placed on the discharge of selenium-bearing solutions.

In the other process, the hexavalent selenium is reduced using concentrated hydrochloric acid or ferrous iron salts catalysed by chloride ions as the reductant. The process generates large volumes of ferric chloride effluent, which is extremely corrosive and problematic to discharge.

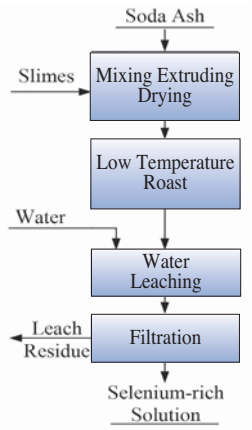

Figure 4—Flow sheet for anode slimes treatment with soda ash roasting (Hoffmann, 1989)

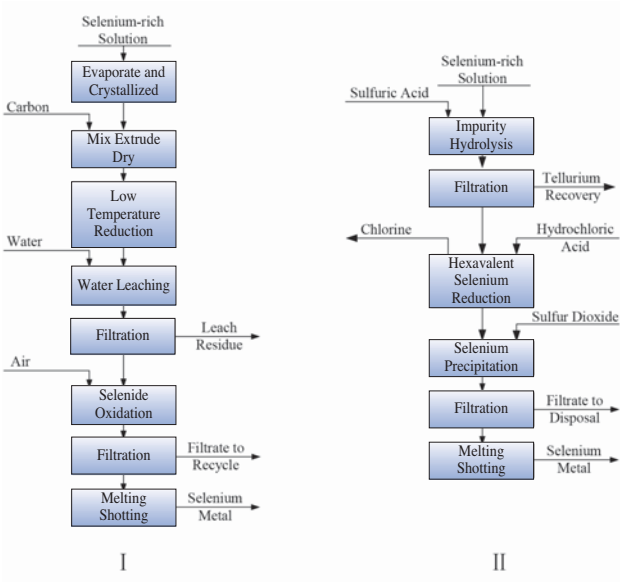

Figure 5—Flow sheet for selenium-rich solution treatment: (I) reduction by carbon; (II) reduction by ferrous ions (Hoffmann 1989)

Oxidizing roast

Oxidation roasting of anode slimes can be employed to eliminate selenium following sulphuric acid leaching of the slimes (Morrison, 1977; Hyvarinen, *et al.*, 1984). Anode slimes are roasted to convert selenium to selenium dioxide, which reacts with water to form selenic acid in the dust collector. The selenic acid is reacted with copper powder, carbon (soot), and SO_2 in the furnace gas, and it is reduced to selenium or insoluble selenide. The process is shown in Figure 6.

Chlorination processes

The chlorination of anode slimes has been the focus of considerable research (Hyvarinen *et al.*, 1984). Both wet and dry chlorination process have been developed. Dry chlorination processes have not proven to be industrially viable, while wet chlorination of refinery slimes is a rapid and simple method with high extraction of selenium from slimes. The wet chlorination process may involve changing all of the process chemistry, not just the removal of selenium (Hoffmann, 1989).

Wet chlorination of slimes involves sparging slimes slurried in water or hydrochloric acid with chlorine gas at about 100°C to oxidize and dissolve selenium and selenides. The selenium in solution may be converted initially to the hexavalent state by chlorine, and then reduced to the tetravalent state as the pH decreases. Selenium can be reduced selectively from the chlorination liquor by sulphur dioxide.

Conclusion

Since the first observation of selenium in the laboratory, more than 100 selenium minerals have been discovered and reported. The minerals are mainly selenides, selenium sulphides, and oxygen-containing selenides. Sulphur is the primary element in selenium minerals as a consequence of its chemical similarity with selenium, while Cu, Bi, Pb, Ag, and Te are the other main elements, followed by Co, Ni, Fe, and Sb.

Selenium deposits can be divided into independent deposits and accompanying deposits. A few independent selenium deposits have been reported, such as the Pakarharkar deposit in Bolivia and Yutangba Se deposit in China. Se resources occur mainly in combined deposits.

Accompanying deposits can be divided into several genetic types, with magmatic, porphyry, hydrothermal, and sedimentary type deposits being dominant. Selenium

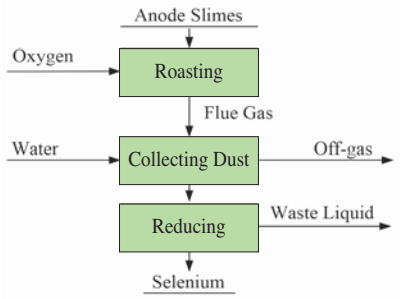

Figure 6—Flow sheet for anode slimes treatment with oxidizing roasting (Yang *et al.*, 2005)

minerals are often closely associated with other minerals in very fine particles in combined deposits. Although numerous selenium deposits have been discovered all over the world, there are few deposits that are commercially viable. Industrial production of selenium is mainly as a by-product of other metals, such as copper, iron, and lead. Selenium is produced primarily from the anode mud of copper refineries, and this process has been investigated widely.

In investigations of the selenium minerals, comprehensive mineralogical studies of numerous minerals have not been conducted due to their restricted occurrence, small particle size, and experimental limitations. Furthermore, the mechanism of selenium mineral formation remains unclear. Selenium minerals are often associated with gold, although no independent minerals consisting of selenium and gold have been discovered. The relationship between selenium and sulphur in minerals is still unclear.

References

Brown Jr, R.D. 1998. Selenium and tellurium. US Geological Survey, Arlington, VA.

Butterman, W.R. and Brown, R.D. 2004. Selenium. *Mineral Commodity Profiles*. US Department of the Interior, US Geological Survey, Arlington, VA.

Coleman, R.G. and Delevaux, M.H. 1957. Occurrence of selenium in sulfides from some sedimentary rocks of the western United States. *Economic Geology*, vol. 52, no. 5. pp. 499–527.

Cooper, W.C. 1990. The treatment of copper refinery anode slimes. *JOM*, vol. 42, no. 8. pp. 45–49.

Daming, P. 1996. Seldom selenium resource in China. *China Non-metallic Mining Industry Herald* (in Chinese)

Davis, R., Clark, A.M., and Criddle, A.J. 1977. Palladseite, a new mineral from Itabira, Minas Gerais, Brazil. *Mineralogical Magazine*, vol. 41, no. 123. pp. M10–M13.

Elkin, E. and Margrave, J. 1982. Selenium and selenium compounds. *Kirk-Othmer Encyclopedia of Chemical Technology,* vol. 20. Wiley, New York. pp. 575–601.

Förster, H.J., Cooper, M.A., Roberts, A.M., Stanley, C.J., Criddle, A.J., Hawthorne, F.C., Laflamme, J.H.G., and Tischendorf, G. 2003. Schlemaite, (Cu,)6(Pb,Bi)Se4, a new mineral species from Niederschlema–Alberoda, Erzgebirge, Germany: description and crystal structure. *Canadian Mineralogist*, vol. 41, no. 6. pp. 1433–1444.

Förster, H.J., Rhede, D., and Tischendorf, G. 2004. Mineralogy of the Niederschlema–Alberoda U–Se–polymetallic deposit, Erzgebirge, Germany. I. Jolliffeite, NiAsSe, the rare Se-dominant analogue of gersdorffite. *Canadian Mineralogist*, vol. 42, no. 3. pp. 841–849.

Feng, C. and Jiajun, L. 2002. An outline of selenium resources and its exploitation and utilization. *Geology and Resources*, vol. 11, no. 3. pp. 152–156 (in Chinese).

Fishbein, L. 1983. Environmental selenium and its significance. *Fundamental and Applied Toxicology*, vol. 3, no. 5. pp. 411–419.

Greenwood, N.N. and Earnshaw, A. 1984. Chemistry of the Elements. Butterworth-Heinemann.

Hawley, J.E. and Nichol, I. 1959. Selenium in some Canadian sulfides. *Economic Geology*, vol. 54, no.4. pp. 608–628.

Hoffman, J.E. and King, M.G. 1997. Selenium and selenium compounds. *Encyclopedia of Chemical Technology*. Wiley, New York. pp. 686–719.

Hoffmann, J.E. 1989. Recovering selenium and tellurium from copper refinery slimes. *JOM*, vol. 41, no. 7. pp. 33–38.

Hoffmann, J.E., Parker, P.D., and Sabo, A.C. 1976. Extraction and purification of silver from sulfates. US patent 3996046. Amax Inc.

Howard III, H. 1977. Geochemistry of selenium: formation of ferroselite and selenium behavior in the vicinity of oxidizing sulfide and uranium deposits. *Geochimica et Cosmochimica Acta*, vol. 41, no. 11. pp. 1665–1678.

Huayun, W.H.X. 1998. A review of selenium minerals. *Acta Petrrologica et Mineralogica*, vol. 17, no. 3. pp. 261–265 (in Chinese).

Hyvarinen, O. Rosenberg, E., and Lindroos, L. 1984. Selenium and precious metals recovery from copper anode slimes at Outokumpu Pori Refinery. *Precious Metals: Mining, Extraction and Processing*. Kudryk, V., Corrigan, D.A., and Liang, W.W. (eds). AIME/TMS, The Minerals, Metals and Materials Society, Warrendale, PA. pp. 37–548.

Jiajun, L., Minghua, Z., Jianming, L., Yufeng, Z., Xuexiang, G., Bin, Z., Li, L., and Wenquan, L. 1997. Selenium enrichment in Cambrian stratabound gold deposits in the western Qinling Mountains. *Acta Geologica Sinica* (English Edition), vol. 71, no. 4. pp. 423–432 (in Chinese).

Kaiser, E. 1954. Selenium in sulfide ores. *Geological Society of America Bulletin*, vol. 65. p. 1379.

Kampf, A.R., Mills, S.J., and Pinch, W.W. 2011. Plumboselite, $Pb_3O_2(SeO_3)$, a new oxidation-zone mineral from Tsumeb, Namibia. *Mineralogy and Petrology*, vol. 101, no. 1. pp. 75–80.

Kucha, H. 1982. Platinum-group metals in the Zechstein copper deposits, Poland. *Economic Geology*, vol. 77, no. 6. pp. 1578–1591.

Lakin, H.W. 1972. Selenium accumulation in soils and its absorption by plants and animals. *Geological Society of America Bulletin*, vol. 83, no. 1. pp. 181–190.

Layton-Matthews, D., Scott, S.D., P, J.M., and Leybourne, M.I. 2005. Transport and deposition of selenium in felsic volcanic-hosted massive sulfide deposits of the Finlayson Lake District, Yukon Territory, Canada. *Mineral Deposit Research: Meeting the Global Challenge*. Proceedings of the Eighth Biennial SGA Meeting, Beijing, China, 18-21 August 2005. Mao, J. and Bierlein, F.P. (eds). Springer. pp. 643–646.

Zheng, M., Liu, J., Liu, J., and Lu, W. 1993. The first discovery and preliminary study of selenio-sulfantimonide in China. *Journal of Mineralogy and Petrology*, vol. 13, no. 2. pp. 9–13 (in Chinese).

Morrison, B.H. 1977. Slimes treatment process. US patent 4,047,939. Norand Mines Ltd.

Paar, W., Roberts, A.C., Criddle, J., and Topa, D. 1998. A new mineral, chrisstanleyite, $Ag_2Pd_3Se_4$ from Hope's Nose, Torquay, Devon, England. *Mineralogical Magazine*, vol. 62, no. 411. pp. 257–264.

Paar, W.H., Topa, D., Makovicky, E., Sureda, R.J., de Brodtkorb, M.K., Nickel, E., and Putz, H. 2004. Jaguéite, $Cu_2Pd_3Se_4$, a new mineral species from El Chire, La Rioja, Argentina. *Canadian Mineralogist*, vol. 42, no. 6. pp. 1745–1755.

Simon, G., Kesler, S.E., and Essene, E.J. 1997. Phase relations among selenides, tellurides, and oxides; II, Applications to selenide-bearing ore deposits. *Economic Geology*, vol. 92, no. 4. pp. 468–484.

Stanley, C., Criddle, A., and Lloyd, D. 1990. Precious and base metal selenide mineralization at Hope's Nose, Torquay, Devon. *Mineralogical Magazine*, vol. 54. pp. 485–493.

Stanley, C. J., Criddle, A.J. Förster, H-J., and Roberts, A.C. 2002. Tischendorfite, $Pd_8Hg_3Se_9$, a new mineral species from Tilkerode, Harz Mountains, Germany. *Canadian Mineralogist*, vol. 40, no. 2. pp. 739–745.

Thompson, M., Roach, C., and Braddock, W. 1956. New occurrences of native selenium. *American Mineralogist*, vol. 41. pp. 156–157.

Wen, H. and Qiu, Y. 1999. Organic and inorganic occurrence of selenium in Laerma Se-Au deposit. *Science in China Series D: Earth Sciences*, vol. 42, no. 6. pp. 662–669 (in Chinese).

Yang, C., Zhang, X., and Lan, D. 2005. Present situation and trend of selenium removal technique from copper anode slime. *Sichuan Nonferrous Metals*, vol. 1. pp. 22–25 (in Chinese).

Yunfen, L., Yueying, L., Mingming, Y., Kuishou, D., Naijue, Z., and Fang, G. 1990. Selenian miargyrite--a new variety of miargyrite. *Geological Review* (in Chinese).

Zhu, J., Liang, X., Qang, M., Wang, F., Ling, H., and Liu, S. 2003. Advances in studying occurrence modes of selenium in environment. *Bulletin of Mineralogy, Petrology and Geochemistry*, vol. 22, no. 1. pp. 75–81 (in Chinese).

Zhu, J. and Zheng, B. *et al.* 2005. Morphology features and genesis of native selenium. *Bulletin of Mineralogy, Petrology and Geochemistry*, vol. 19, no. 4. pp. 353–355 (in Chinese).

Zuomin, H. 1997. Aulacogens of middle late Proterozoic period along the northern margin of North China Platform. *Geology of Chemical Minerals*, vol. 1 (in Chinese). ◆

Photographs courtesy of
Jason Pieterse and Chris Pistorius

SCHOOL
PRODUCTION of CLEAN STEEL

25–26 July 2016

Mintek, Johannesburg

Register 4 delegates and get the fifth registration free

POSTER COMPETITION!
Abstract Submission Deadline **1 June 2016**
Prize: An overseas trip to work with Prof. Pistorius at CMU in Pittsburgh

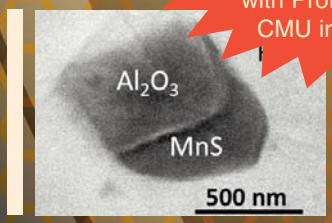

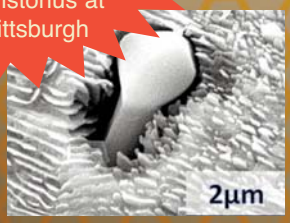

Announcement

LECTURER

Prof. C Pistorius

Chris Pistorius is the POSCO Professor of Iron and Steelmaking in the Department of Materials Science and Engineering at Carnegie Mellon University (Pittsburgh, PA, USA), where he has been since 2008. Previously he was Professor and Head of Department of Materials Science and Metallurgical Engineering at the University of Pretoria. He holds Bachelor's and Master's degrees in Metallurgical Engineering from the University of Pretoria, and a PhD from the University of Cambridge, United Kingdom. His current research interests include the fundamentals of ironmaking and steelmaking reactions, and electrochemistry of corrosion and metals production.

WHO SHOULD ATTEND

The school is aimed at delegates from steel producing companies in South Africa or those who support them, and includes:

- Senior management
- First line management
- Process/development engineers
- Researchers
- Middle management
- Plant/production engineers
- Design engineers

EXHIBITION/SPONSORSHIP

Sponsorship opportunities are available. Companies wishing to sponsor or exhibit should contact the Conference Co-ordinator.

SAIMM
THE SOUTHERN AFRICAN INSTITUTE OF MINING AND METALLURGY

For further information contact:
Conference Co-ordinator, Camielah Jardine
SAIMM, P O Box 61127, Marshalltown 2107
Tel: (011) 834-1273/7 • Fax: (011) 833-8156 or (011) 838-5923
E-mail: camielah@saimm.co.za • Website: http://www.saimm.co.za

INTRODUCTION

South Africa has a proud history in the production of both mild steel and stainless steel with production facilities in Gauteng, Kwazulu-Natal, Mpumalanga, the Eastern and Western Cape provinces. At these facilities steel is produced from scrap or from ore via ironmaking facilities.

The Center for Iron and Steelmaking Research at Carnegie Mellon University in Pittsburgh, Pennsylvania, USA has a proud history on iron and steelmaking. Collaboration between CMU and the South African iron and steel industry includes a school on steelmaking presented by Prof. Richard Fruehan in Vanderbijlpark in 1996.
At Clean Steel 2016 Prof. Chris Pistorius will continue the collaboration by addressing the following topics:

CONTROLLING DISSOLVED ELEMENTS

1. What is clean steel?
2. Relevant process conditions in blast furnace, steelmaking converter, electric arc furnace, ladle furnace and caster (temperatures, oxygen activity, slag basicity, stirring).
3. Control of dissolved elements (C, H, N, O, P, S, Cu, Sn):
   a. Sources (raw materials; environment)
   b. Thermodynamic and kinetic principles of control
   c. Practical control methods:
      i. hot metal desulfurization and dephosphorization
      ii. metal-slag reactions in blast furnace, steelmaking and ladle
      iii. clean tapping
      iv. metal-gas reactions, including nitrogen pick-up
      v. deoxidation
      vi. role of slag
      vii. mitigating the surface quality effects of Cu & Sn.

CONTROLLING MICRO-INCLUSIONS

1. Principles of control:
   a. inclusion composition evolution over time
   b. removing inclusions to slag or fluxes: gas stirring and flotation kinetics
   c. inclusion-metal-slag reactions: equilibria and kinetics (spinel formation)
   d. calcium modification.
2. Sources of micro-inclusions:
   a. deoxidation and reoxidation products
   b. ladle glaze
   c. inclusions in ferro-alloys and ferro-alloy reaction products
   d. mold flux entrainment
   e. reoxidation.
3. Assessing micro-inclusions:
   a. overall steel composition
   b. caster behavior
   c. microanalysis (polished sections; extracted inclusions)
   d. other analytical approaches.
4. Summary: general guidelines for clean-steel practice; opportunities to learn more and share information.

Sponsors:

ALS ADVANCED LABORATORY SOLUTIONS

South African Iron and Steel Institute

Abstract Announcement & Registration

The Southern African Institute of Mining and Metallurgy

in collaboration with the SAIMM Western Cape Branch is hosting the

Hydrometallurgy Conference 2016

Sustainable Hydrometallurgical Extraction of Metals

31 July 2016—Workshop • 1–3 August 2016—Conference

Belmont Mount Nelson Hotel, Cape Town

KEYNOTE SPEAKERS
F. Crundwell
M. Nicol
K. Osseo-Asare
M. Reuter
S. Bhargava

- Register 4 delegates and get the fifth registration free
- Book and pay full conference by 1 July 2016 and attend the workshop for free (limited to the first 50 registrations)

Metals play a significant role in industrialisation and technological advancements. Do you ever wonder then what life would be like without metal resources?

The depletion of natural rich ore deposits coupled with a fall in grade, a decline in productivity, rising operational and energy costs, concerns on sustainability and environmental impact of mining and metal related activities have been affecting the mining and metals industry in the recent past. Unless innovative methods that look at the smart use and recovery of metals from metal resources are developed, the world will be faced by a metal supply risk that will impact on future economic growth and technological development.

The SAIMM Hydrometallurgy Conference, 2016, will bring together internationally and locally recognized experts, industries, R&D establishments, academia as well as students to explore how future metal demands can be met through modern hydrometallurgical technologies that can:

- Assist in sustainable metal extraction
- Lower energy costs
- Minimise the impact on the environment

WHO SHOULD ATTEND

The conference will be of value to:

- Hydrometallurgical plant managers and metallurgists
- Equipment and reagent suppliers to the hydrometallurgical industry
- Hydrometallurgical technology development companies
- Mining industry consultants
- Research and academic personnel

SPONSORSHIP/EXHIBITIONS

Companies wishing to sponsor or exhibit should contact the Conference Co-ordinator

SAIMM
THE SOUTHERN AFRICAN INSTITUTE OF MINING AND METALLURGY

Funding Sponsor

science & technology
Department: Science and Technology
REPUBLIC OF SOUTH AFRICA

NRF National Research Foundation

Sponsors

CIDRA Minerals Processing
Outotec
CYTEC SOLVAY GROUP
TOTAL COMMITTED TO BETTER ENERGY
FLSmidth
WorleyParsons resources & energy

For further information contact:

Head of Conferencing, Raymond van der Berg
Saimm, P O Box 61127, Marshalltown 2107
Tel: +27 (0) 11 834-1273/7 · E-mail: raymond@saimm.co.za
Website: http://www.saimm.co.za

INTERNATIONAL ACTIVITIES

2016

19–20 July 2016 — Innovations in Mining Conference 2016
'Redesigning the Mining and Mineral Processing Cost Structure'
Holiday Inn Bulawayo
Contact: Raymond van der Berg
Tel: +27 11 834-1273/7, Fax: +27 11 838-5923/833-8156
E-mail: raymond@saimm.co.za, Website: http://www.saimm.co.za

25–26 July 2016 —Production of Clean Steel
Mintek, Randburg
Contact: Camielah Jardine
Tel: +27 11 834-1273/7, Fax: +27 11 838-5923/833-8156
E-mail: camielah@saimm.co.za, Website: http://www.saimm.co.za

31 July–3 August 2016 — Hydrometallurgy Conference 2016
'Sustainable Hydrometallurgical Extraction of Metals' in collaboration with MinProc and the Western Cape Branch
Belmont Mount Nelson Hotel, Cape Town
Contact: Raymond van der Berg
Tel: +27 11 834-1273/7, Fax: +27 11 838-5923/833-8156
E-mail: raymond@saimm.co.za, Website: http://www.saimm.co.za

8 August 2016 — South African Underground Coal Gasification Association
2nd Underground Coal Gasification Network Workshop
CDH Sandton, Johannesburg
Contact: Shehzaad Kauchali
Email: shehzaad.kauchali@wits.ac.za
Website: http://www.saucga.org.za

9–12 August 2016 — Thirty Third Annual International Pittsburgh Coal Conference 2016
International Convention Centre, Cape Town, South Africa
Contact: Raquel (South Africa)
Tel: +27 11 475-2750 or +27 82 509-6485
Email: pcc@@ap22ude.co.za
Contact: H.M. Peck (International)
Tel: +1(412) 624-7440, Fax: +1(412) 624-1480
Email: ipcc@pitt.edu, Website: http://www.pccpitt.org

16–18 August 2016 — The Tenth International Heavy Minerals Conference '*Expanding the horizon*'
Sun City, South Africa
Contact: Camielah Jardine
Tel: +27 11 834-1273/7, Fax: +27 11 838-5923/833-8156
E-mail: camielah@saimm.co.za, Website: http://www.saimm.co.za

27 August–4 September 2016 — 35th International Geological Congress
Cape Town, South Africa
Contact: Craig Smith
Tel: +27 11 492-3370, Fax: +27 11 492-3371
E-mail: craig.smith@gssa.org.za

31 August–2 September 2016 — MINESafe Conference Striving for Zero Harm
Emperors Palace, Hotel Casino Convention Resort
Contact: Raymond van der Berg
Tel: +27 11 834-1273/7, Fax: +27 11 838-5923/833-8156
E-mail: raymond@saimm.co.za, Website: http://www.saimm.co.za

12–13 September 2016 — Mining for the Future 2016
'The Future for Mining starts Now'
Electra Mining, Nasrec, Johanannesburg
Contact: Camielah Jardine
Tel: +27 11 834-1273/7, Fax: +27 11 838-5923/833-8156
E-mail: camielah@saimm.co.za, Website: http://www.saimm.co.za

12–14 September 2016 — 8th International Symposium on Ground Support in Mining and Underground Construction
Kulturens Hus – Conference & Congress, Luleå, Sweden
Contact: Erling Nordlund
Tel: +46-920493535, Fax: +46-920491935
E-mail: erling.nordlund@ltu.se, Website:
http://groundsupport2016.com

19–21 October 2016 — AMI Ferrous and Base Metals Development Network Conference 2016
Southern Sun Elangeni Maharani, KwaZulu-Natal, South Africa
Contact: Raymond van der Berg
Tel: +27 11 834-1273/7, Fax: +27 11 838-5923/833-8156
E-mail: raymond@saimm.co.za, Website: http://www.saimm.co.za

25 October 2016 — The Young Professionals Week, 14th Annual Student Colloquium
Mintek, Randburg
Contact: Raymond van der Berg
Tel: +27 11 834-1273/7, Fax: +27 11 838-5923/833-8156
E-mail: raymond@saimm.co.za, Website: http://www.saimm.co.za

2017

9–10 March 2017 — 3rd Young Professionals Conference
Innovation Hub, Pretoria, South Africa
Contact: Camielah Jardine
Tel: +27 11 834-1273/7, Fax: +27 11 838-5923/833-8156
E-mail: camielah@saimm.co.za, Website: http://www.saimm.co.za

25–28 June 2017 — Emc 2017: European Metallurgical Conference
Leipzig, Germany
Contact: Paul-Ernst-Straße
Tel: +49 5323 9379-0, Fax: +49 5323 9379-37
E-mail: EMC@gdmg.de, Website: http://emc.gdmb.de

27–29 June 2017 —4th Mineral Project Valuation
Mine Design Lab, Chamber of Mines Building, The University of the Witwatersrand, Johannesburg
Contact: Raymond van der Berg
Tel: +27 11 834-1273/7, Fax: +27 11 838-5923/833-8156
E-mail: raymond@saimm.co.za, Website: http://www.saimm.co.za

2–7 October 2017 —AfriRock 2017: ISRM International Symposium 'Rock Mechanics for Africa'
Cape Town Convention Centre, Cape Town
Contact: Raymond van der Berg
Tel: +27 11 834-1273/7, Fax: +27 11 838-5923/833-8156
E-mail: raymond@saimm.co.za, Website: http://www.saimm.co.za

9–10 March 2017 — 6th Sulphur and Sulphuric Acid 2017 Conference
South Africa
Contact: Camielah Jardine
Tel: +27 11 834-1273/7, Fax: +27 11 838-5923/833-8156
E-mail: camielah@saimm.co.za, Website: http://www.saimm.co.za

Company Affiliates

The following organizations have been admitted to the Institute as Company Affiliates

3 M South Africa

AECOM SA (Pty) Ltd

AEL Mining Services Limited

Air Liquide (PTY) Ltd

AMEC Mining and Metals

AMIRA International Africa (Pty) Ltd

ANDRITZ Delkor(Pty) Ltd

Anglo Operations Ltd

Anglo Platinum Management Services (Pty) Ltd

Aurecon South Africa (Pty) Ltd

Aveng Moolmans (Pty) Ltd

Axis House (Pty) Ltd

Bafokeng Rasimone Platinum Mine

Barloworld Equipment -Mining

BASF Holdings SA (Pty) Ltd

BCL Limited

Becker Mining (Pty) Ltd

BedRock Mining Support (Pty) Ltd

Bell Equipment Company (Pty) Ltd

Blue Cube Systems (Pty) Ltd

Caledonia Mining Corporation

CDM Group

CGG Services SA

Chamber of Mines

Concor Mining

Concor Technicrete

Council for Geoscience Library

CSIR-Natural Resources and the Environment

Data Mine SA

Department of Water Affairs and Forestry

Digby Wells and Associates

Downer EDI Mining

DRA Mineral Projects (Pty) Ltd

DTP Mining

Duraset

Elbroc Mining Products (Pty) Ltd

Engineering and Project Company Ltd

eThekwini Municipality

Exxaro Coal (Pty) Ltd

Exxaro Resources Limited

FLSmidth Minerals (Pty) Ltd

Fluor Daniel SA (Pty) Ltd

Franki Africa (Pty) Ltd Johannesburg

Fraser Alexander Group

Geobrugg Southern Africa

GIBB (Pty) Ltd

Glencore

Goba (Pty) Ltd

Hall Core Drilling (Pty) Ltd

Hatch (Pty) Ltd

Herrenknecht AG

HPE Hydro Power Equipment (Pty) Ltd

IMS Engineering (Pty) Ltd

Ivanhoe Mines SA

JENNMAR South Africa

Joy Global Inc. (Africa)

Kadumane Manganese Resources

Leco Africa (Pty) Limited

Longyear South Africa (Pty) Ltd

Lonmin Plc

Magnetech (Pty) Ltd

Magotteaux(PTY) LTD

MBE Minerals SA Pty Ltd

MCC Contracts (Pty) Ltd

MDM Technical Africa (Pty) Ltd

Metalock Industrial Services Africa (Pty)Ltd

Metorex Limited

Metso Minerals (South Africa) (Pty) Ltd

Minerals Operations Executive (Pty) Ltd

MineRP Holding (Pty) Ltd

Mintek

MIP Process Technologies

Modular Mining Systems Africa (Pty) Ltd

MSA Group (Pty) Ltd

Multotec (Pty) Ltd

Murray and Roberts Cementation

Nalco Africa (Pty) Ltd

Namakwa Sands (Pty) Ltd

New Concept Mining (Pty) Limited

Northam Platinum Ltd - Zondereinde

PANalytical (Pty) Ltd

Paterson and Cooke Consulting Engineers (Pty) Ltd

Polysius A Division Of Thyssenkrupp Industrial Solutions (Pty) Ltd

Precious Metals Refiners

Rand Refinery Limited

Redpath Mining (South Africa) (Pty) Ltd

Rosond (Pty) Ltd

Royal Bafokeng Platinum

Roymec Tecvhnologies (Pty) Ltd

Runge Pincock Minarco Limited

Rustenburg Platinum Mines Limited

Salene Mining (Pty) Ltd

Sandvik Mining and Construction Delmas (Pty) Ltd

Sandvik Mining and Construction RSA(Pty) Ltd

SANIRE

Sasol Mining(Pty) Ltd

Sebilo Resources (Pty) Ltd

SENET (Pty) Ltd

Senmin International (Pty) Ltd

Smec SA

SMS Siemag South Africa (Pty) Ltd

Sound Mining Solutions (Pty) Ltd

South 32

SRK Consulting SA (Pty) Ltd

Technology Innovation Agency

Time Mining and Processing (Pty) Ltd

Tomra Sorting Solutions Mining (Pty) Ltd

Ukwazi Mining Solutions (Pty) Ltd

Umgeni Water

VBKOM Consulting Engineers

Webber Wentzel

Weir Minerals Africa

WorleyParsons (Pty) Ltd

Forthcoming SAIMM events...

EXHIBITS/SPONSORSHIP
Companies wishing to sponsor and/or exhibit at any of these events should contact the conference co-ordinator as soon as possible

For the past 120 years, the Southern African Institute of Mining and Metallurgy, has promoted technical excellence in the minerals industry. We strive to continuously stay at the cutting edge of new developments in the mining and metallurgy industry. The SAIMM acts as the corporate voice for the mining and metallurgy industry in the South African economy. We actively encourage contact and networking between members and the strengthening of ties. The SAIMM offers a variety of conferences that are designed to bring you technical knowledge and information of interest for the good of the industry. Here is a glimpse of the events we have lined up for 2016. Visit our website for more information.

SAIMM
THE SOUTHERN AFRICAN INSTITUTE OF MINING AND METALLURGY

For further information contact:
Conferencing, SAIMM
P O Box 61127, Marshalltown 2107
Tel: (011) 834-1273/7
Fax: (011) 833-8156 or (011) 838-5923
E-mail: raymond@saimm.co.za

SAIMM DIARY

2016

- **CONFERENCE**
  Innovations in Mining Conference 2016
  19–20 July 2016, Holiday Inn Bulawayo
- **SCHOOL**
  Production of Clean Steel
  25–26 July 2016, Mintek, Randburg
- **CONFERENCE**
  Hydrometallurgy Conference 2016 *'Sustainable Hydrometallurgical Extraction of Metals'* in collaboration with MinProc and the Western Cape Branch
  31 July–3 August 2016, Belmont Mount Nelson Hotel, Cape Town
- **CONFERENCE**
  The Tenth International Heavy Minerals Conference *'Expanding the horizon'*
  16–18 August 2016, Sun City, South Africa
- **CONFERENCE**
  MINESafe Conference Striving for Zero Harm
  31 August–2 September 2016, Emperors Palace, Hotel Casino Convention Resort,
- **CONFERENCE**
  Mining for the Future 2016 *'The Future for Mining starts Now'*
  12–13 September 2016, Electra Mining, Nasrec, Johannesburg
- **CONFERENCE**
  AMI Ferrous and Base Metals Development Network Conference 2016
  19–21 October 2016, Southern Sun Elangeni Maharani, KwaZulu-Natal
- **COLLOQUIUM**
  The Young Professionals Week
  14th Annual Student Colloquium
  25 October 2016, Mintek, Randburg

2017

- **CONFERENCE**
  3rd Young Professionals Conference
  9–10 March 2017, Innovation Hub, Pretoria
- **CONFERENCE**
  4th Mineral Project Valuation School
  27–29 June 2017, The University of the Witwatersrand, Johannesburg
- **SYMPOSIUM**
  AfriRock 2017: ISRM International Symposium *'Rock Mechanics for Africa'*
  2–7 October 2017, Cape Town Convention Centre, Cape Town
- **CONFERENCE**
  6th Sulphur and Sulphuric Acid 2017 Conference
  9–10 March 2017, South Africa

MINING WITH

ELBROC
MINING PRODUCTS (PTY) LTD

Safety First!

OMNI 150

AVAILABLE IN 20 TON AND 40 TON

The 'Sacrificial' hydraulic prop that performs in accordance with the COMRO guidelines for rockburst and rockfall conditions.

- 150mm diameter
- Covers stoping widths up to 6m
- Controlled yielding

- Safe remote installation
- Superb energy absorption
- Light, easy and quick to install
- Constant support resistance
- Cannot be over extended
- Resilient in rockburst conditions
- Standard attachments
- Can accommodate numerous seismic events
- Reusable for specific applications (only 20 Ton prop)
- Longer lengths available on request

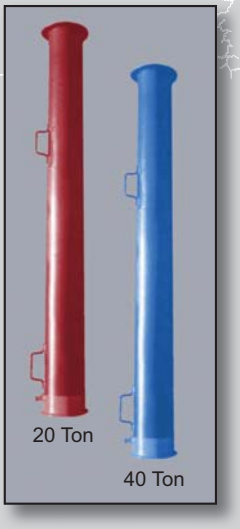

T-Prop

ELBROC TEMPORARY SUPPORT PROP

- Elbroc T-Prop performs in accordance with guidelines for rockfall conditions
- Easy installation
- Covers stoping widths from 0.9 meters to 4.8 meters
- Other sizes available on request
- Various lengths load spreaders available – 140m, 400m (standard) and 600m

- Remote release from 5 meters away
- Can be refurbished
- Cam foot piece can be used on various sizes
- Load spreader and hooks for safety netting

FOR OUR FULL PRODUCT RANGE
PLEASE VISIT OUR WEBPAGE

SABS ISO 9001

a member of the rbh royal bafokeng holdings

Tel: 011 974-8013 • sales@elbroc.co.za
www.elbroc.co.za

mogs mining, oil and gas services